THE UNIVERSITY *of* EDINBURGH

Monitoring intracellular redox potential in single cells using SERS nanosensors

THE UNIVERSITY
of EDINBURGH

Kate Fisher

Degree of Doctor of Philosophy

2015

Declaration

I hereby declare that the work presented in this thesis is my own unless otherwise credited and that the work has not been submitted for any other degree or professional qualification.

Abstract

Intracellular redox potential affects cellular function and its dysregulation is associated with disease. Current methods of monitoring intracellular redox potential are limited because they typically only report potentials of the redox buffer glutathione. Our group has developed redox-active probe molecules that change bond order depending on the probe oxidation state, and are instead sensitive to overall redox potential within the cell. Gold nanoshells coated with the probe form a novel intracellular redox nanosensor, and spectral discrimination of the oxidised and reduced states by Surface-Enhanced Raman Scattering (SERS) allows calculation of redox potential.

Prior work by the group provided basic proof-of-principle for its use in measuring intracellular redox potential. The aim of this project, therefore, was to develop the tools and techniques to enable its application to meaningful biological questions, and extend the method into a pathologically relevant cell line. The initial stages of the project standardised the functionalisation of gold nanoshells with the NQ probe molecule and the application of the nanosensors to the A549 human lung cancer cell line. Toxicity tests confirmed the nanosensor was non-toxic. A protocol was then developed for rapidly obtaining SERS maps to enable localisation of nanosensors within the cell. This was successful, and the protocols can be applied to any combination of adherent cell type and nanosensor. A bespoke piece of software was created to determine redox potential and pH from SERS maps to produce a colourmap showing spatial variation of redox potential and pH with subcellular resolution. This software enables more rapid and precise calculation of redox potential or pH than manual processing. As a test case, changes in intracellular redox potential in response to treatment with toxic metal nanoparticles were studied and shown to correlate with other measures of oxidative stress.

Hypoxia (abnormally low oxygen levels) is relevant in disease. Investigating redox potential in hypoxic cells requires precise control of the oxygen concentration during

the acquisition of SERS spectra. To facilitate such experiments, a specialised imaging chamber was designed, constructed and tested. Such environmental control enables experiments to be carried out at various oxygen concentrations as well as under optimal cellular physiological conditions, enabling not only the response to alterations in oxygen levels to be studied but also extending the biological model system to more closely reflect animal physiology.

Finally, a device was constructed that allowed the acquisition of SERS spectra from both intracellular and extracellular nanosensors in the same experiment, as the relationship between intracellular and extracellular redox potential is incompletely understood. The intracellular and extracellular nanosensors are spatially separated, allowing clear discrimination of the SERS spectra obtained simply by changing the orientation of the device. This device enables the effect of quantitative modification of extracellular redox potential on intracellular redox potential to be investigated.

In summary, the work has greatly extended a method of measuring intracellular redox potential. It was taken from the proof-of-principle stage to being a robust method, capable of providing useful quantitative biological information. Improvements have been made in production and toxicity testing of the nanosensors, robustness of SERS data acquisition and analysis, environmental control during SERS data acquisition and application to disease-relevant cell culture models. The result is that we are now able to rapidly and reproducibly determine intracellular redox potential in single cells.

Lay Summary

Intracellular redox potential is an important property involved in many functions inside biological cells. It is tightly regulated, and diseases such as diabetes, cancer and neurodegeneration are associated with dysregulation. Intracellular redox potential is challenging to measure as it consists of many different components. Most methods only measure the most abundant component, glutathione, however it is not firmly established that the amount of glutathione is a true reflection of overall redox potential. Our group has developed a method to measure overall redox potential that does not measure individual contributions of each component. Instead, we have constructed nanosensors that respond to changes in overall redox potential, which we can measure with a technique called Surface-Enhanced Raman Scattering (SERS).

Previous work by the group provided basic proof-of-principle for the use of these nanosensors in measuring intracellular redox potential. The aim of this project, therefore, was to develop the tools and techniques to enable its application to meaningful biological questions, using a cell type that is more relevant to human disease. The results confirm that the nanosensors are non-toxic in cells and the protocols developed can also be applied to any combination of cell type and nanosensor. A bespoke piece of sofware was created to analyse the data obtained, which enabled a rapid and more precise determination of intracellular redox potential than previous methods. As a test case, changes in intracellular redox potential in response to treatment with toxic metal nanoparticles were studied and shown to correlate with other methods of measuring toxicity in cells.

Hypoxia is the result of too little oxygen being available for the usual process cells use to generate energy. It occurs in cancer and has been shown to contribute to treatment resistance. In order to investigate intracellular redox potential under these low oxygen conditions, the amount of oxygen available to the cells must be carefully controlled. A specialised airtight chamber was designed, built and tested to enable SERS to be performed on cells maintained in low oxygen levels. This chamber also

allows an environment to be maintained that more closely resembles that found in animal physiology.

Finally, a device was constructed which allowed both intracellular and extracellular redox potential to be measured during the same experiment. This enables us to modify the extracellular potential to known values and investigate how the intracellular redox potential changes in response to such modifications. This is important as the relationship between the intracellular and extracellular potential is incompletely understood.

In summary, this project has greatly extended a method of measuring intracellular redox potential. It was taken from the proof-of-principle stage to being a robust method, capable of providing useful quantitative biological information. The result is that we are now able to rapidly and reproducibly determine intracellular redox potential in single cells.

Publications

The following publication formed the basis for Section 1.4. A pdf version of the paper is included in the Appendix.

K.M.Fisher and C.J. Campbell, Ratiometric biological nanosensors., *Biochemical Society Transactions* 42 (4) 899-904, 2014.

Acknowledgements

Firstly, I would like to thank my supervisor, Dr Colin Campbell, for giving me the opportunity to work on this project and whose patient guidance, encouragement and support have been invaluable. From our research group I am particularly grateful to Lauren Jamieson and Dr Jing Jiang for providing me with the calibration data for Chapter 4, and the rest have always kept me entertained: Anna-Maria Maciejuk, Dr Patrick Thomson, Vicky Camus, Hannah Johnston, Dr Lina Mati, Dr Sarah McAughtrie and Sam Stanfield. I would also like to thank my second supervisor, Prof Ken Donaldson, and Jen McLeish at the MRC Centre for Inflammation Research, University of Edinburgh, for providing the cells and the engineered metal nanoparticles for Chapter 5, and for advising me on toxicological aspects.

I am grateful to Prof Eleanor Campbell and her group (particularly Dr Kirsten Strain, Dr Oleg Nerushev and Dr Andrei Gromov) for use of the Raman spectrometer and their advice, and also to Dr Eliza Makou and Dr Nicky McIntosh for use of their autoclave and lab. The school's support staff have also been incredibly helpful and have contributed to my enjoyment of my time here.

The following group of people have done an outstanding job in restoring my sanity on a daily basis: my PhD partner in crime Richard Perry (for the #megarofls), Dr Charlotte Brady (for Disney, Marvel and gin), Dr Martin Ward and Dr Damion Corrigan (for their general wisdom and calm, unstinting patience), Lauren again (for her inspiration), Ewen Blair (for his internet curation), David Ferrier, Andrew Piper, Elaine Sutherland, Dr Murray Low, Dr Dave French, Simon Reeves, Justin Elliott and Anthony Buchoux. Fellow demonstrators Dr Calum Waterson, Faye Cruickshank and Dr Matt Wilson made Friday afternoon first year undergraduate labs even more fun than the first years themselves did.

Finally and most importantly, I would never have been able to even contemplate doing a PhD were it not for the love, support and encouragement of my family and Jamie. This thesis is dedicated to them.

Contents

List of Figures

List of Tables

List of Abbreviations

AAPH	2,2′-Azobis(2-amidinopropane) dihydrochloride
AgNP	Silver nanoparticles
ANOVA	Analysis of variance
AQ	bis-(2-anthraquinone carboxamide)
ATP	Adenosine triphosphate
CCD	Charge-coupled device
Cys	Cysteine
CySS	Cystine
DCF	Dichlorofluorescein
DCFH	Dichlorofluorescin
DCFH-DA	Dichloro-dihydro-fluorescein diacetate
DMEM	Dulbecco's modified Eagle's medium
DMSO	Dimethyl sulfoxide
DNA	Deoxyribonucleic acid
ECM	Extracellular matrix
ETC	Electron transfer chain
FACS	Fluorescence-activated cell sorting
FAD	Flavin adenine dinucleotide
FBS	Foetal bovine serum
GPx	Glutathione peroxidase
GR	Glutathione reductase
GSH	Glutathione
GSSG	Glutathione disulfide
H_2O_2	Hydrogen peroxide
HBSS	Hanks Balanced Salt Solution
HO-1	Hemeoxygenase-1
HOCl	Hypoclorous acid

HOMO	Highest occupied molecular orbital
HPF	2-[6-(4´- hydroxy)phenoxy-3H-xanthen-3-on-9-yl]benzoic acid
LDH	Lactate dehydrogenase
LOOH	Lipid hydroperoxide
LUMO	Lowest unoccupied molecular orbital
NAD^+	Oxidised nicotinamide adenine dinucleotide
NADH	Reduced nicotinamide adenine dinucleotide
$NADP^+$	Oxidised nicotinamide adenine dinucleotide phosphate
NADPH	Reduced nicotinamide adenine dinucleotide phosphate
NIR	Near infra-red
NQ	1,8-diaza-4,5-dithia-1,8-di(2-chloro-[1,4]-naphthoquinone-3-yl)octane
NQ-NS	NQ-functionalised nanoshells
NS	Nanoshells
$O_2^{\bullet-}$	Superoxide anion
$ONOO^-$	Peroxynitrite
PBS	Phosphate-buffered saline
PDI	Protein disulfide isomerase
PDMS	Polydimethylsiloxane
PLL	Poly-L-lysine
Prx	Peroxiredoxins
qPCR	Quantitative real-time polymerase chain reaction
RNA	Ribonucleic acid
RNS	Reactive nitrogen species
ROS	Reactive oxygen species
SERS	Surface-enhanced Raman scattering
SNR	Signal to noise ratio
TEM	Transmission electron microscopy
Trx	Thioredoxin
TrxR	Thioredoxin reductase
ZnONP	Zinc oxide nanoparticles
$^{\bullet}NO$	Nitric oxide
$^{\bullet}OH$	Hydroxyl radical

Chapter 1: Introduction

1.1 Intracellular redox potential

Redox potential is the propensity of a chemical species to donate or accept electrons. The redox potential of a redox couple depends on this propensity together with the concentrations of the oxidised and reduced species. The Nernst equation allows the calculation of redox potentials under non-standard conditions [1]:

$$E = E^{\ominus} + \frac{RT}{nF} ln \frac{[\mathrm{Ox}]}{[\mathrm{Red}]} \tag{1.1}$$

where E is the redox potential (V), $E^{\ominus}$ is the standard redox potential (V), R is the universal gas constant (J K^{-1} mol^{-1}), T is the temperature (K), n is the number of electrons transferred, F is the Faraday constant (C mol^{-1}), [Ox] is the concentration of oxidised species and [Red] is the concentration of reduced species.

Electron transfer drives energy transduction in biological cells. Electrons are transferred from reduced nicotinamide adenine dinucleotide (NADH) to molecular O_2 via a set of proteins that make up the electron transfer chain. As many functions of the cell are redox regulated (e.g. signalling, protein, DNA and RNA synthesis, and cell growth and death), the redox potential as defined by the Nernst equation clearly has biological significance [2–4].

The overall redox potential of a cell can be viewed as the balance between the generation of reactive oxygen/nitrogen species (ROS/RNS; Figure 1.1) and the antioxidants that degrade them. Examples of ROS and RNS are superoxide anion ($O_2^{\bullet -}$), hydrogen peroxide (H_2O_2), hydroxyl radical ($^{\bullet}OH$), hypoclorous acid (HOCl), nitric oxide ($^{\bullet}NO$) and peroxynitrite ($ONOO^-$). Most ROS generation is endogenous, with some of the main souces described below:

As a by-product of respiration. During cellular respiration, single electrons are transferred between complexes of proteins in the mitochondrial electron transfer

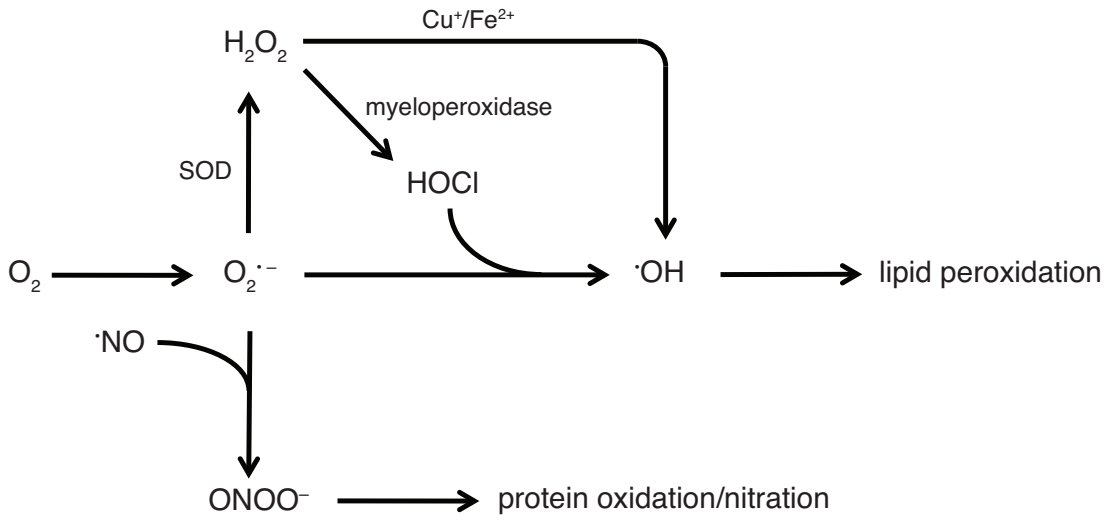

Figure 1.1: Pathways of intracellular RNS production: breakdown of $O_2^{\bullet-}$ leading to various ROS and the reactive nitrogen species peroxynitrite, $ONOO^-$.

chain (ETC). This flow of electrons drives protons from the mitochondrial matrix into the intermembrane space to create a proton gradient across the inner mitochondrial membrane, which drives the production of adenosine triphosphate (ATP), the energy unit of the cell [5]. The flow of electrons through the ETC ends with the controlled reduction of molecular O_2 to H_2O. However, due to the high affinity of O_2 for electrons, there are points within the ETC where a single electron can be transferred to O_2 instead, producing superoxide, $O_2^{\bullet-}$. Production of $O_2^{\bullet-}$ increases with increasing $[O_2]$, an increased $NADH/NAD^+$ ratio, and an increased protonic potential across the inner mitochondrial membrane [6–9].

NADPH oxidases. Nicotinamide adenine dinucleotide phosphate (NADPH) oxidases are a family of membrane proteins that transfer one electron from NADPH, on one side of the membrane, to O_2 on the other to produce $O_2^{\bullet-}$. They were initially discovered in phagocytic cells as the component of the 'respiratory burst', in which large concentrations of superoxide are released inside the cell to kill pathogens [10]. However, isoforms have since been discovered in most cell types and in various subcellular locations [11, 12]; the superoxide produced has been shown to play a role in signalling through its conversion to H_2O_2 (see below).

Protein folding. Protein function depends on their 3-dimensional structure and the structures of extracellular proteins are often stabilised by disulfide bonds [5].

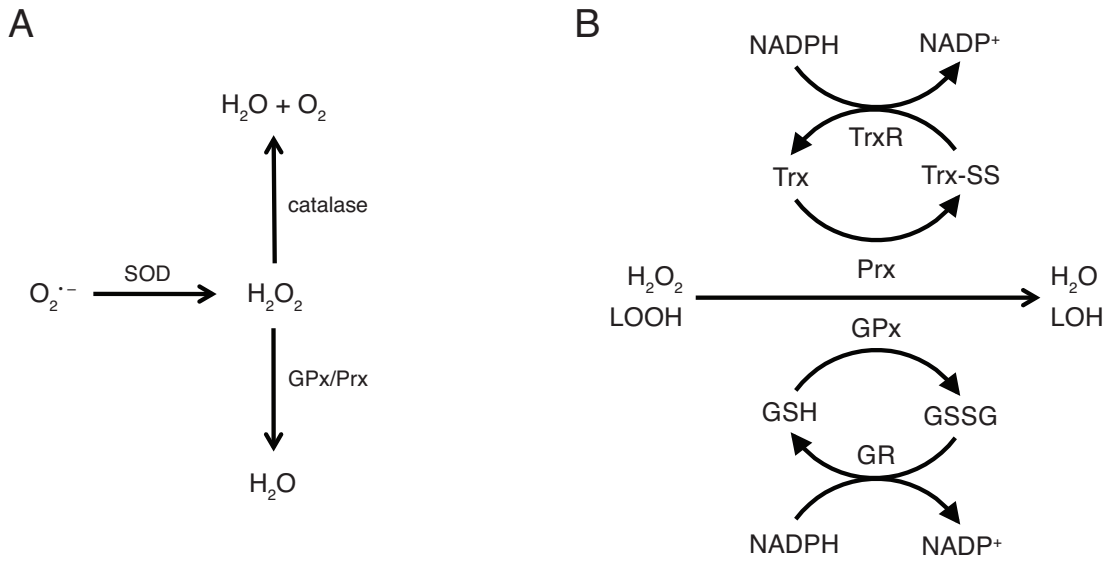

Figure 1.2: Degradation of ROS. (A) Degradation of $O_2^{\bullet -}$ and H_2O_2. (B) Degradation of H_2O_2 and lipid hydroperoxides (LOOH) via the reversible oxidation of glutathione (GSH) and thioredoxin (Trx) by glutathione peroxidases (GPx) and peroxiredoxins (Prx). GSH and Trx are regenerated by glutathione reductase (GR) and thioredoxin reductase (TrxR), respectively, both of which transfer the electrons required from NADPH.

Extracellular proteins undergo folding in the endoplasmic reticulum, where proteins such as protein disulfide isomerase (PDI) catalyse the oxidation of two cysteine residues into a disulfide. The protein Ero1 catalyses the transfer of electrons from PDI to molecular O_2 to produce H_2O_2 [13–16].

Detoxification of $O_2^{\bullet -}$ is a multi-step process which proceeds via intermediate ROS (Figure 1.2 A). $O_2^{\bullet -}$ can either spontaneously dismutate or be enzymatically reduced by superoxide dismutases to H_2O_2 [17], which can then be further reduced to $^{\bullet}OH$, HOCl or H_2O through, for example, Fenton reactions, myeloperoxidase activity and catalase activity, respectively [18] (Figure 1.1). $O_2^{\bullet -}$ can also react with $^{\bullet}NO$ to generate peroxynitrite, $ONOO^-$. These intermediate ROS can cause harmful oxidation of biomolecules, however some signalling pathways use these oxidised biomolecules to sense the redox status of the cell, as discussed further below. Antioxidant enzymes or small molecules transfer electrons from thiol/disulfide redox couples to reduce/eliminate these intermediate ROS and oxidised biomolecules; these couples are oxidised in the process and then re-reduced by accepting electrons from other species (Figure 1.2 B; reviewed in [18–20]). There are several thiol/disulfide redox couples in the cell involved in the reduction of ROS and

oxidised biomolecules and the major ones are described below:

Glutathione: the glutathione couple (glutathione/glutathione disulfide (GSH/GSSG); Figure 1.3) is considered the main redox buffer in the cell as it is mostly in the reduced form (GSH), and with an intracellular concentration range of 1-11 mM it forms the largest pool of reducing equivalents [2]. It reduces lipid hydroperoxides and H_2O_2 through the catalytic activity of two enzymes, glutathione peroxidase (GPx) and glutathione reductase (GR) [21, 22] (Figure 1.2 B). Glutathione peroxidase is first oxidised by hydroperoxides and is then glutathiolynated at selenium by one molecule of GSH. A second molecule of GSH binds to the first and GSSG is released from the now reduced peroxidase [23, 24]. Glutathione reductase binds NADPH and GSSG and transfers two electrons from NADPH to GSSG via a flavin adenine dinucleotide (FAD) cofactor [25]. Cysteine residues of proteins can also be modified by GSH, modulating their function [26], discussed below on page 9.

Thioredoxin: thioredoxins (Trx) enzymatically reduce disulfide bonds in proteins and are regenerated by thioredoxin reductase (TrxR) [18]. Their targets include transcription factors and other proteins involved in cell proliferation [27], underscoring the importance of redox regulation in cell function. In addition to their reduction by glutathione peroxidase, hydroperoxidases can also be reduced by peroxiredoxins (Prx), which obtain the two electrons for this reduction from thioredoxin [28–30]. Thioredoxin is in turn bound and reduced by thioredoxin reductase, which contains an active site similar to that in glutathione reductase, again with NADPH as the electron donor [31, 32] (Figure 1.2 B).

NADPH/NADP$^+$: the nicotinamide adenine dinucleotide phosphate (NADPH/NADP$^+$; Figure 1.4) couple provides the electrons to reduce both GSSG and oxidised thioredoxin (see above). NADP$^+$ is reduced back to NADPH primarily by glucose 6-phosphate dehydrogenase in the pentose phosphate pathway, but also through the action of NADP$^+$-dependent isocitrate dehydrogenases, NADP$^+$-dependent malic enzymes and mitochondrial transhydrogenase [33].

Ascorbic acid/dehydroascorbic acid: Ascorbic acid (vitamin C; Figure 1.5) is an important antioxidant both intracellularly and extracellularly, and can degrade a

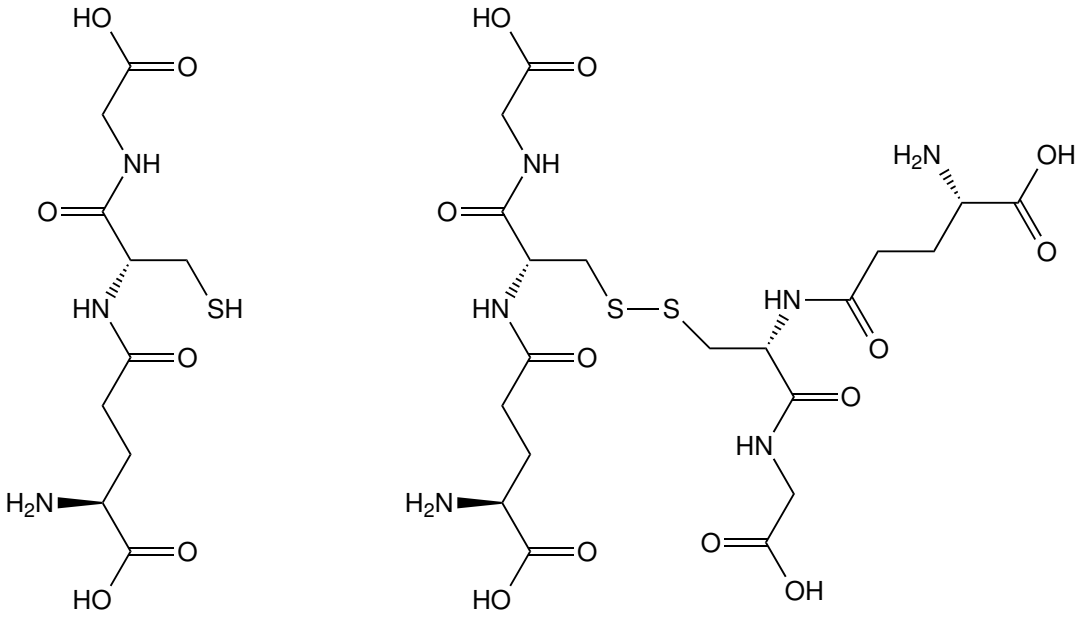

Figure 1.3: The structures of glutathione (GSH; left) and glutathione disulfide (GSSG; right).

number of ROS and lipid hydroperoxides, the latter via α-tocopherol (vitamin E) [34]. It is oxidised to dehydroascorbic acid, which can be reduced back to ascorbic acid by both GSH and thioredoxin reductase [35, 36].

Cysteine/cystine: the other major redox couple is the cysteine/cystine couple [37], which has an important role in extracellular redox potential and is discussed in Section 1.2.

Importantly, these redox couples are not necessarily in equilibrium with each other, can vary independently of each other and are at different concentrations in different organelles [4]. For instance, the concentration of intracellular ascorbic acid was shown to decrease in a human endothelial cell line in response to exogenously generated $^{\bullet}$NO, but there was no change in the concentration of GSH [38]. Another study in male rats showed that concentrations of GSH decreased in certain brain regions in response to hypoglycaemia, but levels of ascorbic acid or α-tocopherol did not change [39]. In terms of inhomogeneity, the nucleus appears to be at a more reducing potential than the cytoplasm, possibly to protect critical cysteine residues of transcription factors from becoming oxidised [40]. Although there is some question as to the reliability of results reporting nuclear GSH concentrations (reviewed in [4]),

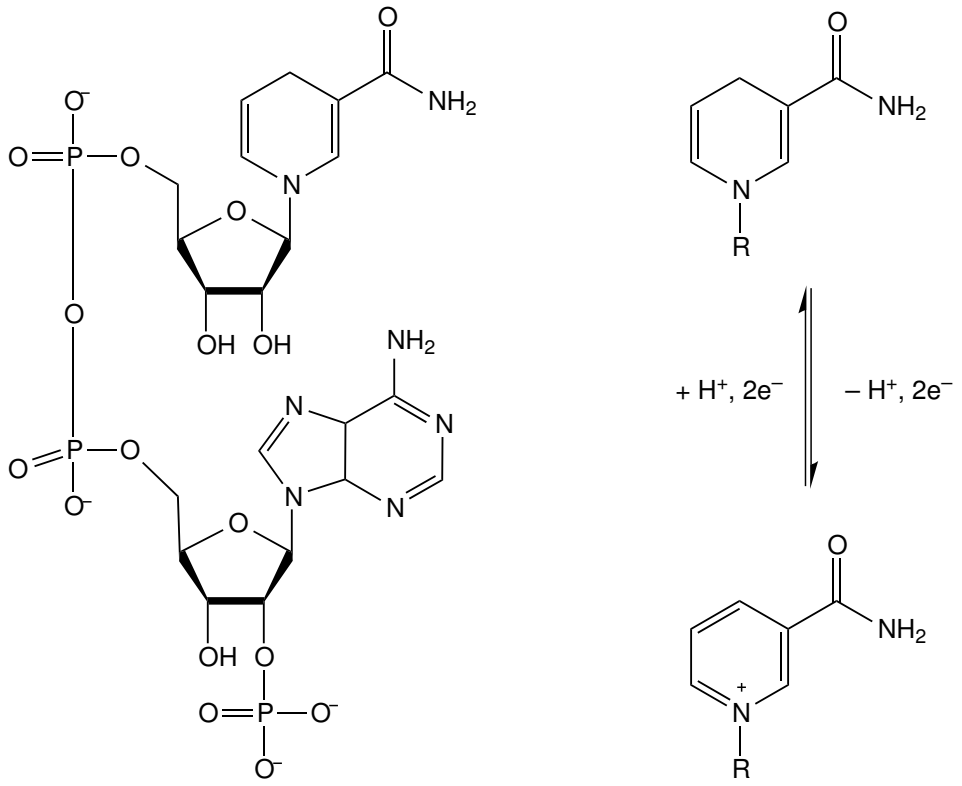

Figure 1.4: The structure of reduced nicotinamide adenine dinucleotide phosphate (NADPH; left) and interconversion between reduced (NADPH) and oxidised ($NADP^+$) forms (right).

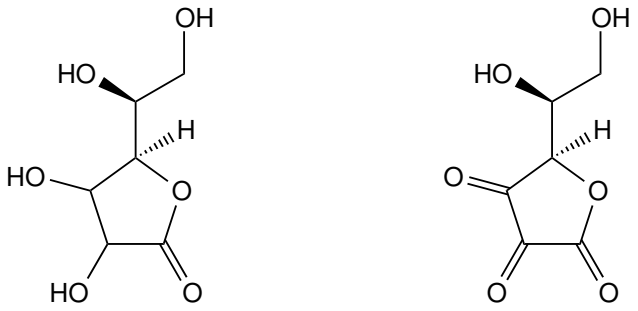

Figure 1.5: The structures of ascorbic acid (left) and dehydroascorbic acid (right).

increased protein *S*-glutathionylation has been shown in the cytoplasm compared to the nucleus in response to oxidative stress caused by glucose or glutamine depletion [41] which could indicate a higher nuclear GSH:GSSG ratio. More recently, a study using genetically-encoded fluorescent proteins equilibrated with the GSH/GSSG redox couple indicated that the GSH redox potential in the nucleus was similar to that in the cytoplasm [42]. As the thioredoxin redox potential has been shown to be slightly more negative in the nucleus than in the cytoplasm [43], it would seem that the overall nuclear redox potential is more negative than the cytosolic redox potential.

It is generally suggested that the overall mitochondrial redox potential is more reduced than the cytoplasm [44], however some studies have shown the glutathione redox potential in the intermembrane space to be more oxidised than that in the cytoplasm [45, 46] and another found no difference [47]. Similarly, in the matrix, the glutathione redox potential has been found to be both similar to that in the cytoplasm [45, 47] and more oxidised [46]. The redox potential of thioredoxin has been found to be more reducing [48], so it may be that, as with the nucleus, the overall redox potential in mitochondria is more reducing than the cytoplasm. This more reducing environment may protect mitochondria from superoxide generated by respiration. Finally the endoplasmic reticulum is held at a more oxidising potential to facilitate protein folding by encouraging the formation of disulfide bridges [49–51], possibly due to the production of H_2O_2 during protein folding (see above).

Together, these features allow localised and dynamic responses to differing concentrations of ROS and fine control of cell function and homeostasis. As mentioned above, intracellular redox potential both controls and reflects the biological activity of cells. An example of this is the change in redox potential over the lifetime of the cell, for example, proliferating cells have a more reduced (negative) potential than non-proliferating cells [3, 52], while cell death via apoptosis is characterised by a more oxidised (positive) potential [2] (Figure 1.6). Further increases in potential result in necrosis, an uncoordinated form of cell death, where

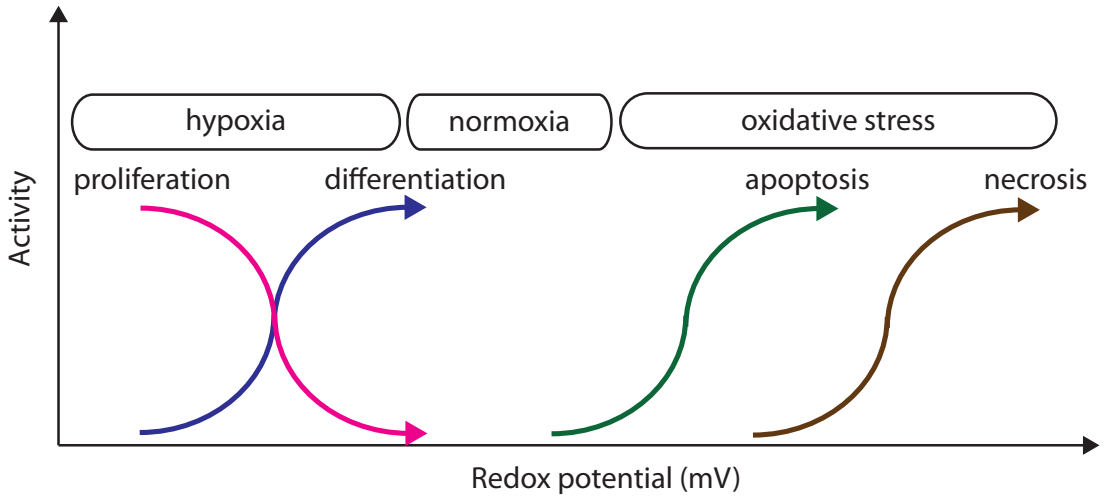

Figure 1.6: The variation of redox potential throughout the cell cycle. Adapted from [2].

cells lyse and the intracellular and extracellular potentials reach thermodynamic equilibrium.

The means by which such regulation is achieved is still being unravelled. Most ROS react fairly indiscriminately with biological molecules and don't diffuse very far from their site of production. The exceptions are H_2O_2 and $^{\bullet}NO$, which have been identified as signalling molecules at low concentrations as they have slow reaction rates with other biological molecules and require transport across membranes (reviewed in [53–56]). The specificity required for signalling can occur through colocalisation of ROS and their target proteins and also the structural features of target proteins. ROS are produced in localised regions of the cell and if target proteins were also localised to the same subcellular location, this would provide some specificity. For example, peroxiredoxins degrade H_2O_2, but a high concentration of H_2O_2 produced in one region will overwhelm this antioxidant capacity locally, enabling oxidation of other molecules in the region [57]. Target proteins contain structural features that can increase the rate of reaction of ROS with specific residues. Many proteins contain cysteine residues with a pK_a much less than that of free cysteine, due to positively charged or polar neighbouring residues [58]. Such a low pK_a means that the cysteine residue exists as the anionic form at physiological pH, which is a stronger nucleophile than the neutral form and therefore more reactive [59]. For example the catalytic site cysteine of the protein

tyrosine phosphatase PTP-1B has a pK_a of 5-5.6, compared to the pK_a of 8-9 of free cysteine [60, 61]. In PTP-1B, the reactive cysteine is reversibly oxidised by H_2O_2 and inhibits its catalytic activity [62, 63]. The oxidised intermediate has been identified as being a sulfenic acid [62, 64], a sulfenyl-amide [63] or glutathionylated [65, 66]; the latter two protect the sulfenic acid from further irreversible oxidation.

Other structural features of proteins also contribute to reactivity of cysteine residues, for example the pK_a of the peroxidatic cysteine in the peroxyredoxin Prx2 is estimated to be 5-6, similar to that of PTP-1B, but the rate constants of its reaction with H_2O_2 is orders of magnitude faster: 1.3×10^7 M^{-1} s^{-1} compared to 20 M^{-1} s^{-1} [64, 67]. This is most likely to be due to differences in the catalytic site environment, that do not affect pK_a (such as the precise tertiary structure), as other oxidants had much lower rates of reaction with Prx2 [67].

Proteins can undergo various post-translational modifications that affect their structure and therefore function [5]. Modifications relevant to redox environment include *S*-glutathionylation (GSH-protein adduct), *S*-nitrosylation (NO-protein adduct) and the formation of sulfenic/sulfinic acids or disulfide bonds [53] (Figure 1.7). S-nitrosylation and formation of sulfenic acids or disulfide bonds can also be followed by S-glutathionylation, as seen with PTP-1B above [26, 65, 66] and Prx2 [57]. These modifications are reversible through the action of enzymes such as glutaredoxin, thioredoxin, sulfiredoxin and PDI [68–70]. Phosphatases are critical modulators of intracellular signalling pathways [5]. The family of protein tyrosine phosphatases, to which PTP-1B belongs, all contain a catalytic site cysteine with low pK_a, which can be oxidised thus disabling the phosphatase activity [71–73]. Thus redox-regulated modifications provide a variety of means of controlling protein function and therefore signalling.

Reactive cysteine residues have been found in proteins involved in many different cellular functions. Transcription factors are a class of proteins that bind to specific sequences of DNA, increasing or decreasing expression of a gene. Nrf2 is an example of a transcription factor that is regulated by redox potential. Under normal conditions, levels of cytoplasmic Nrf2 are controlled by its interaction with another

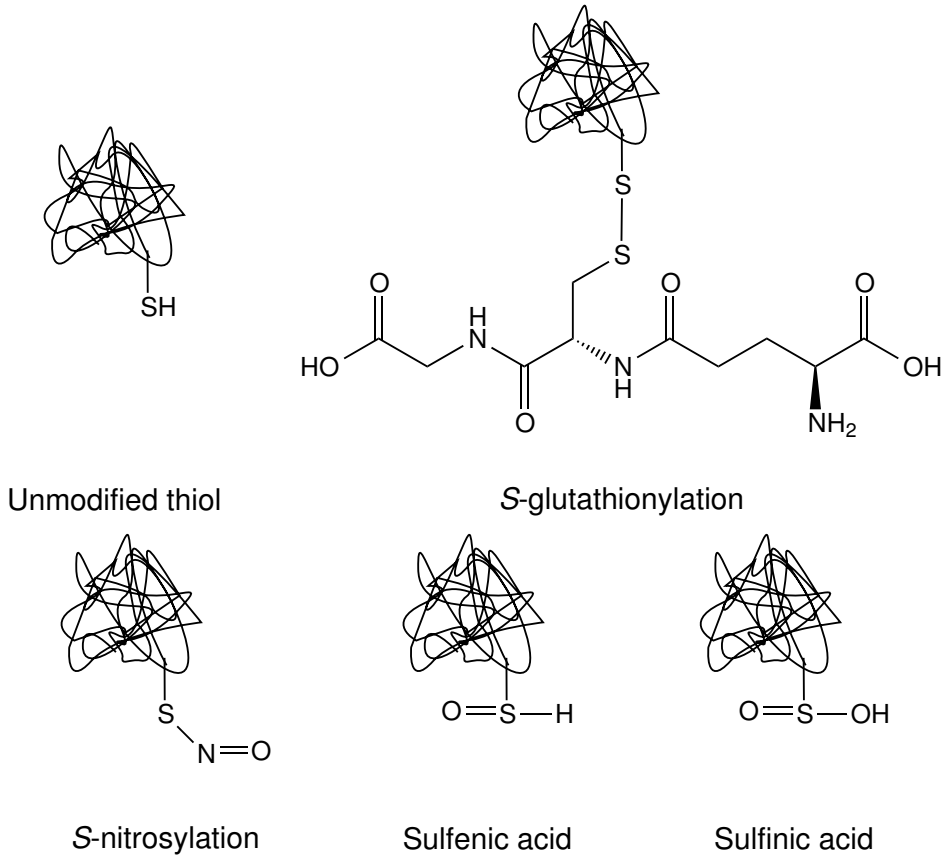

Figure 1.7: Common cysteine residue modifications in proteins: *S*-glutathionylation (top right), *S*-nitrosylation (bottom left), sulfenic acid (bottom middle) and sulfinic acid (bottom right).

protein, Keap1, which targets Nrf2 for degradation [74]. This interaction is dependent on three cysteine residues in Keap1, which when oxidised induce a conformational change, inhibiting binding with Nrf2 [75]. Nrf2 is then able to translocate to the nucleus and upregulate expression of its target genes, many of which are antioxidants and include the NADPH regenerating enzymes glucose 6-phosphate dehydrogenase and malic enzyme, as well as glutathione perioxidase and glutathione reductase [76].

Another redox-regulated transcription factor family is the NF-$\varkappa$B family, which upregulates expression of proteins involved in the inflammatory response. The NF-$\varkappa$B family consists of homodimers or heterodimers from a pool of five proteins: p50, p52, p65, RelB, and c-Rel [77], which, as with Nrf2 , are bound to an inhibitor (I$\varkappa$B) in the cytoplasm when inactive. The DNA-binding ability of the p50-p65 heterodimer has been shown to depend on the redox state of a conserved reactive

cysteine residue in the p50 DNA-binding domain, which must be in the reduced state for binding [78]. Studies have shown that S-glutathionylation, S-nitrosylation and formation of a sulfenic acid at this residue inhibit DNA binding [79, 80]. Another conserved reactive cysteine residue has been identified in the p65 DNA-binding domain, with S-nitrosylation inhibiting DNA binding [81]. NF-$\varkappa$B can be activated by oxidants, either directly or by oxidation of phosphatases that inhibit its activation (reviewed in [77]), which suggests that the reactive cysteine residues in p50 and p65 could be oxidised, but on translocation to the nucleus these residues need to be reduced in order to bind DNA. Nuclear thioredoxin has been shown to reduce the p50 reactive cysteine residue and promote DNA binding [82–84]. As mentioned above, the thioredoxin redox potential is probably more reduced in the nucleus than in the cytoplasm [43], and together with evidence that there is little or no change in nuclear redox potential in response to stimuli that increase the cytoplasmic redox potential [41], this suggests that even with oxidative induction of NF-$\varkappa$B the relevant cysteines can still be reduced in the nucleus.

One of the genes upregulated by NF-$\varkappa$B is cyclin D1, an important regulator of the cell cycle. Cyclin D is required for the transition into the DNA synthesis phase (S phase) from the initial growth phase (G_1) [85]. As NF-$\varkappa$B can be activated by oxidants, this upregulation is consistent with the observation that a more reducing environment inhibits this transition [86, 87]. Additionally, GSH levels have been found to be higher in the second growth and cell division phases (G_2/M phase) than in G_1 [88]. Together, these data suggest that the cell cycle is regulated to some degree by changes in redox potential.

In summary, redox-mediated control of protein structure and function has widespread effects encompassing almost every aspect of cell function. Accurate measurement of intracellular redox potential will enable a better understanding of its influence on biological and pathological processes. In addition, identifying reactive cysteine residues and the results of specific oxidative modifications to them will enable a more structured approach to elucidating the effects of subtle changes in

intracellular redox potential and enable the visualisation of the myriad interactions in pathway maps [89].

1.2 Extracellular redox potential

The extracellular redox potential contains contributions from the same redox couples as intracellular redox potential but at different concentrations. Whereas glutathione is the most abundant intracellular redox couple, the cysteine/cystine (Cys/CySS) redox couple (Figure 1.8) has the highest concentration outside the cell and is tightly regulated [37, 90]. The extracellular redox potential is more oxidising than the intracellular redox potential, and, as with intracellular redox couples, extracellular redox couples are also not necessarily in equilibrium with each other [91, 92].

The extracellular redox potential is important. For example, changes in the ratio of extracellular Cys/CySS have been shown to trigger intracellular signalling pathways resulting in proliferation of murine lung fibroblasts [93] and a more oxidised extracellular potential leads to increased intracellular levels of NADPH oxidase-derived H_2O_2, activating the NF-$\varkappa$B transcription factor [94]. The intracellular GSH/GSSG ratio was unaffected by the increase in extracellular redox potential. The extracellular redox potential is sensed by exofacial thiol residues on plasma membrane proteins of these cells [93, 94]. Some plasma membrane growth factor receptors and ion channels have redox-sensitive extracellular cysteine residues, and may thus be important modulators [95–97]. Recently, neuronal voltage-gated

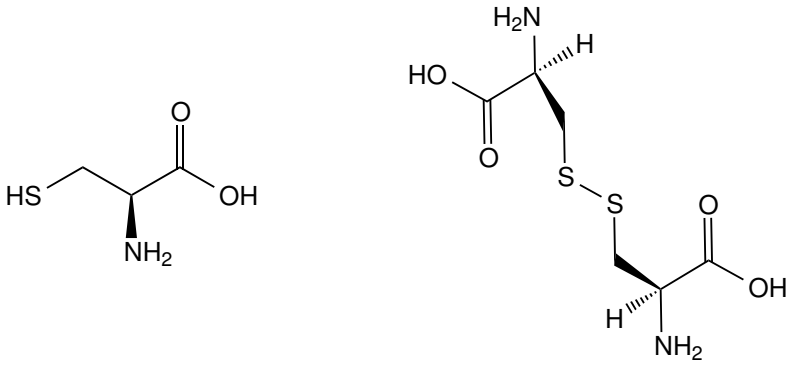

Figure 1.8: The structures of L-cysteine (Cys; left) and cystine (CySS; right).

sodium channels have also been found to contain a conserved extracellular cysteine residue [98], so a variety of cell surface receptors and channels could be responsible for translating changes in extracellular redox potential into intracellular signals.

In the immune system, a more reduced extracellular redox potential causes activation and proliferation of T-cells due to increased availability of cysteine following activity of dendritic cells [99]. Intracellular GSH levels are important in T-cell proliferation [100, 101] and the limiting step in GSH synthesis is intracellular availability of cysteine [99]. Cysteine can either be imported into the cell as cystine (which is at much higher concentrations extracellularly than cysteine) and then reduced, or generated by the transulfuration pathway, in which methionine is converted to cystathionine and cysteine [90]. However, T-cells are not efficient at importing cystine, whereas they are much more efficient at importing cysteine [99], hence their need for an increase in the extracellular Cys/CySS ratio. It is not clear whether dendritic cells directly release cysteine, or whether they release GSH, which is then degraded to release cysteine. Low extracellular levels of GSH are maintained by the activity of two peptidases that cleave GSH into glutamate, cysteine and glycine [90]. Some studies saw no increase in extracellular levels of GSH [99], however others showed that inhibiting the export of GSH decreased extracellular cysteine levels [102], so perhaps export of both cysteine and GSH contribute to the increase in the extracellular Cys/CySS ratio.

As with T-cells, neurons in the brain are unable to import cystine and rely on extracellular export of GSH from astrocytes that is degraded extracellularly [103, 104]. Degraded GSH in the form of cysteine or a cysteine-glycine dipeptide can be imported by neurons and used for intracellular GSH synthesis. Both neurons and astrocytes can import dehydroascorbic acid, whereas only neurons can also import ascorbic acid [105]. Astrocytes are primarily metabolic support cells for neurons, so it is possible that neurons subject to oxidative stress could export dehydroascorbic acid, which would then be taken up by astrocytes, thus protecting neurons from oxidative damage. This is supported by the fact that low levels of dehydroasorbic acid compared to ascorbic acid are found under normal conditions [106].

1.3 Effects of dysregulation

If the concentration of ROS increases beyond the point where antioxidants can degrade them, then the intracellular redox potential becomes more oxidising, causing oxidative stress [20] (Figure 1.6). Several diseases and pathological processes are associated with oxidative stress, such as chronic inflammation, diabetes, atherosclerosis, cancer and neurodegeneration [20, 107, 108]. Oxidation of the extracellular redox potential (for both GSH/GSSG and Cys/CySS couples) has been reported in ageing, smoking, chemotherapy and cardiovascular disease [4]. A decreased ratio of Cys/CySS (so a more oxidising potential) in human blood correlates with increased levels of IL-1β, a secreted signalling molecule involved in chronic inflammation [109], whereas an increased ratio of Cys/CySS has been shown to have a neuroprotective effect on neuronal cultures from a mouse model of Alzheimer's disease [110]. Finally, decreased levels of GSH in the brain have been demonstrated in patients with Alzheimer's disease and multiple sclerosis [111], and decreased levels of both GSH and ascorbic acid were found in the blood of patients with glaucoma [112, 113].

The most obvious consequences of oxidative stress are oxidised proteins. As discussed in Section 1.1, oxidation affects protein function through modification of reactive cysteine residues. Such modifications can be irreversible, for example, the catalytic cysteine of peroxiredoxins can be irreversibly oxidised to sulfonic acid by H_2O_2 [114]. Prolonged inactivation of peroxiredoxins could therefore lead to a localised build-up of irreversibly oxidised proteins, affecting cell function through inhibition of signalling pathways.

The pentose phosphate pathway converts glucose to NADPH and phosphorylated sugars, which can be used in nucleic acid synthesis or transferred back into the glycolytic pathway [5]. Increased levels of $NADP^+$ activate this pathway, therefore prolonged oxidative stress could lead to impaired energy metabolism due to the increased amount of glucose used, especially in the brain. Indeed, mice which were deficient in neuronal SOD2 died at 4 weeks with severe energy failure and growth retardation [115].

Neutrophils can secrete myeloperoxidase, an enzyme that catalyses the degradation of H_2O_2 to HOCl (see Figure 1.1), which can oxidise proteins of the extracellular matrix (ECM; a support structure for cells, for example, collagen in tendons and ligaments or elastin in blood vessels). High levels of myeloperoxidase are found in the blood of patients who had had heart attacks [116] and are a predictor of future adverse cardiac events [117]. Oxidative damage to the ECM by HOCl can disrupt cell adhesion to the matrix, disrupting normal cell signalling [118, 119].

Hypoxia is the result of too little oxygen being available for oxidative phosphorylation and occurs in wound healing, ischaemia and cancer [120, 121]. Redox potential becomes more reducing in hypoxic conditions, both intracellularly [122], and extracellularly [123, 124], presumably due to the increase in the production of NADPH via the pentose phosphate pathway. Paradoxically, hypoxia is also associated with an increase in ROS [46, 125], and may upregulate proliferation through the oxidative inactivation of phosphatases such as PTEN and PTP-1B [126–128]. Mitochondrial ROS are necessary for cellular adaptation to hypoxia and the mitochondrial intermembrane space is more oxidised in hypoxia [46], apparently due to an increase in superoxide production within the ETC [129]. In addition, NADPH oxidase 2 (Nox2) is upregulated by intermittent hypoxia [130], providing an additional source of ROS. The transcription factor Nrf2, activated by a more positive redox potential, not only upregulates expression of antioxidant genes, but is also involved in tumorigenesis [131]. Therefore it would seem that increased ROS levels are important in initiating cancer, but increased antioxidant levels prevent a runaway increase that would lead to cell death.

1.4 Measuring intracellular redox potential

1.4.1 Intracellular biological nanosensors

Intracellular biological nanosensors are an important tool in the biochemist's arsenal of techniques for the study of cellular processes. They can provide information about changes in highly regulated physiological properties critical to cell survival, such as pH and redox potential, as well as concentrations of oxygen and calcium.

The most common intracellular nanosensors are those based on fluorescence. Fluorescence is an established imaging modality that is highly sensitive and can have excellent spatial resolution [132]. Broadly speaking there are two types of fluorescent sensors: small-molecule dyes and proteins. Dyes can be synthesised using well-established chemical routes and their photophysical characteristics are generally well understood. However, they are not very soluble in water and can cross the cell membrane, leading to a decrease in signal over time [133–135]. Conjugating the dye to a nanoparticle substrate can increase the Signal to Noise Ratio (SNR), however care must be taken that the dye does not dissociate from its substrate. Fluorescent proteins derived from jellyfish and corals have enabled researchers to develop a range of proteins, which (through genetic engineering) can be adapted for sensing specific analytes and targeted to specific organelles. Derivatives have been developed that are photostable and have a range of excitation/emission wavelengths that allow spectral multiplexing [136]. However, these genetically encoded sensors are pH sensitive, so changes in pH need to be taken into account when measuring analytes other than pH.

One of the problems with fluorescent sensors is photobleaching, where the fluorescence intensity is degraded due to photon-induced cleavage of the fluorophore [132] Bioluminescence-based sensors do not require an external source of excitation and so avoid this pitfall [137]. Examples of such sensors include sensors for pH [138], Ca^{2+} [139] and protein-protein interactions [140].

There are, broadly speaking, three categories of intracellular sensor:

Reaction-based: these sensors cannot respond reversibly to changes in the intracellular environment, due to the output being a permanent change in structure of the sensor molecule. Such sensors can report on the concentration of the species of interest in order to discriminate between normal and pathological states, but cannot monitor changes in concentrations over time. Examples include an H_2O_2 sensor where fluorescence emission wavelength is changed by the cleavage of a hydrophobic boronic ester by H_2O_2 to generate a hydrophilic alcohol [141] and an

Hg^{2+} sensor where a non-fluorescent spirolactam is converted to a fluorescent rhodamine by a cyclisation of a thiosemicarbazide [142].

Non-ratiometric - the output of these sensors is the intensity of a single emission peak, for example the GCaMP Ca^{2+} sensor has a single emission peak at 510 nm [143]. However, the intensity is dependent on sensor concentration and variations in intensity of the excitation source and therefore a change in intensity does not necessarily correspond to a change in concentration [144].

Ratiometric - the output of these sensors is a ratio of two signals, for example a fluorophore may show two emission peaks in response to different excitation wavelengths, or a nanosensor could utilise two fluorophores, whose emission wavelengths are different [133, 144]. Such sensors can therefore report quantitative values irrespective of sensor concentration or intensity of excitation source.

The most desirable type of intracellular nanosensor is therefore one that combines a ratiometric output with a reversible response, as this allows monitoring changes in the property of interest over time and is independent of absolute sensor concentration. The following two sections will describe selected examples of the latest advances in ratiometric nanosensors for reversibly monitoring various components of intracellular redox potential in live cells.

1.4.2 Reactive oxygen and nitrogen species

As seen in Section 1.1, reactive oxygen species (ROS) and reactive nitrogen species (RNS) are a by-product of cellular respiration (Figure 1.1) and appear to play an important role in signalling [145, 146]. In order to understand the roles of these ROS and RNS better, there is currently a significant effort in developing tools that allow quantification with good spatiotemporal resolution. This section details some recent studies where nanosensors have been employed to study ROS and RNS in cells.

HOCl is produced in leucocytes through peroxidation of chloride ions, and is involved in pathogen destruction [147]. However, unnecessary production of HOCl can lead to inflammatory problems, as in atherosclerosis, neurodegenerative

diseases, rheumatoid arthritis and cancer [148]. Peroxynitrite, $ONOO^-$, is formed from $^\bullet NO$ and $O_2^{\bullet-}$, and is highly reactive, oxidising and nitrating proteins and affecting mitochondrial metabolism, and is also involved in pathogen destruction [149]. Differentiating peroxynitrite from other ROS is difficult since probes must use a selective reaction between peroxynitrite and another molecule that doesn't occur with other oxidising molecules. Polymeric micelles have been developed that are optically bright and photostable, and which react selectively for $ONOO^-$ over $^\bullet NO$, $O_2^{\bullet-}$, $^\bullet OH$ and ClO^- [150]. They have been used to demonstrate that tumour cells generate a higher concentration of $ONOO^-$ compared to normal cells. The generation of such ROS may underpin the genomic instability that is a hallmark of cancer [151].

Photoacoustic imaging detects the ultrasound waves generated from localised heating of tissue resulting from near-infrared laser radiation and enables non-invasive imaging of tissues at high spatial resolution [152]. Pu *et al*. [153] designed fluorescent semiconducting polymer nanoparticles that were photoacoustically active. Coupling these to a ROS-sensitive dye that was selective for $ONOO^-$ and ClO^- allowed the detection of increased concentrations of these species in macrophages stimulated with lipopolysaccharide (LPS) or interferon gamma (IFN-γ). Furthermore, this nanosensor was able to detect *in-situ* generated $ONOO^-$ and ClO^- in living mice injected with zymosan, a polysaccharide that causes inflammation.

BSA-protected gold nanoclusters conjugated with a $^\bullet OH$ specific probe (2-[6-(4´-hydroxy)phenoxy-3H-xanthen-3-on-9-yl]benzoic acid (HPF)), designed so that HPF emission reports on $^\bullet OH$ and the emission of the nanoclusters acts as a reference signal, have been used to measure $^\bullet OH$ concentrations in HeLa cells [154]. The nanoclusters displayed a basal level of fluorescence in resting cells and were able to detect the production of $^\bullet OH$ due to LPS stimulation; however pretreatment with DMSO, an $^\bullet OH$ scavenger, resulted in no increase in $^\bullet OH$ concentration.

1.4.3 Redox potential and antioxidants

As discussed in Section 1.1, intracellular redox potential is a balance between ROS and the antioxidants that degrade them. There are several redox couples within the cell, with the GSH/GSSG couple being the most abundant and therefore the target for most nanosensors. This section details some recent studies where nanosensors have been employed to study those redox couples.

The 'gold standard' for ratiometric redox potential measurements is the use of roGFPs, a green fluorescent protein modified with redox-active surface cysteine residues [155]. Each excitation maximum corresponds with a distinct oxidation state of the molecule, thus providing a ratio of oxidised to reduced species from which the redox potential can be calculated using the Nernst equation. Many roGFPs have now been engineered to cover different potential ranges and, like other GFP sensors, can be expressed in the organelle of choice, including the more oxidising environment of the endoplasmic reticulum [50, 51]. roGFPs sense the redox state of glutathione through interaction with glutaredoxins [156], and other redox couples are not thought to affect roGFP redox state [51]. Furthermore, to ensure that changes in intracellular glutaredoxin levels do not affect sensor readout, a nanosensor has been developed that fuses roGFP with human glutaredoxin-1 [157]. This also had the effect of decreasing the equilibration time between nanosensor and the glutathione redox potential.

Recent advances in this field include the use of light sheet-based fluorescent microscopy where the plane is illuminated by 2 lasers with different emission wavelengths, to detect the oxidised and reduced forms of roGFP. The ratio of the emission intensities at the different excitation wavelengths provides a ratiometric output of glutathione redox potential. This technique was used to measure the effect of staurosporine in glioblastoma spheroids (a 3D tissue model), and showed an increase in oxidation in both the cytoplasm and the mitochondria, with higher levels in the centre of the spheroids compared to the periphery [158]. In another example of organelle-specific targeting, expression of a roGFP in the mitochondria of rat islet

β-cells measured an increase in mitochondrial oxidation on addition of exogenous H_2O_2 and on glucose starvation [159].

Cysteine is discriminated from most other amino acids by its strong nucleophilicity, but it is difficult to distinguish between different thiols, e.g. glutathione and cysteine using dye-based nanosensors [160]. However, progress has been made in this area with the development of fluorescent nanosensors that use the cysteine-mediated cleavage of an acrylic acid moiety [161] or cysteine-mediated spirocyclisation [162]. Since the reaction requires the presence of a free amine adjacent to the sulfhydryl, these nanosensors are specific to free cysteine and homocysteine, and are unreactive when cysteine is incorporated in a larger peptide or protein such as glutathione.

1.4.4 Our approach

Fluorescent nanosensors have been an invaluable tool in the measurement of analytes and especially in the elucidation of Ca^{2+}-mediated signalling. However, the drawbacks of using fluorescent nanosensors include problems with photostability, photobleaching and cell autofluorescence at visible wavelengths. Furthermore, for investigating parameters such as redox potential, which is not an analyte, but a consequence of the concentrations of ROS and antioxidants, measuring the contribution of all the individual species is not feasible.

Our approach bypasses the problems involved in calculating global redox potential from individual redox couples. Our group has designed redox active reporter molecules based on quinones, which are active over a wider range of redox potentials then roGFPs [163]. These reporters change bond order depending on whether they are oxidised or reduced. Changes in the polarisation of bonds can be detected by Raman spectroscopy (described in the next section), thus allowing spectral discrimination between the oxidised and reduced forms of the reporter molecule. By covalently attaching our reporter molecules to gold nanoshells the Raman signal is amplified by up to 10^8 [164], a technique called surface-enhanced Raman spectroscopy (SERS). By recording spectra at different redox potentials using a potentiostat, a calibration curve can be obtained that shows how the SERS spectrum

changes in response to local redox potential changes. [163]. Our method does not suffer from photostability or photobleaching problems and also does not require the time-consuming expression of fluorescent proteins in cells. Furthermore, the use of infrared wavelengths minimises phototoxicity and cellular autofluorescence.

1.5 Raman spectroscopy

Spectroscopy is a technique for investigating the interaction of electromagnetic radiation with matter. Vibrational spectroscopy is a form of spectroscopy that detects the vibrations of bonds within molecules and can be used to determine the identity and structure of molecules. Raman spectroscopy is a type of vibrational spectroscopy that detects vibrations that alter the polarisability of the electron cloud, for example the symmetrical stretch in CO_2. When molecules are irradiated by laser light, the surrounding electron cloud can absorb photons and be transferred to a higher energy state, called a virtual state. Most of the time, the photons are then re-emitted at the same wavelength as those absorbed – this is called elastic, or Rayleigh, scattering (Figure 1.9). This is because the virtual state does not last long enough for the nucleii to move [165]. Sometimes, however, the nuclei do move, in which case energy is transferred from the photons to the molecule, and the re-emitted photons are of a different energy to the incident photons - this is inelastic, or Raman, scattering. There are two types of Raman scattering: in Stokes scattering, the molecule emits a photon of lower energy than that absorbed, and the molecule relaxes to a higher vibrational state than it was in previously. In the more rare anti-Stokes scattering, the emitted photon is of greater energy as the molecule has to be in an excited vibrational state prior to absorbing the photon [166]. Anti-Stokes scattering is rare because most molecules are in their ground vibrational state at room temperature. The vibration of different molecular bonds results in different amounts of inelastic scattering, so the difference in energies between incident and scattered photons is characteristic for certain types of bond [165]. Therefore each molecular species will have a characteristic Raman spectrum of peaks due to scattering by combinations of different bond vibrations. Also, different bonds within a molecule are polarisable to

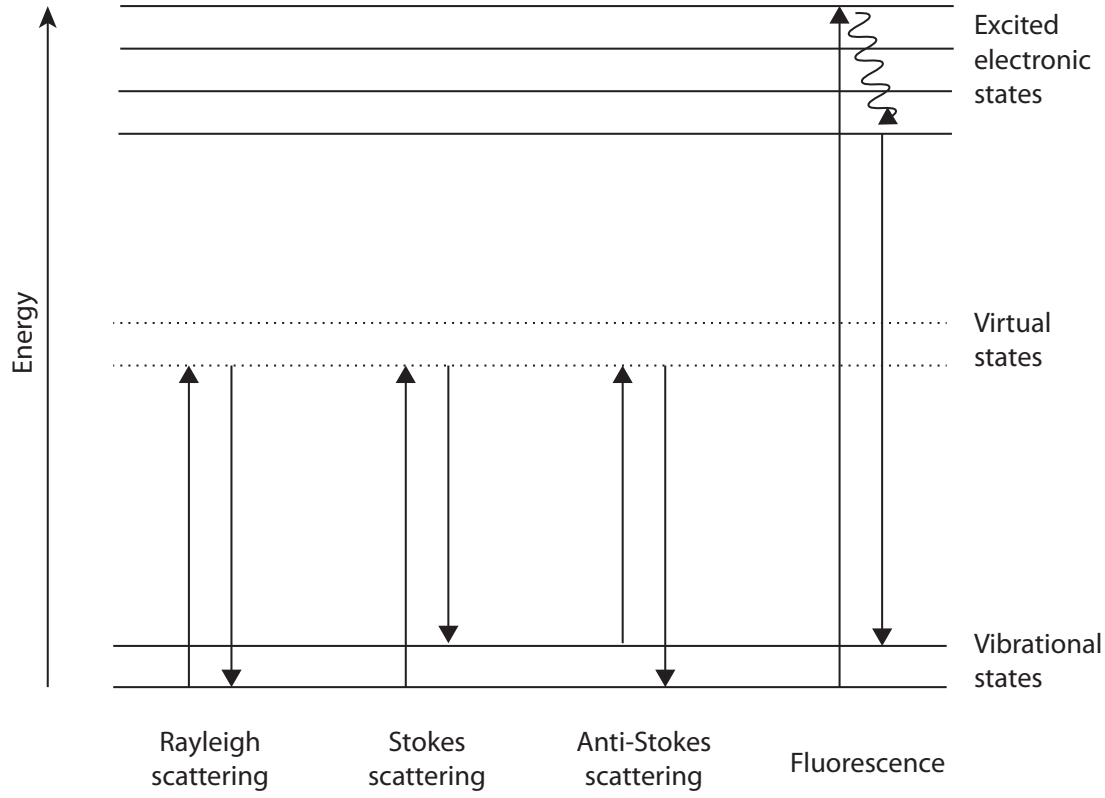

Figure 1.9: Energy-level diagram showing different scattering processes and those associated with fluorescence. Upward arrows indicate the energy of the absorbed photon, downward arrows indicate the energy of the scattered photon. In Rayleigh scattering, the emitted photon has the same energy as the absorbed photon, while in Raman scattering the emitted photon has a lower energy (Stokes scattering) or a higher energy (anti-Stokes scattering). Visible wavelengths can excite electrons to energies higher than the virtual states and can result in fluorescence.

different degrees - the more polarisable a bond, the more intense the Raman peak due to that bond vibration [166].

Raman spectroscopy is particularly useful for biological applications because water is a weak Raman scatterer, due to hydrogen bonding [165]. However, at visible wavelengths electrons in many biological molecules can be excited to a electronic state that is higher in energy than the virtual state, causing fluorescence which can overwhelm the signal from Raman scattering [166] (Figure 1.9). At near infra-red (NIR) wavelengths the lower energy photons are much less likely to excite electrons to a higher electronic state, so even though the intensity of Raman scattering decreases with increasing wavelength of incident light, the reduction in the intensity of the fluorescence is greater in its effect on the measurable signal. Furthermore molecules absorb NIR wavelength photons with less efficiency than visible

wavelength photons, so the laser power can be higher, offsetting the intensity reduction somewhat. For this reason the gold nanoshells used by the group are resonant at the NIR wavelength of 785 nm.

1.5.1 Surface-enhanced Raman spectroscopy

Stokes scattering is quite rare (only 1 in 10^6–10^{10} photons)[164], with typical Raman cross-sections being of the order of 10^{-30} to 10^{-25} cm^2 per molecule, compared to 10^{-17} to 10^{-16} cm^2 per molecule in fluorescence spectroscopy[167]. In the 1970s it was discovered that the Raman signal of pyridine was increased by a factor of 10^6 when adsorbed onto a roughened silver surface [168, 169]. Surface-enhanced Raman spectroscopy (SERS) is of particular use in biosensing, where the analyte of interest is adsorbed onto a metal nanoparticle, and it is also able to detect single molecules [167, 170, 171].

There are two types of enhancement with their exact mechanisms and the relative contributions of each still under debate [172], but the main component is electromagnetic enhancement. When a metal nanoparticle is irradiated with light, the valence d electrons at the surface are induced to oscillate with the electric field of the incident light (Figure 1.10). This is known as localised surface plasmon resonance and increases the electric field at the surface. The oscillation and electric field increase is induced most efficiently at a certain wavelength of light determined by the metal as well as the shape and size of the nanoparticle, so by varying these factors metal nanoparticles can be tuned to be resonant at particular wavelengths [166, 173]. The increase in electric field increases the polarisation of the electron cloud around molecules adsorbed onto the metal nanoparticle, thus making Raman scattering more likely. The electromagnetic enhancement is increased further if the metal nanoparticles are aggregated, with so-called 'hot spots' at the junction between nanoparticles producing the greatest enhancement [165]. Surface enhancement is a distance dependent effect - the electric field surrounding a spherical nanoparticle decreases with $(a/r)^3$, where a is the radius of the nanoparticle and r is the distance

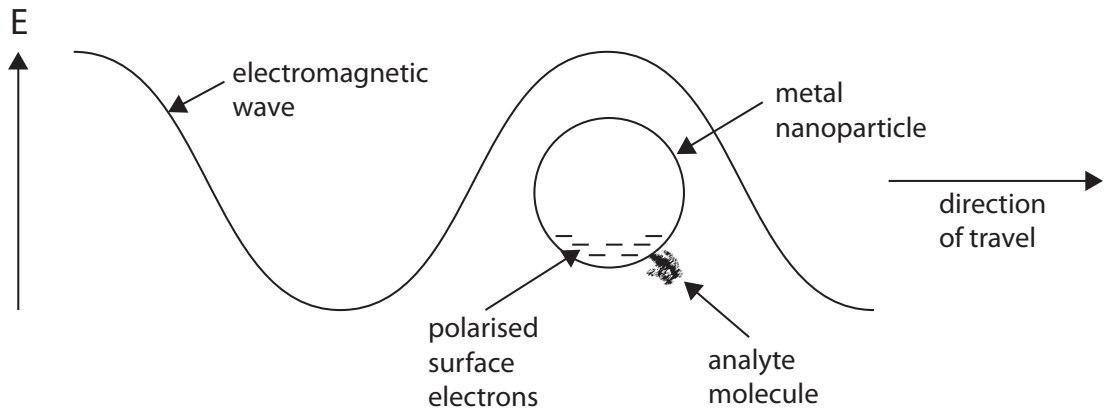

Figure 1.10: Electromagnetic enhancement in SERS. Surface electrons on the metal nanoparticle are induced to oscillate in line with the electric field (E) of incident light, known as localised surface plasmon resonance. This oscillation increases the electric field experienced by the molecule, increasing its polarisability and consequently the Raman signal. Adapted from [166].

from the surface [166]. This distance dependence makes SERS a very sensitive detection technique.

The second type of enhancement is called chemical or charge transfer enhancement. Binding of an analyte molecule to the nanoparticle changes the electron distribution of both as the molecular orbitals interact and electrons can be exchanged between the two [166]. This exchange can be from the Fermi level of the metal to the lowest unoccupied molecular orbital (LUMO) of the analyte molecule, or from the highest occupied molecule orbital (HOMO) of the analyte molecule to the Fermi level of the metal [174] (Figure 1.11). Such exchanges increase the polarisability of the electron cloud surrounding the molecule, increasing the Raman signal. This has a much smaller effect on enhancement than does electromagnetic enhancement, although the relative contributions of each depend on the nature of the nanoparticle and analyte molecule [172].

1.6 Project scope

Intracellular redox potential is of critical importance in cell function and survival and is tightly regulated through the independent activity of various redox couples. Most current methods of measuring redox potential rely on the GSH/GSSG couple, as this

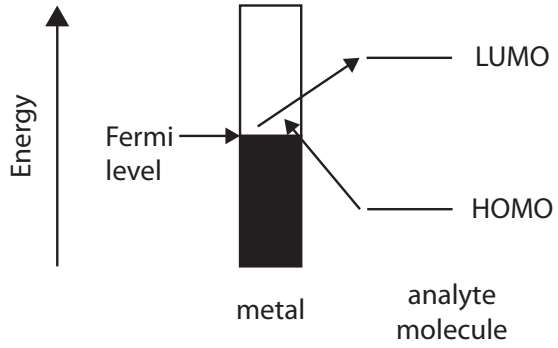

Figure 1.11: Chemical (or charge transfer) enhancement in SERS. Adsorption of an analyte molecule onto a metal nanoparticle allows the transfer of electrons between the HOMO of the molecule and the Fermi level of the metal, or between the Fermi level of the metal and the LUMO of the molecule. Adapted from [165].

pool is the most abundant and provides the greatest number of reducing equivalents. However, these methods do not take into account contributions from other redox couples, whose ratios can vary independently of the GSH/GSSG couple. Previous work by the group has shown that gold nanoshells can be taken up by mouse fibroblasts and are non-toxic [175]. Nanoshells coated with redox-sensitive reporter molecules are also non-toxic in this cell line and enable the non-invasive measurement of intracellular redox potential without affecting it [163]. These nanosensors have been used to show the correlation between redox potential and caspase activity during apoptosis.

The initial aim of this project was therefore to extend the group's previous work into a more pathologically relevant cell line, and standardise the procedures involved. The cell line chosen was the A549 carcinoma human alveolar basal epithelial cell line, which is used not only as a model of lung cancer [176, 177], but also in studies of inflammation [178] and nanoparticle toxicity [179, 180]. The change in intracellular redox potential in response to metal nanoparticle toxicity was then investigated.

Many studies have focussed on intracellular redox potential under conditions of oxidative stress, but there are fewer on redox potential under hypoxic conditions. The increase in NADH and NADPH in hypoxia should decrease the redox potential and work by the group has shown that this is the case in chemically induced hypoxia [122]. However, in order to measure redox potential in cells subject to hypoxia, the oxygen concentration must be precisely controlled during the acquisition of SERS

spectra. Therefore the final aim of this project was to construct a specialised imaging chamber to allow measurements of redox potential to be carried out at various oxygen concentrations.

Chapter 2: Methods

2.1 Functionalisation of nanoshells (NS)

2.1.1 NQ-NS

1–2 mg of 1,8-diaza-4,5-dithia-1,8-di(2-chloro-[1,4]-naphthoquinone-3-yl)octane (NQ) was dissolved in 100% ethanol, then heated and sonicated for 30 min before being filtered through cotton wool. The filtrate was then heated and sonicated for a further 10 min before being filtered through cotton wool for a second time. This filtrate was then filtered through a Millex GP PES 33 mm 0.22 μm filter (Millipore) and diluted 10-fold with sterile filtered water (Sigma Aldrich), before being added to 2.2×10^9 gold nanoshells (Nanospectra Biosciences Ltd) and incubated overnight at room temperature. The nanoshells were then washed 3 times with sterile filtered water, with ~200 μl of water being left after each wash. The nanoshells have a peak absorbance at ~780 nm, with an absorbance of 1 corresponding to 2.2×10^9 NS/ml. Absorbances were measured with a Cary 50 UV-Vis spectrophotometer and spectra recorded from 200–900 nm.

2.1.2 AQ-NS

1-2 mg of bis-(2-anthraquinone carboxamide) (AQ) was dissolved in 1% dimethyl sulfoxide (DMSO), filtered through cotton wool twice and then filtered through a Millex GP PES 33 mm 0.22 μm filter (Millipore). The filtrate was added to 2.2×10^9 gold nanoshells (Nanospectra Biosciences Ltd) and incubated overnight at room temperature in foil. The nanoshells were then washed 3 times with sterile filtered water, with ~200 μl of water being left after each wash. The nanoshells have a peak absorbance at ~780 nm, with an absorbance of 1 corresponding to 2.2×10^9 NS/ml. Absorbances were measured with a Cary 50 UV-Vis spectrophotometer and spectra recorded from 200–900 nm.

2.1.3 MBA-NS

1-2 mg of *para*-mercapto benzoic acid (MBA) was dissolved in 100% ethanol, filtered through cotton wool twice and then filtered through a Millex GP PES 33 mm 0.22 μm filter (Millipore) and diluted 10-fold with sterile filtered water (Sigma Aldrich), before being added to 2.2×10^9 gold nanoshells (Nanospectra Biosciences Ltd) and incubated overnight at room temperature in foil. The nanoshells were then washed 3 times with sterile filtered water, with ~200 μl of supernatant being left after each wash. The nanoshells have a peak absorbance at ~780 nm, with an absorbance of 1 corresponding to 2.2×10^9 NS/ml. Absorbances were measured with a Cary 50 UV-Vis spectrophotometer and spectra recorded from 200–900 nm.

2.2 Cell culture

A549 cells were grown as monolayers in Dulbecco's modified Eagle's medium (DMEM), supplemented with 10% heat-inactivated foetal bovine serum (FBS), 10,000 units/ml penicillin/streptomycin and 200 mM L-glutamine (all Life Technologies) (complete medium). NQ-NS incubation was carried out in serum-free medium, i.e. complete medium lacking FBS. Cells were grown in an incubator at 37 ºC with a humidified 5% CO_2 atmosphere.

2.3 Cytotoxicity assays

2.3.1 Lactate dehydrogenase assay

A549 cells were plated at a density of 6.25×10^4 cells/well in 24-well TC-surface treated plates. The following day the medium was replaced with serum-free medium for 1.5 hours before overnight incubation with various concentrations of NQ-NS (range 0-500 fM). Cells were washed twice with phosphate-buffered saline (PBS) to remove any NQ-NS not taken up by the cells. Triton-X 100 (the positive control) was added at a final concentration of 0.1% to cells containing no NQ-NS and the plates incubated for 20 min at 37 ºC and 5% CO_2. The supernatant was then removed for

assaying with LDH cytotoxicity detection kit (Roche) as per the manufacturer's instructions.

2.3.2 alamarBlue®

A549 cells were plated at a density of 6.25 × 10^4 cells/well in 24-well TC-surface treated plates. The following day the medium was replaced with serum-free medium for 1.5 hours before overnight incubation with various concentrations of NQ-NS (range 0-500 fM). Cells were washed twice with PBS to remove any NQ-NS not taken up by the cells. Triton-X 100 (the positive control) was added at a final concentration of 0.1% to cells containing no NQ-NS and the plates incubated for 20 min at 37 ºC and 5% CO_2. The cell layer was assayed with alamarBlue® (Life Technologies) as per the manufacturer's instructions.

2.3.3 Fluorescence-activated cell sorting (FACS)

A549 cells were plated at a density of 6.25 × 10^4 cells/well in 24-well TC-surface treated plates. The following day the medium was replaced with serum-free medium for 1.5 hours before overnight incubation with various concentrations of NQ-NS (range 0-500 fM). 8 μM staurosporine (the positive control; Sigma Aldrich) was added to cells containing no NQ-NS and the plates incubated for 4 hours at 37 ºC and 5% CO_2. The supernatant was transferred to labelled FACS tubes (BD Biosciences) and the cell layer rinsed with cold PBS (Sigma Aldrich) before being harvested in 150 μl 0.05% Trypsin/EDTA (PAA) for 3 min at 37 ºC and 5% CO_2. 0.5 ml/well complete medium was then added and the cells transferred to their respective FACS tubes. The cells were then washed in 1 ml PBS and then in 1 ml 2 mM calcium chloride in Hanks Balanced Salt Solution (HBSS) (PAA), before being resuspended in 400 μl 0.001% Annexin V conjugated to Alexa488 (Molecular Probes) in 2 mM calcium chloride in HBSS. After initial analysis by FACS, 1 μl of 1 mg/ml propidium iodide (Molecular Probes) was added to each tube and the FACS analysis repeated.

2.3.4 Statistics and data analysis

Differences between NQ-NS concentration compared to negative control were tested using one-way analysis of variance (ANOVA), followed by the Bonferroni multiple comparison test. Individual p values and significance levels are reported in each figure.

Models for fitting data using nonlinear regression were compared using the F-test. For models with the same number of parameters the F-statistic was calculated as:

$$F = \frac{SS_1}{SS_2} \tag{2.1}$$

where SS_1 is the sum of squared residuals for one model and SS_2 is the sum of squared residuals for the second model. For models with different numbers of parameters the F-statistic was calculated as:

$$F = \frac{(SS_1 - SS_2)/(DOF_1 - DOF_2)}{SS_2/DOF_2} \tag{2.2}$$

where SS_1 and DOF_1 are the sum of squared residuals and degrees of freedom, respectively, of the model with fewer parameters, and SS_2 and DOF_2 are the sum of squared residuals and the degrees of freedom, respectively, of the model with more parameters. Individual p values are reported in each table.

2.4 Transmission electron microscopy (TEM)

A549 cells were plated at a density of 2×10^5 cells/well in 6-well TC-surface treated plates. The following day the medium was replaced with serum-free medium for 1.5 hours before overnight incubation with 200 fM NQ-NS. Cells were washed twice with PBS and fixed for 20 min in pre-warmed 3% (v/v) glutaraldehyde in 0.1 M sodium cacodylate buffer. Cells were then transferred into 2 ml microcentrifuge tubes, centrifuged and the pellet washed three times with 0.1 M sodium cacodylate

buffer. The pellet was then incubated overnight with 1% (w/v) osmium tetroxide in 0.1 M sodium cacodylate buffer. The cells were washed with 0.1 M sodium cacodylate buffer, dehydrated with acetone (50-100%, in steps of 50%, 70%, 90% and 100%) and embedded in epoxy resin. Ultra-thin sections of the sample were taken using a diamond knife, positioned on grids and stained with 2% aqueous uranyl acetate. The grids were examined and photographed at an accelerating voltage of 80 keV in a CM120 Biotwin (Philips) transmission electron microscope connected to a digital camera.

2.5 Surface-enhanced Raman spectroscopy

2.5.1 Preparation of cells

A549 cells were plated at a density of 2×10^5 cells/dish on 35 mm diameter glass-bottomed imaging dishes (Greiner Bio-One). The following day the medium was replaced with serum-free medium for 1.5 hours before overnight incubation with 200 fM NQ-NS, AQ-NS or MBA-NS. Cells were washed twice with PBS and 3 ml complete medium added, before performing Raman spectroscopy.

2.5.2 Metal nanoparticle treatment

A549 cells were plated at a density of 2×10^5 cells/dish on 35 mm diameter glass-bottomed imaging dishes (Greiner Bio-One). The following day the medium was replaced with serum-free medium for 1.5 hours before overnight incubation with 200 fM NQ-NS. Cells were washed twice with PBS and 3 ml complete medium added. Cells were then either treated with 0.5 mg/ml AgNP, 0.5 mg/ml ZnONP or 30 mM AAPH (positive control) or were left untreated. Cells were incubated at 37 ºC and 5% CO_2 until Raman spectroscopy was performed at 0, 1, 2, 3 and 4 hours after treatment. Spectra were acquired from each sample for 1 hour. Spectra were processed with customised scripts in Matlab to determine redox potential, as described in Chapter 4. Differences in redox potential between treatment groups and the negative control were tested using ANOVA followed by the Holm-Šidák multiple comparison test.

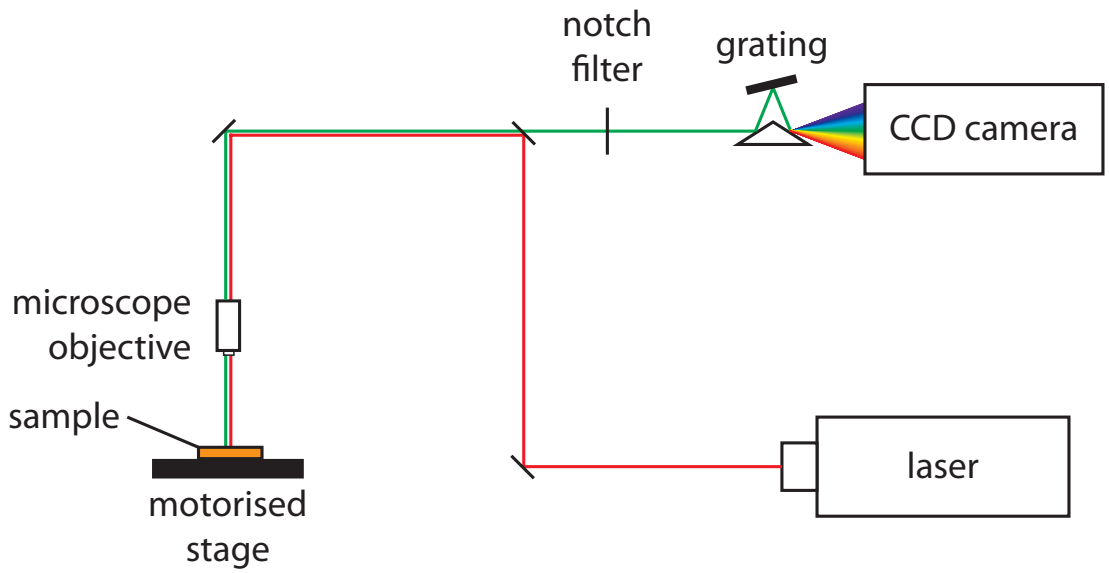

Figure 2.1: Schematic of a Raman spectrometer. Laser light is focussed onto the sample via mirrors and the microscope objective. Scattered light is collected by the objective, filtered and focussed onto a CCD camera via a diffraction grating.

2.5.3 Spectra acquisition

Raman spectroscopy was performed with a Renishaw InVia Reflex microRaman spectrometer with a 785 nm diode laser. A schematic of the setup is shown in Figure 2.1. Spectra were acquired between a Stokes Raman shift range of 1350-1800 cm^{-1}.

Single spectra were acquired with a 50× Olympus super long working distance objective (NA = 0.45) to give a focal diameter of 2.1 μm using a point focus lens, and a power density at the sample of 66 μW $μm^{-2}$. The integration time was 30 s unless specified otherwise.

SERS maps from cells were obtained with a 50× Olympus super long working distance objective (NA = 0.45) to give a line with dimensions 24.95 × 2.1 μm using a line focus lens. Raster scans were performed with a computer controlled *x*,*y*-stage, a step size of 5 μm, an integration time of 3 s and a power density at the sample of 330 μW $μm^{-2}$. The co-ordinates of signals from nanosensors were recorded and further Raster scans were performed centred on these co-ordinates with a step size of 1 μm, an integration time of 30 s and a power density at the sample of 66 μW $μm^{-2}$.

Raman spectroscopy was also performed with an Ocean Optics QE65 Pro detector, an Ocean Optics RPB probe and a 785 nm Innovative Photonic Solutions Fat Boy Laser. The focal diameter of the laser beam was 100 μm, giving a power density at the sample of 38 μW μm^{-2}. The integration time was 30 s.

Spectra were processed with customised scripts in Matlab, as described in Chapter 4.

2.6 Polydimethylsiloxane devices

Glass microscope slides were cut into three equal pieces and sonicated in dH_2O and a small amount of detergent for 30 min. The glass pieces were then rinsed with dH_2O and sonicated in dH_2O for a further 10 min, before being cleaned with air plasma in a PP Plasma Prep III Plasma Etcher (SPI) for 60 min. Nail varnish was carefully applied to the glass pieces to mark the position of each well and dried under N_2. Sylgard® 182 Silicone Elastomer base and curing agent (both Dow Corning) were combined in a 10:1 ratio and mixed thoroughly before being poured into the petri dish containing the glass pieces and then vacuum degassed. The petri dish was then heated to 85 °C for 2 hours. The following day the cured PDMS was cut to the shape of the glass pieces and wells were cut over the nail varnish marks. The nail varnish was removed with acetone and the wells rinsed with ddH_2O.

Devices were cleaned with air plasma for 10 min immediately prior to plating cells. A549 cells were plated at a density of ~2.5×10^3 cells/well and the well filled with culture medium. The following day the medium was replaced with serum-free medium for 1.5 hours before overnight incubation with 200 fM NQ-NS. Cells were washed twice with PBS and enough complete medium added to entirely fill the well. 18 mm diameter No. 1 glass coverslips were incubated with 0.1 mg/ml poly-L-lysine (PLL) in PBS for 2 hours then washed twice with ddH_2O and left to dry.
2.2×10^7 NQ-NS were dried onto the PLL-coated coverslips and the coverslip placed on top of the well to form a seal. Intracellular SERS maps were acquired as described in Section 2.5 above, with the device inverted to minimise obstruction to the laser.

Single extracellular SERS spectra were acquired using the point focus lens with a power density at the sample of 66 μW μm^{-2} and an integration time of 30 s.

Chapter 3: Optimisation

3.1 Introduction

Previous work in the group had established proof of principle in designing and constructing intracellular nanosensors consisting of redox active reporter molecules adsorbed onto gold nanoshells (Section 1.6). The nanosensors had been tested in NIH/3T3 murine fibroblast cells, so in order to extend the method into cell types that are more relevant in human disease they required evaluation in more relevant human cell lines. Studies of nanoparticle uptake have shown that amount and method of internalisation vary between different cell types [181, 182]. IC_{50} toxicity values (in terms of growth inhibition) and also vary, indicating that a concentration toxic in one cell type may be non-toxic in another. Therefore nanosensors should be evaluated for toxicity and uptake separately in each cell type used. In this thesis the A549 carcinoma human alveolar basal epithelial cell line was chosen as it is used in models of squamous non-small cell lung cancer [176, 177], lung inflammation [178] and nanoparticle toxicity [179, 180]. 30-35% of lung cancers are squamous non-small cell lung cancer [183]. Alveolar basal epithelial cells are found in the alveoli (air sacs) of mammalian lungs [184] and form a single-cell layer separating the interior of the alveoli from blood capillaries. Although they are the barrier between inhaled air and the blood supply, they are also very thin in order to facilitate the movement of oxygen, carbon dioxide and water into and out of the lungs. Overall, therefore the A549 cell line provides an ideal model in which to assess the performance of our nanosensors.

In this chapter, the process of functionalisation of 150 nm diameter gold nanoshells with a reporter molecule is optimised, the toxicity and intracellular location of the nanosensors in A549 cells is investigated and a rapid, reproducible method of locating the nanosensors and acquiring SERS spectra from them developed.

3.2 NQ functionalisation of gold nanoshells

Previous work indicated that functionalisation of gold nanoparticles with 1 mM 1,8-diaza-4,5-dithia-1,8-di(2-chloro-[1,4]-naphthoquinone-3-yl)octane (hereafter referred to as NQ) should be carried out in 10% ethanol in water, but the procedure had not been standardised. A 1 mM solution of NQ cannot be achieved in this solvent, or indeed in 100% ethanol, even after heating and sonicating, and NQ then precipitates on dilution with water.

The concentration of the NQ solution was decreased to 100 μM as at this concentration NQ dissolved better in 100% ethanol, although not fully. Filtration through cotton wool did not remove all undissolved particles of NQ (Figure 3.1). Further filtration through a 0.22 μm filter removed more undissolved particles and adding water to give a final concentration of 10% ethanol did not cause any visible precipitation. Nanoshells incubated overnight with this solution gave a similar redshift in the UV-visible absorption spectrum to that previously reported, suggesting that the nanoshells were successfully functionalised [185]. The nanoshells have a peak absorbance at ~780 nm; after functionalisation this resonance is slightly redshifted, due to the higher refractive index of adsorbed NQ compared to water (Figure 3.2).

The nanosensors are to be used in cells, therefore it is important to remove undissolved particles to avoid any potential toxicity of free NQ. Overnight incubation of nanoshells with NQ was followed by two centrifugation and wash steps (using ddH_2O) to remove unbound NQ. UV-visible absorption spectra showed that some loss of functionalised nanoparticles occurred during these wash steps (Figure 3.3 top). Upon centrifugation, the nanoshells do not form a stable pellet, leading to the unwanted removal of nanoshells whilst pipetting off the supernatant. Leaving ~200 μl of supernatant in the tube and adding an extra wash step reduced the loss and still removed unbound NQ (Figure 3.3 bottom). The standardised protocol is given in Section 2.1.1.

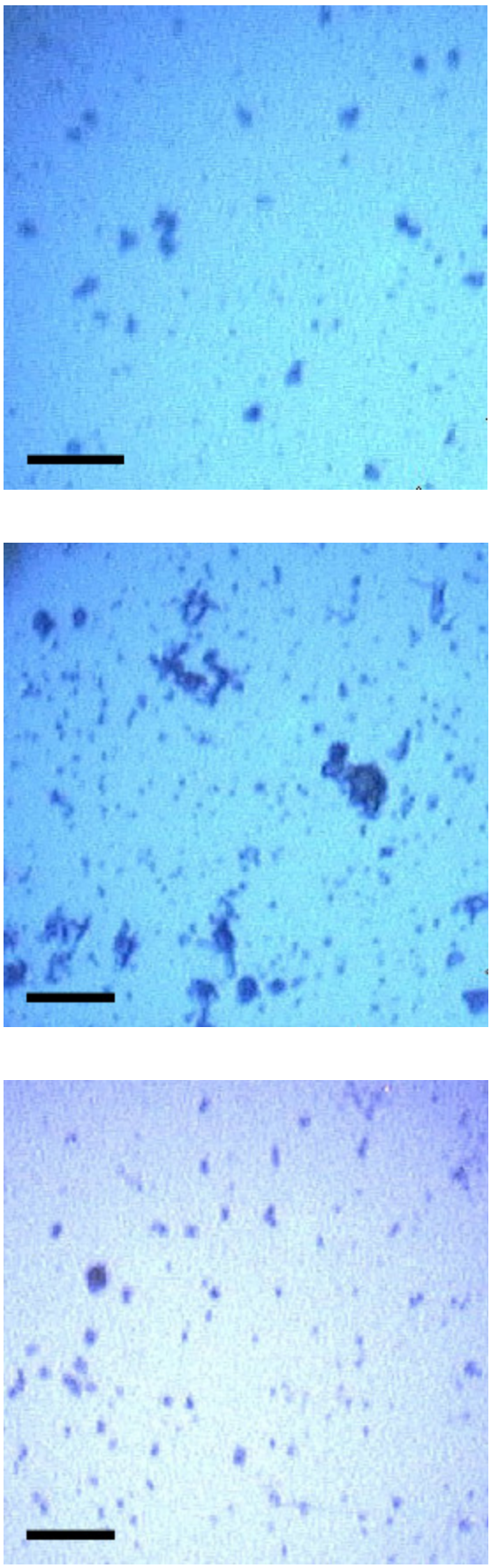

Figure 3.1: Representative 500× white light microscope images of bare nanoshells (top), NQ-functionalised NS filtered twice through cotton wool (middle) and filtered additionally through a 0.22 μm filter (bottom). 10 μl of each sample was dried onto a glass coverslip. Scale bar = 10 μm.

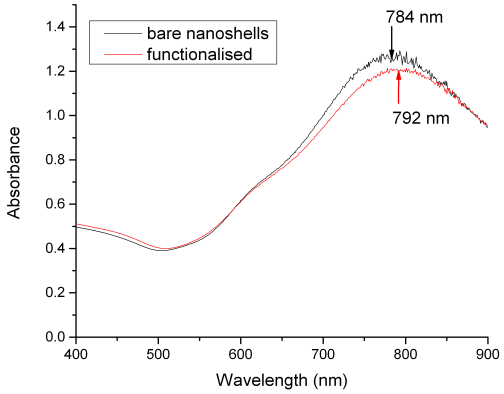

Figure 3.2: UV-visible absorption spectrum of bare and NQ-functionalised nanoshells showing redshift in the peak absorbance of the nanoshells upon functionalisation with NQ.

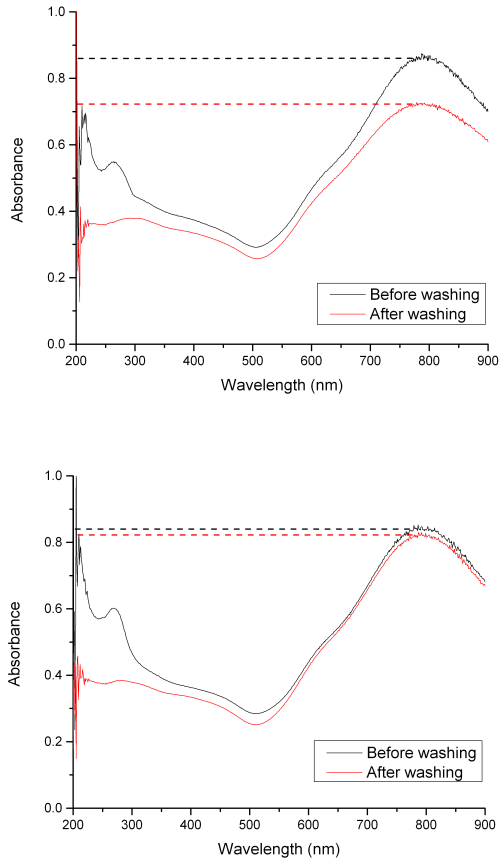

Figure 3.3: Top: UV-visible absorption spectrum showing the decrease in concentration of nanoshells due to loss after washing. Bottom: UV-visible absorption spectrum showing a smaller decrease in concentration after more careful wash steps. The functionalised nanoshells have a peak absorbance of ~790 nm and the peak height is related to their concentration [186].

3.3 Cytotoxicity

There are two main forms of cell death: apoptosis and necrosis. Apoptosis is a highly regulated process that can be initiated in response to various stresses such as glucose deprivation, heat stress or hypoxia, but is also necessary in development (for example in the formation of fingers and toes). The apoptotic pathway leads to the controlled breakdown of cellular components into membrane-enclosed apoptotic bodies, which are then phagocytosed by macrophages [187]. Necrosis can be triggered by the same factors as apoptosis as well as infection or bacterial toxins, but instead leads to uncontrolled rupture of the cell membrane and consequent release of cellular components into the extracellular medium, leading to inflammation. Apoptosis does not lead to inflammation unless it occurs on a large scale or phagocytic activity is deficient [188]. Nanoshells functionalised with NQ (hereafter referred to as NQ-NS) were incubated overnight in serum-free media with A549 cells, as previous work by the group has shown that nanoshell uptake by cells is increased in serum-free media [175]. In order to investigate whether NQ-NS are toxic in A549 cells the following assays were performed after overnight incubation with NQ-NS.

3.3.1 Lactate dehydrogenase assay

Lactate dehydrogenase (LDH) is a stable intracellular enzyme that reduces NAD^+ to NADH in the conversion of lactate to pyruvate. It is released upon rupture of cells undergoing apoptosis or necrosis, therefore measuring the amount of LDH in the medium of cultured cells gives an indication of membrane integrity and whether cell death has occurred. The assay uses a tetrazolium salt that reacts with NADH stoichiometrically to form red-coloured formazan (Figure 3.4), the absorbance of which can be measured with a spectrophotometer at 490 nm to give a readout of concentration. The tetrazolium salt is unable to penetrate the cell membrane, therefore only the amount of LDH in the culture medium is measured, indicating the degree of cell death. After overnight incubation with NQ-NS, A549 cells were washed twice with PBS to remove any NQ-NS that had not been taken up. 0.1% Triton X was then added to positive control wells in order to disrupt the cell

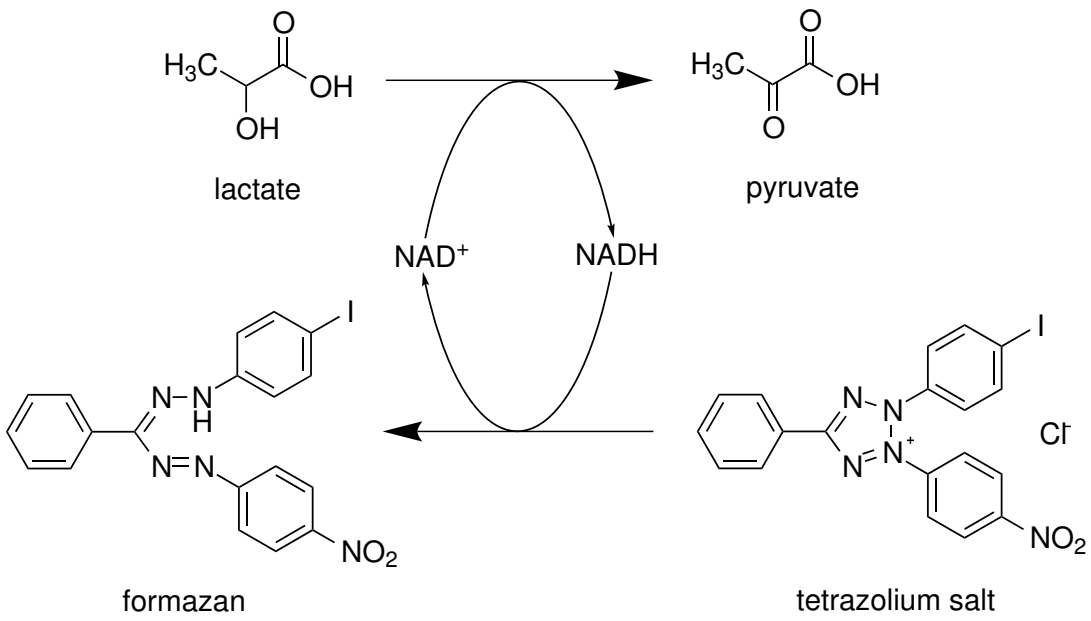

Figure 3.4: Scheme showing the principle behind the lactate dehydrogenase assay. The tetrazolium salt cannot penetrate cell membranes. However, during apoptosis or necrosis lactate dehydrogenase is released into the culture medium, where it reduces NAD^+ to NADH. The NADH generated reacts with the tetrazolium salt to form formazan, the absorbance of which can be measured with a spectrophotometer to give a readout of concentration.

membrane, and the plates incubated for 20 min at 37 ºC and 5% CO_2. The supernatant was then removed for assaying with LDH cytotoxicity detection kit (Roche) as per the manufacturer's instructions.

The cytotoxicity of various concentrations of NQ-NS is shown in Figure 3.5. None of the concentrations of NQ-NS used caused a significant change in absorbance at 490 nm compared to the negative control. The absorbance for the positive control, 0.1% Triton X, is not shown as it was too high to be measured quantitatively.

3.3.2 alamarBlue® assay

Resazurin is a non-toxic, cell-permeable molecule that is continually reduced to resorufin in viable cells through electron donation from intracellular redox cofactors such as NADPH and FADH and also cytochromes [189]. In less healthy cells this reduction is performed at a slower rate compared to healthy cells. The alamarBlue® assay measures the conversion of blue resazurin to red resorufin (Figure 3.6). Measuring the absorbance of resorufin spectrophotometrically at 570 nm indicates

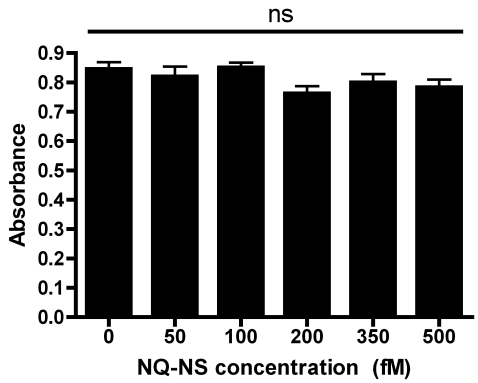

Figure 3.5: NQ-NS do not affect membrane integrity in A549 cells as measured by the lactate dehydrogenase assay. Error bars represent the standard error of the mean (n = 3, ns: $p > 0.05$).

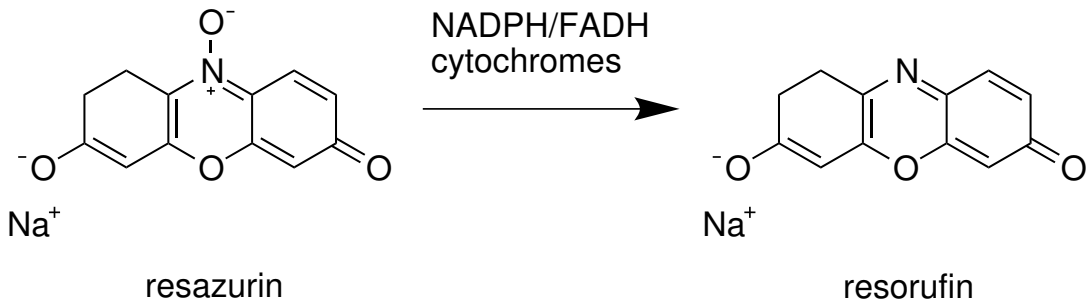

Figure 3.6: Scheme showing the principle behind the alamarBlue® assay. Blue resazurin is reduced to red resorufin by intracellular redox cofactors and cytochromes. The absorbance of resorufin can be measured spectrophotometrically at 570 nm; the higher the absorbance, the more metabolically active the cells are.

whether cells are healthy, as the lower the absorbance the less metabolically active the cells are. The non-toxic nature of resazurin allows the monitoring of live cell cultures over an extended period of time, in contrast to the LDH assay where the supernatant is removed for analysis, or the MTT assay where the insoluble formazan generated is toxic to cells. After overnight incubation with NQ-NS, A549 cells were washed twice with PBS to remove any NQ-NS that had not been taken up. 0.1% Triton X was then added to positive control wells in order to disrupt the cell membrane, and the plates incubated for 20 min at 37 ºC and 5% CO_2. The cell layer was then assayed with alamarBlue® (Life Technologies) as per the manufacturer's instructions.

Figure 3.7 shows that the viability of cells treated with different concentrations of NQ-NS is not significantly different to the viability of healthy cells.

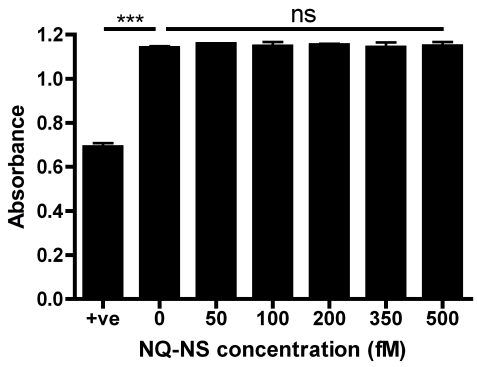

Figure 3.7: NQ-NS do not affect cell viability in A549 cells as measured by the alamarBlue® assay. Error bars represent the standard error of the mean (+ve: 0.1% Triton X; $n = 3$, *** $p < 0.001$, ns: $p > 0.05$)

3.3.3 *Fluorescence-activated cell sorting (FACS)*

In the early stages of apoptosis, the cell membrane remains intact, but phosphatidylserine molecules translocate from the inner face of the cell membrane to the outer face. The protein Annexin V preferentially binds to phosphatidylserine over other phospholipids in a calcium-dependent manner. By conjugating Annexin V with the green fluorescent dye Alexa 488, the cells can be fluorescently labelled to provide a measure of early-stage apoptosis.

Propidium iodide is a fluorescent dye that intercalates with DNA and RNA, but is excluded from viable or early-stage apoptotic cells, which have an intact membrane. Measuring the increase in fluorescence due to intercalation can be used to quantify late-apoptotic or necrotic cells, when the cell membrane is compromised and propidium iodide is able to enter the cells and access DNA or RNA.

The capacity of NQ-NS to cause apoptosis and/or necrosis was investigated using flow cytometry. After overnight incubation with NQ-NS, A549 cells were washed twice with PBS to remove any NQ-NS that had not been taken up. 8 μM staurosporine was added to positive control wells and the plates incubated for 4 hours at 37 °C and 5% CO_2. Cells and supernatant were transferred to FACS tubes, washed in 1 ml PBS and then in 1 ml 2 mM calcium chloride in Hanks Balanced Salt Solution (HBSS), before being resuspended in 400 μl 0.001% Annexin V conjugated to Alexa488 in 2 mM calcium chloride in HBSS. Cells were then passed single-file

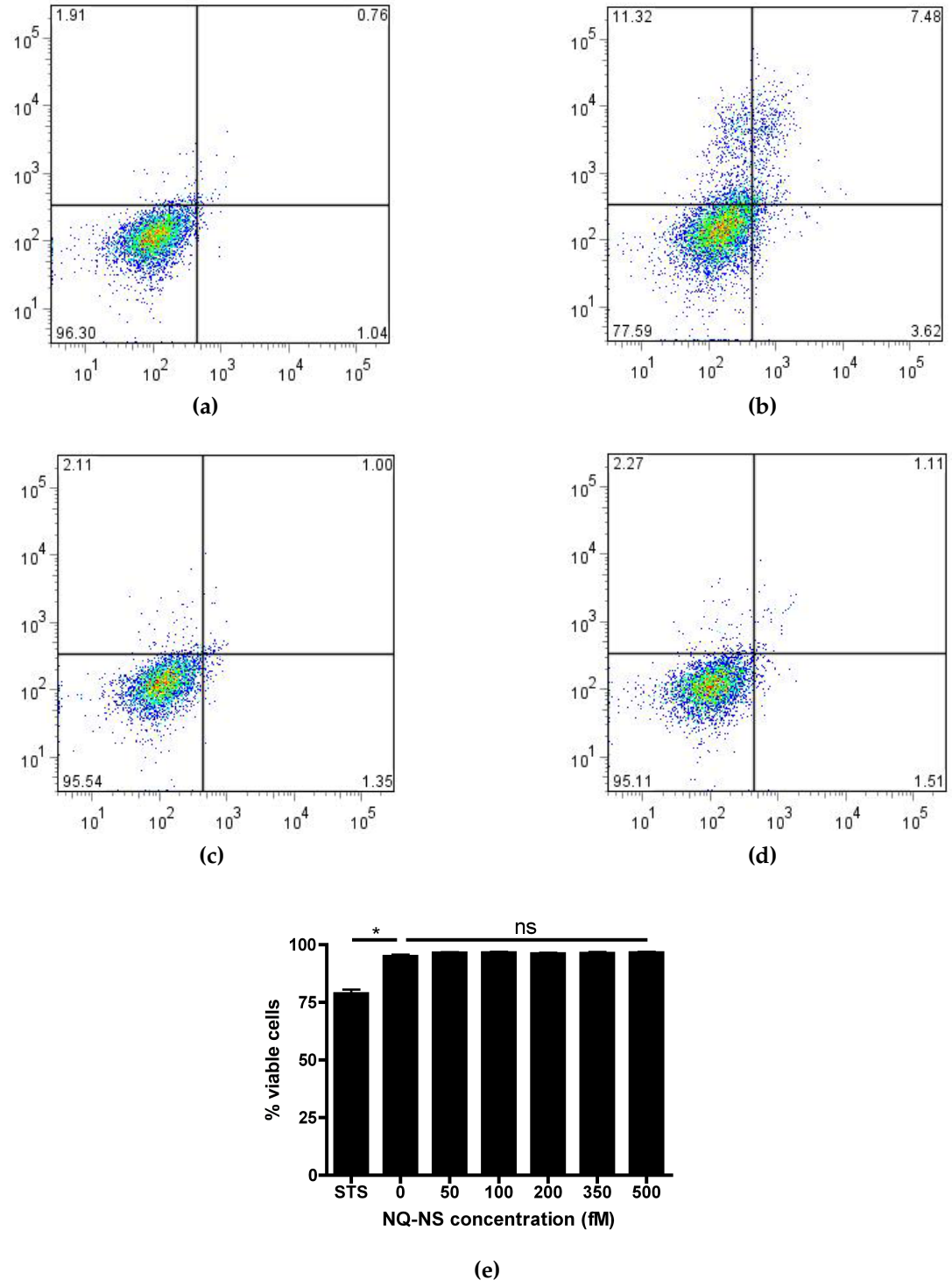

Figure 3.8: FACS analysis of NQ-NS in A549 cells. (a-d): the x-axis for each graph shows the intensity of Alexa488-labelled Annexin V and the y-axis shows the intensity of propidium iodide. Quadrants correspond to (clockwise from top left): necrotic cells; necrotic & apoptotic cells; apoptotic cells; viable cells, with the percentage of cells in each quadrant given. (a): untreated cells; (b): cells treated with 8 μM staurosporine for 4 hours; (c): cells treated overnight with 50 fM NQ-NS; (d): cells treated overnight with 500 fM NQ-NS; (e) viability of cells at different concentrations of NQ-NS. Error bars represent the standard error of the mean (STS: 8 μM staurosporine for 4 hours; $n = 3$; * $p < 0.01$, ns: $p > 0.05$).

through one or more laser beams and the fluorescence intensity from Alexa488-labelled Annexin V was recorded. 1 mg/ml propidium iodide was then added to each tube, the cells were then passed single-file through one or more laser beams and the fluorescence intensity from propidium iodide was recorded. The intensities for the cell population can be displayed on a dot plot, as in Figure 3.8, which shows that NQ-NS cause no change in either propidium iodide or Annexin V staining at concentrations of up to 500 fM compared with untreated cells.

3.4 Intracellular localisation of NQ-NS

It is important to know the final location of NQ-NS after they have been taken up by the cell. Studies have shown that nanoparticles can have a variety of fates after endocytosis (reviewed in [190, 191]), so it is therefore possible that the redox potential inside lysosomes or vesicles instead of the cytoplasm is measured with SERS.

The final location within cells of NQ-NS was investigated with transmission electron microscopy (TEM). TEM is a microscopy technique where a very thin section of the sample is irradiated with electrons, producing higher resolution images than with light. Gold and other heavy metals present in the sample absorb electrons, thus appearing as a black area on the image. Cells were prepared as detailed in Section 2.4. Figure 3.9 shows NQ-NS free in the cytosol and not enclosed within any visible structures, indicating that they were not inside vesicles. Therefore it appears that the redox potential measured inside cells is that of the cytoplasm. A concentration of 200 fM NQ-NS enabled most cells to take up $\geq$1 nanosensor.

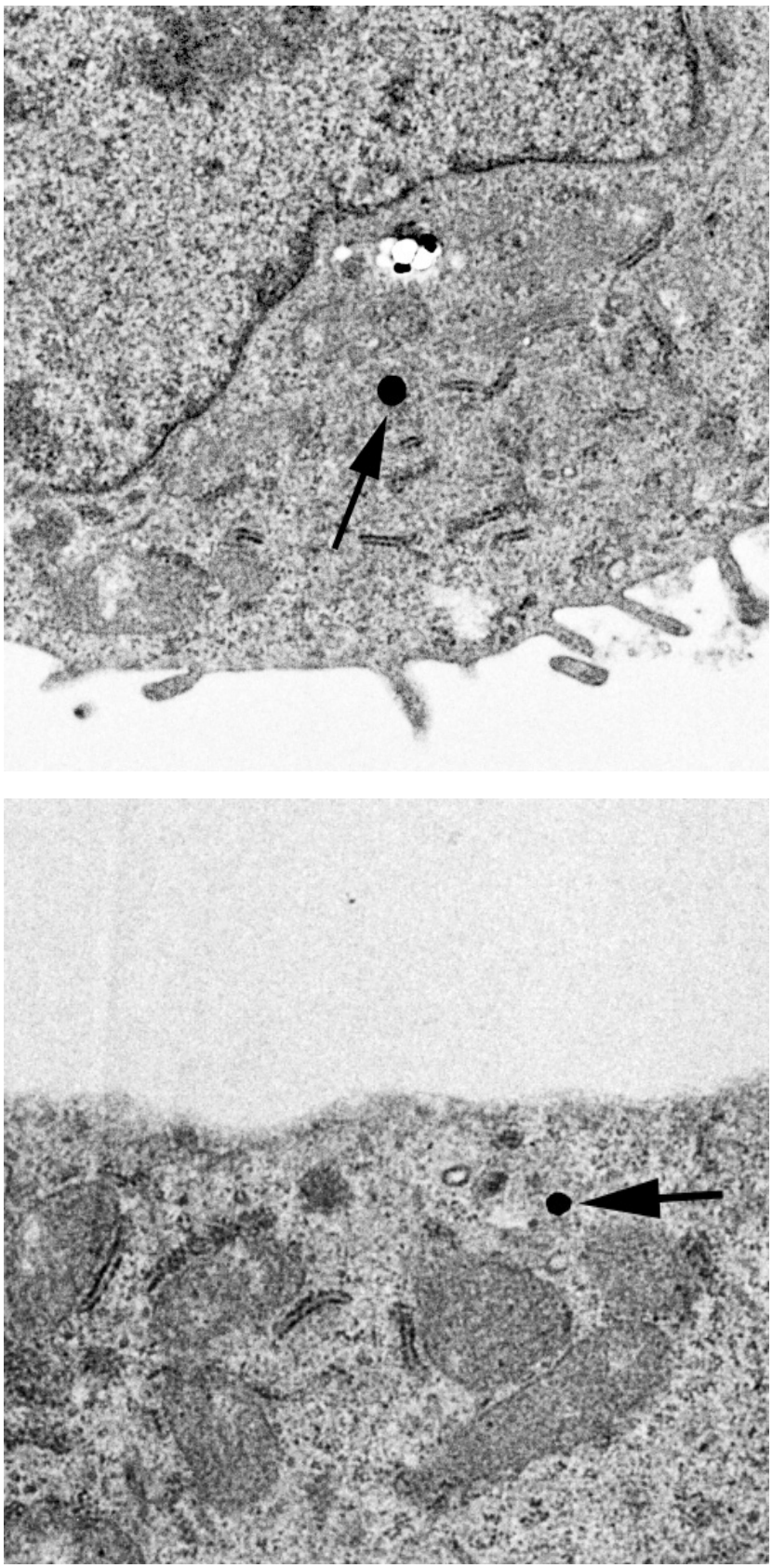

Figure 3.9: Representative TEM images of NQ-NS (marked with arrows) inside A549 cells, showing that NQ-NS are free in the cytoplasm and not encased in vesicles.

3.5 Acquisition of SERS spectra

The microscope objective used with the Renishaw inVia Reflex microRaman system is a super long working distance objective with a numerical aperture of 0.45, limiting the resolution to 600 nm, with a field of view under white light illumination of 125 × 100 μm. The nanosensors used in this thesis are 150 nm in diameter so use of this objective prevents the visual identification of nanosensors in cells, therefore a method to quickly and reliably locate the nanosensors is required. The spectrometer is equipped with a line focus lens that allows collection of light from a line instead of from a point on the sample (Figure 3.10). The scattered light from the line is collected onto a CCD camera and can be separated into vertical bins of 1, 3, 7 and 21 spectra, allowing for spatial resolution along the line. The instrument software allows the user to define a grid over an area of the sample and select the distance between each point on the grid in the x-axis and the number of bins (1, 3, 7 or 21).

Non-confluent A549 cells have a diameter of up to 40-60 μm, resulting in an area of 5,000-11,000 μm^2, so a large number of acquisitions are required to obtain Raman spectra from the whole cell (96-210 for the areas quoted). In addition, an integration time of 30 seconds is necessary to obtain spectra with a sufficiently high signal-to-noise ratio (SNR) from which to determine redox potential. Therefore, obtaining spectra covering an entire cell could take a prohibitively long time, especially where the goal is to monitor changes in redox potential over time. However, as nanosensors are not found in great numbers in cells (Section 3.4), it is not necessary to obtain high SNR spectra from the entire cell, only the parts that contain nanosensors. Therefore using a high laser power with a short integration time was investigated as a method of rapidly locating NQ-NS within a cell, so that high SNR spectra could be obtained from just the immediate vicinity of the nanosensor. Both laser power and integration time have an effect on SNR: a higher laser power can be used with a shorter integration time to resolve a signal, albeit with low SNR. With biological samples it is especially important that the laser power and integration times used do not damage the samples, therefore a trade-off is required between the two in order to maintain cell viability yet obtain spectra with a sufficiently high SNR.

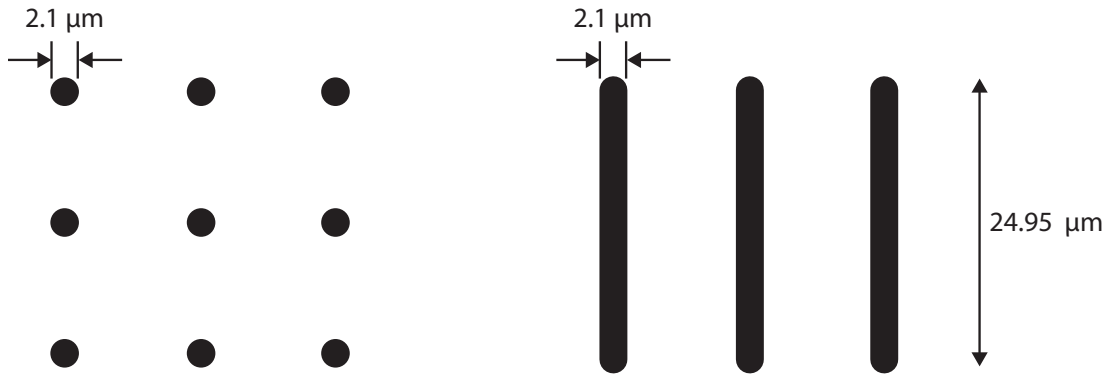

Figure 3.10: Difference in area of sample covered by point focus lens (left) and line focus lens (right). The focal diameter of the point focus lens is 2.1 µm, whereas the line focus lens covers an area of 2.1 × 24.95 µm. The CCD image produced using the line focus lens can be separated into 1, 3, 7 or 21 bins, providing vertical resolution. More of the sample can be covered with the same integration time with the line focus lens than with the point focus lens: in this diagram 3 acquisitions using the line focus lens covers a larger area than 9 acquisitions using the point focus lens, and produces a total of 3, 9, 21 or 63 spectra depending on the number of bins per line chosen.

In order to accomplish this, it was first necessary to establish the shortest integration time at the lowest laser power to obtain a signal from NQ-NS distinguishable above background. Then the minimum distance for the step in the x-axis in order to still obtain signals was determined.

Figure 3.11 shows the effect of varying laser power and integration time with the aim of distinguishing the NQ-NS signal from background. It indicates that an integration time of 3 seconds at 50% laser power (equivalent to a power density of 330 µW µm^{-2} at the sample) is enough to resolve a signal from NQ-NS dried onto a poly-L-lysine (PLL)-coated imaging dish and covered with PBS. NQ-NS aggregate upon drying and therefore the signal will be stronger from a dried aggregate than from less aggregated intracellular NQ-NS. 100% laser power and a 2 second integration time is also sufficient to distinguish NQ-NS signals, however the total laser power incident on the sample is greater than for 50% laser power and a 3 second integration time. Furthermore, some of the spectra (marked with an asterisk in Figure 3.11) show extra peaks at the left-hand side. These are usually observed when NQ-NS are irradiated in air with high laser powers. The spectra were obtained in PBS to allow heat dissipation from the laser in order to mitigate this effect, and the presence of the peaks confirms the requirement for using the lowest laser power possible.

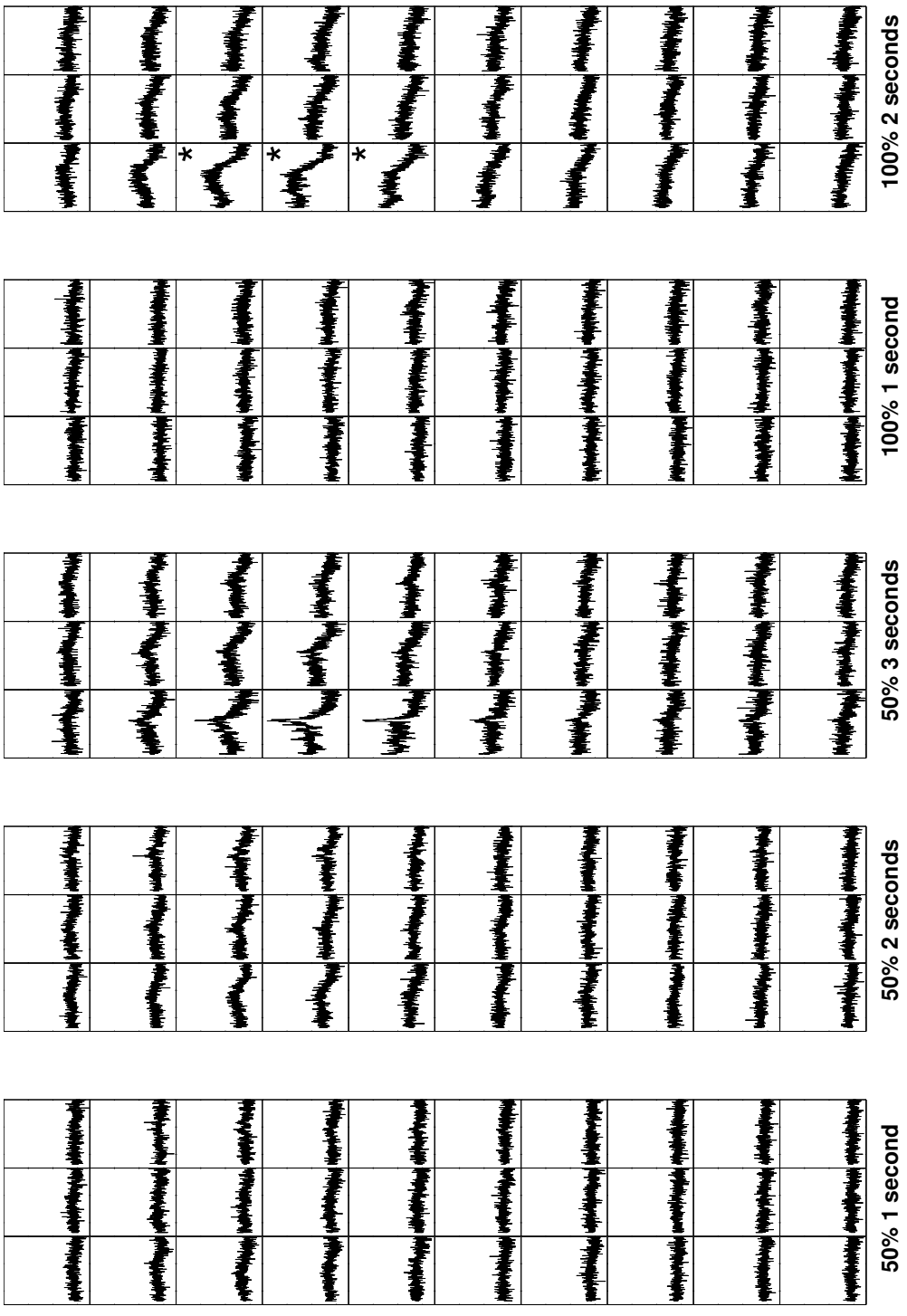

Figure 3.11: Comparison of various laser powers (50% or 100%) and integration times (1, 2 or 3 seconds). NQ-NS were dried onto a PLL-coated imaging dish and covered with 3 ml PBS. Spectra were acquired at 1 µm steps in a straight line over the same NQ-NS aggregate. 50% laser power and a 3 second integration time is sufficient to distinguish the NQ-NS signal from background. Asterisks denote spectra containing extra peaks at the left-hand side and are discussed in the text.

Figure 3.12 shows the effect on signal intensity with increasing distance from the source of the signal. It is apparent that intensity decreases quite rapidly and that no signal is obtained further than 2 μm from the source (middle column). Therefore the laser line must be 2-3 μm wide which means that each line in the grid described above would need to be separated by 2-3 μm in order to detect all NQ-NS in a given area. Therefore even a small area would take a long time: for example, a 100 μm × 100 μm grid with lines separated by 2 μm consists of 204 lines. At 3 seconds per spectrum, it would take just over 10 minutes to obtain spectra from this area. In order to minimise the time taken to locate NQ-NS within a cell, a step size of 5 μm was chosen in the x-axis, as this enables a whole cell (generally of a diameter of up to 60 μm) to be covered in less than 4-5 minutes. This means that only 40-60% of the area is covered and that some NQ-NS may not be located, however in practice it was found that at least 1 signal per cell was obtained with a 5 μm step size.

Once any NQ-NS in a cell have been located it is then possible to obtain spectra with a higher SNR from the immediate vicinity. With a 5 μm step in the x-axis, a nanosensor must be somwhere within 2-3 μm of the co-ordinates of the signal. Therefore I decided to obtain spectra covering an area of 3 μm either side of the co-ordinates with a 1 μm step in the x-axis to ensure coverage. This smaller map of 7 line spectra was acquired with a laser power of 10% (equivalent to a power density of 66 $\mu W\ \mu m^{-2}$ at the sample) and an integration time of 30 seconds. Each line consists of 21 spectra, so one map consists of a total of 147 spectra and is obtained in less than 4 minutes. Figure 3.13 summarises the acquisition of SERS spectra from intracellular NQ-NS.

Previously, cells had been grown on quartz coverslips in a petri dish in order to keep background fluorescence to a minimum, however, cells do not adhere well to quartz. Furthermore, the culture medium was held onto the quartz coverslip by surface tension in order to minimise the volume of NQ-NS required. This makes transport of the samples difficult, so instead cells were grown in 35 mm imaging dishes, which have glass coverslip bottoms treated with a proprietary physical surface treatment to enhance cell adhesion. The diameter of the dishes is wide enough so the meniscus of

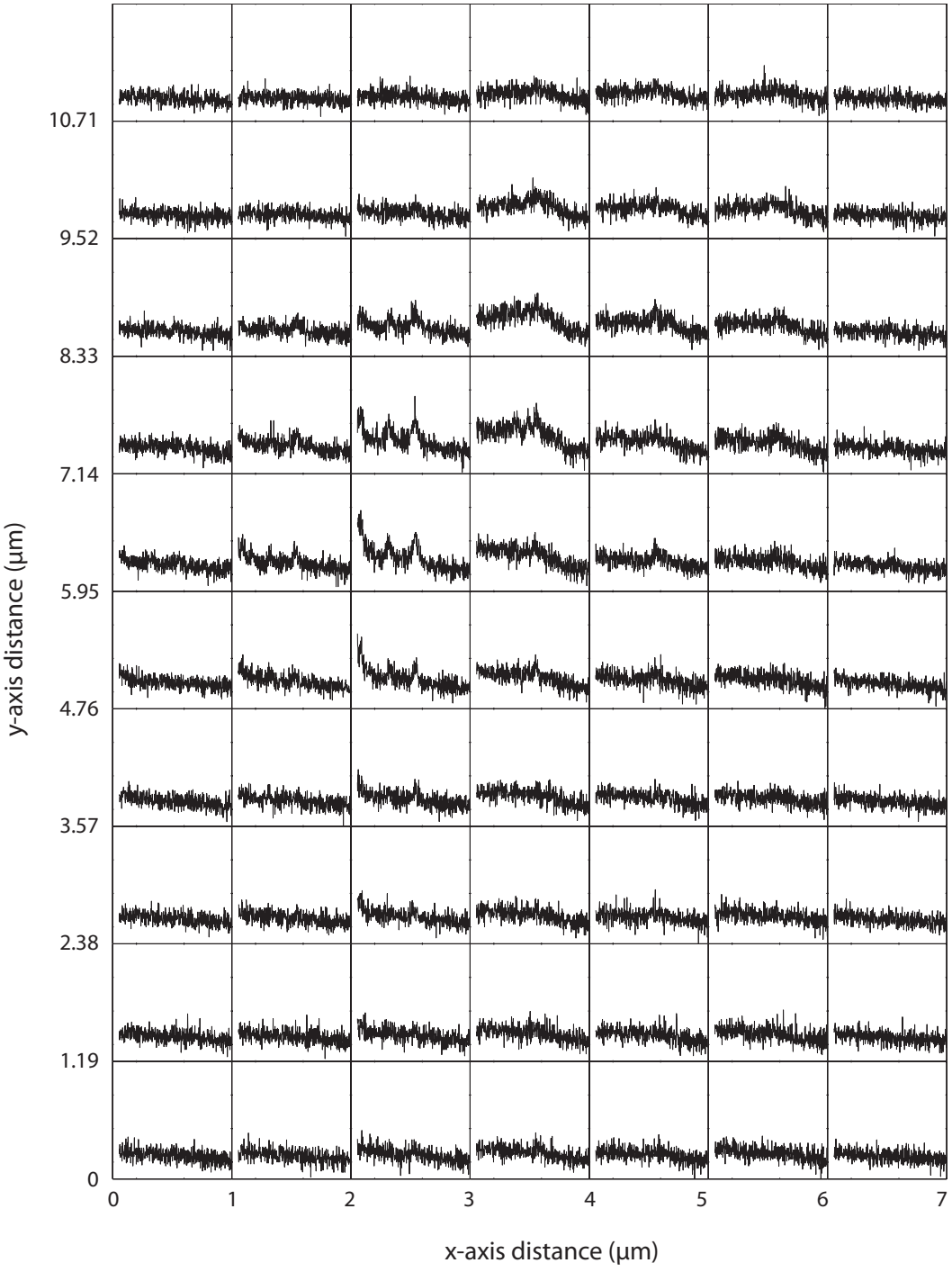

Figure 3.12: Effect of distance on signal intensity from NQ-NS dried onto a PLL-coated imaging dish and covered with 3 ml PBS. Spectra were acquired at 1 μm steps in a straight line over the same NQ-NS aggregate in Figure 3.11, with an acquisition time of 3 seconds and a laser power of 50%. The aggregate is located in the middle column, and its signal is not distinguishable further than 2 μm away.

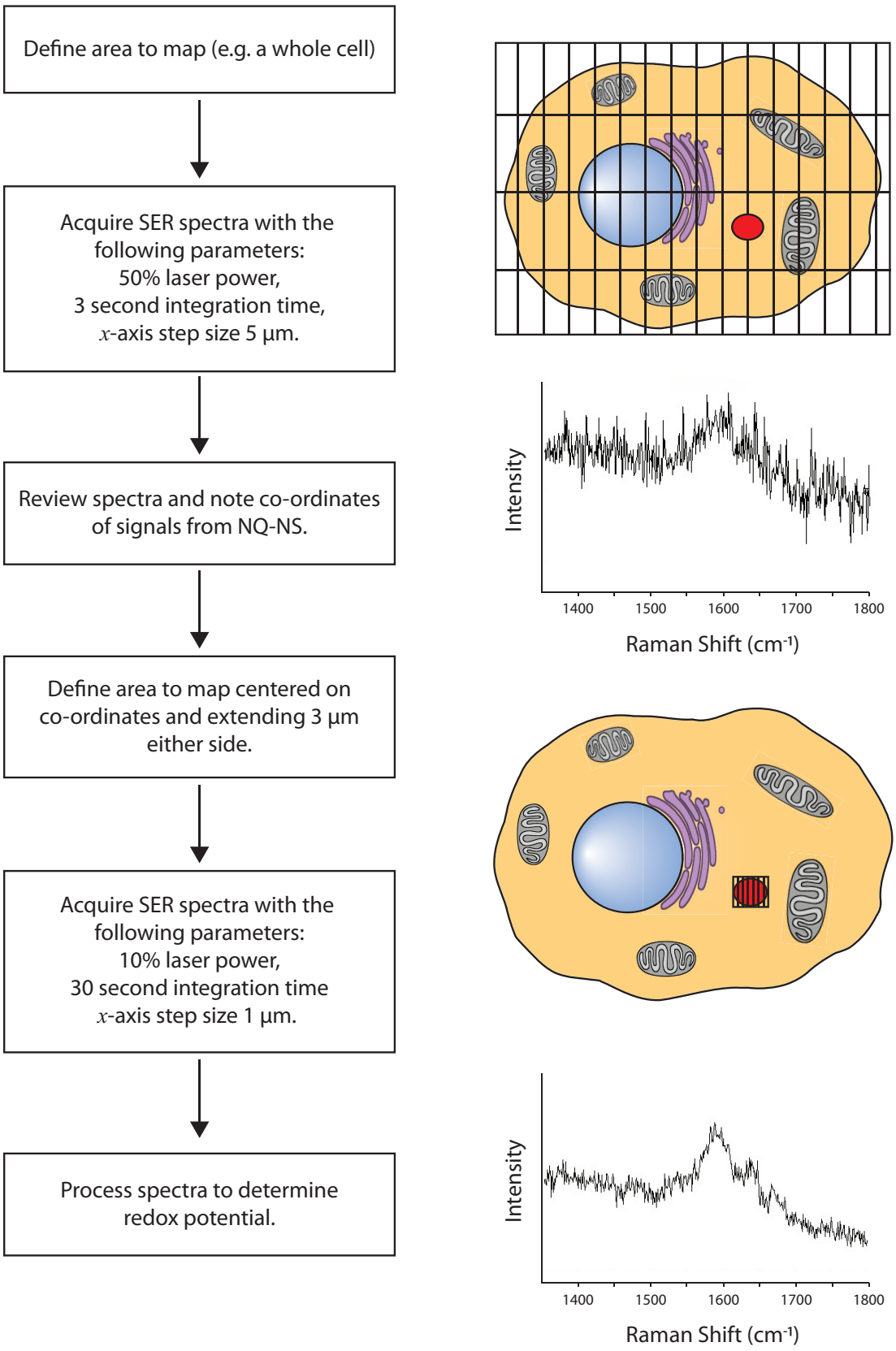

Figure 3.13: Left column: workflow for acquiring SERS spectra from intracellular NQ-NS. Right column (from the top): (1) grid overlaid on a cell showing the area to map; the distance between vertical lines is 5 µm and the distance between horizontal lines is 24.95 µm, to show the number of acquisitions using the line focus lens. (2) Representative SERS spectrum from NQ-NS with a 3 second integration time. (3) Grid overlaid on the co-ordinates of the NQ-NS signal; the distance between vertical lines is 1 µm. (4) Representative SERS spectrum from NQ-NS with a 30 second integration time.

the cell medium is flat above the coverslip bottom and scattering of laser light does not occur. The coverslip bottoms have low background fluorescence compared to the NQ-NS signal, albeit not as low as quartz, but could still be taken into account during data processing (discussed further in Chapter 4).

3.6 Discussion

In this chapter, the process for functionalising gold nanoshells with NQ was standardised. Standardisation of a technique is important to ensure that reproducible results are obtained and the technique can easily be taught to others. The absorbance at ~790 nm allowed the concentration of NQ-NS to be determined spectrophotometrically and the loss due to washing quantified, allowing accurate concentrations to be added to cell cultures for the toxicity assays.

The work in this chapter also established that NQ-NS are non-toxic in A549 cells up to concentrations of 500 fM. The LDH assay showed that NQ-NS do not impair membrane integrity, the alamarBlue® assay showed that they did not change cells' metabolic reducing ability, and FACS showed that they did not cause apoptosis or necrosis. Previous work by the group showed that NQ-NS did not cause oxidative stress in NIH/3T3 murine fibroblast cells [163]. While it is unlikely that NQ-NS would cause oxidative stress in other cell types, it would be useful to confirm this in the A549 cell line. The oxidative stress assay used previously was the dichloro-dihydro-fluorescein diacetate (DCFH-DA) assay, in which the oxidation by ROS of non-fluorescent dichlorofluorescin (DCFH) to fluorescent dichlorofluorescein (DCF) is measured fluorometrically. This assay indicated that NQ-NS did not cause oxidative stress, in other words, the intracellular redox potential was not perturbed beyond the ability of the cell to cope with an increase in ROS, however it cannot indicate whether the potential was perturbed slightly, activating NF-$\varkappa$B, for example (see Section 1.1). NF-$\varkappa$B upregulates the expression of various antioxidant genes, so it would be useful to measure any increase in the expression of these genes in response to NQ-NS using quantitative real-time polymerase chain reaction (qPCR). Such an

assay would be more sensitive than the DCFH-DA assay as it would allow very small changes in redox potential caused by NQ-NS to be detected.

Transmission electron micrographs showed that, at a concentration of 200 fM NQ-NS, most cells took up at least one nanosensor into the cytoplasm, however the exact method of internalisation is unknown. It is possible that the nanosensors are initially taken up into endosomes and then after a period of time are released into the cytoplasm, instead of being transported into lysosomes. This could be investigated by performing TEM studies at various timepoints after adding NQ-NS, or using confocal microscopy and fluorescently tagging both NQ-NS and membranes. However, as the nanosensors appear to be free in the cytoplasm after overnight incubation this was not pursued further.

The limitations of locating the nanosensors and the integration times required to obtain spectra with good SNR were overcome by 'pre-scanning' cells at high laser power and short integration times to quickly obtain approximate locations of any NQ-NS within the scan area. Acquiring spectra from only these locations at low laser power and longer integration times resulted in spectra with a good enough SNR to determine the redox potential (discussed in Chapter 4). This method enables spectra from approximately three cells per hour to be acquired, so it is still time-consuming. A faster scanning method is available with the Renishaw True Raman Imaging system, where the laser is defocussed over a wide area and the scattered light filtered to the desired frequency range. This would allow the locations of nanosensors to be obtained rapidly. Furthermore, upgrading to a near-infrared enhanced CCD camera would increase the SNR, allowing integration times to be decreased. A different method of locating the nanosensors could be used, for example by exploiting their autofluoresence [192]. This would require a combined confocal fluorescence Raman microscope. Autofluorescence imaging of tissue samples has been utilised by the Notingher group to automatically select regions of interest for Raman microscopy [193–195]. This has the advantage of reducing the number of sampling points, allowing the technique to potentially be used as a rapid diagnostic tool during surgery to check for the complete resection of tumours.

The results from this chapter suggest that NQ-NS are able to passively measure intracellular redox potential in A549 cells, and intracellular SERS spectra can be obtained from them relatively quickly at a high enough SNR for redox potential to be determined. The determination of redox potential from SERS spectra is the subject of the next chapter.

Chapter 4: Data analysis

4.1 Introduction

A consequence of optimising the acquisition of maps of SERS spectra (Section 3.5) is the number of spectra that can be acquired in a short space of time. The spectra require processing in order to determine redox potential, which is a time-consuming process. This chapter describes the development of an algorithm in Matlab to automate and speed up processing of SERS spectra.

As shown in Section 3.5, one single map of 147 spectra covering an area of 6 μm × 25 μm takes less than 4 minutes. Therefore in the course of 3 hours it is possible to generate 15-20 maps; a total of >2200 individual spectra. Manual processing takes approximately 3 minutes per spectrum and even though not every individual spectrum will require processing, a significant amount of time still needs to be invested. The manual processing of data involves:

- Visually identifying those spectra which require processing.
- Applying a smoothing algorithm to the spectrum.
- Manually placing a baseline consisting of 8 points and subtracting it from the smoothed data.
- Obtaining values for peak heights from the maximum value in the range of each peak.

There are a number of drawbacks to manual processing in addition to the length of time required:

- *Intra*-individual bias and variance - because the baseline is manually specified, differences in its placement can occur due to fatigue, mood etc. It is also possible that the baseline is subconsciously placed in order to achieve the expected redox potential, for example with data from NQ-NS in oxidised environments.

- *Inter*-individual bias and variance - different people will specify the baseline slightly differently which could lead to small but systematic differences in peak height ratios. Furthermore, each person may have differing criteria for deciding which spectra should be processed, leading to possible differences in the average redox potential determined through the exclusion or inclusion of spectra with a lower signal to noise ratio (SNR).
- The smoothing algorithm maintains peak height, thus also maintaining the noise, so the measurement of peak height is affected by noise. This effect is exacerbated by the presence of spikes of noise on one peak and not the other.

Automating the process of data analysis would address these drawbacks in addition to being faster. A peak fitting approach could be used to ascertain peak height, which would have the advantage of being less affected by noise than the manual method, as well as removing the bias and variance inherent in manual processing as the same criteria would be applied to all spectra. Peak fitting would also allow the investigation of other parameters such as peak width and area, which may also change with redox potential, giving more options for ratiometric analysis. Therefore peak fitting could provide a more accurate method of estimating redox potential from SERS spectra.

Peak fitting is a common method of analysis in spectroscopy as the peaks have characteristic shapes that can be modelled by specific functions [196]. This allows a physical model to be tested and data extracted from the model. The function parameters can provide information on the physical properties of the analyte under investigation. For example, in Raman, fluorescence and UV-visible spectroscopy the intensity of a peak is proportional to concentration [197].

There are several examples of automated processing of Raman spectra in the literature, with most focusing on baseline subtraction to remove the large background signals from various sources, including autofluorescence from biological samples [198–201]. For many applications, SERS spectral analysis is performed in order to detect/classify components of a sample [202], and accurate peak finding can be problematic when dealing with an unknown number of peaks, especially when

they are overlapping [196]. However, the peaks in our SERS spectra should only be from our reporter molecule and furthermore, we are not interested in fitting all of the peaks in a spectrum but only those needed for a ratiometric measurement. Therefore it would be possible to constrain the parameters of the peak fitting to produce a more accurate physical model.

In this chapter, a peak fitting algorithm for the automatic processing of SERS spectra is developed, tested on redox potential and pH nanosensors and compared to the manual method of processing. The peak fitting algorithm provides information about peak centre, height, width and area, and is used to provide a combination of ratiometric measurements of redox potential or pH. This information is then used to produce colourmaps showing the distribution of redox potential or pH within cells. The method is shown to be faster and more precise than the manual method.

4.2 Background subtraction

There are three components composing a SERS spectrum from our functionalised nanosensors: the substrate background, the nanoshells themselves and the reporter molecule. In this section the background from substrate and bare nanoshells is determined and an algorithm for its automatic subtraction is developed. As calibration spectra and intracellular spectra are obtained on different substrates it is important to account for different background contributions in order to accurately estimate intracellular redox potential or pH from calibration data.

4.2.1 Substrate (background subtraction)

In order to automate spectra processing, the background needs to be quantified. In bulk Raman spectra a baseline is often subtracted – this is particularly common at visible wavelengths where fluorescence is high and dwarfs the peaks of interest. However, fluorescence from organic molecules is considerably lower at shorter or longer wavelengths [203]. The Raman spectra described in this thesis were obtained with a near infra-red laser excitation source of 785 nm in order to minimise such

fluorescence. Therefore subtracting a slowly varying baseline, calculated separately for each spectrum was not thought necessary, as it was possible to obtain reference spectra from different substrates for subtraction. The intention, therefore, was to characterise the background for each substrate and subtract that from each spectrum, as this would be quicker than calculating a separate background for each spectrum.

Initially an averaged background of the relevant substrate was subtracted from spectra: 20 spectra of gold or quartz for calibration data, and for intracellular data 20 maps of 147 spectra were acquired from the surface of a bare imaging dish and then the spectra at each location were averaged; this produced an 'average map' consisting of 147 spectra, each of which is the average of 20 spectra at that particular location in the map. However, while subtraction worked well for calibration data, which were of high intensity and contained peaks significantly higher than the background, it was more problematic for intracellular data as the SNR is lower and the non-flat surface of cells can make focussing of the laser more difficult. Therefore, subtracting the averaged background can result in under- or over-subtraction (Figure 4.1). Furthermore, not all maps may consist of 147 spectra and may consist of any multiple of 21 (each acquisition using the line focus lens consists of a line of 21 spectra). An automated processing algorithm needs to take the size of the map and the variability in focussing into account and therefore subtraction of individually calculated backgrounds was in fact necessary. Although the background is variable, it still retains the same general shape (Figure 4.1 left), so an average background was scaled to certain points on the spectrum prior to subtraction as described below.

The background subtraction algorithm was developed using the pH-sensitive MBA reporter molecule (described in detail in Section 4.3.1) as it had resolved peaks with relatively flat background between them, unlike spectra obtained from NQ-NS and AQ-NS, which both showed overlapping peaks and more of a sloping background (Figures 4.5 and 4.7). Calibration data was acquired at various pH between 3.7 and 13.1 on a gold substrate. A plot of all calibration data (Figure 4.2 top) shows that the intensity at the left-hand side of the spectrum is more variable than that at the right-hand side, even though the gold background is flat (Figure 4.3, left), and that

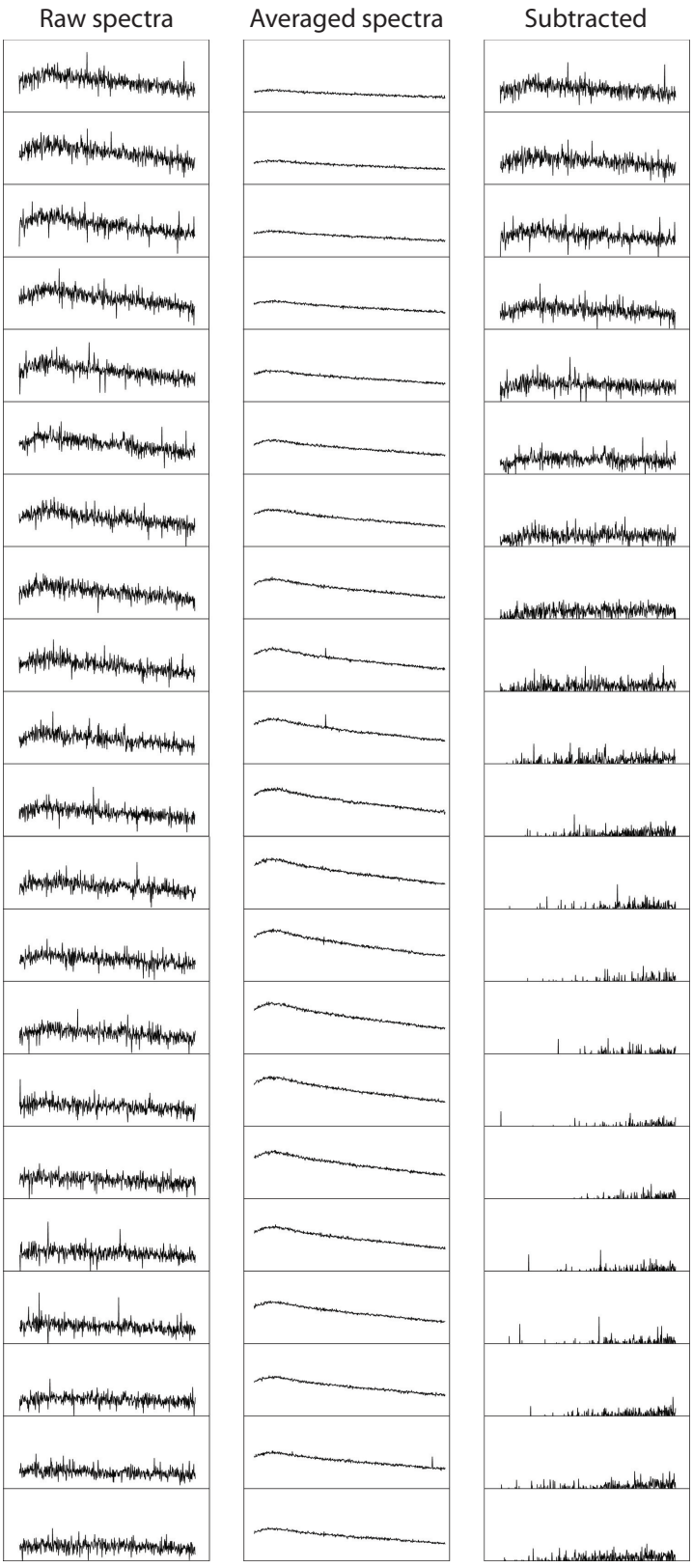

Figure 4.1: Subtraction of an averaged background leads to under- or over-subtraction in intracellular spectra consisting of only imaging dish background. The left column (raw spectra) represents a single 30 second acquisition using the line focus lens, covering a distance of 24.95 μm and separated into 21 bins (see Section 3.5). The slope of the background varies down the line, from steepest at the top to flattest at the bottom. Middle column: averaged spectra of imaging dish background, averaged for each bin. The slope of the background again varies down the line, however here it is steepest in the middle and flattest at the top and bottom. Right column: subtracting the average background per bin from the raw intracellular spectra results in over- or under-subtraction; this is due to the non-flat surface of the cell. The scale of the y-axis is the same in all spectra to emphasise the under- and over-subtraction.

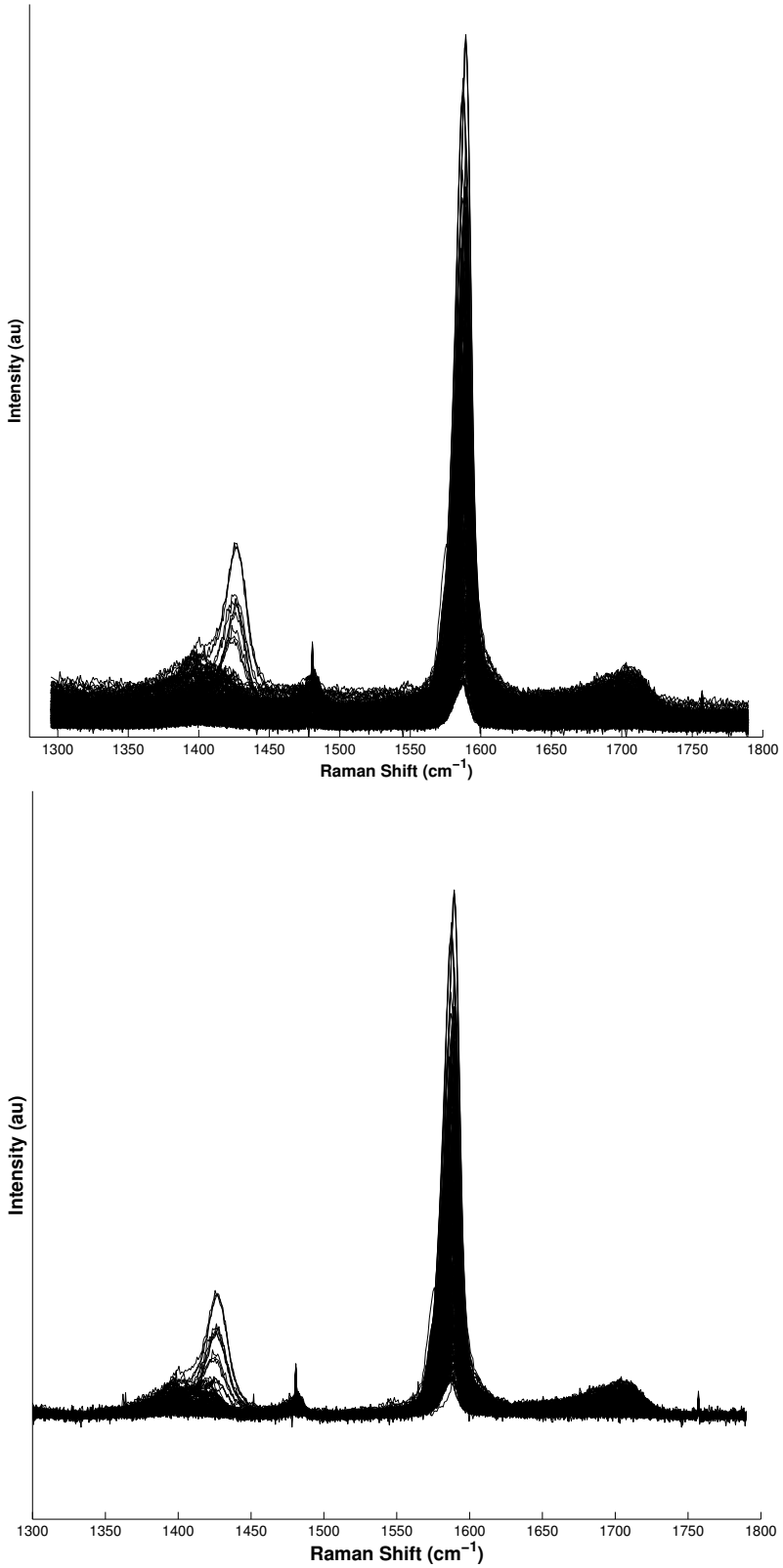

Figure 4.2: Calibration spectra for MBA-NS (top) before and (bottom) after subtracting a scaled linear gold background. Subtraction reduces the variability of the background intensity at the left and right hand sides.

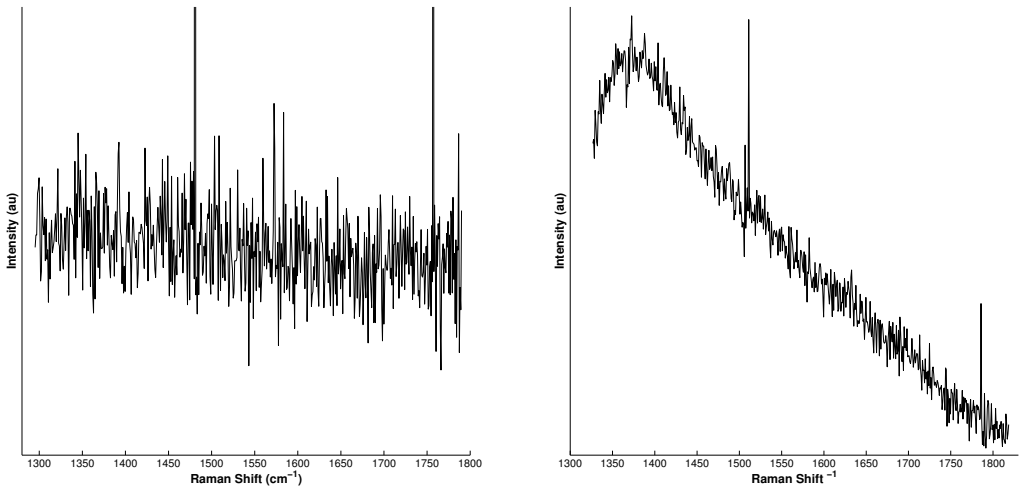

Figure 4.3: Average of 20 spectra from (left) gold background, and (right) glass-bottomed imaging dish.

Polynomial order	Sum of squared residuals	F-statistic (vs. 1st order polynomial)
1	77,519	
2	77,518	0.007 (p = 0.99)
3	77,143	1.393 (p = 0.25)
4	77,127	0.965 (p = 0.38)
5	76,894	1.157 (p = 0.31)
6	76,859	0.976 (p = 0.38)

Table 4.1: Comparison of polynomial models for the Raman spectrum of the gold substrate. A p value of >0.05 indicates that the higher order polynomial model is not statistically more accurate than the 1st order polynomial model.

spectra also appear to be on a slope. In order to remove this variability, robust regression in the form of a weighted linear least squares fit with lower weight given to outliers was used, in order to minimise the effect of noise spikes on the fit. In addition to the robust regression, smoothing to the first 118 data points and the last 85 data points of the calibration data was used, and the minimum in each section found. The average gold background was found to be best modelled by a line, compared to higher polynomials (Table 4.1); this line was scaled to the intensities of these minima and then subtracted from the raw calibration data. This subtraction

successfully reduced the variability in background intensities of the calibration data (Figure 4.2 bottom).

For intracellular spectra obtained on a glass-bottomed imaging dish the subtraction was modified slightly. The imaging dish background is not linear (Figure 4.3, right) so a smoothed averaged imaging dish background was scaled to the intensities of the smoothed ends of the spectra at Raman shifts of 1350 cm^{-1} and 1785 cm^{-1}. The shift at 1350 cm^{-1} was chosen as this was near the peak intensity of the imaging dish (Figure 4.3 right) and also in an area of minimum intensity of the MBA spectrum (Figure 4.2 bottom). The shift at 1785 cm^{-1} was chosen as the spectra of both imaging dish and MBA had minimum intensities here. This method did not cause over- or under-subtraction in intracellular spectra independently of whether signals from MBA-NS were present (Figure 4.4).

Calibration data for NQ-NS were also obtained on a gold background and acquired at various redox potentials between -460 and -250 mV (vs. NHE). From Figure 4.5 (top) it can be seen that the apparent slope is steeper than for MBA-NS (Figure 4.2 top), with much more variation at the left hand side. Subtraction of the gold background was accomplished using the same method as for MBA, and successfully reduced the variability in background intensities of the calibration data (Figure 4.5 bottom). However, for intracellular spectra the subtraction had to be modified further, as there is a peak ~1350 cm^{-1}, coincident with the maximum of the imaging dish, so instead the averaged imaging dish background was scaled between the lowest intensity of smoothed spectra in the region 1350-1500 cm^{-1} and the intensity at 1785 cm^{-1}. Again, this method did not cause over- or under-subtraction in intracellular spectra independently of whether signals from NQ-NS were present (Figure 4.6).

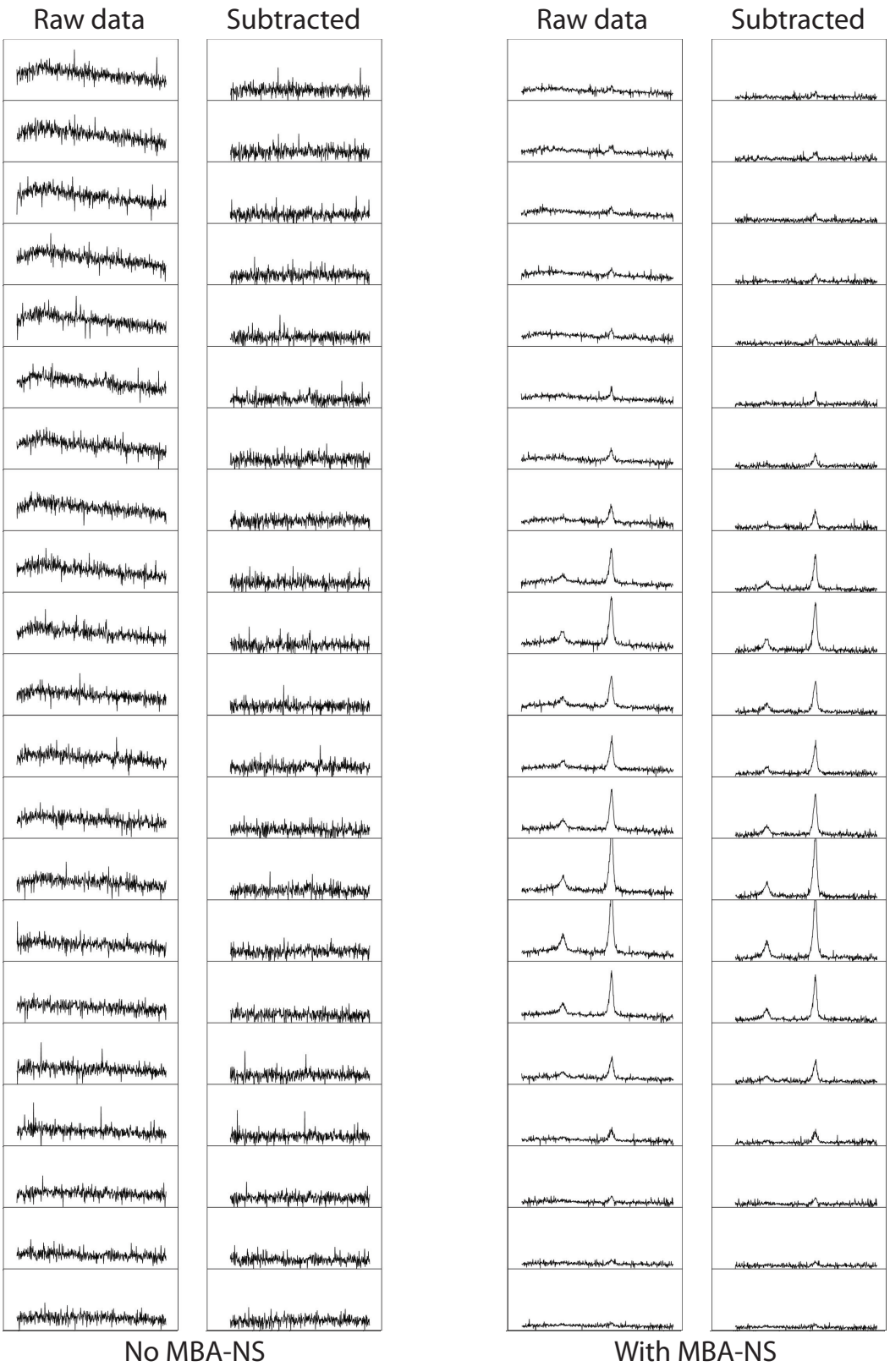

Figure 4.4: Subtraction of a scaled smoothed average background successfully compensates for the variability in imaging dish background and does not lead to over- or under-subtraction in intracellular spectra, irrespective of whether signals from MBA-NS are present. Acquisition conditions and layout are as in Figure 4.1.

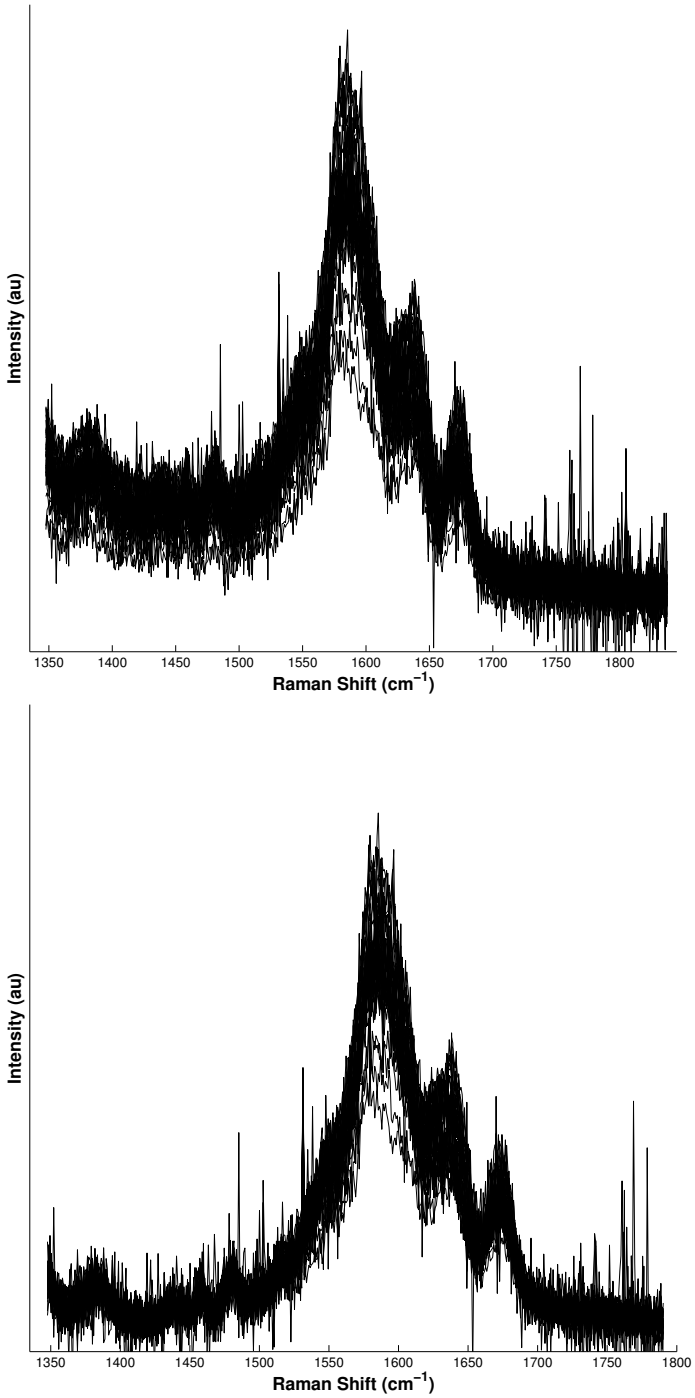

Figure 4.5: Calibration data for NQ-NS (top) before and (bottom) after subtracting a scaled gold background. Subtraction reduces the variability of the background intensity at the left and right hand sides.

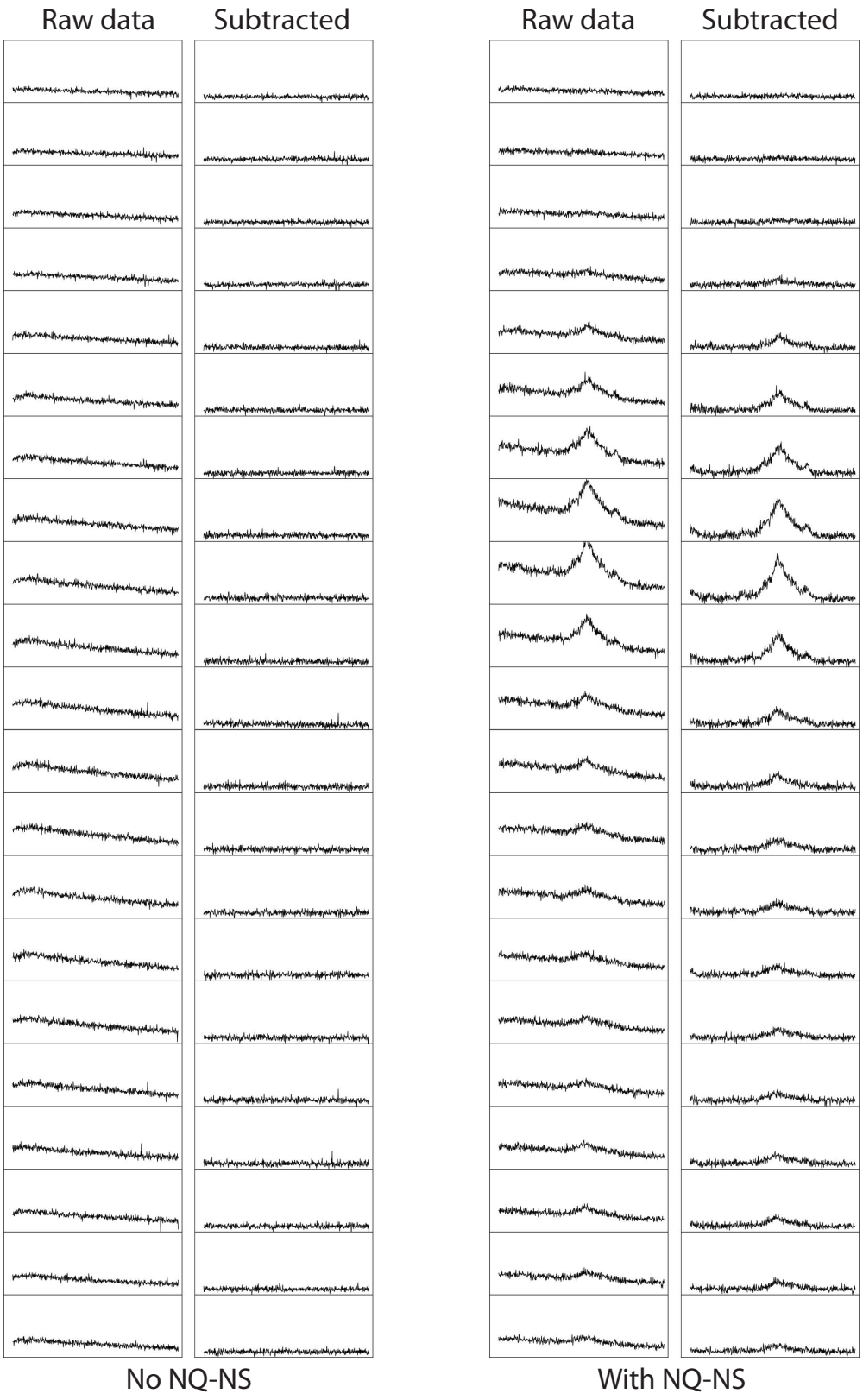

Figure 4.6: Subtraction of a scaled smoothed average background successfully compensates for the variability in imaging dish background and does not lead to over- or under-subtraction in intracellular spectra, irrespective of whether signals from NQ-NS are present. Acquisition conditions and layout are as in Figure 4.1.

Calibration data for the redox active AQ-NS nanosensor were also obtained on a gold background and acquired at various redox potentials between -460 and -130 mV (vs. NHE). From Figure 4.7 (top) it can be seen that the apparent slope of the data is steeper than for NQ-NS (Figure 4.5 top), and with considerably more variation in intensities, along with the presence of a transient peak at ~1400 cm^{-1}. The linear gold background subtraction was thus modified to only apply to the region between 1475 and 1800 cm^{-1}, which contained the peaks of interest but not the transient peak. This successfully reduced the variability in background intensities of the calibration data (Figure 4.7 bottom). As the average imaging dish background can be modelled by a line between 1475-1800 cm^{-1}, a linear background was subtracted from intracellular data in this wavenumber range, scaled between the lowest intensity of smoothed spectra in the region 1475-1525 cm^{-1} and the intensity at 1785 cm^{-1}. Again, this method did not cause over- or under-subtraction in intracellular spectra independently of whether signals from AQ-NS were present (Figure 4.8).

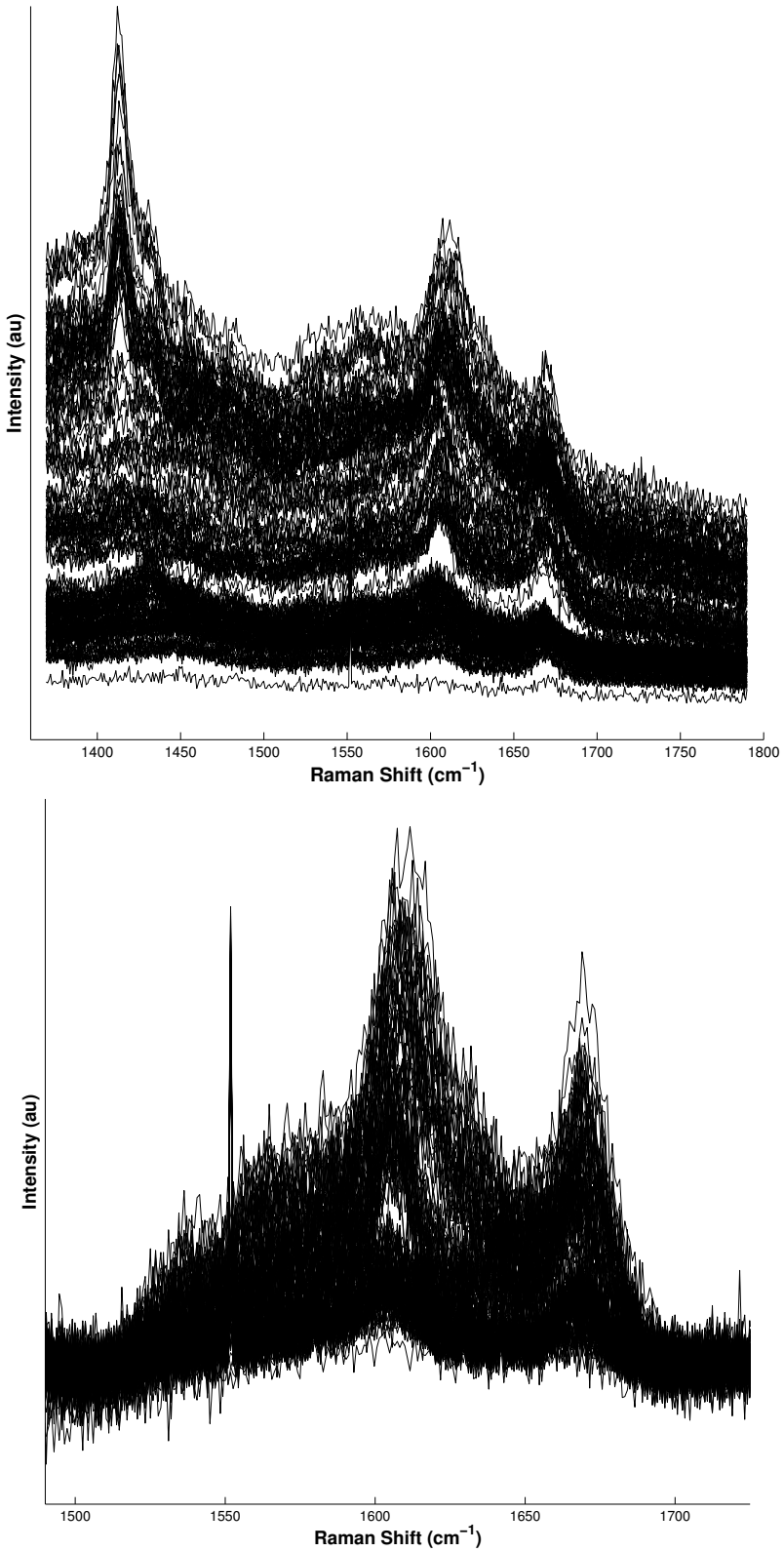

Figure 4.7: Calibration data for AQ-NS (top) before and (bottom) after subtracting a scaled gold background. The subtraction has been constrained to the region containing the peaks of interest. Subtraction reduces the variability of the background intensity at 1500 cm^{-1} and the right hand side.

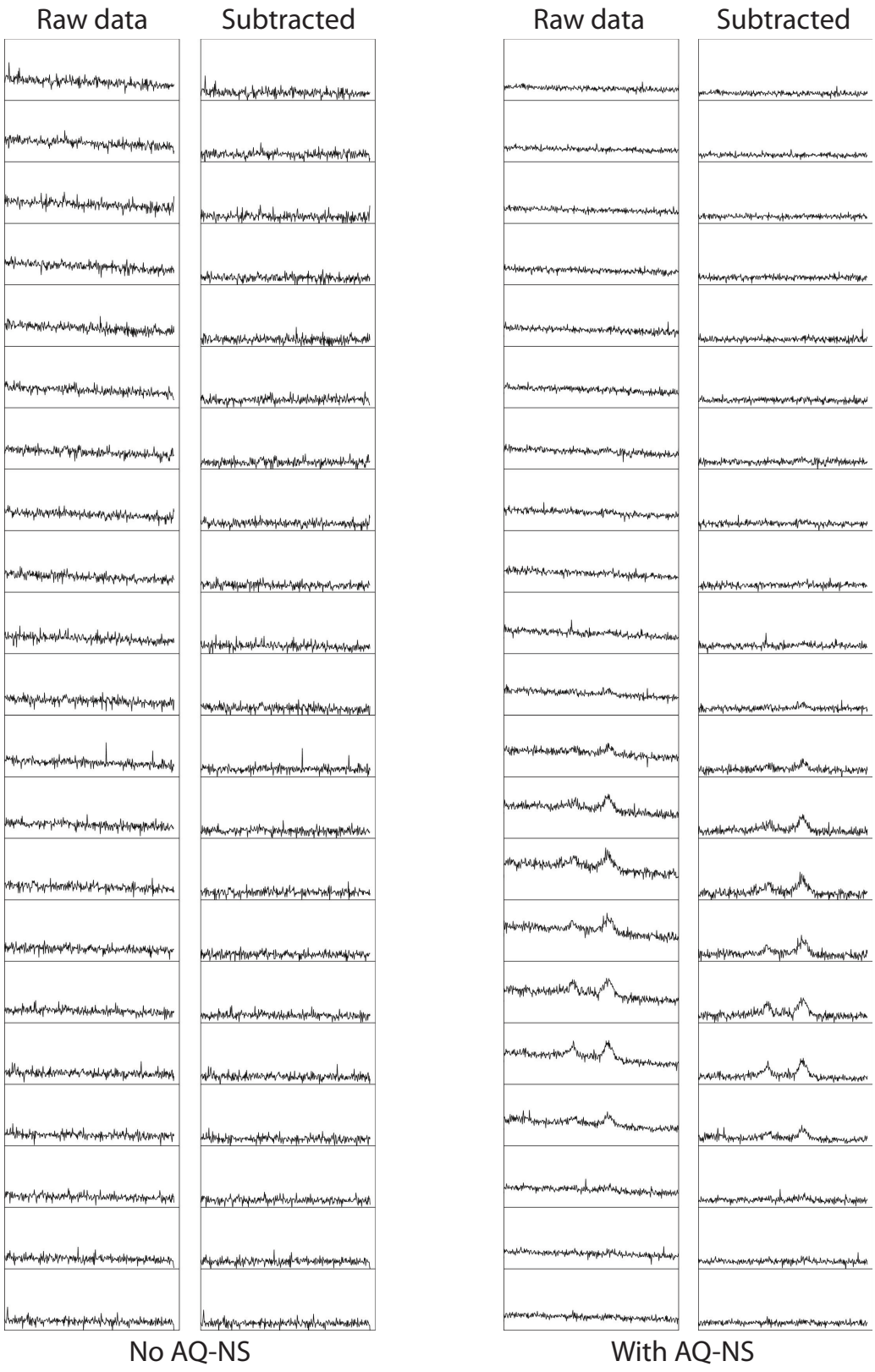

Figure 4.8: Subtraction of a scaled smoothed average background successfully compensates for the variability in imaging dish background and does not lead to over- or under-subtraction in intracellular spectra, irrespective of whether signals from AQ-NS are present. Acquisition conditions and layout are as in Figure 4.1.

4.2.2 Gold nanoshells

Raman spectra were obtained from small aggregates of bare gold nanoshells dried onto a glass-bottomed imaging dish. It was found that spectra from the bare nanoshells were indistinguishable from those from the glass-bottomed imaging dish they were dried onto, indicating that bare nanoshells are not Raman active. Figure 4.9 shows representative Raman spectra from a glass-bottomed imaging dish and a small aggregate of bare nanoshells dried onto a glass-bottomed imaging dish. Therefore there was no need to add this to the model.

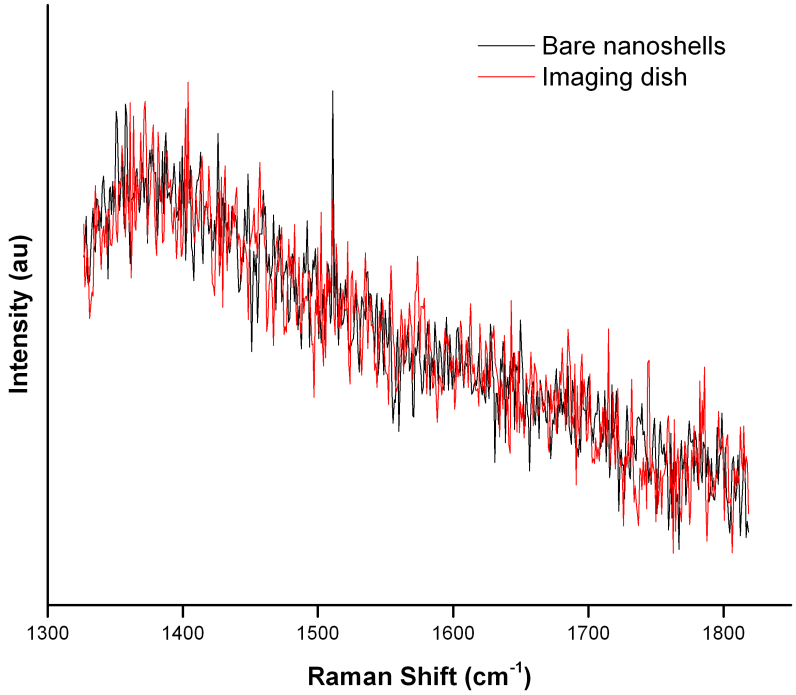

Figure 4.9: The Raman spectrum from a small aggregate of bare nanoshells dried onto a glass-bottomed imaging dish (red) is no different to the Raman spectrum of the glass-bottomed imaging dish (black). (NB: the spike at ~1500 cm^{-1} in the black spectrum is due to a hot pixel on the CCD camera).

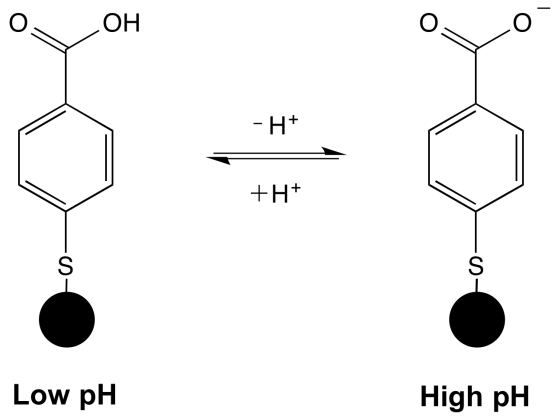

Figure 4.10: Structure of the MBA reporter molecule conjugated to a gold nanoshell (black circle) via a gold-thiol bond. The protonated form (left) predominates at low pH, whereas the deprotonated form (right) predominates at high pH.

4.3 Peak fitting for various reporter molecules

4.3.1 MBA – pH sensor

The pH-sensitive *para*-mercaptobenzoic acid (MBA; Figure 4.10) molecule has been shown to be a good SERS-based reporter molecule for intracellular use [204]. Calibration data were supplied by Lauren Jamieson and consisted of 3 independent datasets, each having $\geq$5 spectra per pH obtained using the Renishaw inVia Reflex microRaman system, making a total of 303 spectra, covering a range of 3.7 to 13.1 pH units. Figure 4.11 shows how peaks in the spectrum change with pH: the peak at ~1590 cm^{-1} is due to ring breathing [175, 205]; it is the most intense peak in the spectrum in the region 1300-1800 cm^{-1} and is therefore a good candidate for a reference peak, being present at both high and low pH. The centre of this peak can be seen to shift to the left as pH increases. The peak at ~1400 cm^{-1} is not distinguishable at low pH and increases as pH increases; it is due to COO^- stretching [175, 204, 205]. At pH >8.5 this peak moves to higher wavenumbers (~1420 cm^{-1}) and becomes more intense. The peak at ~1700 cm^{-1} shows the opposite: it is highest at low pH and decreases with increasing pH; it is due to C=O stretching [204, 205]. The opportunity therefore exists to use all 3 of these peak heights and areas in order to estimate pH, as well as the shift in centre of the 1590 cm^{-1} peak.

The profile of each peak was investigated as to whether a Gaussian or Lorentzian peak was more appropriate. For the peak at ~1590 cm^{-1} the residuals (the distance of

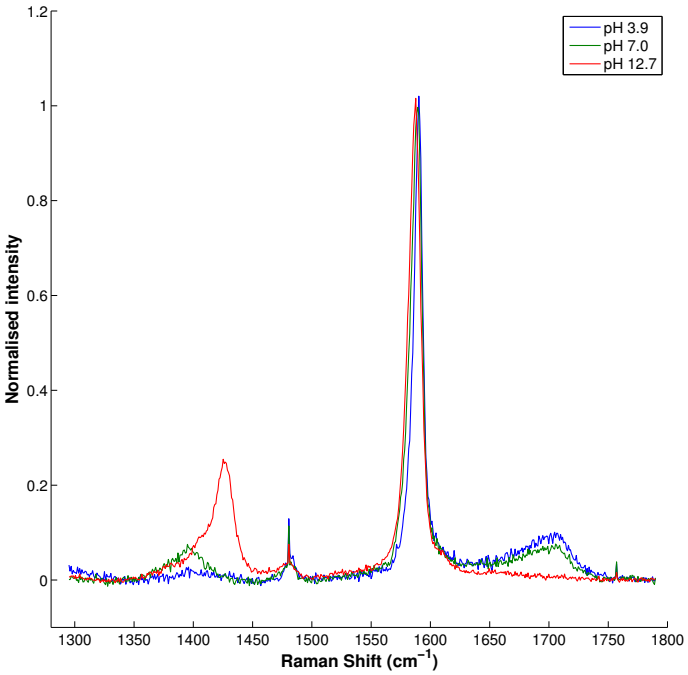

Figure 4.11: Change in the position and intensity of 3 peaks in the MBA-NS Raman spectrum. Spectra have been background subtracted and normalised to the intensity of the peak at ~1590 cm^{-1}.

each data point from the fit at the corresponding Raman shift) were not normally distributed for either a Lorentzian or Gaussian peak – the fitted peak was consistently to the left of the raw data peak (Figure 4.12(a)). This suggested either a degree of asymmetry (which could be modelled by adding a slope term) or the presence of 2 closely overlapping peaks (as the peak centre was found to depend on pH). Four models were therefore compared: a Lorentzian peak on a slope; a Gaussian peak on a slope; two closely overlapping Lorentzian peaks; and two closely overlapping Gaussian peaks. The best model was selected by performing an F-test on the average sum of squared residuals as detailed in Section 2.3.4. Table 4.2 shows that the Lorentzian peak on a slope model was statistically the more accurate model of the four compared - the improvement in the normality of the residuals can be seen in Figure 4.12(b).

The fit equation is given by Equation 4.1:

$$y = \frac{a}{1 + (\frac{x_c - b}{c})^2} + mx + d \tag{4.1}$$

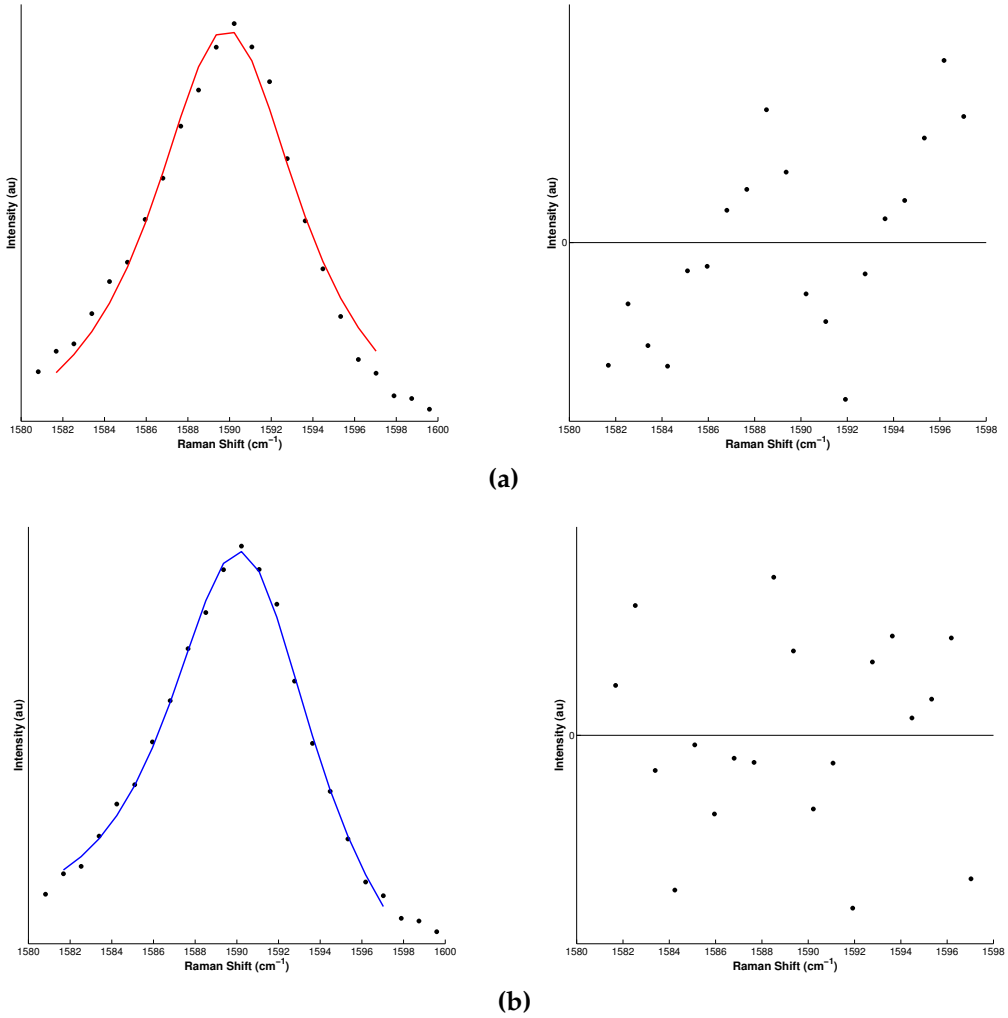

Figure 4.12: Improvement of the Lorentzian peak fit to the peak at ~1590 cm^{-1} in the MBA-NS Raman spectrum by adding a pedestal to the fit equation (a) example of a Lorentzian fit to a background subtracted spectrum (left) and the residuals (right); (b) Lorentzian peak on a slope fit to the same spectrum in (a) (left) and the residuals (right).

Fit type	Average sum of squared residuals	Average residual variance	F-statistic
Lorentzian + slope	110,155	6,120	
Gaussian + slope	124,703	6,928	1.132 (p = 0.30) vs. Lorentzian + slope†
2 Lorentzian peaks	122,426	6,751	N/A vs. Lorentzian + slope* 0.121 (p = 0.87) vs. Gaussian + slope†
2 Gaussian peaks	98,062	5,438	0.802 (p = 0.42) vs. Lorentzian + slope† 1.766 (p = 0.16) vs. Gaussian + slope† 0.801 (p = 0.42) vs. 2 Lorentzian peaks†

Table 4.2: Comparison of average sum of squared residuals and average residual variance for various fit types for the peak ~1590 cm^{-1} in the MBA-NS Raman spectrum. *The F-statistic cannot be calculated where the model with more parameters has a larger average sum of squared residuals than the model with fewer parameters, therefore the model with fewer parameters is the better model. †A p value of >0.05 indicates that the one model is not statistically more accurate than other, so the slope model should be used as it has fewer parameters. The Lorentzian + slope model is better overall as it has a smaller average sum of squared residuals and residual variance than the Gaussian + slope model.

where a is the peak amplitude, b is the peak centre, c is the peak width, m is the slope gradient and d is the slope intercept.

The same process was used for the peaks at ~1400 cm^{-1} and ~1700 cm^{-1}. The peak at ~1400 cm^{-1} was modelled by a single peak and the calibration data were separated into three ranges: pH <6, 6-8.5 and >8.5, due to the low SNR at low pH and the shift of the peak centre at high pH. Table 4.3 shows that a Lorentzian peak on a slope is also the statistically more accurate model.

The peak at ~1700 cm^{-1} is clearly asymmetric (Figure 4.11) and as its centre was not found to depend on pH only the Lorentzian peak on a slope and the Gaussian peak on a slope models were compared. The calibration data was split into 2 ranges: pH

pH range	Fit type	Average sum of squared residuals	Average residual variance	F-statistic
Mid pH	Lorentzian	68,327	1,135	
	Gaussian	64,615	1,074	0.946 (p = 0.38) vs. Lorentzian
	Lorentzian + slope	57,355	956	5.356 (p = 0.01) vs. Lorentzian† 3.544 (p = 0.03) vs. Gaussian†
	Gaussian + slope	58,978	983	4.438 (p = 0.01) vs. Lorentzian† 2.676 (p = 0.07) vs. Gaussian† 1.028 (p = 0.35) vs. Lorentzian + slope
High pH	Lorentzian	1,171,926	13,842	
	Gaussian	629,865	9,704	0.537 (p = 0.58) vs. Lorentzian
	Lorentzian + slope	91,106	1,518	332.174 (p <0.001) vs. Lorentzian† 165.580 (p <0.001) vs. Gaussian†
	Gaussian + slope	145,700	2,428	197.215 (p <0.001) vs. Lorentzian† 93.044 (p <0.001) vs. Gaussian† 1.599 (p = 0.20) vs. Lorentzian + slope

Table 4.3: Comparison of average sum of squared residuals and average residual variance for various fit types for the peak ~1400 cm^{-1} in the MBA-NS Raman spectrum. †A small p value (<0.05) indicates that the slope model is statistically more accurate than the non-slope model, taking into account the expected improvement in the sum of squared residuals due to the extra two parameters. For both mid-range (pH 6-8.5) and high pH (>8.5) the Lorentzian + slope model is better overall as it has a smaller average sum of squared residuals and residual variance than the Gaussian + slope model.

Fit type	Average sum of squared residuals	Average residual variance	F-statistic†
Lorentzian + slope	86,559	1,124	
Gaussian + slope	89,260	1,159	1.031 (p = 0.35) vs. Lorentzian + slope

Table 4.4: Comparison of average sum of squared residuals and average residual variance for two fit types for the peak ~1700 cm^{-1} in the MBA-NS Raman spectrum. †A p value >0.05 indicates that both models are an equally good fit, however the Lorentzian + slope model was chosen as it has a smaller sum of squared residuals for pH <6. Calibration data for pH >6 were not used due to the low SNR at higher pH.

<6 and pH >6 due to the low SNR at higher pH. Table 4.4 shows that the Lorentzian peak on a slope (Equation 4.1) is the better model as the sum of squared residuals is smaller than for the Gaussian + slope model.

Each of the three peaks in each spectrum was then fitted separately and the calibration data grouped by pH in order to investigate relationships between various fit parameters and pH. Weighted means of the various parameters at each pH were calculated using inverse weighting to reduce the effect of values with a large error:

$$\mu^* = \frac{\sum w_i x_i}{\sum w_i} \tag{4.2}$$

where x_i are the individual parameter values and the weights, w_i, are defined as the reciprocal of the square of the standard error obtained from the fitting process:

$$w_i = \frac{1}{\sigma^2} \tag{4.3}$$

The standard deviation of the weighted mean used is:

$$\sqrt{\frac{\sum w_i (x_i - \mu^*)^2}{\sum w_i - (\sum {w_i}^2 / \sum w_i)}} \tag{4.4}$$

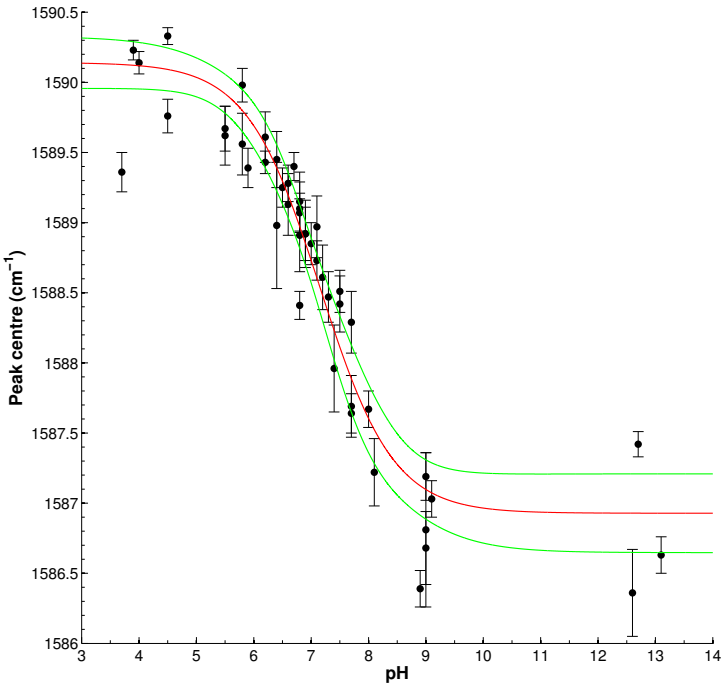

Figure 4.13: MBA-NS: variation of the centre of the peak at ~1590 cm^{-1} with pH (Renishaw system). A Boltzmann curve (red line) has been fitted to points which are the weighted means from three independent datasets; error bars are the standard deviation of the weighted mean; green lines are the 95% non-simultaneous confidence bands.

It was found that the centre of the peak at ~1590 cm^{-1} varied with pH, indicating that this parameter could be used to estimate pH. The centre of the peak at ~1400 cm^{-1} shifted to higher wavenumbers at high pH, but otherwise did not vary with pH. The centre of the peak at ~1700 cm^{-1} did not change with pH. None of the peaks' widths changed appreciably with pH. The following ratios of peak heights and areas were dependent on pH: 1590/1400, 1590/1700 and 1400/1700, indicating that a combination of seven parameters could be used to estimate pH.

The three datasets were combined, a Boltzmann curve fitted and 95% confidence bands calculated for each parameter that changed with pH (Figures 4.13, 4.14 and 4.15). From these it can be seen that each calibration is most accurate over a pH range of approximately 6-8; outside this range the estimated pH is subject to large error. The aim of using this probe was to measure intracellular pH, which should be within this range, so acceptable ranges were therefore determined for each parameter as the values of the Boltzmann fit at pH 6 and 8 (Table 4.5). The pH was then estimated from each of the seven calibration graphs, with an overall error in pH determined

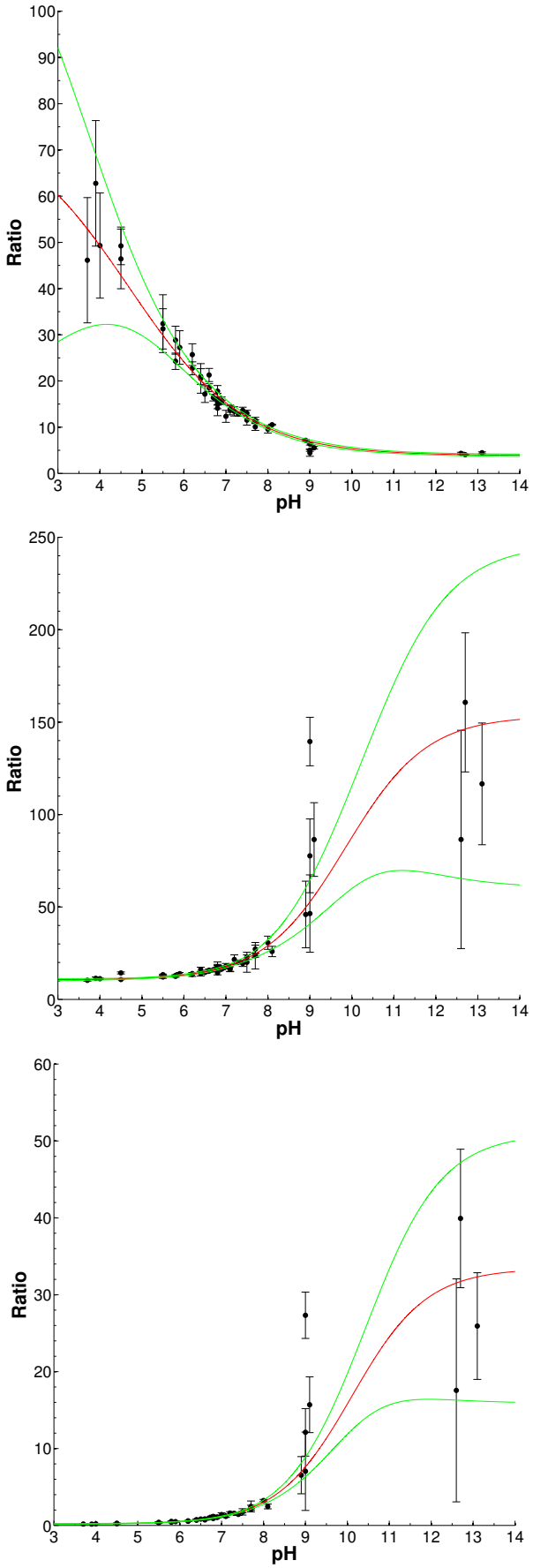

Figure 4.14: MBA-NS: variation of 1590/1400 (top), 1590/1700 (middle) and 1400/1700 (bottom) peak height ratios with pH (Renishaw system). A Boltzmann curve (red line) has been fitted to points which are the weighted means from three independent datasets; error bars are the standard deviation of the weighted mean; green lines are the 95% non-simultaneous confidence bands.

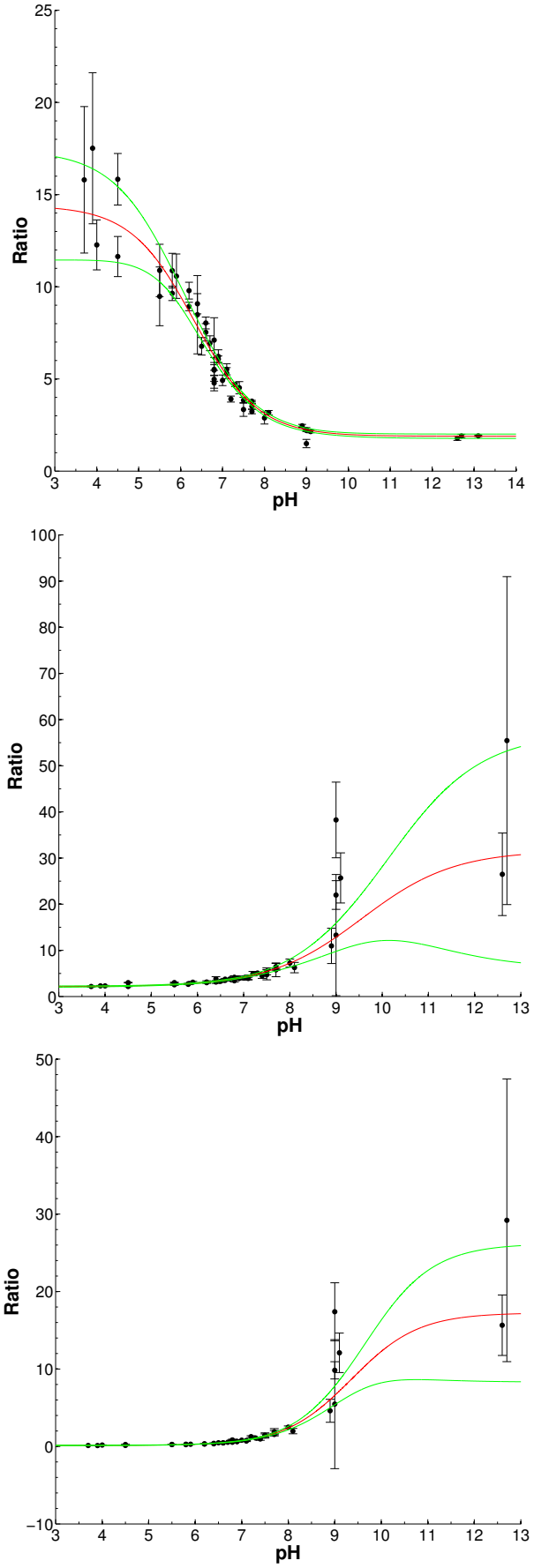

Figure 4.15: MBA-NS: variation of 1590/1400 (top), 1590/1700 (middle) and 1400/1700 (bottom) peak area ratios with pH (Renishaw system). A Boltzmann curve (red line) has been fitted to points which are the weighted means from three independent datasets; error bars are the standard deviation of the weighted mean; green lines are the 95% non-simultaneous confidence bands.

Parameter	Lower value	Upper value
1590 peak centre	1587.597	1589.6910
1590/1400 peak height	9.871	24.143
1590/1700 peak height	13.230	29.099
1400/1700 peak height	0.503	3.024
1590/1400 peak area	3.129	9.471
1590/1700 peak area	2.920	7.222
1400/1700 peak area	0.291	2.374

Table 4.5: Acceptable ranges for each parameter of MBA-NS, corresponding to the values of the Boltzmann fits for each parameter at pH 6 and 8 (Renishaw system). The estimated pH for each parameter is only calculated if the parameter is within the range given.

from both the error in the Boltzmann fit and the error in the peak centre, height ratio or area ratio. The estimated pH from each parameter was combined into a weighted mean (Equation 4.2) to give a more accurate estimation of pH, with the standard deviation of the weighted mean calculated as in Equation 4.4. Spectra were marked as 'pH <6' or 'pH >8' as appropriate if they met either of the following conditions:

- if 2 or more area ratios were outside the ranges given in Table 4.5
- if 3 or more of the peak centre or height ratios were outside the ranges given in Table 4.5.

When used to analyse the calibration data, this method resulted in an average standard deviation of ±0.16 pH units. Individual 95% confidence intervals were calculated from the individual standard deviations of each spectrum, where the estimated pH was in the range 6-8; Figure 4.16 shows estimated pH versus actual pH for those spectra for which confidence intervals were calculated. Overall, 92.4% (very close to the expected value of 95%) of the calibration spectra were correctly identified as belonging to one of the following categories:

- pH <6
- pH >8
- the error range associated with the estimated pH contained the actual pH.

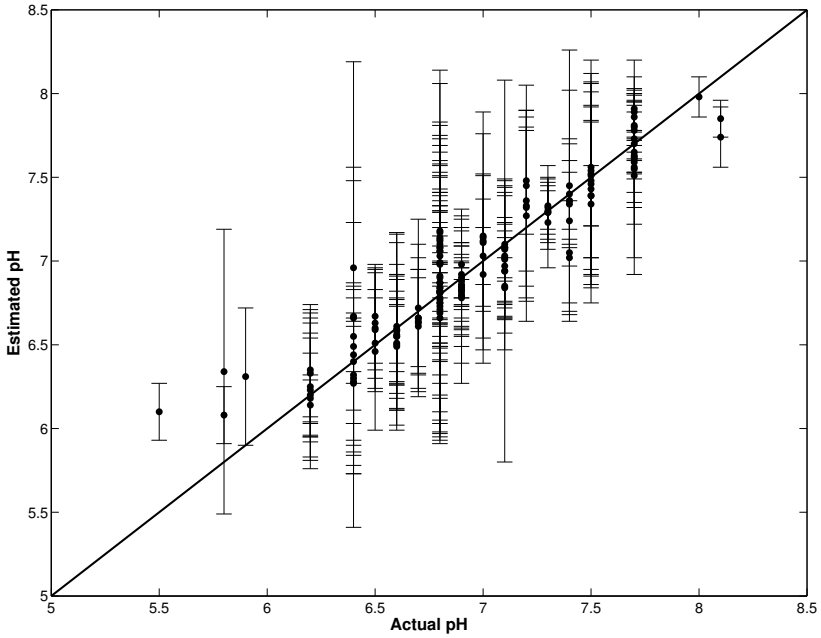

Figure 4.16: Comparison of the estimated pH with 95% confidence interval versus actual pH of the calibration spectra used in the calibration of MBA-NS (Renishaw system). The estimated pH is a weighted mean of the pH estimated from each of the seven calibration curves. The thick line indicates where estimated pH = actual pH. The calibration spectra (n = 303) were classified as pH <6, pH 6-8 or pH >8; only those classified as pH 6-8 are shown. Of these 303 spectra, three (1.0%) were incorrectly classified as having an estimated pH <6; five (1.7%) were incorrectly classified as having an estimated pH >8 and 15 (5.0%) had a 95% confidence interval that did not include the actual pH.

	Manual processing	**Automated processing**
Mean estimated pH	6.56	7.14
Standard deviation	0.29	0.09
Mean error	-	0.28
Time per spectrum	3 minutes	1 second

Table 4.6: Comparison of manual and automated processing methods in the estimation of pH from 10 consecutive spectra obtained from MBA-NS dried onto an imaging dish (Renishaw system). The manual processing method does not provide an error associated with the estimated pH. The automated processing method results in much less variation in estimated pH from each of the 10 spectra, and the processing time per spectrum is reduced by nearly 200-fold.

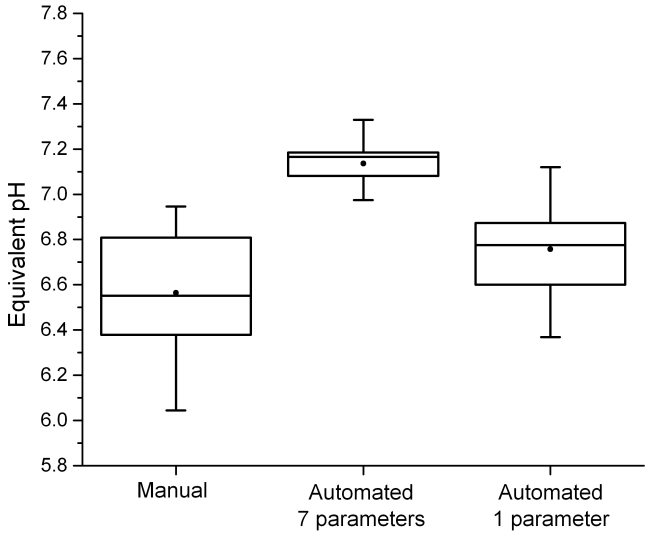

Figure 4.17: Boxplots showing the median, 1st and 3rd quarter percentiles, range and mean (filled circle) for the estimation of pH from 10 consecutive spectra obtained from MBA-NS dried onto an imaging dish from both manual and automated processing methods (Renishaw system). The manual method uses only one parameter to estimate pH: the height ratio of the peaks at ~1400 and ~1590 cm^{-1}; the pH estimated by the automated processing method using only this parameter is shown for comparison (Automated 1 parameter). The automated processing methods uses a total of seven parameters to estimate pH and results in a much smaller range than the manual processing method.

The algorithm was then compared to the manual processing method. The variability of spectra can be determined by acquiring consecutive spectra from the same aggregate of MBA-functionalised nanoshells dried onto a quartz coverslip. What is being tested here is the variability between the manual and automatic processing methods, so it is important to obtain consecutive spectra that are very similar. To this end, 10 consecutive spectra were obtained from MBA-NS dried onto an imaging dish and then processed by both methods. The manual process uses only one parameter to estimate pH: the ratio of the peak heights of the peaks at ~1400 and ~1590 cm^{-1}, whereas the automated process uses seven parameters. A comparison of the two methods is given in Table 4.6 and Figure 4.17. Manual processing of the 10 spectra resulted in a mean pH of 6.56 with a standard deviation of 0.29, whereas the automated processing resulted in a mean pH of 7.14 with a standard deviation of 0.09. The manual process does not provide an error associated with the estimated pH, whereas the automated process results in an associated mean error of 0.28 pH

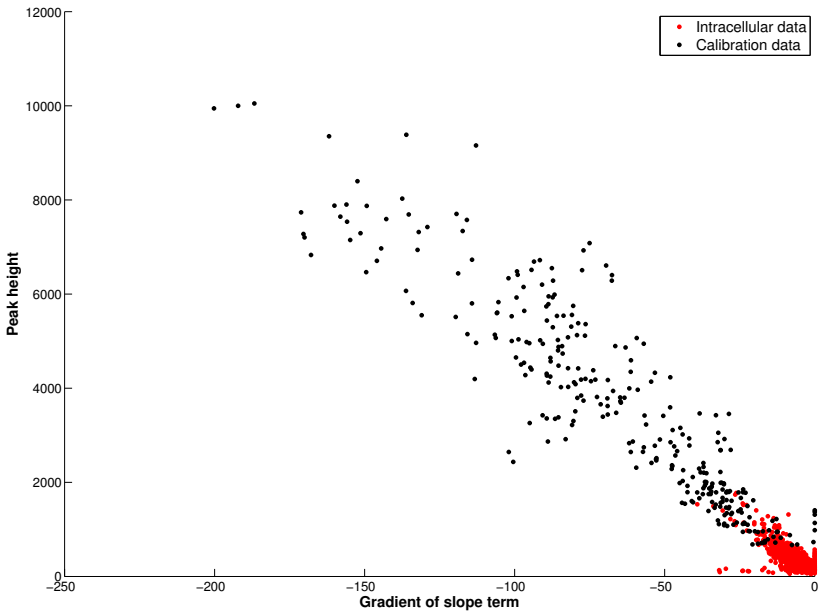

Figure 4.18: Correlation between the slope term and height from the fit for the peak at ~1590 cm^{-1}in the Raman spectrum of MBA-NS (Renishaw system).

units. Furthermore, automated processing is nearly 200 times faster than manual processing. The lower pH estimated by the manual method could be due to only using one parameter as the mean estimated pH of the same parameter by the automated method is 6.76 with a standard deviation of 0.21, lower than the mean derived from all seven parameters. These results show that not only is processing faster by 2 orders of magnitude, there is less variability in the automated processing method and the combination of seven parameters enables a more robust estimation of pH.

The algorithm was then used with intracellular data also provided by Lauren Jamieson. To see if the background subtraction method produced the same results in intracellular data as with the calibration data, the gradient of the slope term of the fit to the peak at ~1590 cm^{-1} was plotted against its height, as there was a correlation between the two in the calibration data. Figure 4.18 shows a good overlap of data from 39 maps of intracellular nanosensors and calibration data. This indicates that the background subtraction method described above in Section 4.2.1 successfully removes the variability in background intensities, independent of the source and shape of the background.

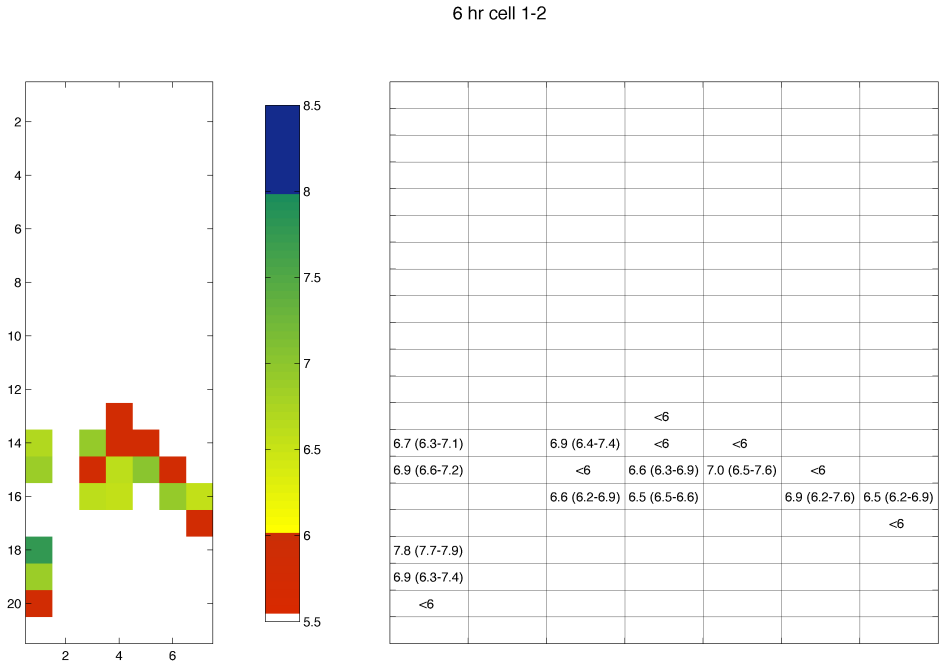

Figure 4.19: Spatial distribution of estimated pH values: (left) colourmap of estimated pH values; (right) gridmap showing the estimated pH values with range from a map acquisition of a cell containing MBA-NS (Renishaw system).

Colourmaps of the intracellular data were produced by plotting the estimated pH in the location given by its spectrum number (Figure 4.19). These allow the spatial distribution of pH values to be visualised, both by colour and by value. The time to process the 147 spectra in one map and produce a colourmap with the automated method was 48 seconds. With the manual method this would take 45-90 minutes, depending on the number of spectra that require processing as not all 147 spectra will contain a signal from MBA-NS.

The automated processing method was then used to process Raman spectra obtained on a different spectrometer, the Ocean Optics fibre optic Raman system (for details see Section 2.5). This is important as a similar result would confirm the robustness of the method, especially as the two spectrometers were so different. Calibration data from this spectrometer were also supplied by Lauren Jamieson and consisted of 3 independent datasets, each having $\geq$5 spectra per pH and totalling 203 spectra, covering a range of 3.9 to 13.1 pH units. The data were processed in exactly the same way as for the Renishaw system data above and the calibration curves and acceptable

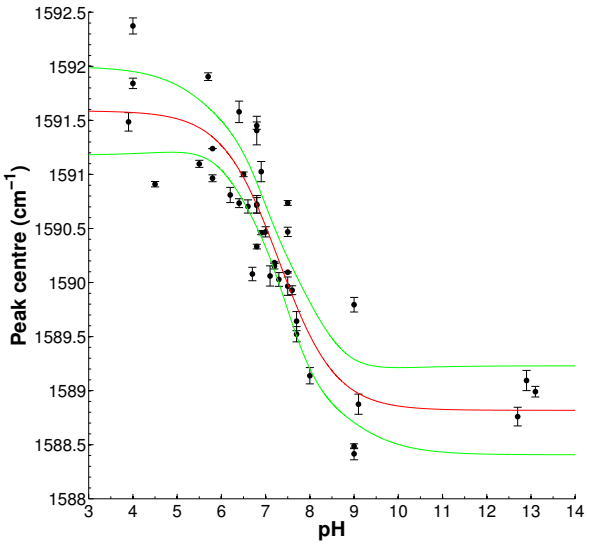

Figure 4.20: MBA-NS: variation of the centre of the peak at ~1590 cm^{-1} with pH (Ocean Optics system). A Boltzmann curve (red line) has been fitted to points which are the weighted means from three independent datasets; error bars are the standard deviation of the weighted mean; green lines are the 95% non-simultaneous confidence bands.

ranges for each parameter are shown in Figures 4.20, 4.21 and Table 4.7, respectively. When used to analyse the calibration data, the average standard deviation of the weighted mean was ±0.19 pH units. Once again, 95% confidence intervals were calculated for each of the calibration spectra that had an estimated pH in the range 6-8, and Figure 4.22 shows estimated pH versus actual pH of those spectra for which confidence intervals were calculated. Overall, 90% (very close to the expected value of 95%) of the calibration spectra were correctly identified as belonging to one of the following categories:

- pH <6
- pH >8
- the error range associated with the estimated pH contained the actual pH.

A comparison of the individual Boltzmann fit parameters and associated statistics is given in Table 4.8 for the calibration data obtained from both Renishaw and Ocean Optics systems. Interestingly, the values for the ~1590 cm^{-1} peak centre are different for the two systems: the values obtained for the data from the Renishaw system range from 1586.9 cm^{-1} to 1590.1 cm^{-1}, whereas the values obtained for data from the Ocean Optics system range from 1588.8 cm^{-1} to 1591.6 cm^{-1}. Furthermore the data

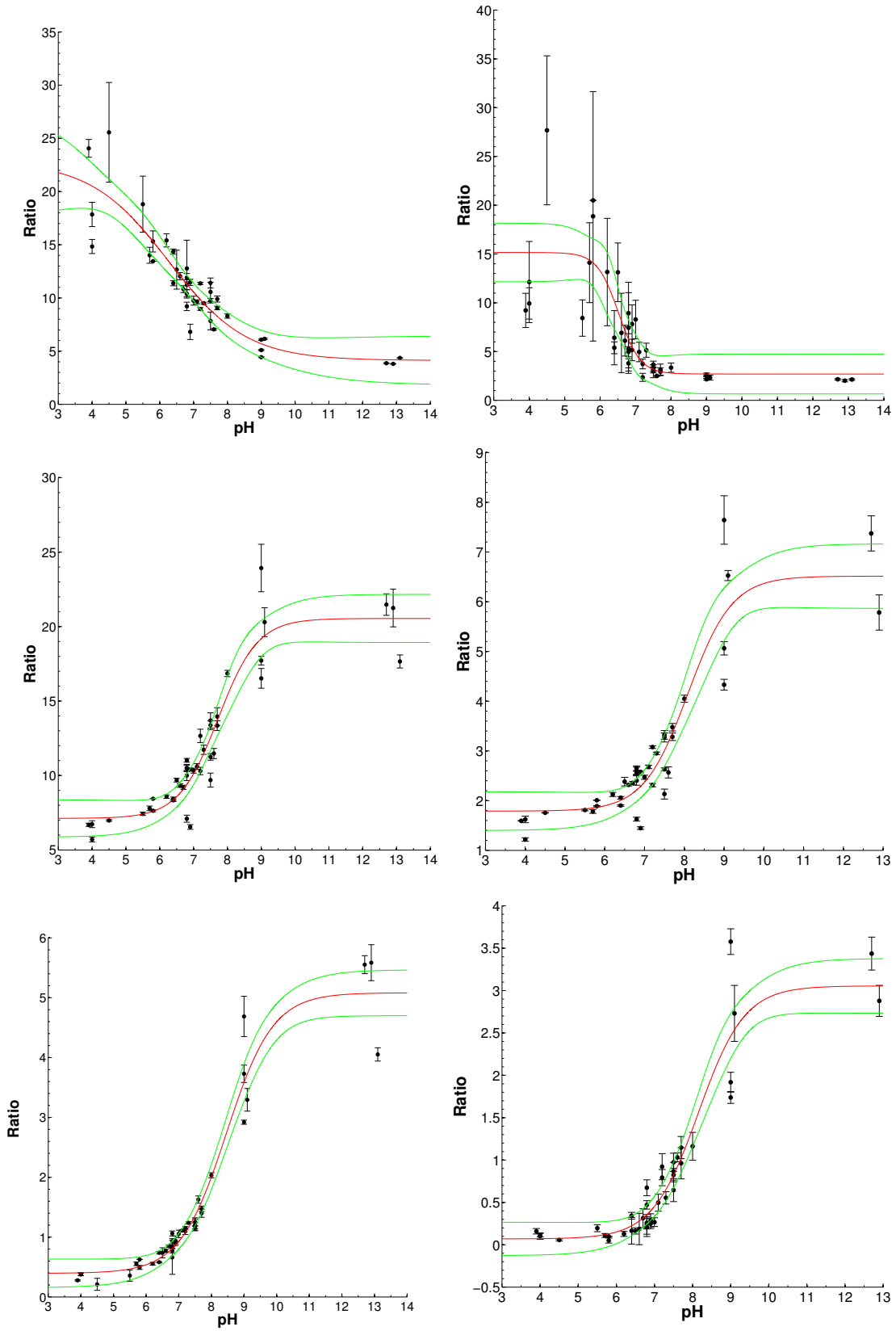

Figure 4.21: MBA-NS: variation of 1590/1400 (top), 1590/1700 (middle) and 1400/1700 (bottom) peak height (left) and peak area (right) ratios with pH (Ocean Optics system). A Boltzmann curve (red line) has been fitted to points which are the weighted means from three independent datasets; error bars are the standard deviation of the weighted mean; green lines are the 95% non-simultaneous confidence bands.

Parameter	Lower value	Upper value
1590 peak centre	1589.512	1591.268
1590/1400 peak height	7.490	14.511
1590/1700 peak height	7.782	15.374
1400/1700 peak height	0.539	2.005
1590/1400 peak area	2.796	13.259
1590/1700 peak area	1.898	3.962
1400/1700 peak area	0.151	1.371

Table 4.7: Acceptable ranges for each parameter of MBA-NS, corresponding to the values of the Boltzmann fits for each parameter at pH 6 and 8 (Ocean Optics system). The estimated pH for each parameter is only calculated if the parameter is within the range given.

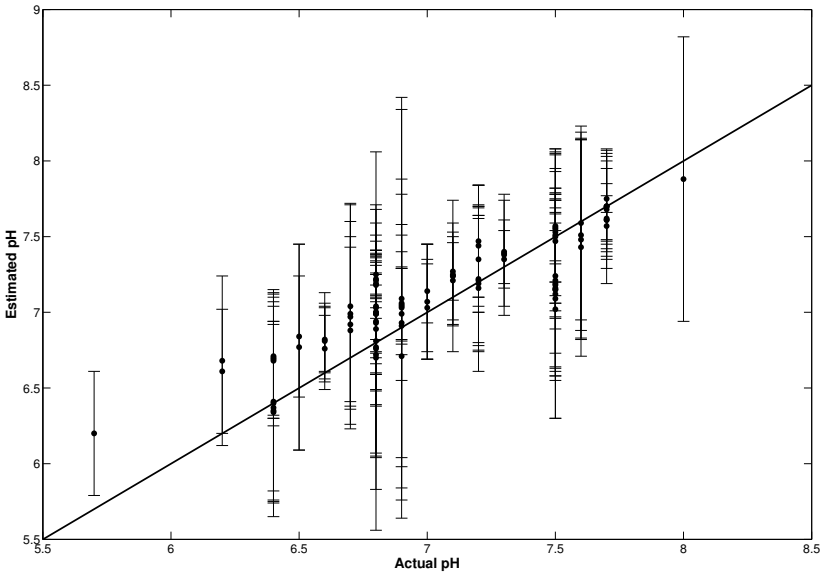

Figure 4.22: Comparison of the estimated pH with 95% confidence intervals versus actual pH of the calibration spectra used in the calibration of MBA-NS (Ocean Optics system). The estimated pH is a weighted mean of the pH estimated from each of the seven calibration curves. The thick line indicates where estimated pH = actual pH. The calibration spectra (n = 203) were either classified as pH <6, 6-8 or >8; only those classified as pH 6-8 are shown. Of these 203 spectra, nine (4.4%) were incorrectly classified as having an estimated pH <6; one (0.5%) was incorrectly classified as having an estimated pH >8 and 12 (5.9%) had a 95% confidence interval that did not include the actual pH.

Parameter/ statistic	1590 cm^{-1} peak centre	1590/1400 height ratio	1590/1700 height ratio	1400/1700 height ratio	1590/1400 area ratio	1590/1700 area ratio	1400/1700 area ratio
Max. value	1590.13 (± 0.09) 1591.59 (± 0.20)	76.82 (± 33.3) 22.82 (± 2.88)	153.39 (± 46.11) 20.55 (± 0.80)	33.44 (± 8.70) 5.08 (± 0.19)	14.41 (± 1.49) 15.16 (± 1.48)	31.63 (± 12.66) 6.51 (± 0.32)	17.25 (± 4.43) 3.06 (± 0.16)
Min. value	1586.93 (± 0.14) 1588.82 (± 0.20)	3.84 (± 0.16) 4.12 (± 1.14)	10.58 (± 0.32) 7.12 (± 0.62)	0.18 (± 0.03) 0.40 (± 0.12)	1.89 (± 0.06) 2.70 (± 1.01)	2.12 (± 0.09) 1.79 (± 0.19)	0.13 (± 0.02) 0.07 (± 0.10)
Range	3.20 2.77	72.98 18.70	142.81 13.43	33.26 4.68	12.52 12.46	29.51 4.72	17.12 2.99
Midpoint (pH)	7.16 (± 0.10) 7.30 (± 0.17)	4.69 (± 0.10) 6.26 (± 0.41)	9.84 (± 0.51) 7.73 (± 0.13)	10.11 (± 0.33) 8.46 (± 0.11)	6.33 (± 0.18) 6.52 (± 0.16)	9.56 (± 0.64) 8.09 (± 0.16)	9.36 (± 0.26) 8.16 (± 0.13)
Value at midpoint	1588.53 1590.20	40.30 13.46	81.84 13.85	16.83 2.74	8.13 8.94	16.91 4.15	8.69 1.57
Slope	0.63 (± 0.10) 0.64 (± 0.17)	1.38 (± 0.14) 1.15 (± 0.34)	0.97 (± 0.11) 0.58 (± 0.12)	0.89 (± 0.05) 0.71 (± 0.08)	0.76 (± 0.06) 0.30 (± 0.14)	1.00 (± 0.12) 0.56 (± 0.12)	0.72 (± 0.04) 0.60 (± 0.09)
Adjusted R^2	0.93 0.80	0.97 0.82	0.88 0.88	0.95 0.95	0.97 0.63	0.91 0.87	0.95 0.92

Table 4.8: Comparison of Boltzmann fit parameters and statistics from the calibration curves for MBA-NS generated from data obtained from the Renishaw system (top rows) and Ocean Optics system (bottom rows).

from the Renishaw system has a wider range than the data from the Ocean Optics system (3.2 cm^{-1} and 2.8 cm^{-1}, respectively), but the pH values at the midpoints of the curves are similar (7.2 and 7.3, respectively), as are the slopes at the midpoint (0.63 and 0.64, respectively). One reason for the difference in peak centre could be due to the fact that wavenumber calibration is carried out on the Renishaw system but not on the Ocean Optics system - this could account for the difference in peak centre at the midpoint (1588.4 and 1590.1 cm^{-1}, respectively). Also, the wavenumber resolution is much lower on the Ocean Optics system and the peak is described by only 7 points compared to 19 points for the same wavenumber region on the Renishaw system. This would account for the larger error in the fit parameters (Table 4.8) of the Ocean Optics data and could lead to the slightly narrower range.

The peak height ratios are not as affected by the value of the respective peak centres because the height is maximum of the fit. The error in height ratios arises from the low SNR for the pH-sensitive peaks when they are at their minimum, resulting in a small denominator with a large error. This is why there is much more error in the maximum values of the Boltzmann fit parameters for both the Renishaw and Ocean Optics systems than in the minimum values. The Renishaw system also has a lower SNR than the Ocean Optics system, which leads to more variability in the height of the pH-sensitive peaks at their minimum, further increasing the error in the maximum value of the Boltzmann fit parameters. Furthermore, the Renishaw system has a higher average peak intensity overall, making the maximum value of the height and area ratios much larger. Consequently the range is larger (as the minimum values are approximately the same on both systems), the midpoint is shifted, the value at the midpoint is higher and the slope is steeper. Finally, the lower adjusted R^2 value for the Ocean Optics calibration is due to there being more variability between datasets.

4.3.2 NQ - redox potential sensor

Calibration data for the NQ-NS nanosensor (Figure 4.23) was supplied by Jing Jiang and consisted of 5 spectra per redox potential obtained using the Renishaw system, making a total of 40 spectra. Figure 4.24 shows how peaks in the spectrum change

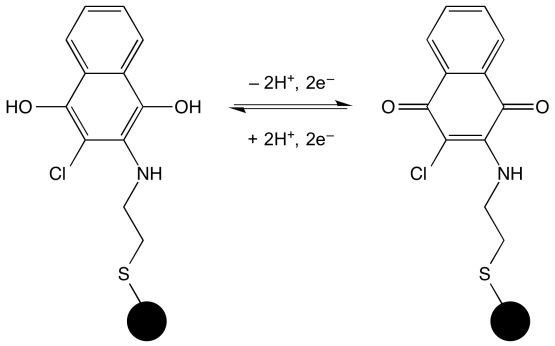

Figure 4.23: Reduced (left) and oxidised (right) structures of the NQ reporter molecule conjugated to a gold nanoshell (black circle) via a gold-thiol bond.

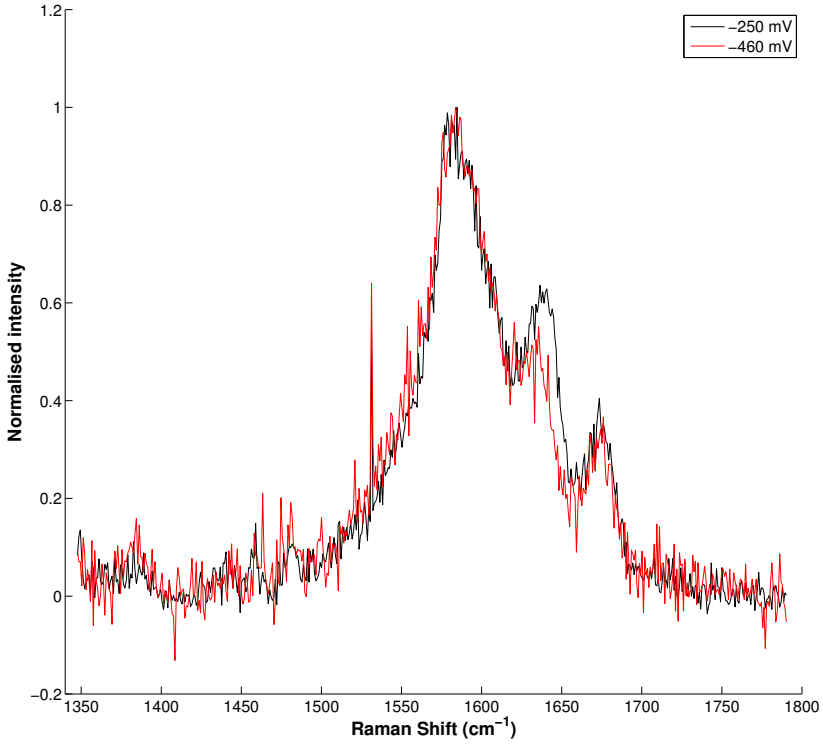

Figure 4.24: Redox-dependent change in the intensity of the peak at ~1640 cm^{-1} in the NQ-NS Raman spectrum. Spectra have been background subtracted and normalised to the intensity of the peak at 1577 cm^{-1}.

with redox potential: the peak at ~1580 cm^{-1} is actually composed of two peaks at 1577 cm^{-1} and 1602 cm^{-1} (symmetric ring breathing and aryl ring stretching with N-H wagging, respectively). This peak is the most intense peak in the region 1300-1800 cm^{-1}, so it is a good candidate for the reference peak, whereas the peak at ~1640 cm^{-1} is due to C=O stretching and increases with increasing oxidation. For NQ, then, there is the possibility of using peak height and area ratios of a combination of the three peaks at 1577 cm^{-1}, 1602 cm^{-1} and 1640 cm^{-1}.

As for the MBA-NS nanosensor, the peak profiles were established, and the same profile was used for each of the three peaks. Table 4.9 shows that the Lorentzian peaks model was the statistically more accurate model of the four compared. Therefore the data were modelled by the sum of three Lorentzian peaks (Equation 4.5):

$$y = \frac{a1}{1 + (\frac{x_c - b1}{c1})^2} + \frac{a2}{1 + (\frac{x_c - b2}{c2})^2} + \frac{a3}{1 + (\frac{x_c - b3}{c3})^2} \tag{4.5}$$

where $a1$, $a2$ and $a3$ are the peak amplitudes; $b1$, $b2$ and $b3$ are the peak centres; and $c1$, $c2$ and $c3$ are the peak widths of the peaks at 1577, 1602 and 1640 cm^{-1}.

After fitting, the calibration data were grouped by redox potential in order to investigate relationships between various fit parameters and redox potential. Weighted means and standard deviations of the various parameters at each redox potential were calculated using the same inverse weighting method as for the MBA-NS nanosensor (Equations 4.2 and 4.4). It was found that the ratio of the height of the peaks at 1577 and ~1640 cm^{-1} varied with redox potential, as did the equivalent area ratios. The centres of the peaks at 1577 and 1602 cm^{-1} did not change with redox potential, and the centre of the peak at ~1640 cm^{-1} varied with redox potential but not in a manner that could be used to estimate redox potential (Figure 4.25). None of the peaks' widths changed with redox potential. Therefore calibration curves were only constructed for the peak height and area ratios of the peaks at 1577 and ~1640 cm^{-1}.

Fit type	Average sum of squared residuals	Average residual variance	F statistic†
Lorentzian	234,468	2,632	
Lorentzian + slope	226,996	2,550	1.300 (p = 0.27) vs. Lorentzian 1.303 (p = 0.27) vs. Gaussian
Gaussian	234,486	2,632	1.000 (p = 0.36) vs. Lorentzian
Gaussian + slope	231,545	2,601	0.499 (p = 0.60) vs. Lorentzian 0.502 (p = 0.60) vs. Gaussian 1.020 (p = 0.36) vs. Lorentzian + slope

Table 4.9: Comparison of average sum of squared residuals and average residual variance for various fit types for the three overlapping peaks in the NQ-NS Raman spectrum. †A p value of >0.05 indicates that one model is not statistically more accurate than the other model. The Lorentzian model is best overall as it has fewer parameters and a smaller average sum of squared residuals and residual variance than the Gaussian model.

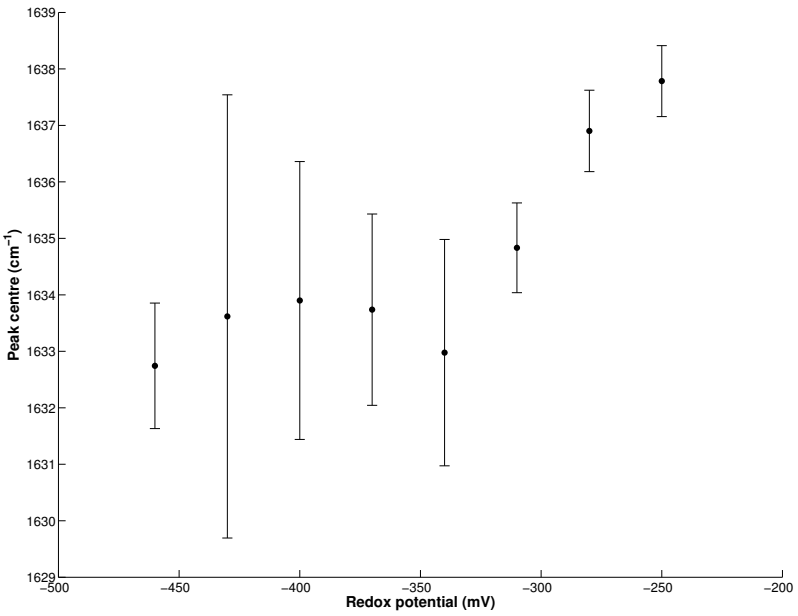

Figure 4.25: NQ-NS: variation of the centre of the peak at ~1640 cm^{-1} with redox potential (Renishaw system). Points are the weighted means of 5 data points; error bars are the standard deviation of the weighted mean.

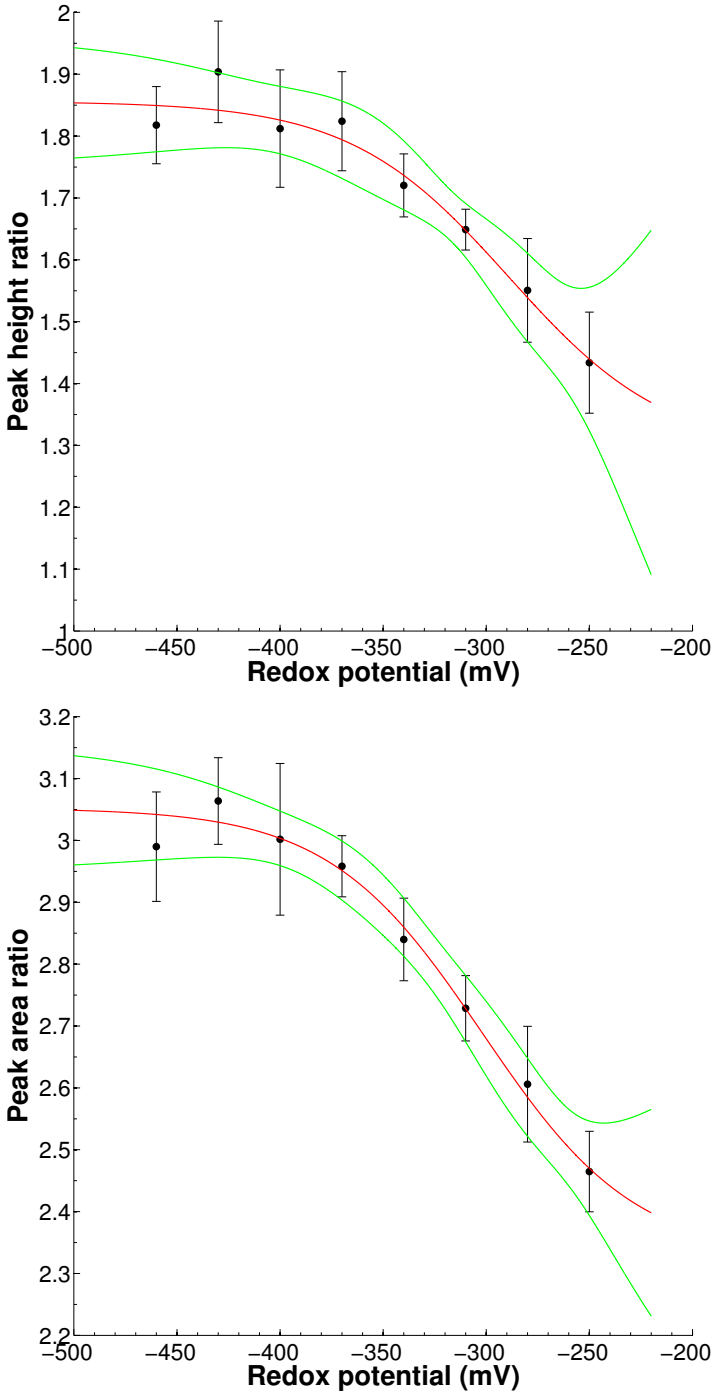

Figure 4.26: NQ-NS: variation of 1577/1645 cm^{-1} peak height (top) and peak area (bottom) ratios with redox potential (Renishaw system). A Boltzmann curve (red line) has been fitted to points which are the weighted means of 5 data points; error bars are the standard deviation of the weighted mean; green lines are the 95% non-simultaneous confidence bands.

Parameter	Lower value	Upper value
Peak height ratio	1.440	1.826
Peak area ratio	2.470	3.003

Table 4.10: Acceptable ranges for each parameter of NQ-NS, corresponding to the values of the Boltzmann fits at -400 and -250 mV (Renishaw system). The estimated redox potential for each parameter is only calculated if the parameter is within the range given.

A Boltzmann curve was fitted and 95% confidence bands were calculated for both of these parameters (Figure 4.26). Acceptable ranges for the ratios were determined as the values at -400 and -250 mV (Table 4.10), as this is the region where the curves change most rapidly. The redox potential was then estimated from both calibration graphs, with the overall error in redox potential determined from both the error in the Boltzmann fit and the error in the peak height or area ratio. With only two parameters used to estimate redox potential, there is a possibility that one parameter with a large error can skew the estimated redox potential away from the actual potential. Therefore the estimated redox potential from each parameter was combined into a weighted mean to avoid this effect (Equation 4.2). The standard deviation of the weighted mean was calculated using Equation 4.4. Spectra were marked as 'reduced' or 'oxidised' if either or both ratios were outside the ranges given in Table 4.10.

When used to analyse the calibration data, this method resulted in an average standard deviation of 23.3 mV. Individual 95% confidence intervals were calculated from the individual standard deviations of each spectrum, where the estimated redox potential was in the range -400 to -250 mV; Figure 4.27 shows estimated versus actual redox potential for those spectra for which confidence intervals were calculated. Overall, 85% of the calibration spectra were correctly identified as belonging to one of the following categories:

- redox potential <-400 mV
- redox potential >-250 mV
- the error range associated with the estimated redox potential contained the actual redox potential.

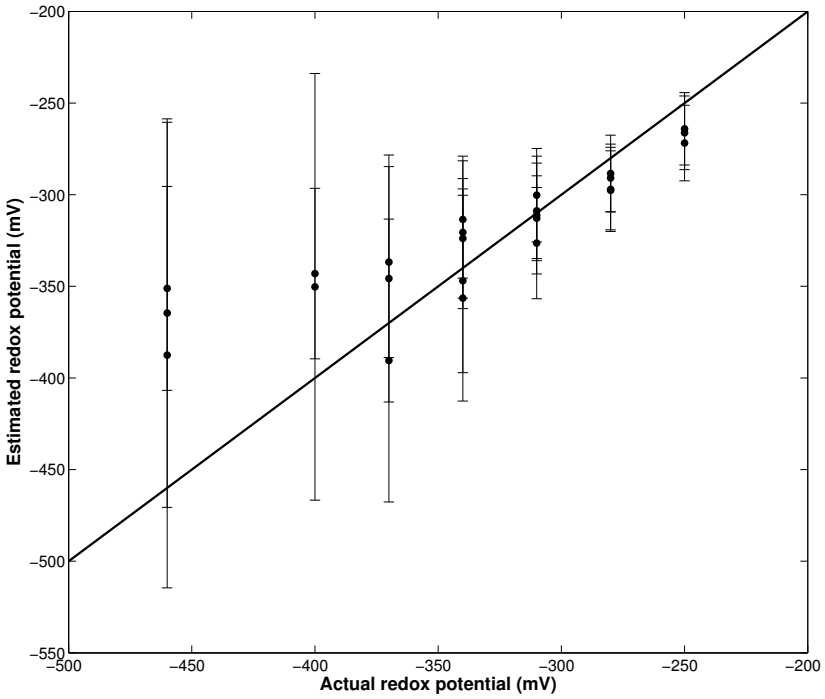

Figure 4.27: Comparison of the estimated redox potential with 95% confidence interval versus actual redox potential of the calibration spectra used in the calibration of NQ-NS (Renishaw system). The estimated redox potential is a weighted mean of the potentials estimated from both calibration curves. The thick line indicates where estimated = actual redox potential. The calibration spectra (n = 40) were either classified as having a potential <-400 mV, -400 to -250 mV or >-250 mV; only those classified as being in the range -400 to -250 mV are shown. Of these 40 spectra, two (5.0%) were incorrectly classified as having an estimated redox potential <-400 mV; one (2.5%) was incorrectly classified as having an estimated redox potential >-250 mV and three (7.5%) had a 95% confidence interval that did not include the actual redox potential.

The low accuracy is due to only one calibration dataset being available and which shows a fair amount of variability between spectra acquired at the same redox potential. Obtaining more data would improve the accuracy of the weighted mean, and also improve the error in the calibration curve. In addition, data were collected at equally spaced redox potentials; due to the sigmoid shape of the calibration curve, this could mean a further loss of accuracy in the region of -350 to -250 mV where the slope is steepest. Figure 4.27 shows that the 95% confidence intervals are greatest at more reducing potentials. This is due to the larger error in the height of the peak at 1640 cm^{-1} as it decreases with decreasing redox potential. This peak becomes a shoulder on the combined peaks at 1577 and 1602 cm^{-1}, resulting in increased error in the fit in this region at more reduced potentials. This error could be minimised by improving the SNR of the Renishaw system.

	Manual processing	Automated processing
Mean estimated redox potential (mV)	-257.4	-259.3
Standard deviation (mV)	3.0	2.8
Mean error (mV)		20.9

Table 4.11: Comparison of manual and automated processing methods in the estimation of redox potential from 10 consecutive spectra obtained from NQ-NS dried onto an imaging dish (Renishaw system). The manual processing method does not provide an error associated with estimated redox potential.

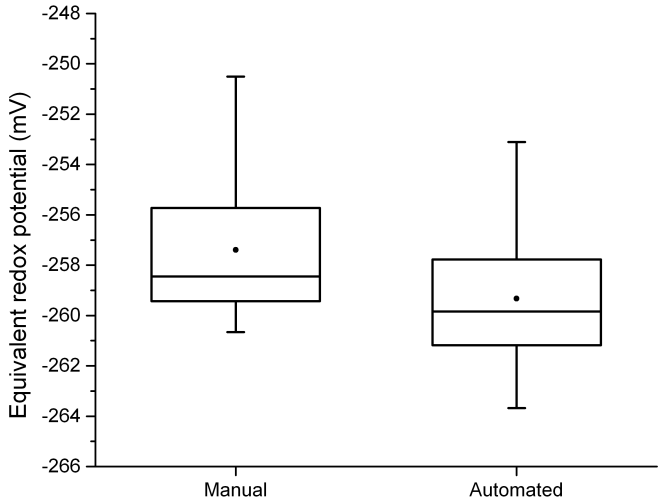

Figure 4.28: Boxplots showing the median, 1st and 3rd quarter percentiles, range and mean (filled circle) for the estimation of redox potential from 10 consecutive spectra obtained from NQ-NS dried onto an imaging dish, for both manual and automated processing methods (Renishaw system).

The algorithm was then compared to the manual processing method. Ten consecutive spectra were obtained from NQ-NS dried onto an imaging dish and processed by both methods. The manual process uses only the peak height ratio, whereas the automated process uses both the peak height and area ratios. A comparison of the two methods is given in Table 4.11 and Figure 4.28. Manual processing of the 10 spectra results in a mean redox potential of -257.4 mV with a standard deviation of 3.0 mV, whereas the automated processing results in a mean redox potential of -259.3 mV with a standard deviation of 2.8 mV. The manual process does not provide an error associated with the estimated redox potential, whereas the automated process results in an associated mean error of 20.9 mV.

The automated processing method was used to process intracellular spectra, the results of which form Chapter 5.

Calibration data was also supplied by Jing Jiang from the Ocean Optics fibre optic Raman system and consisted of $\geq$5 spectra per redox potential; a total of 56 spectra spanning -365 to -65 mV (vs. NHE). The data were processed in exactly the same way as for the Renishaw system data above. This dataset, however, showed both the 1577 and 1640 cm^{-1} peak centres varying with redox potential in addition to the peak height and area ratios. Therefore a combination of four parameters, instead of two, could be used to estimate redox potential. Figure 4.29 shows the calibration curves for these parameters and Table 4.12 provides acceptable ranges, determined as the values at -250 mV and -150 mV for the 1577 cm^{-1} peak centre and -350 mV and -150 mV for the other three parameters, as these are the regions where the curves change most rapidly.

When used to analyse the calibration data, the average standard deviation of the weighted mean was 10.1 mV. Once again, 95% confidence intervals were calculated for each of the calibration spectra that had an estimated redox potential in the range of -250 to -150 mV (for the 1577 cm^{-1} peak centre) or -350 to -150 mV (for the other parameters). Figure 4.30 shows estimated versus actual redox potential for those spectra for which confidence intervals were calculated. Overall, 89.3% (close to the

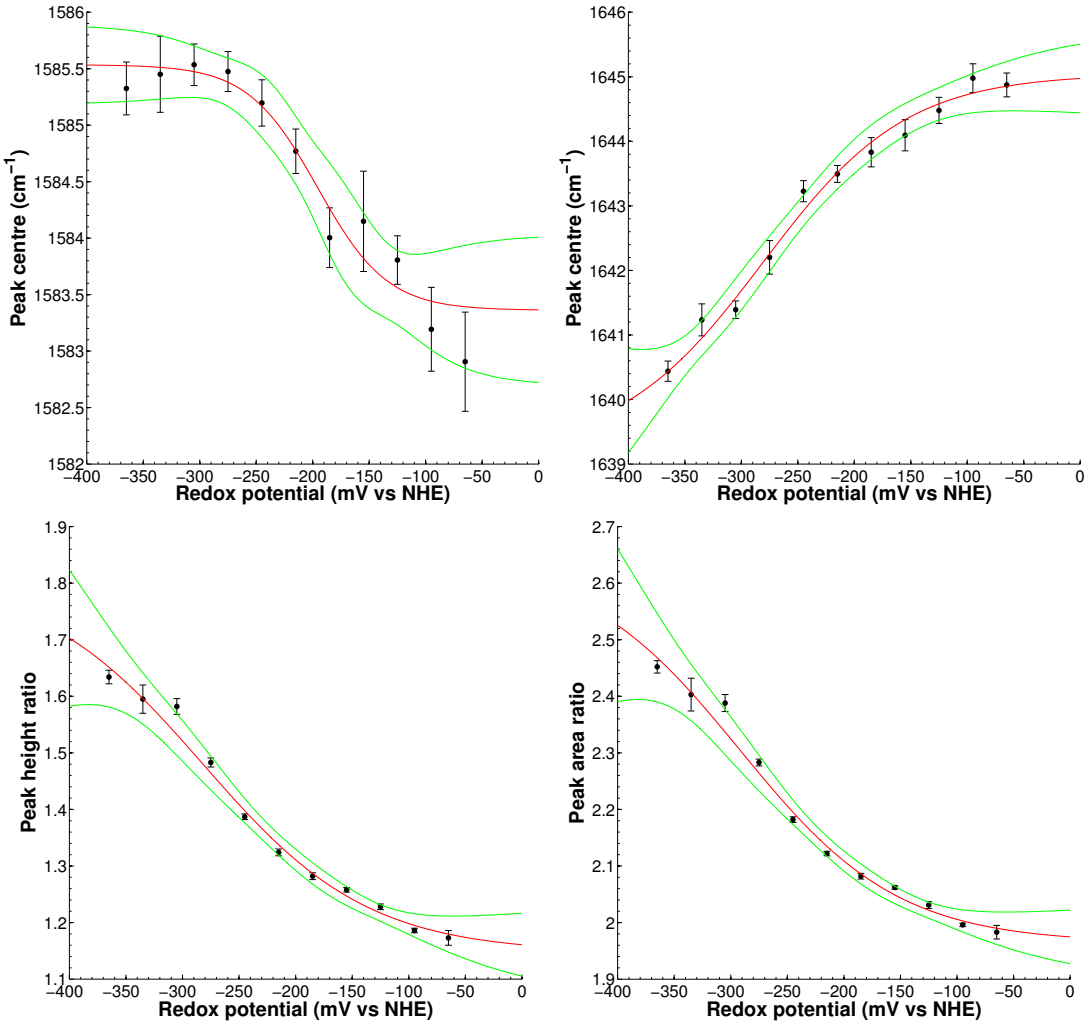

Figure 4.29: NQ-NS: variation of the 1577 cm^{-1} peak centre (top left), the 1645 cm^{-1} peak centre (top right), 1577/1645 cm^{-1} peak height (bottom left) and peak area (bottom right) ratios with redox potential (Ocean Optics system). A Boltzmann curve (red line) has been fitted to points which are the weighted means of $\geq$5 data points; error bars are the standard deviation of the weighted mean; green lines are the 95% non-simultaneous confidence bands.

Parameter	Lower value	Upper value
1577 cm^{-1} peak centre	1583.765	1585.215
1640 cm^{-1} peak centre	1640.676	1644.383
Peak height ratio	1.241	1.625
Peak area ratio	2.044	2.439

Table 4.12: Acceptable ranges for each parameter of NQ-NS, corresponding to the values of the Boltzmann fits at -250 and -150 mV for the 1577 cm^{-1} peak centre and -350 mV and -150 mV for the other parameters (Ocean Optics system). The estimated redox potential for each parameter is only calculated if the parameter is within the range given.

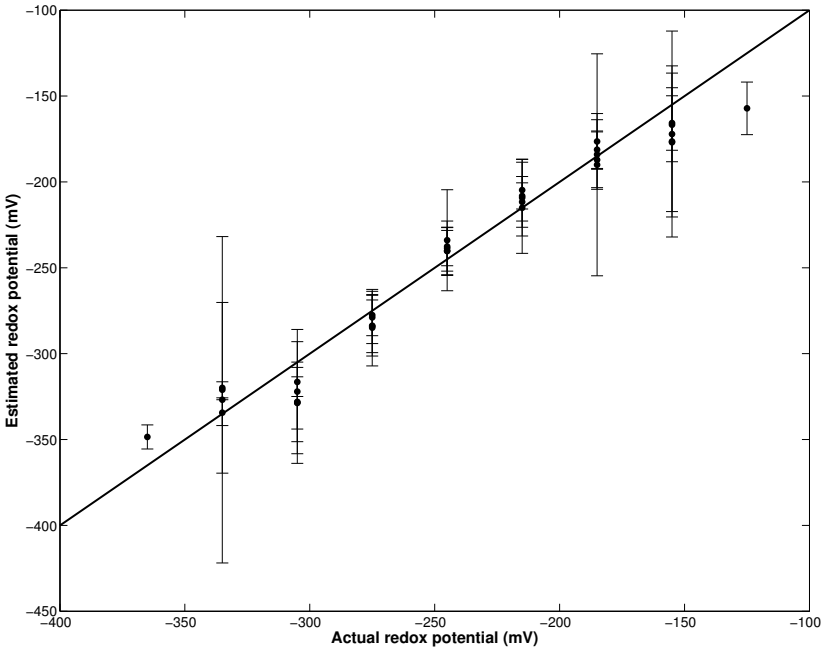

Figure 4.30: Comparison of the estimated redox potential with 95% confidence intervals versus actual redox potential of the calibration spectra used in the calibration of NQ-NS (Ocean Optics system). The estimated redox potential is a weighted mean of the potential estimated from each of the four calibration curves. The thick line indicates where estimated = actual redox potential. The calibration spectra (n = 56) were classified as having a potential <-350 mV, -350 to -150 mV or >-150 mV; only those classified as being in the range -350 to -150 mV are shown. Of these 56 spectra, one (1.8%) was incorrectly classified as having an estimated redox potential <-350 mV; none were incorrectly classified as having an estimated redox potential >-150 mV; and five (8.9%) had a 95% confidence interval that did not include the actual pH.

expected value of 95%) of the calibration spectra were correctly identified as belonging to one of the following categories:

- redox potential <-350 mV
- redox potential >-150 mV
- the error range associated with the estimated redox potential contained the actual redox potential.

Again, this low accuracy is due to only one calibration dataset being available; obtaining more data would improve the accuracy of the weighted mean and increase the accuracy towards 95%. Data were also collected at equally spaced redox potentials, so obtaining more data in the region of -350 to -150 mV, where the slope is steepest, should also improve the accuracy.

The standard deviation of the weighted mean is approximately half that of calibration data obtained on the Renishaw system, which could be due to using a combination of four parameters, instead of two, to estimate redox potential. It could also be due to reduced error in the peak centres, height and area ratios resulting from a higher SNR in the calibration data. Unfortunately, the data obtained on the two systems covered different redox potential ranges. From Figure 4.26, which shows the calibration curves of data obtained on the Renishaw system, it appears that the range could have been extended to more oxidising potentials. In contrast, from Figure 4.29, which shows the calibration curves of data obtained on the Ocean Optics system, it appears that the range could have been extended to slightly more reducing potentials. The difference in ranges covered explains why the 1577 cm^{-1} peak centre was found to be insensitive to redox potential in the data from the Renishaw system, but not in data from the Ocean Optics system: the sensitivity only becomes apparent at potentials >-250 mV, which is the limit of the data from the Renishaw system. It could also explain why the distribution of the 95% confidence intervals in the estimated versus actual redox potential graphs is different between the two systems. The intervals calculated from the Ocean Optics data are larger at both the reduced and oxidised ends of the range, whereas those from the Renishaw data are larger only at the reduced end of the range - we could expect larger intervals if the range was extended to more oxidised potentials to match the Ocean Optics data.

A comparison of the individual Boltzmann fit parameters and associated statistics for the peak height and area ratios is given in Table 4.13 for the calibration data obtained on both systems. As the range of redox potentials of the data obtained on the two systems is different, it is not surprising that the fit parameters differ. The midpoints calculated from the Ocean Optics data are close to the midpoint potential of -283 mV determined previously [163], whilst those calculated from the Renishaw system data are more reduced due to the calibration data not extending to potentials where the NQ molecule is fully oxidised. More datasets that cover the full potential range of NQ-NS would be needed in order to perform a reliable comparison on data from the two systems.

Parameter / statistic	Peak height ratio	Peak area ratio
Max. value	1.86 (± 0.04) 1.81 (± 0.16)	3.05 (± 0.04) 2.65 (± 0.18)
Min. value	1.29 (± 0.27) 1.15 (± 0.04)	2.33 (± 0.14) 1.96 (± 0.03)
Range	0.57 0.66	0.72 0.69
Midpoint (mV)	-289.05 (± 37.44) -282.02 (± 32.75)	-301.95 (± 15.54) -291.72 (± 35.01)
Value at midpoint	1.54 1.48	2.69 2.31
Slope	-38.54 (± 21.25) -73.20 (± 22.80)	-37.27 (± 11.34) -70.01 (± 20.28)
Adjusted R^2	0.93 0.98	0.98 0.98

Table 4.13: Comparison of Boltzmann fit parameters and statistics from the calibration curves for NQ-NS generated from data obtained from the Renishaw system (top rows) and Ocean Optics system (bottom rows).

4.3.3 AQ - redox potential sensor

Calibration data for the AQ-NS nanosensor (Figure 4.31) were supplied by Jing Jiang and consisted of 3 independent datasets, each having $\geq$5 spectra per redox potential obtained using the Renishaw system, making a total of 182 spectra. Figure 4.32 shows how peaks in the spectrum change with redox potential: the peak at ~1600 cm^{-1} is due to amide stretching with symmetric ring breathing and is the most intense peak in the region 1300-1800 cm^{-1}, making it a good candidate for a reference peak. Density functional theory data shows this peak at 1595 cm^{-1} in the fully reduced state and at 1606 cm^{-1} in the fully oxidised state [122], so it may be possible to use the peak centre as an additional parameter to estimate redox potential. The peak at 1668 cm^{-1} is due to C=O stretching and its intensity increases with oxidation, indicating the possibility of using peak height and area ratios to estimate redox potential. Density functional theory also indicates a third peak at ~1640 cm^{-1} due to aromatic C-C stretching, which although neither redox-dependent nor intense enough to be used

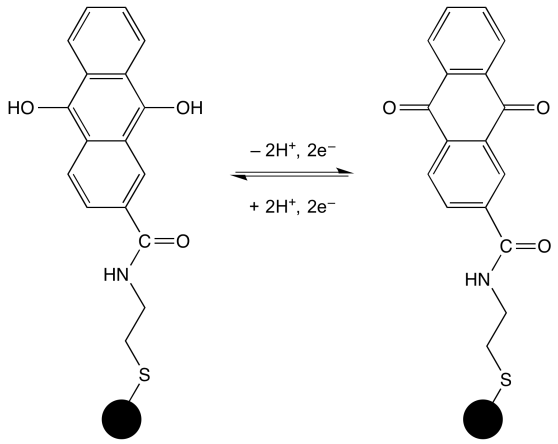

Figure 4.31: Reduced (left) and oxidised (right) structures of the AQ reporter molecule conjugated to a gold nanoshell (black circle) via a gold-thiol bond.

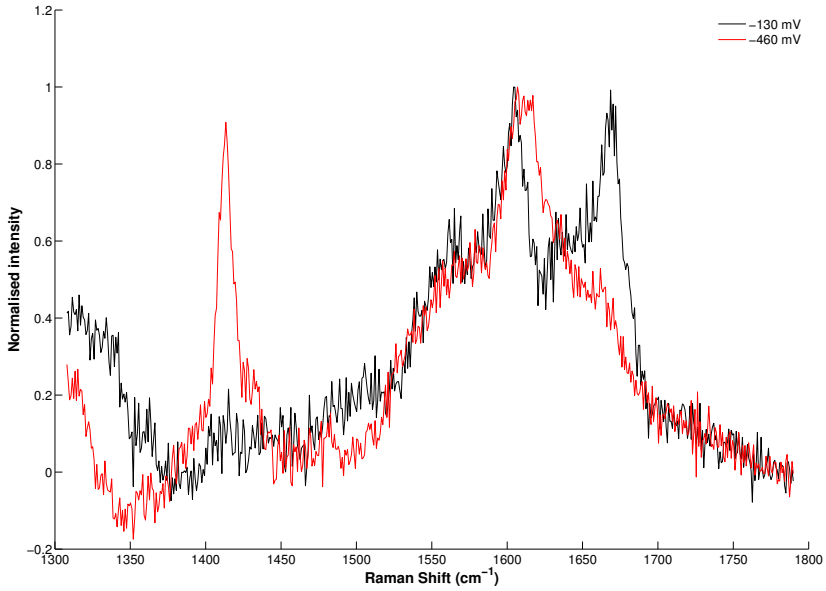

Figure 4.32: Redox-dependent change in the intensity of the peak at 1668 cm^{-1} in the AQ-NS Raman spectrum. Spectra have been background subtracted and normalised to the intensity of the peak at ~1600 cm^{-1}. The height of the peak at ~1415 cm^{-1} in the reduced AQ spectrum, was not redox-dependent.

Fit type	Average sum of squared residuals	Average residual variance	F-statistic†
Lorentzian	419,267	3,301	
Lorentzian + slope	256,683	2,021	37.054 ($p < 0.001$) vs. Lorentzian 28.106 ($p < 0.001$) vs. Gaussian
Gaussian	380,007	2,992	0.906 ($p = 0.40$) vs. Lorentzian
Gaussian + slope	396,483	3,117	3.362 ($p = 0.036$) vs. Lorentzian NA vs. Gaussian* 1.545 ($p = 0.21$) vs. Lorentzian + slope

Table 4.14: Comparison of average sum of squared residuals and average residual variance for various fit types for the three overlapping peaks in the AQ-NS Raman spectrum. †A small p value (<0.05) indicates that the slope model is statistically more accurate than the non-slope model, taking into account the expected improvement in the sum of squared residuals due to the extra two parameters. *The F-statistic cannot be calculated where the model with more parameters has a larger average sum of squared residuals than the model with fewer parameters, therefore the model with fewer parameters is the better model. The Lorentzian + slope model is better overall as it has a smaller average sum of squared residuals and residual variance than the Gaussian + slope model.

as a reference peak, still needs to be included in the model. Finally, the height of the peak at ~1415 cm^{-1} in the reduced AQ spectrum was not redox-dependent.

As with the NQ-NS nanosensor, the peak profiles were established and the same profile was used for all three peaks. Table 4.14 shows that the Lorentzian peaks + slope model was the statistically more accurate model of the four compared. Therefore the data were modelled by the sum of three Lorentzian peaks and a slope term (Equation 4.6):

$$y = \frac{a1}{1 + (\frac{x_c - b1}{c1})^2} + \frac{a2}{1 + (\frac{x_c - b2}{c2})^2} + \frac{a3}{1 + (\frac{x_c - b3}{c3})^2} + mx + d \tag{4.6}$$

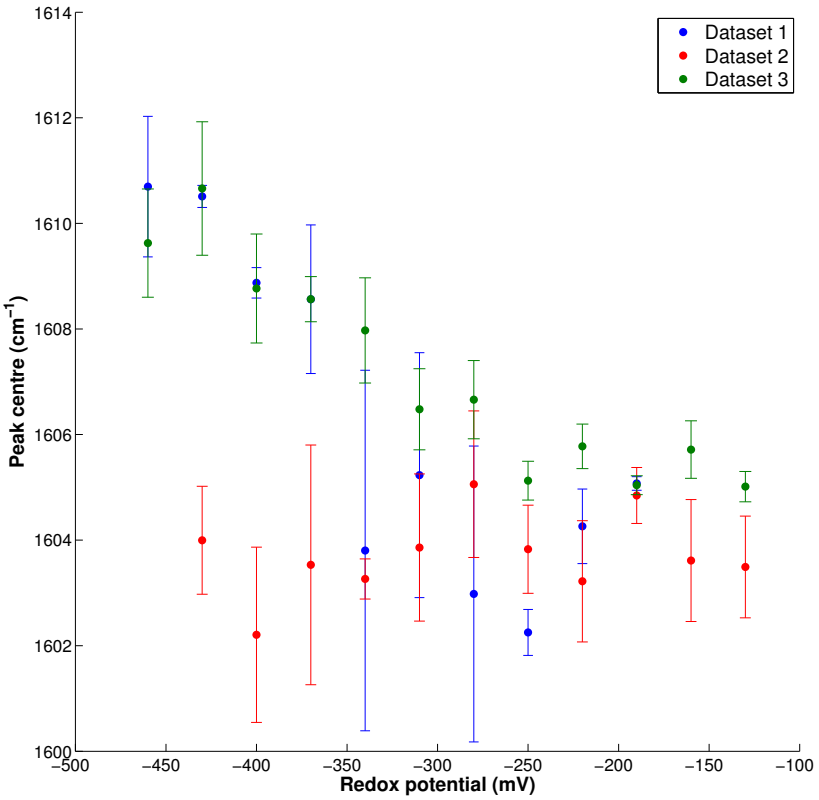

Figure 4.33: AQ-NS: variation of the centre of the peak at ~1600 cm^{-1} with redox potential (Renishaw system). Points are the weighted means of three independent datasets; error bars are the standard deviation of the weighted mean.

where $a1$, $a2$ and $a3$ are the peak amplitudes; $b1$, $b2$ and $b3$ are the peak centres; $c1$, $c2$ and $c3$ are the peak widths of the peaks at ~1600, 1640 and 1668 cm^{-1}; m is the slope gradient and d the slope intercept.

After fitting, the calibration data were grouped by redox potential in order to investigate relationships between various fit parameters and redox potential. Weighted means and standard deviations of the various parameters at each redox potential were calculated using the same inverse weighting method as for the MBA-NS nanosensor (Equations 4.2 and 4.4). Contrary to expectation from the DFT data, it was found that the ~1600 cm^{-1} peak centre did not vary with redox potential consistently in all three datasets (Figure 4.33). None of the peak widths changed with redox potential, but it was found that the ratio of the both the heights and areas of the peaks at ~1600 and 1668 cm^{-1} did vary with redox potential. Therefore calibration curves were only constructed for the peak height and area ratios of these peaks.

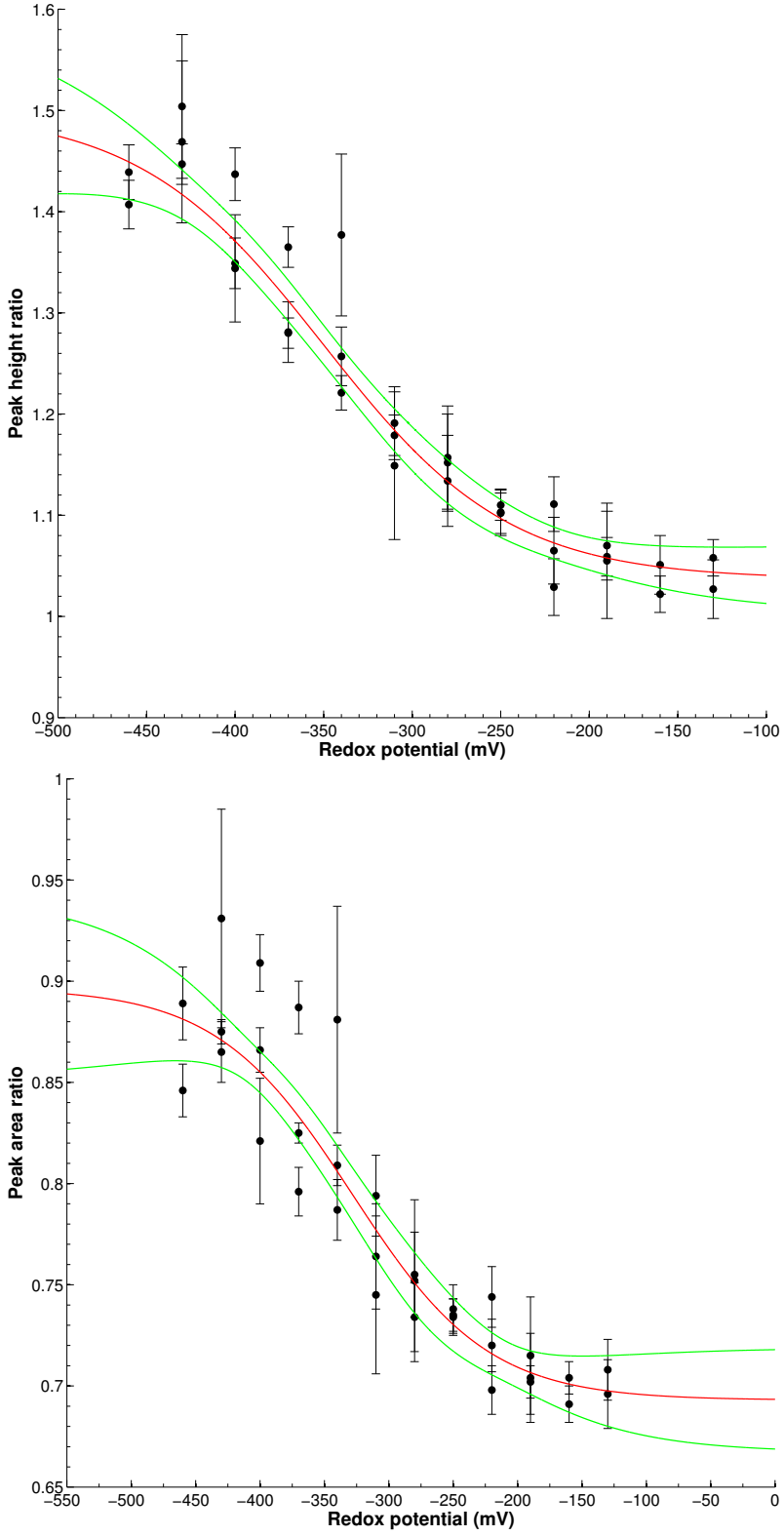

Figure 4.34: AQ-NS: variation of 1600/1668 cm^{-1} peak height (top) and peak area (bottom) ratios with redox potential (Renishaw system). A Boltzmann curve (red line) has been fitted to points which are the weighted means of three independent datasets; error bars are the standard deviation of the weighted mean; green lines are the 95% non-simultaneous confidence bands.

Parameter	Lower value	Upper value
Peak height ratio	1.097	1.371
Peak area ratio	0.730	0.855

Table 4.15: Acceptable ranges for each parameter of AQ-NS, corresponding to the values of the Boltzmann fits at -400 and -250 mV (Renishaw system). The estimated redox potential for each parameter is only calculated if the parameter is within the range given.

A Boltzmann curve was fitted and 95% confidence bands were calculated for both of these parameters (Figure 4.34). Acceptable ranges for the ratios were determined as the values at -400 and -250 mV (Table 4.15), as this is the region where the curves change most rapidly. The redox potential was then estimated from both calibration graphs, with the error determined from the error in the peak height or area ratio. The estimated redox potential from each parameter was combined into a weighted mean (Equation 4.2) to reduce the effect of one parameter having a significantly different estimated redox potential to that of the other parameter if it has a large error. The standard deviation of the weighted mean was calculated using Equation 4.4. Spectra were marked as 'reduced' or 'oxidised' if either or both ratios were outside the ranges given in Table 4.15.

When used to analyse the calibration data, this method resulted in an average standard deviation of 10.5 mV. Individual 95% confidence intervals were calculated from the individual standard deviations of each spectrum, where the estimated redox potential was in the range -400 to -250 mV; Figure 4.35 shows estimated versus actual redox potential for those spectra for which confidence intervals were calculated. Overall, 88.5% of the calibration spectra were correctly identified as belonging to one of the following categories:

- redox potential <-400 mV
- redox potential >-250 mV
- the error range associated with the estimated redox potential contained the actual redox potential.

The low accuracy is most likely due to the variability between the datasets

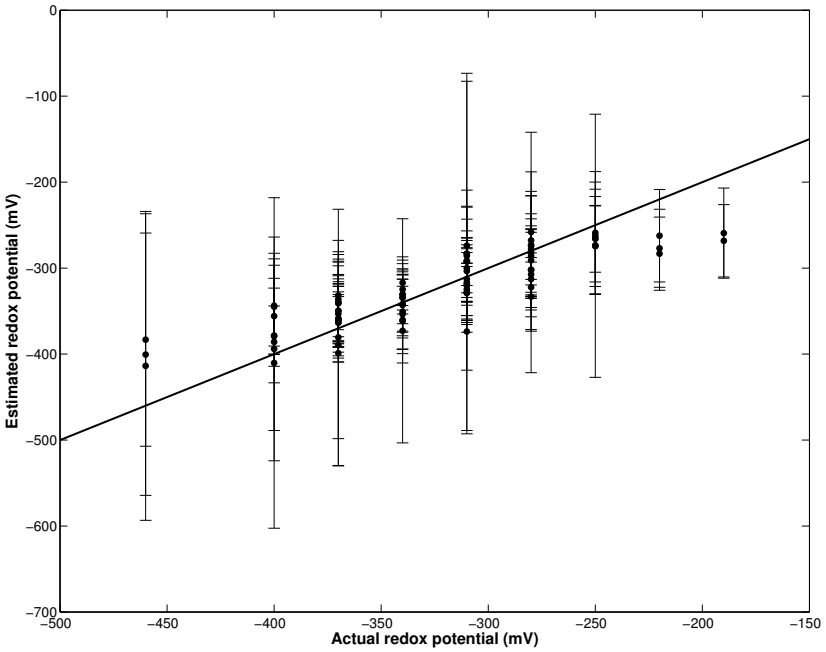

Figure 4.35: Comparison of the estimated redox potential with 95% confidence interval versus actual redox potential of the calibration spectra used in the calibration of AQ-NS (Renishaw system). The estimated redox potential is a weighted mean of the potentials estimated from both calibration curves. The thick line indicates where estimated = actual redox potential. The calibration spectra (n = 182) were classified as having a potential <-400 mV, -400 to -250 mV or >-250 mV; only those classified as being in the range -400 to -250 mV are shown. Of these 182 spectra, five (2.7%) were incorrectly classified as having an estimated redox potential <-400 mV; four (2.2%) were incorrectly classified as having an estimated redox potential >-250 mV and 12 (6.6%) had a 95% confidence interval that did not include the actual redox potential.

(Figure 4.36), especially for the peak area ratio. Obtaining more datasets would confirm whether this variability is inherent or if Dataset 1 is anomalous. Data were also collected at equally spaced redox potentials; due to the sigmoid shape of the calibration curve, this could mean a further loss of accuracy in the region of -400 to -250 mV where the slope is steepest.

Figure 4.35 shows that some of the 95% confidence intervals for estimated redox potential are >100 mV. This is due to a low SNR in the corresponding spectra, leading to a large error in the fit, and consequently the peak heights and areas.

The algorithm was then compared to the manual processing method. Ten consecutive spectra were obtained from AQ-NS dried onto an imaging dish and processed by both methods. The manual process uses only the peak height ratio, whereas the automated process uses both the peak height and area ratios. As AQ-NS

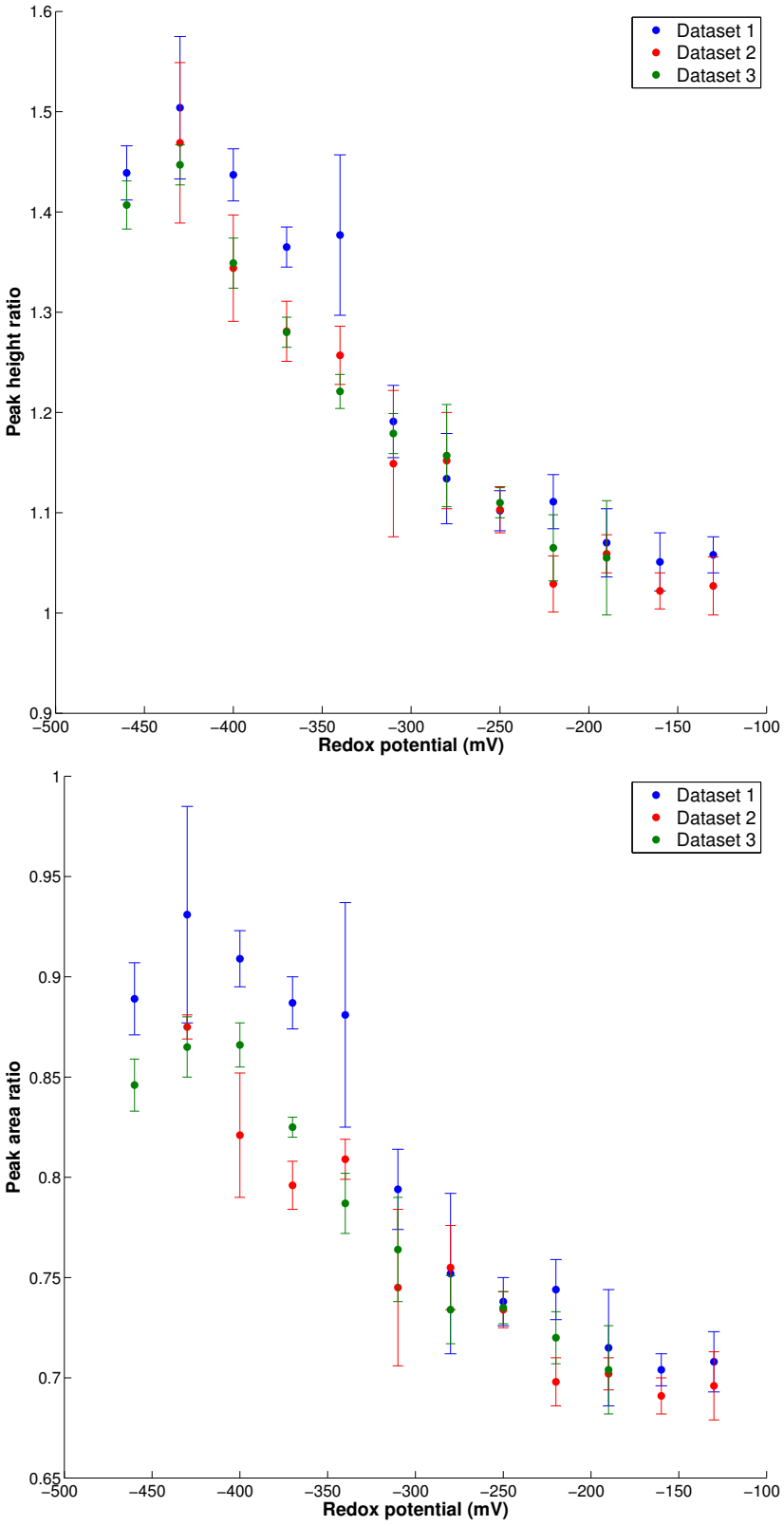

Figure 4.36: Peak height (top) and area (bottom) ratios of AQ-NS by dataset (Renishaw system). Dataset 1 is markedly different to Datasets 2 and 3 at more reducing potentials.

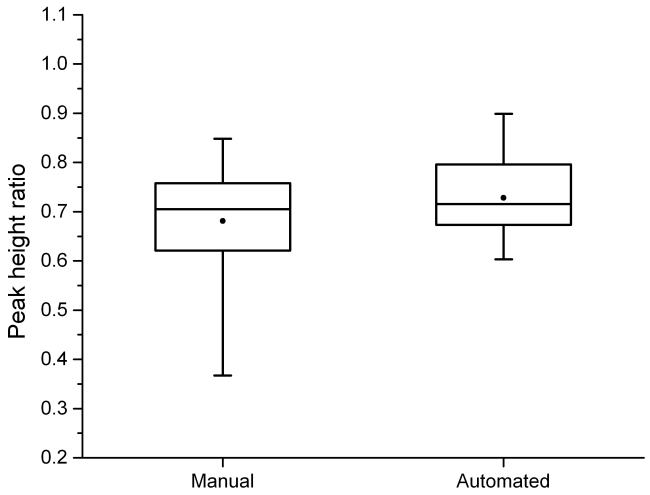

Figure 4.37: Boxplots showing the median, 1st and 3rd quarter percentiles, range and mean (filled circle) for peak height ratios from 10 consecutive spectra obtained from AQ-NS dried onto an imaging dish, for both manual and automated processing methods (Renishaw system).

	Manual processing	**Automated processing**
Mean peak height ratio	0.68	0.73
Standard deviation	0.12	0.08

Table 4.16: Comparison of manual and automated processing methods in the determination of peak height ratio from 10 consecutive spectra obtained from AQ-NS dried onto an imaging dish (Renishaw system).

is fully oxidised at atmospheric oxygen levels, only the peak height ratios could be compared (Figure 4.37 and Table 4.16). Manual processing of the 10 spectra resulted in a mean peak height ratio of 0.68 with a standard deviation of 0.12, whereas automated processing results in a mean peak height ratio of 0.73 with a standard deviation of 0.08.

Calibration data were also supplied by Jing Jiang from the Ocean Optics fibre optic Raman system and consisted of two independent datasets, each having $\geq$5 spectra per redox potential; a total of 216 spectra spanning -490 to -40 mV (vs. NHE). The data were processed in exactly the same way as for the Renishaw system data above, and the calibration curves and acceptable ranges for each parameter are shown in

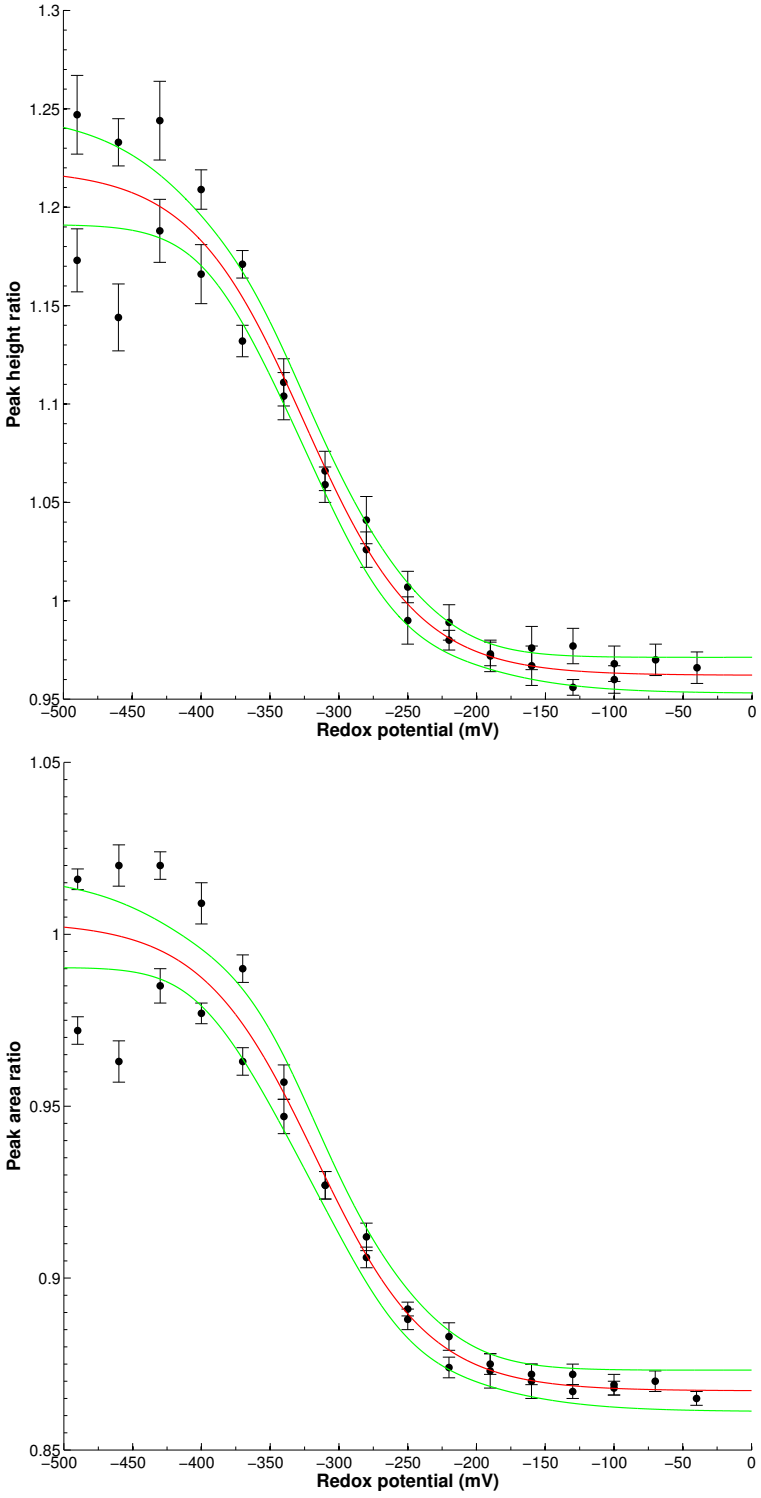

Figure 4.38: AQ-NS: variation of 1600/1668 cm^{-1} peak height (top) and peak area (bottom) ratios with redox potential (Ocean Optics system). A Boltzmann curve (red line) has been fitted to points which are the weighted means of three independent datasets; error bars are the standard deviation of the weighted mean; green lines are the 95% non-simultaneous confidence bands.

Parameter	Lower value	Upper value
Peak height ratio	0.998	1.183
Peak area ratio	0.890	0.987

Table 4.17: Acceptable ranges for each parameter of AQ-NS, corresponding to the values of the Boltzmann fits at -400 and -250 mV (Ocean Optics system). The estimated redox potential for each parameter is only calculated if the parameter is within the range given.

Figure 4.38 and Table 4.17, respectively. Once again, the acceptable ranges were determined as the values at -400 mV and -250 mV, as these are the regions where the curves change most rapidly.

When used to analyse the calibration data, this method resulted in an average standard deviation of 5.4 mV. Individual 95% confidence intervals were calculated from the individual standard deviations of each spectrum, where the estimated redox potential was in the range -400 to -250 mV; Figure 4.39 shows estimated versus actual redox potential for those spectra for which confidence intervals were calculated. Overall, 97% of the calibration spectra were correctly identified as belonging to one of the following categories:

- redox potential <-400 mV
- redox potential >-250 mV
- the error range associated with the estimated redox potential contained the actual redox potential.

This high accuracy is mainly due to the extremely large confidence intervals at more reducing potentials. This results from the variability between the two datasets at the more reducing potentials, as seen in Figure 4.38. Obtaining more datasets would confirm whether this variability is inherent or if one of the datasets is anomalous at these potentials. Data were also collected at equally spaced redox potentials; due to the sigmoid shape of the calibration curve, this could mean a further loss of accuracy in the region of -400 to -250 mV where the slope is steepest.

A comparison of the individual Boltzmann fit parameters and associated statistics for the peak height and area ratios is given in Table 4.18 for the calibration data obtained

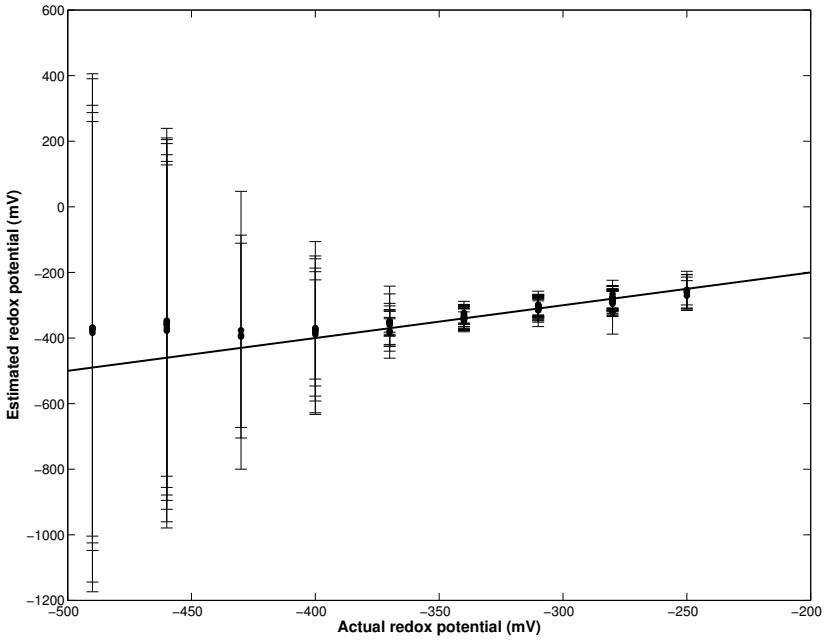

Figure 4.39: Comparison of the estimated redox potential with 95% confidence interval versus actual redox potential of the calibration spectra used in the calibration of AQ-NS (Ocean Optics system). The estimated redox potential is a weighted mean of the potentials estimated from both calibration curves. The thick line indicates where estimated = actual redox potential. The calibration spectra (n = 216) were classified as having a potential <-400 mV, -400 to -250 mV or >-250 mV; only those classified as being in the range -400 to -250 mV are shown. Of these 216 spectra, six (2.8%) were incorrectly classified as having an estimated redox potential <-400 mV; none were incorrectly classified as having an estimated redox potential >-250 mV and none had a 95% confidence interval that did not include the actual redox potential.

on both systems. The midpoints calculated from the Ocean Optics data are close to the half-wave potential of -311 mV determined previously [122], whilst those calculated from the Renishaw data are more reduced but with a larger error. Only two datasets were available from the Ocean Optics system compared to the three available from the Renishaw system, and the data from both systems showed variability at more reduced potentials. This variability could account for the difference in maximum values. Collecting more datasets would hopefully reduce this variability. Data on both systems were collected every 30 mV, so collecting data at smaller intervals over the range -400 to -250 mV, where the slope is steepest, could reduce the errors in the midpoint potentials and slopes. The variability of the data from the Ocean Optics system is smaller at more oxidised potentials than in data from the Renishaw system (compare Figures 4.34 and 4.38), and this leads to a larger adjusted R^2 value.

Parameter / statistic	Peak height ratio	Peak area ratio
Max. value	1.50 (± 0.05) 1.22 (± 0.01)	0.90 (± 0.02) 1.00 (± 0.01)
Min. value	1.04 (± 0.02) 0.96 (± 0.00)	0.69 (± 0.01) 0.87 (± 0.00)
Range	0.46 0.26	0.20 0.14
Midpoint (mV)	-349.98 (± 11.56) -325.16 (± 7.14)	-328.43 (± 14.08) -317.29 (± 8.21)
Value at midpoint	1.27 1.09	0.79 0.94
Slope	52.48 (± 10.26) 41.54 (± 5.32)	52.56 (± 13.68) 41.36 (± 6.29)
Adjusted R^2	0.95 0.97	0.93 0.96

Table 4.18: Comparison of Boltzmann fit parameters and statistics from the calibration curves for AQ-NS generated from data obtained from the Renishaw system (top rows) and Ocean Optics system (bottom rows).

4.4 Discussion

In this chapter an automated method of processing SERS spectra was developed, comprising background subtraction followed by peak fitting to obtain various fit parameters that were used to estimate pH or redox potential. The background subtraction algorithm was successful in reducing the variability of the background intensity in spectra obtained on different substrates (gold and glass-bottomed imaging dishes), independently of whether signals were present from any of the three nanosensors used.

For all three nanosensors it was found that Lorentzian peak profiles were statistically more accurate than Gaussian profiles (Tables 4.2, 4.3, 4.4, 4.9 and 4.14). For the MBA nanosensor the three peaks used did not overlap with any other peaks and so each was fitted separately, whereas for both the NQ and AQ nanosensors the peaks used overlapped and so a single three peak fit was applied.

	System	MBA-NS	NQ-NS	AQ-NS
Average standard deviation of estimated pH or redox potential	Ren	0.16 pH units (2.3%)	23.3 mV (7.2%)	12.9 mV (4.0%)
	OO	0.19 pH units (2.7%)	10.1 mV (4.1%)	18.2 mV (5.5%)
Overall accuracy	Ren	92%	85%	89%
	OO	90%	89%	97%
No. of datasets	Ren	3	1	3
	OO	3	1	2
Total no. of spectra	Ren	303	40	182
	OO	203	56	216

Table 4.19: Comparison of the overall accuracy between the different nanosensors and Raman spectrometers. The average standard deviation is given both as the actual value and as the percentage of the average estimated pH or redox potential. Ren = Renishaw system; OO = Ocean Optics system.

Fit parameters for each peak (centre, width, height and area) were then compared for each nanosensor. The MBA nanosensor had two pH-sensitive peaks, therefore three peak height ratios and three peak area ratios could be used to estimate pH, along with the peak centre of the reference peak. The NQ and AQ nanosensors each had only one peak that varied with redox potential and so these nanosensors had fewer parameters that could be used to estimate redox potential. Table 4.19 summarises the characteristics of all three nanosensors. The combination of seven parameters for the MBA nanosensor led to a small standard deviation and an overall accuracy close to the expected 95%. Only two parameters could be used for the NQ nanosensor on the Renishaw system, and only one dataset was collected which did not appear to cover the fully oxidised end of the range, resulting in a lower overall accuracy and a larger standard deviation. Four parameters were used for the NQ nanosensor on the Ocean Optics system and the potential range of the single dataset included the fully oxidised end. This increase in parameters is reflected in an improved accuracy and standard deviation. Only two parameters could be used for the AQ nanosensor on both systems, however more calibration spectra were available. The standard

deviation is affected by the larger standard deviation at more reduced potentials.

Colourmaps showing the spatial variation of pH were constructed from SERS maps. The flowchart in Figure 4.40 details the steps involved in producing colourmaps from SERS map data.

The automated method was significantly faster than the manual method: nearly 200 times faster in processing a single spectrum, and 50-120 times faster in producing a colourmap of 147 spectra. The automated method was also more precise than the manual method for the MBA and AQ nanosensors and due to the lack of calibration spectra was no worse for the NQ nanosensor. However for the NQ nanosensor it was shown that the estimated values from the automated method were more evenly distributed about the mean than for the manual method, indicating that the automated method was less biased. All spectra are subject to the same criteria and intra- and inter-individual bias and variance are not present in the automated method.

Overall, the automated processing method is much quicker and results in a less variable estimation of pH or redox potential than the manual processing method. Futher improvements can be made by obtaining more data for the NQ and AQ nanosensors on both spectrometers.

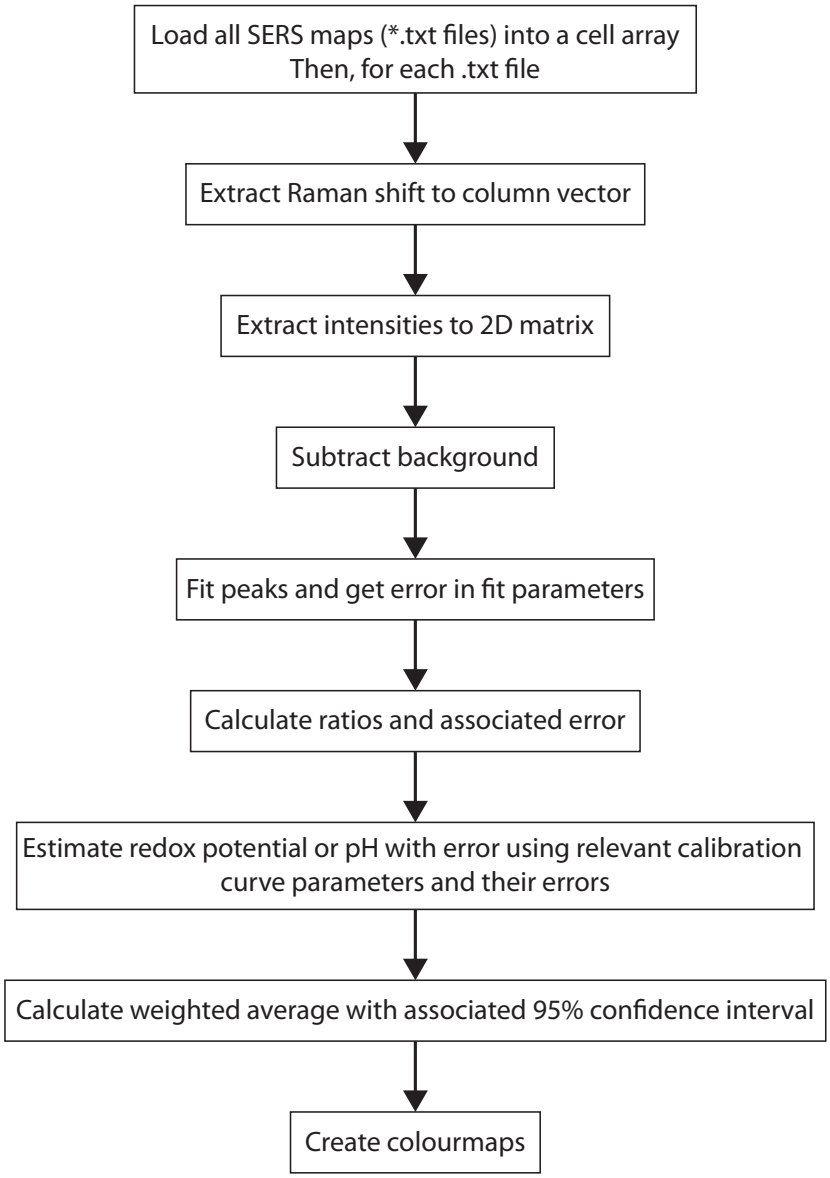

Figure 4.40: Flowchart detailing the steps taken in processing SERS map data to produce colourmaps of pH or redox potential.

Chapter 5: Metal nanoparticle toxicity

5.1 Introduction

The toxicological effects of inhaled particulate matter have been extensively investigated. Inhalation of ultrafine particles, such as in diesel exhaust, has been shown to cause inflammation in several cell types [206]. The toxicity of these species is thought to be related to their large surface area to volume ratio, and/or their ability to act as a carrier of transition metals into the lungs [179]. Nanoparticles have a smaller diameter and greater surface area to volume ratio compared to larger particles and are now manufactured in large quantities for industrial use (for example, in the manufacture of cosmetics, electronics, and paint [207]); therefore it is important to investigate the effects of nanoparticle inhalation during the manufacturing process. Engineered nanoparticles have been shown to have greater toxic effects than ultrafine particles (which are nanoscale ambient, as opposed to engineered, particles; for example air pollution particles) [206], although the effects are strongly dependent on cell type.

As well as being used as a model of lung cancer [176, 177], A549 cells are used in studies of inflammation [178] and nanoparticle toxicity [179, 180]. Both ultrafine particles and metal nanoparticles cause production of ROS in A549 cells [208]. Elevated ROS levels cause upregulated expression of anti-oxidant genes through the Nrf2-KEAP pathway [209] (Section 1.3). At low particle concentrations this upregulation is enough to degrade ROS, however, at higher concentrations, the antioxidant response is insufficient for the levels of ROS produced, and the resulting oxidative stress triggers apoptosis [210].

This well-characterised response of A549 cells to nanoparticles makes them an ideal system in which to compare our measurements of intracellular redox potential with the traditional assays for oxidative stress. This work was carried out in collaboration with Jen McLeish of Ken Donaldson's group at MRC Centre for Inflammation

Research, University of Edinburgh, who prepared the metal nanoparticle solutions, and performed and interpreted the traditional assays for oxidative stress.

5.2 Results

A549 cells were incubated with NQ-NS overnight before sub-lethal treatment with one of 0.5 mg/ml silver nanoparticles (AgNP), 0.5 mg/ml zinc oxide nanoparticles (ZnONP) or 30 mM 2,2'-azobis(2-amidinopropane) dihydrochloride (AAPH; positive control) or were left untreated (see Section 2.2 for full methods). SERS maps were acquired from untreated, Ag-treated and ZnO-treated cells over the following time periods after treatment: 0-1 hours; 1-2 hours; 2-3 hours; 3-4 hours and 4-5 hours. SERS spectra were acquired from AAPH-treated cells during the first hour after treatment only as there was extensive cell death after this period. Cells were kept at 37 ºC and 5% CO_2 until the relevant timepoint.

The protocol used for acquiring SERS map data is described fully in Section 2.5. Briefly, a cell or cells were rapidly scanned to locate any NQ-NS and then detailed scans covering an area of 6 x 25 μm were performed, centred on the location of each NQ-NS signal from the rapid scan.

The automated processing algorithm described in Chapter 4 was used to process all SERS map spectra. After background subtraction, spectra were selected for further processing based on the following criteria:

- R^2 value ≥ 0.6
- height of the peak at 1577 cm^{-1} ≥ 100 counts

No spectra showed complete oxidation of NQ-NS. The automated processing method returned a redox potential with an associated error for each spectrum as described in Chapter 4. A weighted average and standard deviation was then calculated for each time period and each treatment, using the inverse weighting method (Equations 4.2 and 4.4). Figure 5.1 shows the change in redox potential for each time period for all treatments. In the 0-1 hour time period only AAPH-treated cells showed a significant

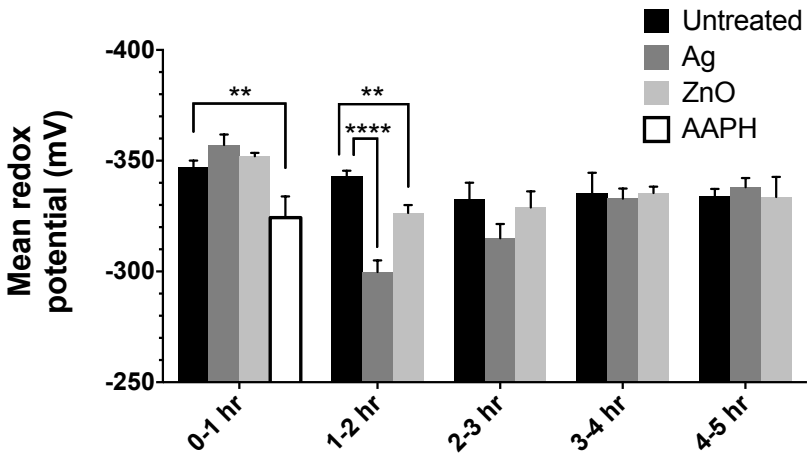

Figure 5.1: Metal nanoparticles increase intracellular redox potential in A549 cells 1-2 hours after treatment. Cells containing NQ-NS were treated with one of 0.5 mg/ml AgNP, 0.5 mg/ml ZnONP or 30 mM AAPH (positive control), or were left untreated. Bars show the weighted mean of redox potentials within each time period and treatment; error bars represent the standard error of the weighted mean; ** p <0.01; **** p <0.0001.

increase in redox potential compared to untreated cells (p = 0.0014). In the 1-2 hour time period, both AgNP- and ZnONP-treated cells showed a significantly increased redox potential compared to untreated cells (p <0.0001 and p = 0.0015, respectively). For the other time periods there was no significant difference in redox potential between untreated cells and metal nanoparticle-treated cells.

Figure 5.2 shows the change in intracellular redox potential over time for each treatment individually. Both metal nanoparticle treatments showed the most oxidised redox potential during the 1-2 hour time period, with AgNP treatment resulting in a more oxidised potential than ZnONP treatment. All time periods showed significantly increased redox potentials with respect to the potential measured during the 0-1 hour time period. In AgNP-treated cells, the redox potential during the 4-5 hour time period was significantly more reduced than the potential during the 1-2 hour or 2-3 hour time periods (p = 0.0008 and p = 0.0208, respectively), but it was still significantly more oxidised at this timepoint than during the 0-1 hour time period. ZnONP treatment showed a similar trend but without reaching significance. The intracellular redox potential in untreated cells did not change significantly over the 5 hours.

Colourmaps of the intracellular data were produced by plotting the estimated redox

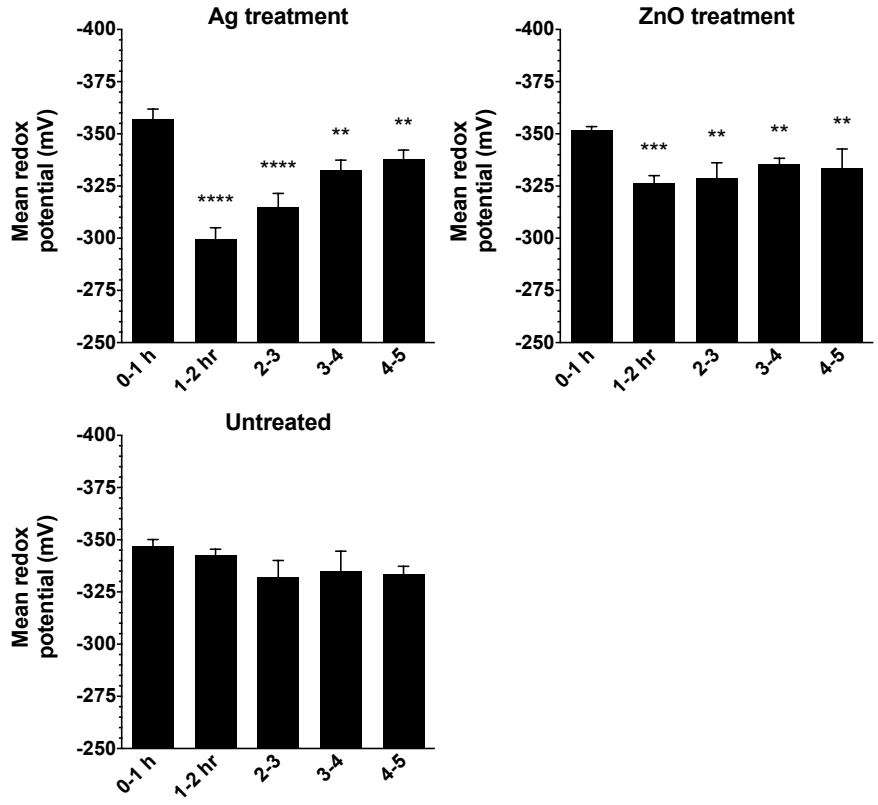

Figure 5.2: Top: Metal nanoparticles cause an increase in intracellular redox potential in A549 cells. Bottom: Untreated cells do not show a change in redox potential over time. Cells containing NQ-NS were treated with one of 0.5 mg/ml AgNP, 0.5 mg/ml ZnONP or 30 mM AAPH (positive control), or were left untreated. Bars show the weighted mean of redox potentials within each time period and treatment; error bars represent the standard error of the weighted mean; ** p <0.01; *** p <0.001; **** p <0.0001.

potential in the location given by its spectrum number (Figure 5.3 shows an example from a ZnO-treated cell). These allow the spatial distribution of redox potentials to be visualised, both by colour and by value. The colourmap shows three separate areas where signals from NQ-NS were detected, with each pixel representing an area of 1 x 1.19 μm. Each NQ-NS has a diameter of 150 nm, so it is probable that there are several NQ-NS in each area, either separate or in aggregates. The individual redox potentials within each area are similar to each other within the error shown, suggesting that the nanosensor(s) are measuring the local redox potential. Figure 5.4 shows the same colourmap super-imposed on a white light brightfield image of the cell the spectra were acquired from, and shows the intracellular location of the NQ-NS.

These results were then compared to traditional assays of oxidative stress performed

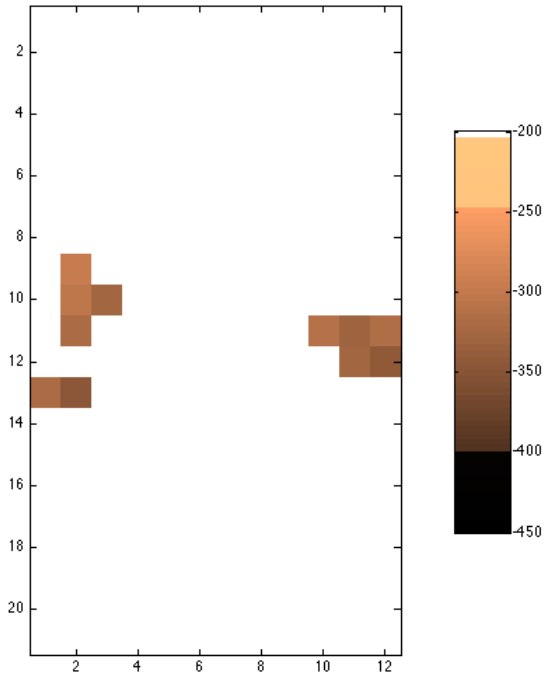

ZnO 1-2 hr-2

	-297 (5)										
	-305 (28)	-326 (3)									
	-319 (28)								-311 (33)	-329 (7)	-316 (1)
										-327 (17)	-343 (35)
-320 (22)	-345 (24)										

Figure 5.3: Spatial distribution of estimated redox potentials from a map acquisition of a ZnO-treated cell containing NQ-NS: (left) colourmap of estimated redox potentials; (right) gridmap showing the estimated redox potentials with standard deviation in brackets. Each pixel of the colourmap represents an area of 1 x 1.19 μm.

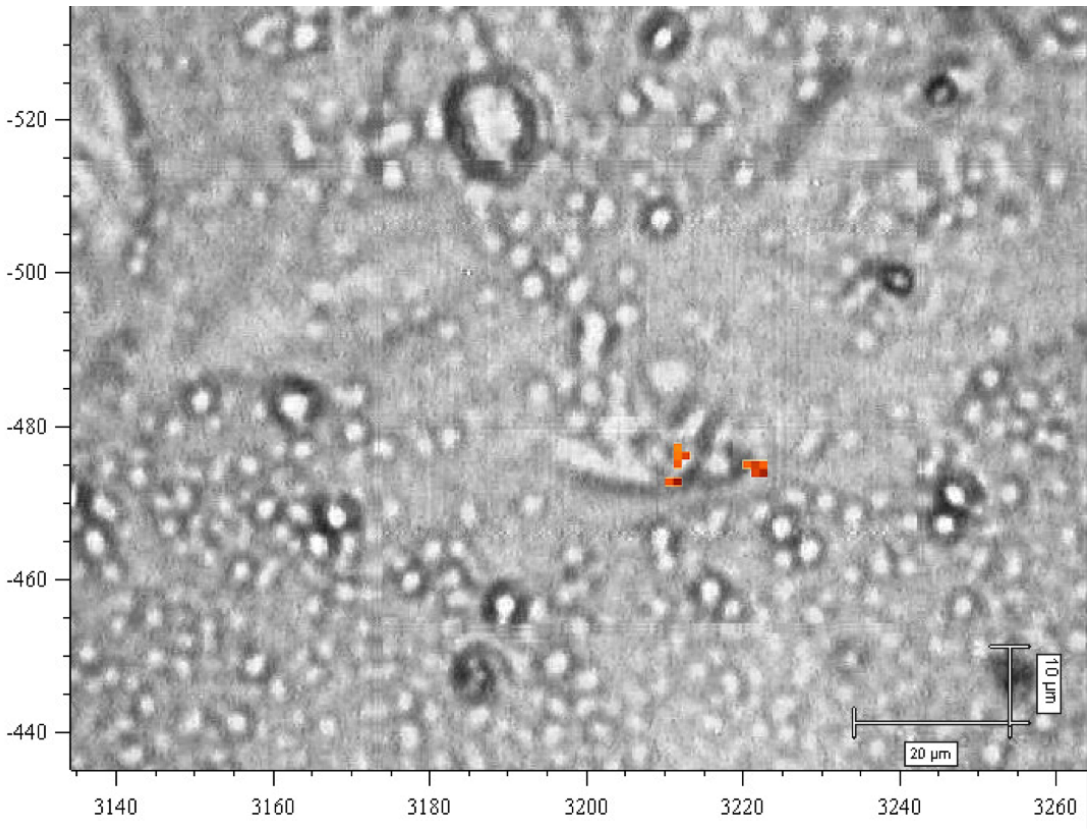

Figure 5.4: Overlay of colourmap from Figure 5.3 (left) on a white light image, showing the intracellular location of NQ-NS.

and interpreted by Jen McLeish in Ken Donaldson's group at the MRC Centre for Inflammation Research, University of Edinburgh. These found that ZnONP, but not AgNP treatment, caused a significant increase in oxidative stress as measured by the dihydroethidium assay. Dihydroethidium is a blue fluorescent dye that is permeable to cells. It is oxidised by superoxide to oxyethidium, whereupon it intercalates with DNA and the fluorescence changes to red. The intensity of red fluorescence as measured by FACS therefore indicates the amount of superoxide generated.

A separate assay to determine the levels of free thiols showed that ZnONP, but not AgNP, treatment caused a signficant reduction in free thiols. This assay used the cell-permeable, non-fluorescent monobromobimane, which, when conjugated to thiols, becomes fluorescent. The intensity of this fluorescence as measured by FACS therefore indicates the levels of free thiols inside cells.

As discussed in Section 1.1, the Nrf2/Keap1 pathway is regulated by redox potential.

Oxidative stress causes Nrf2 to translocate to the nucleus and upregulate expression of its target genes, many of which are antioxidants, including hemeoxygenase-1 (HO-1) [76]. The levels of HO-1 mRNA transcripts were measured using qPCR, and showed that ZnONP, but not AgNP, treatment caused a significant upregulation of the HO-1 transcript after 3 hours.

5.3 Discussion

In this chapter NQ-NS were used to measure the increase in intracellular redox potential in A549 cells treated with sub-lethal doses of engineered metal nanoparticles of Ag and ZnO, which have been shown to be toxic in A549 cells. ZnONP-treated cells showed increased levels of superoxide, decreased levels of free thiols and increased upregulation of antioxidant genes compared to AgNP-treated cells. The intracellular redox potential was shown to be most oxidised during the 1-2 hour time period for both metal NP treatments, with AgNP-treated cells showing more oxidised potentials than ZnONP-treated cells. The increased upregulation of antioxidant genes and decrease in free thiols seen in ZnONP-treated cells, compared to AgNP-treated cells, would enable metal NP-induced ROS to be degraded more efficiently and thus could explain the smaller increase in redox potential.

For both metal NP treatments, the intracellular redox potential was still elevated after 4-5 hours compared to 0-1 hours, indicating that the cells were unable to completely ameliorate the effects of metal NP treatment. In AgNP-treated cells, the redox potential significantly decreased after the initial increase, but did not return to the potential measured during the first hour after treatment. In ZnONP-treated cells this trend did not reach significance, perhaps due to increased upregulation of anti-oxidant genes.

It was not possible to correlate intracellular redox potential with measures of cell viability or levels of apoptosis as spectra were only acquired from intact cells. Therefore only intracellular redox potential in cells that had survived up to the time of measurement could be determined. It would be useful to be able to follow the

changes in intracellular redox potential in an individual cell, however this was not possible as the spectra were acquired at room temperature and atmospheric levels of CO_2. The reduction in CO_2 levels from 5% in an incubator to atmospheric levels causes an increase in the alkalinity of the medium, stressing the cells and leading to cell death after 2-3 hours. Therefore chronic measurements are impossible. The problem of acquiring SERS spectra under physiological conditions is addressed in the next chapter.

In summary, our SERS nanosensor method of measuring intracellular redox potential is capable of measuring pathologically relevant oxidative stress in A549 cells, and is corroborated by traditional assays of oxidative stress.

Chapter 6: Environmental control during SERS measurements

6.1 Introduction

Human cell cultures are usually maintained in a humidified incubator at 37 °C and with a CO_2 concentration of 5%, to simulate the physiological environment of cells within the human body. Cell culture medium contains a buffering system in order to maintain a physiological extracellular pH of 7.3-7.4 [211], with the most common being the bicarbonate/CO_2 system. Cells produce CO_2 as a byproduct of respiration, which decreases the pH of the culture medium through the following equation:

$$CO_2 + H_2O \longleftrightarrow H_2CO_3 \longleftrightarrow HCO_3^- + H^+ \tag{6.1}$$

The addition of sodium bicarbonate drives the equilibrium to the left, increasing the pH, however the CO_2 tension needs to be increased (to 5%) in order to maintain the pH of the culture medium at 7.3-7.4. Sodium bicarbonate also has the advantage of being less toxic than other components of buffering systems and, by providing cells with a source of bicarbonate, allows cells to buffer their intracellular pH. Atmospheric levels of CO_2 lead to an increase in alkalinity of the culture medium, impairing this buffering capability and leading to cell death [212, 213]. pH is a tightly regulated parameter in cells, because protein structure and function can be regulated by pH changes and pH differences drive critically important metabolic processes such as oxidative phosphorylation [211]. A decrease in temperature from 37 °C to room temperature slows down cell growth and can affect the protein levels [214], thus potentially confounding experimental results. Imaging cells under optimal physiological conditions is therefore important to avoid experimental artifacts.

There are a number of methods for controlling the environment that cell cultures experience during imaging experiments, ranging from small chambers that enclose only the cell culture to large enclosures that surround the entire microscope [215].

Small chambers enclosing only the cell culture have the advantage of only requiring a small volume of atmosphere to be controlled and heated, however they are inappropriate where high magnification or high resolution is necessary, as the appropriate microscope objectives require immersion in the culture medium. Therefore these chambers are usually used with a long working distance objective and are thus restricted to magnifications of ×50 or lower. Where high magnification, high resolution water immersion objectives are needed, the microscope itself is encased in a container and a heated stage and objective used. However, these are not airtight and the required air mix is pumped in under slightly positive pressure in order to exclude room air.

One of the aims of the Campbell research group is to measure intracellular redox potential of cells subjected to hypoxia [122], to provide an understanding of how redox potential could be dysregulated within hypoxic regions of tumours and to potentially provide useful insights into treatment resistance (Section 1.3). Therefore, for experiments where a hypoxic environment is necessary, the air mix during spectra acquisition needs to be very precisely controlled.

Due to space constraints, the environment around the Renishaw inVia microRaman system could not be controlled through use of an enclosure, and a heated stage or objectives were not available. A hypoxia incubator was available but a hypoxia workstation was not, so cells could only be incubated and not cultured under hypoxic conditions. Furthermore, commercially available small chambers were prohibitively expensive, therefore it was more cost effective to construct our own small chamber which could be customised to our specifications. This chapter describes the design, build and testing of a specialised chamber to meet the group's specific requirements for long-term measurements of redox potential and pH under both normoxic and hypoxic conditions.

6.2 Specification

The specific requirements of the chamber were:

1. Precise control of air mix. It was imperative that the chamber be airtight so that the O_2 concentration within the chamber would not fluctuate during hypoxic experiments. The more expensive commercially available chambers include the ability to measure CO_2 or O_2 concentrations in real-time. This requires the use of CO_2 and O_2 sensors and readout displays, which are expensive and would add bulk to the chamber. Therefore, for the initial prototype, the chamber would be filled from a cylinder containing a specified air mix (5% CO_2, 21% O_2, balance N_2).
2. Temperature control. The temperature of the cell culture medium should be able to be kept constant over several days.
3. Humidification of air mix. The air mix from a cylinder would need to be humidified in order to reduce evaporation of the culture medium.
4. Fit on the existing microscope stage. The Renishaw inVia microRaman system is equipped with a motorised stage in order to acquire maps, as well as an enclosure to block out stray light. Therefore the chamber would need to be securely fixed to the stage and have the same footprint as the stage so as not to hit the sides of the enclosure during movement of the stage.
5. Fit under the microscope objective. An objective with a super long working distance of 15 mm would be used, which meant that the distance between the top of the chamber and cells adhered to the bottom of a glass-bottomed imaging dish filled with 3 ml of culture medium would have to be $\leq$15 mm.
6. Portable. The chamber would be transported from the tissue culture laboratory to the room containing the Renishaw inVia microRaman system on the floor below. Therefore the chamber and associated items would need to be carried by one person down a flight of stairs and through 4 sets of doors without spilling the culture medium or compromising airtightness.
7. Optically clear top. The top cover directly over the cell culture would need to be optically transparent to the laser light at 785 nm and the resultant Raman

scattered light.

8. Transparent bottom. The bottom should be transparent enough to allow cells to be visualised by a white light illumination source directly underneath.
9. Easily cleaned. In the event of spillage of the culture medium then the chamber must be easily cleaned. Periodic cleaning would also be necessary to keep the interior as sterile as possible so as not to contaminate cell cultures and possibly confound experimental results.

6.3 Design, construction and testing of initial prototype

An initial design concentrated on requirements 1, 4, 5, 6, 7, 8 and 9 from the specification list and a prototype was constructed in collaboration with engineers at the University of Cambridge. The main body of the chamber was formed by a 15.4 mm thick sheet of perspex, into which a 9 mm deep cavity was made (Figure 6.1). Two holes were drilled in the sides connecting to the cavity to allow gas to be passed through. A connector was seated in each hole with three O-rings and each attached to a separate 20 cm length of 6 mm internal diameter Tygon tubing. The lid of the chamber was a 3.2 mm thick sheet of perspex, with a hole drilled in the centre, surrounded by a square recess into which a ~0.15 mm thick glass coverslip was seated and sealed with silicone sealant. A thin glass coverslip was used as it is optically clear and does not significantly reduce the laser power at the sample, therefore meeting requirement 7 from the specification list. An airtight seal between the lid and chamber was achieved with an O-ring seated in a groove in the chamber body surrounding the cavity. The lid was secured to the chamber by 8 nylon screws so as to ensure sufficient compression of the O-ring. The distance between the bottom of the cavity and the top of the lid is 12.2 mm, thus meeting requirement 5 from the specification list. The chamber is portable and easily cleaned, thus meeting requirements 6 and 9, respectively, from the specification list.

To check that the chamber was airtight, culture medium was equilibrated in an humidified incubator at 37 °C with a CO_2 concentration of 5% and the pH measured as 7.6 (within the range specified for the medium). The pH was measured with a

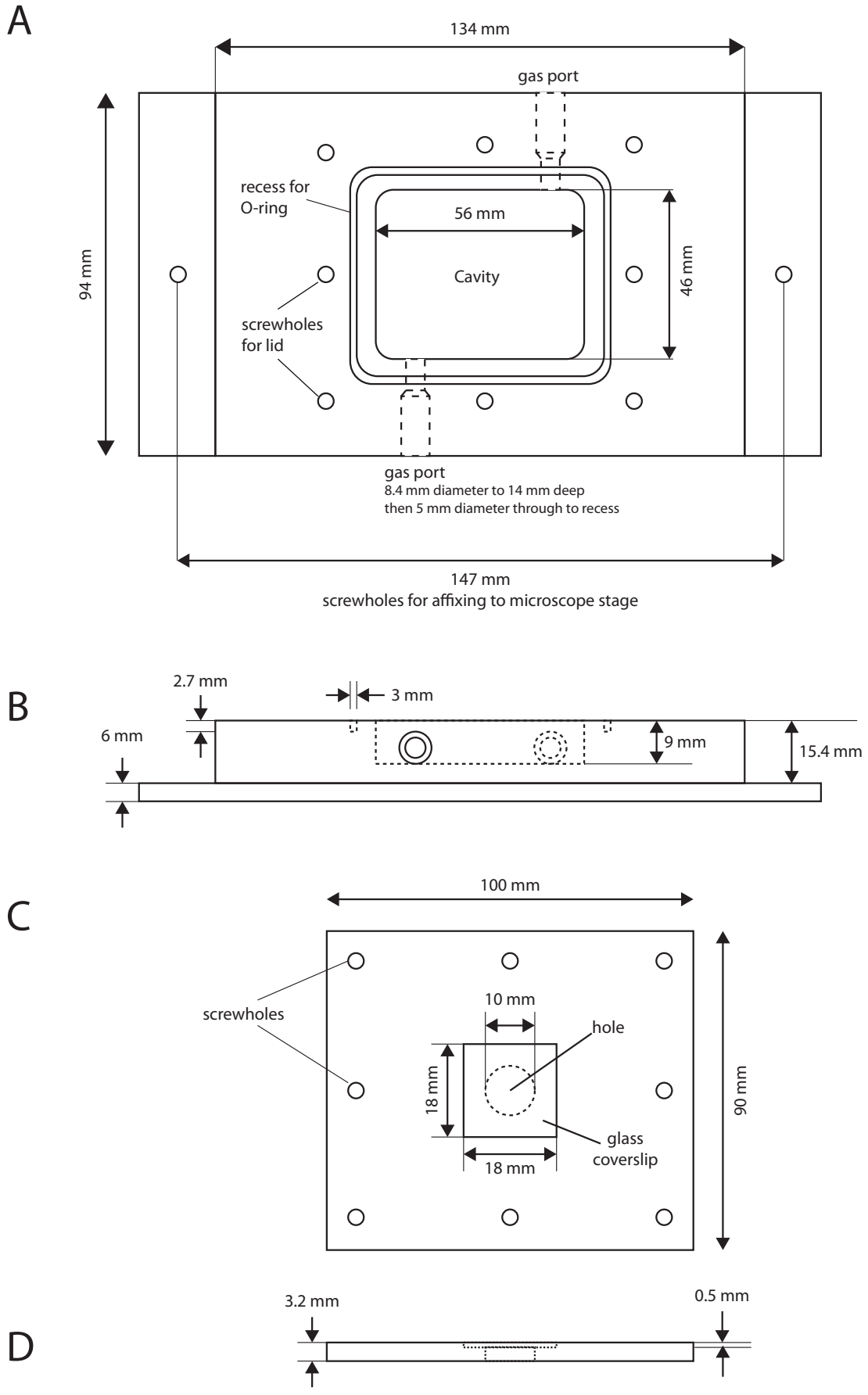

Figure 6.1: Schematic of the initial prototype. A: top view of main chamber; B: side view of main chamber; C: top view of lid; D: side view of lid.

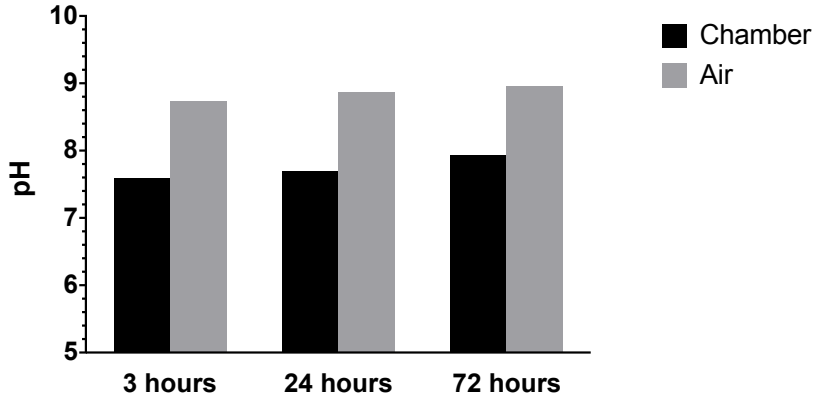

Figure 6.2: The pH of culture medium inside the chamber increased much more slowly than the pH of culture medium exposed to room atmosphere. Two glass-bottomed low-wall imaging dishes were filled with 2 ml of culture medium equilibrated to 37°C and a CO_2 concentration of 5%. One dish was sealed inside the chamber with an atmosphere containing 5% CO_2 and the other was left on the bench top. The pH of the culture medium in both dishes was measured at 3, 24 and 72 hours (freshly equilibrated culture medium was used each time). The initial pH was measured as 7.6.

Mettler Toledo InLab Ultra-Micro pH meter. Two glass-bottomed low-wall imaging dishes (Ibidi μ-Dish 35 mm, height 7 mm) were then filled with 2 ml of this equilibrated culture medium. One was placed in the chamber cavity and the lid securely fastened, whilst the other was left open on the bench top. Gas from a cylinder containing 5% CO_2, 21% O_2 and balance N_2 was flowed through the chamber via one of the lengths of tubing at slightly above ambient pressure for 60 seconds. The two lengths of tubing were then simultaneously bent over on themselves and fixed, to seal the air mix inside. The flow from the gas cylinder was then turned off and the pH of the culture medium in both dishes was measured after 3 hours. This was repeated with fresh equilibrated culture medium twice more, with the pH measured after 24 and 72 hours. Figure 6.2 shows that the pH increase is negligible at 3 hours (pH 7.6) and 24 hours (pH 7.7), whereas it is slightly increased at 72 hours (pH 7.9). This indicates that the pH of the culture medium would be maintained at a physiological level for experiments lasting less than a day, and for longer-term experiments the air mix could be refreshed daily. Furthermore, submerging the (empty) chamber in water showed no airleaks, therefore the chamber was airtight and requirement 1 from the specification list had been met.

The chamber was then affixed to the stage of the Renishaw inVia microRaman system

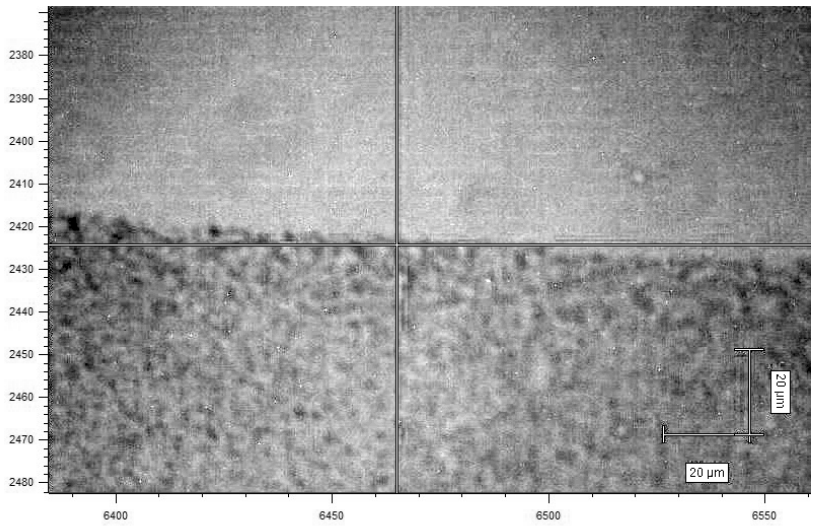

Figure 6.3: 500× white light microscope image of the edge of the NQ-NS spot dried onto a PLL-coated glass-bottomed imaging dish, which was filled with 2 ml of culture medium. Small aggregates of dried NQ-NS are clearly visible (bottom half of image).

using two screws. The chamber did not obstruct the movement of the stage, thus meeting requirement 4 of the specification list.

NQ-NS were then dried onto a PLL-coated glass-bottomed low-wall imaging dish and 2 ml of culture medium added. The dish was placed inside the chamber cavity and the lid fastened. Single SERS spectra were successfully obtained using the point focus lens. The transparent perspex chamber body allowed sufficient white light illumination from underneath the chamber to visualise small aggregates of dried NQ-NS (Figure 6.3), thus meeting requirement 8 of the specification list.

The above results show that the prototype successfully meets the initial requirements listed at the beginning of the section, namely that the chamber is airtight, portable, easily cleaned, can fit on the existing microscope stage and under the microscope objective, and SERS spectra can be successfully acquired through an optically clear top with white light illumination from underneath. The design was subsequently modified to incorporate temperature control; this increased the complexity of the design and is described in the next section.

6.4 Addition of temperature control

As no hypoxia workstation was available to culture cells under hypoxic conditions, the imaging chamber would need to fulfil this function in order to apply nanosensors to hypoxic cells. Therefore a second hole was drilled into the lid, and recessed to accomodate a silicon/PTFE septum, which would allow culture medium changes and the application of nanosensors or other treatment via a needle and syringe. This would also mean that cells would need to remain in the chamber for a number of days, so a stable temperature no higher than 37 °C would be necessary in order to keep the cells in optimal physiological conditions.

Temperature control was achieved by heating recirculating air and introducing bulk heating of the chamber. To avoid localised heating a motor was added to drive the air through the chamber in a circuit. Heating was achieved (1) by running current through four resistors attached to an aluminium plate affixed to the bottom of the chamber, with a hole drilled in the centre to allow light from under the chamber to illuminate the sample; and (2) using a subminiature proportionally controlled heater element within a heater enclosure to heat the air in the chamber system. Tubing connecting all of these elements was insulated to prevent as much heat loss as possible. Temperature sensors were placed on the aluminium plate, in the chamber cavity and heater enclosure. The output voltage of these sensors is linearly proportional to the temperature (°C), allowing the temperature to be measured with a multimeter. The temperature in the heater enclosure was set by a potentiometer to give a temperature of ~40 °C inside the enclosure. The input voltage could be adjusted using a variable power supply in order to give a power output through the heating resistors (R1-R4) that, together with the heater enclosure, could deliver the required temperature in the chamber cavity, allowing for heat loss in the system. Two self-sealing connectors in the system tubing facilitated 'charging' the system with the required airmix avoiding any leakage of room air back into the system and a balloon was added for differential pressure variations due to temperature and atmospheric pressure changes. Figures 6.4, 6.5 and 6.6 show a schematic, circuit diagram and photo of the system, respectively, after these modifications.

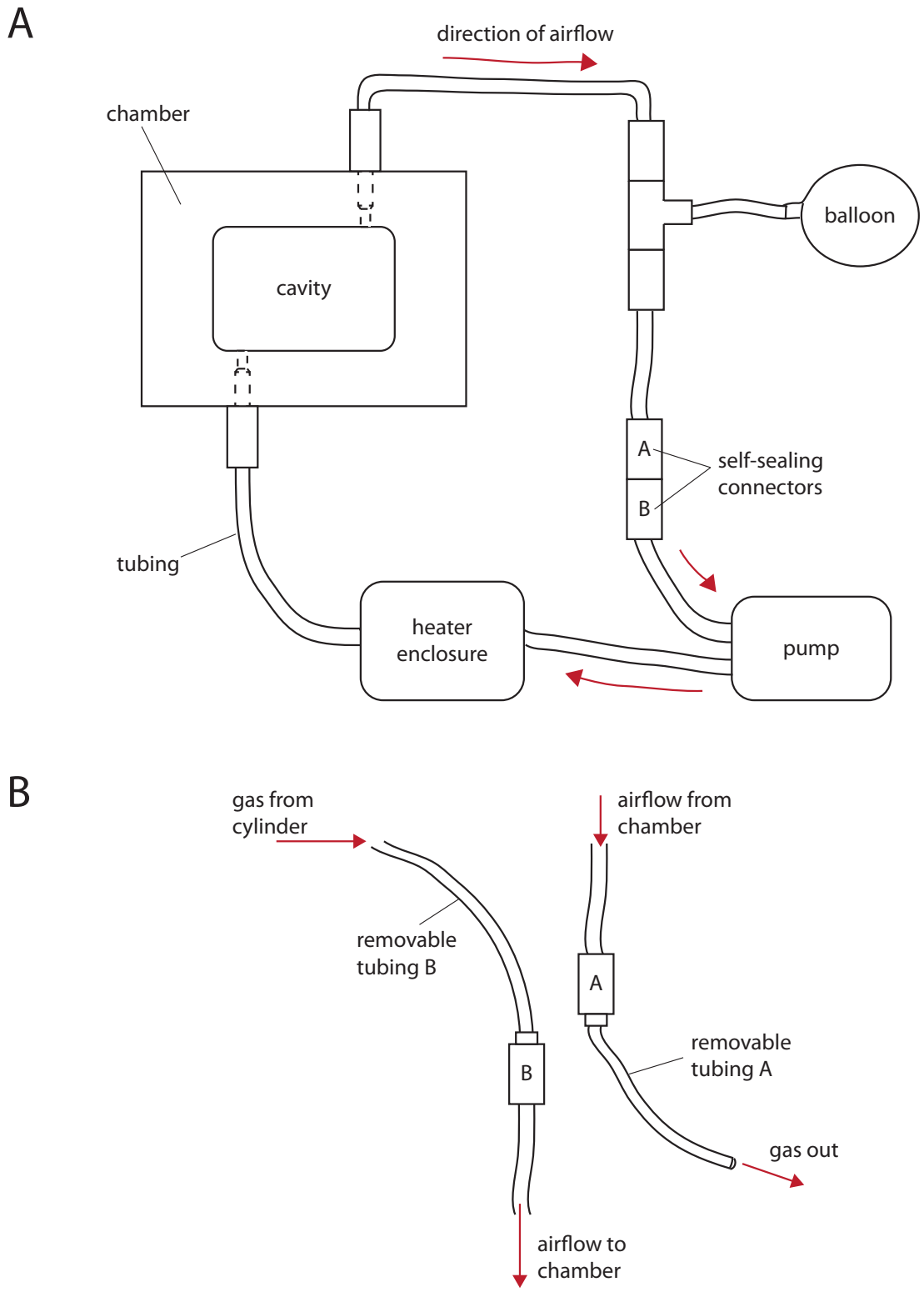

Figure 6.4: (A) Schematic of initial prototype modified to include temperature control. The desired airmix in a cylinder is introduced into the system via the self-sealing connectors. The connectors allow airflow when connected to each other or other (non-sealing) connectors. (B) shows the procedure for introducing the desired airmix into the system: The self-sealing connectors are disconnected from each other and removable tubing is connected to both. The lower connector B is connected to the gas cylinder containing the desired airmix, whilst the upper connector A is connected to a length of open tubing. The airmix is gently flowed through the system for 120 seconds (ensuring the balloon is completely deflated), then removable tubing B is disconnected (sealing that connector), before rapidly disconnecting removable tubing A. The two self-sealing connectors are then connected to each other again to allow flow through the system once more.

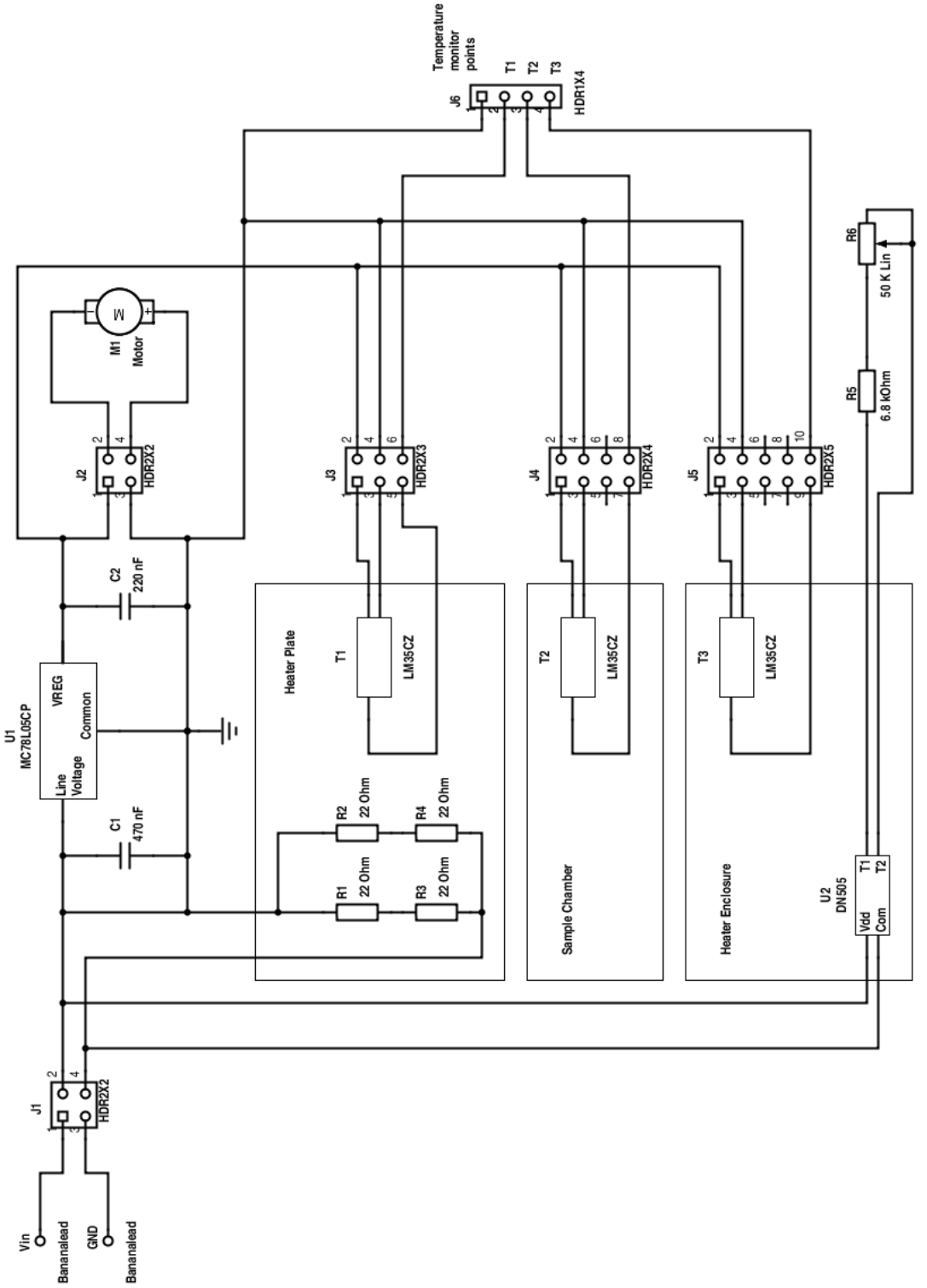

Figure 6.5: Circuit diagram showing how temperature control within the imaging chamber was achieved (1) by running current through four resistors attached to an aluminium plate affixed to the bottom of the chamber (heater plate); and (2) using a subminiature proportionally controlled heater to heat the air in the system (heater enclosure). Temperature sensors (T1, T2 and T3) were placed on the aluminium plate, in the chamber cavity and heater enclosure to monitor temperature in those locations. The power supply voltage was set to give a current through the heating resistors that resulted in a chamber temperature that was maintained and controlled by the heater plate. The voltage regulator supplies the pump motor and the semiconductor temperature sensors.

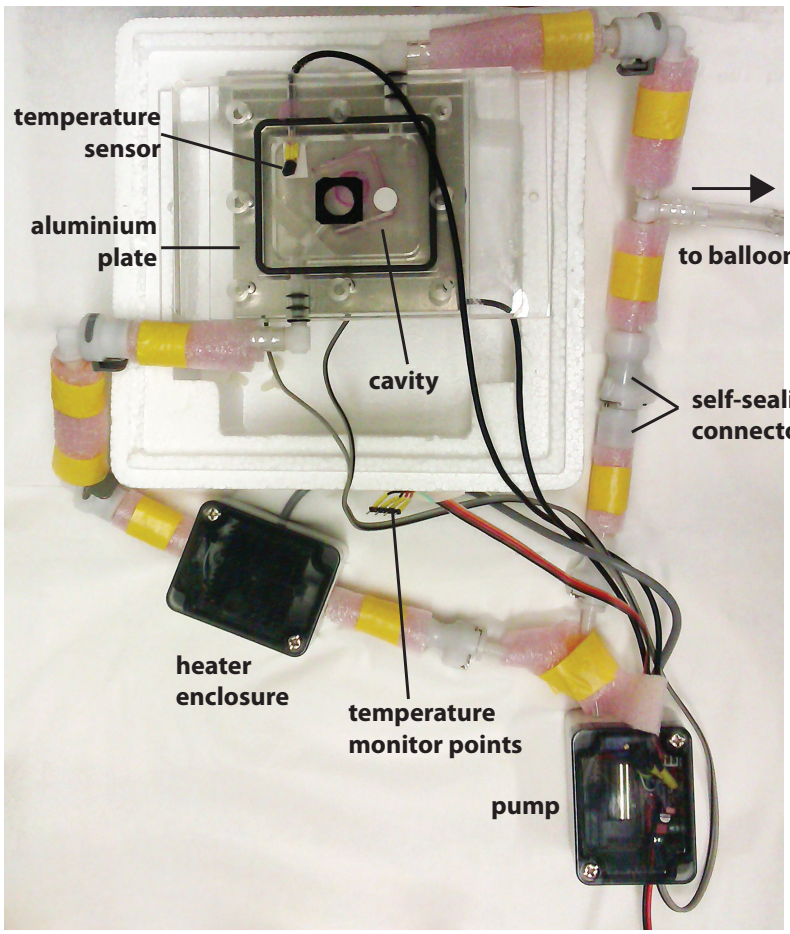

Figure 6.6: Photograph of imaging chamber with temperature control.

The temperature inside the chamber cavity took approximately 60 minutes to reach a maximum from room temperature and was found to be stable over the following 2 hours (Figure 6.7). The maximum temperature inside the chamber cavity reached 35.5 °C with the input voltage set to 9 V. These results suggest that the temperature in the chamber cavity will remain stable over time - as long as the ambient temperature remains stable. Therefore, with this caveat, requirement 2 of the specification list has been met.

To check that the chamber was airtight, the chamber was allowed to reach maximum temperature whereupon a glass-bottomed low-wall imaging dish containing 2.00 ml of equilibrated culture medium (at a pH of 7.6) was placed inside the chamber cavity and the lid re-fastened. The culture medium was eqilibrated in an incubator at 37 °C with a 5% CO_2 concentration. The system was then 'charged' with gas from a cylinder containing 5% CO_2, 21% O_2 and balance N_2 as detailed in Figure 6.4 and the

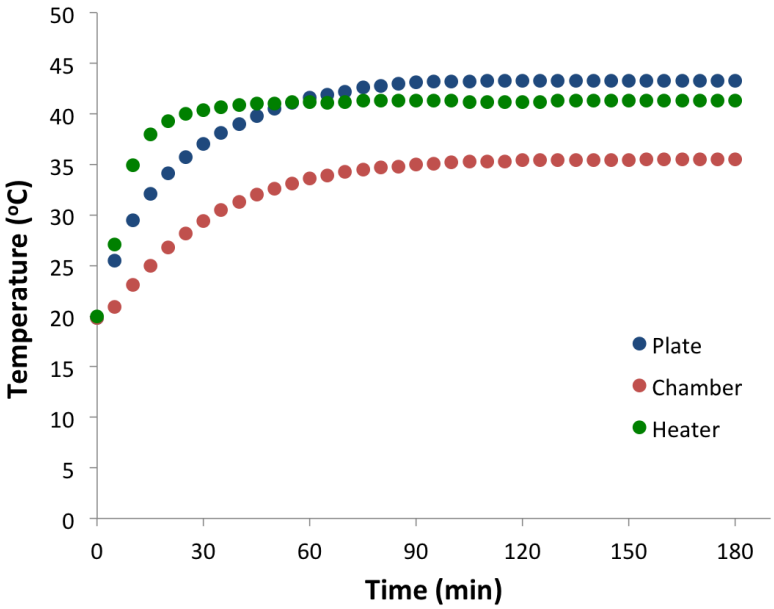

Figure 6.7: Physiological temperatures in the chamber cavity are reached in ~60 minutes and are stable over time. Temperature sensors were placed on the aluminium plate on the bottom of the chamber (plate), inside the chamber cavity (chamber) and inside the heater enclosure (heater). The aluminium plate was heated by running current through 4 resistors affixed to it. The temperatures of the plate and the heater enclosure were set to achieve a final chamber temperature of 35.5 °C.

pH of the culture medium measured after 3 hours. This was elevated by 0.22 pH units and the volume of the culture medium remaining was reduced by 18% to 1.64 ml. However, submerging the whole system in water showed no airleaks. These results imply that evaporation (due to the lack of humidity in the air mix from the cylinder) increases the pH of the culture medium.

Efforts were then made to pre-humidify the gas mix before introducing it into the system, by bubbling it through water. However, this caused condensation on the lid of the chamber, including the coverslip, making it impossible to see the interior of the chamber under the microscope and impeding the laser path to the sample.

6.5 Discussion

This chapter described the design and fabrication of a portable chamber for the purpose of acquiring SERS spectra from intracellular nanosensors in a controlled environment. The initial prototype showed that the chamber was airtight and

suitable for use in experiments where atmostpheric control was necessary. The addition of temperature control caused the culture medium to evaporate, however attempting to reduce this by humidifying the airmix caused condensation on the lid of the chamber, reducing visibility and impeding the laser path. Overall, the following requirements from the specification list in Section 6.2 were met:

1. Precise control of air mix: The chamber in both the initial prototype and with the addition of temperature control was shown to be airtight. Therefore the chamber is suitable for acquiring SERS spectra from intracellular nanosensors in both physiological and hypoxic conditions.
2. Portable: The initial prototype of the chamber was easily carried by hand from the tissue culture laboratory to the room containing the Raman spectrometer on the floor below. The addition of temperature control increased the number of components to transport, however the system was placed into a box for easy transport, without spilling any culture medium.
3. Fit on the existing microscope stage. The chamber was fastened by 2 screws to the motorised stage and did not hinder its movement at all.
4. Fit under the microscope objective. The distance between the bottom of the chamber and the top of the lid is 12.2 mm, less than the 15 mm required by the super long working distance objective.
5. Optically clear top: The use of a glass coverslip embedded into the perspex lid was transparent to the 785 nm laser beam, thus allowing the acquisition of SERS spectra with minimal signal loss.
6. Transparent bottom: The chamber was constructed in perspex, which is transparent to the white light illumination source directly underneath. A hole was cut into the aluminium plate affixed to the bottom of the chamber to allow the light through into the chamber. Small aggregates of NQ-NS dried onto a PLL-coated imaging dish and covered with 2 ml of culture medium were easily visible with this illumination, suggesting that cells would be equally well visible.

7. Easily cleaned: The perspex construction meant that the chamber and lid were easily cleaned.

In addition, a septum was added to allow the exchange of culture medium and the application of nanosensors and/or drug treatments to cells in hypoxic conditions. This enabled the chamber to fulfill some of the functions of a hypoxia workstation, which was not available.

Only two requirements were not successfully met: temperature and humidity control. Although a stable temperature was able to be maintained over several hours, heating the chamber to ~35.5 °C caused evaporation of the culture medium due to the lack of humidity in the air mix. Pre-humidifying the air mix prior to 'charging' the chamber system caused condensation on the lid of the chamber, including the coverslip, impeding the laser path. Heating the lid or only the coverslip should stop this condensation. The heating of the chamber could be improved by embedding the chamber in a directly controlled thermal block with apertures in the top and bottom for the laser beam and white light illumination, respectively.

In summary, the chamber can be used in short-term experiments without temperature control, which would prevent evaporation, but can't be used for longer-term experiments, where the decrease in temperature would reduce cell growth and affect protein levels, potentially confounding experimental results, without further modifications to prevent condensation on the lid.

Chapter 7: Extracellular redox potential

7.1 Introduction

The extracellular redox potential is important for the function of some cell types, for example, T-cells and neurons (Section 1.2) and changes in the extracellular redox potential have been implicated in various diseases such as cardiovascular disease (Section 1.3). One study has shown that a more oxidised extracellular potential does not change the intracellular GSH/GSSG ratio in bovine aortic endothelial cells [94]. However, while the intracellular GSH/GSSG ratio might not respond to extracellular redox changes, it is possible that the *overall* intracellular redox potential did change, as discussed in Section 1.1. Secondly, in the above-mentioned study different Cys/CySS ratios were applied to the culture medium to generate different extracellular redox potentials; over time the ratios tended towards the same values. It is therefore unknown how the GSH/GSSG ratio or overall intracellular redox potential respond to a prolonged oxidised extracellular redox potential.

The simultaneous quantitative measurement of overall extracellular and intracellular potentials has not yet been addressed and the extent of interplay between the two is unknown. The ability to investigate changes in extracellular potential on perturbation of intracellular potential, and *vice versa*, would inform knowledge of pathological processes, for example in cancer, where the redox potential of the tumour microenvironment has been shown to affect proliferation [216, 217].

This chapter describes the construction of a device from which SERS spectra from intra- and extracellular nanosensors can be acquired during the same experiment. As the Cys/CySS redox couple is the most abundant couple extracellularly, with a more oxidising midpoint potential than the GSH/GSSG couple it is expected that the overall extracellular redox potential is more oxidised than the intracellular redox potential [91, 92].

7.2 Results

In order to obtain SERS spectra from extracellular nanosensors, the nanosensors should be immobilised onto a surface. As the nanosensors are to be in contact with cell culture medium, this surface needs to be optically clear. Finally, intracellular and extracellular nanosensors should be spatially separate in order to distinguish between spectra obtained from each. Therefore, the most convenient way to achieve this is to plate cells in a dish filled with culture medium and cap this with a glass slide or coverslip onto which nanosensors have been immobilised.

Members of Eleanor Campbell's group at the School of Chemistry had obtained Raman spectra from liquids using polydimethylsiloxane (PDMS) devices capped by glass slides. PDMS is a commonly used polymer in biological microfluidics applications as it is inert and non-toxic to cells [218]. I therefore adapted these devices for the purpose of obtaining SERS spectra from both intracellular and extracellular nanosensors using the same device.

The devices were constructed by curing PDMS on top of pre-cut glass slides, into which an 8 mm diameter well was cut (Figure 7.1). A549 cells were then plated at the bottom of the well. However, there was some residual PDMS on the surface of the slide at the bottom of the well, making it difficult to see the cells under the microscope. Therefore, the protocol for device formation was modified in that a thin coating of nail varnish was used to mark out the well before the PDMS was applied; this stopped the PDMS adhering to that region of the slide and the nail varnish could be removed with acetone after the well had been cut. This resulted in a flat glass surface for cells to adhere to and cells could easily be visually distinguished under the Raman microscope (Figure 7.2). The height of the PDMS layer was 4-6 mm, giving a well volume of ~200-300 μl. The well was filled with culture medium and a coverslip placed on top, which had been coated with poly-L-lysine (PLL) onto which NQ-NS had been dried. The area of the coverslip covered by nanosensors was easily visible under the Raman microscope (Figure 7.3).

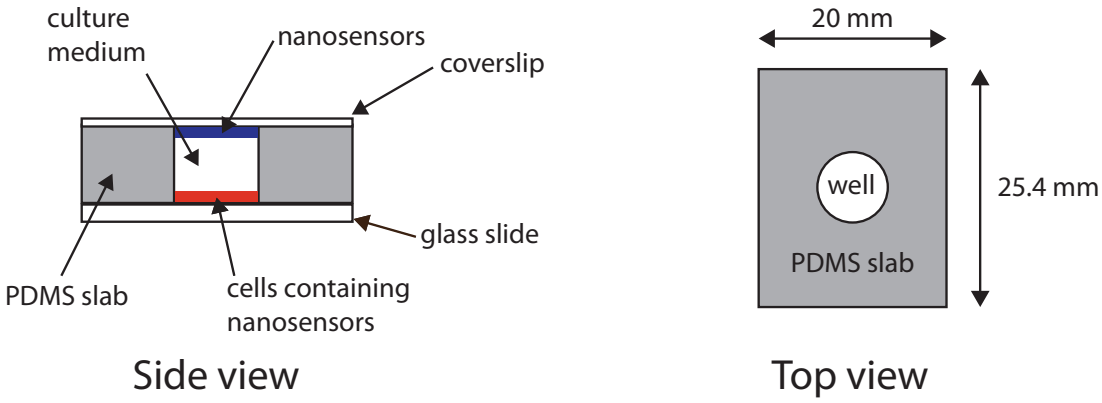

Figure 7.1: Device for measuring intracellular and extracellular redox potentials in the same experiment. The device is constructed from a slab of PDMS into which an 8 mm diameter well was cut and capped by a glass slide (on which nanosensor-containing cells are adhered) and a glass coverslip (on which nanosensors have been immobilised).

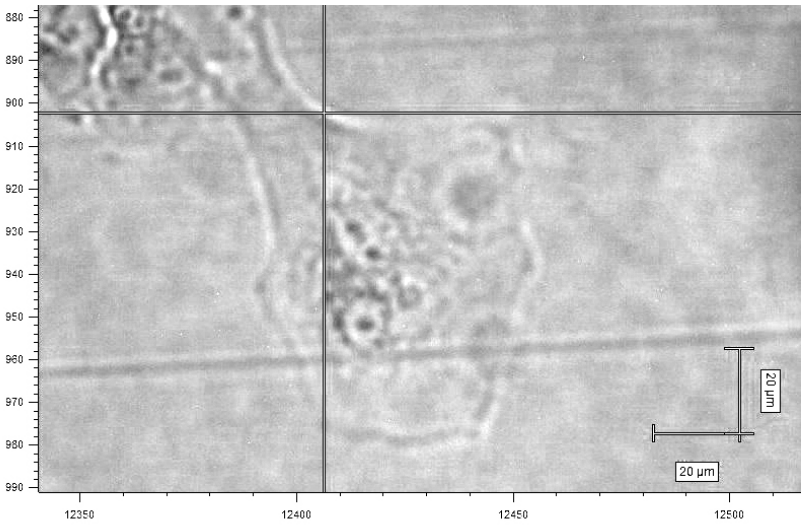

Figure 7.2: Representative 500× white light microscope image of an A549 cell adhered to the glass slide at the bottom of the well in the PDMS device. The image was acquired with the device inverted to place the cell layer at the top to provide minimum obstruction to laser during acquisition of SERS spectra.

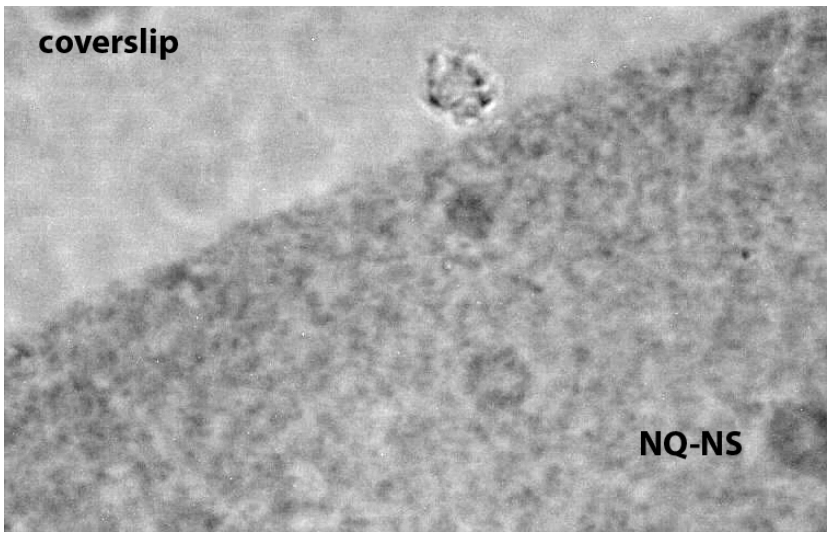

Figure 7.3: 500× white light microscope image of the edge of the NQ-NS spot dried onto a PLL-coated coverslip and placed on top of the device, with the NQ-NS in contact with cell culture medium.

7.3 Acquisition of SERS spectra

A549 cells were plated at the bottom of the well in the device and incubated with NQ-NS (see Section 2.6 for full methods). SERS maps were acquired from intracellular NQ-NS as detailed in Section 2.5, whilst single spectra were acquired from extracellular NQ-NS. As the culture medium is sealed inside the device by the coverslip, the device could be inverted to place the cell layer at the top in order to provide as little obstruction to the laser as possible when acquiring SERS maps from intracellular NQ-NS. To acquire SERS spectra from the extracellular nanosensors the device was then placed with the coverslip uppermost. To ensure that signals from the intracellular and extracellular nanosensors did not overlap, the device was filled with culture medium and capped with a PLL-coated coverslip onto which NQ-NS had been immobilised. Spectra were obtained from the glass slide at the bottom of the well and showed only the Raman spectrum of the slide - no signals from NQ-NS were observed (Figure 7.4). Therefore the spatial separation between intracellular and extracellular nanosensors is adequate to ensure no overlap of spectra.

A representative SERS spectrum from extracellular NQ-NS is shown in Figure 7.5. Comparison with Figure 4.24 indicates NQ is fully reduced. Even after 2 hours of equilibration with the cell culture medium the extracellular redox potential was too

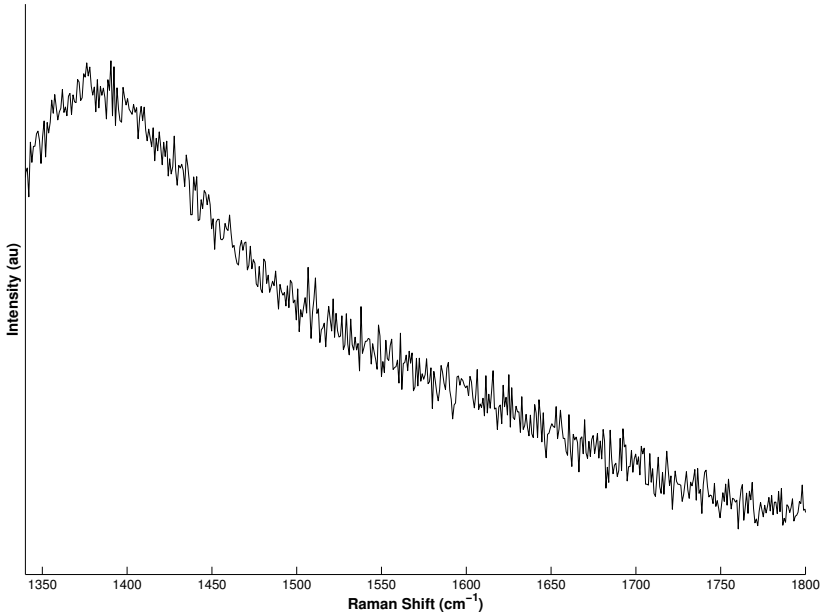

Figure 7.4: Representative Raman spectrum from the glass slide in the absence of cells. The device was set up as in Figure 7.1 except no cells were added. The Raman spectrum shows no contribution from NQ-NS dried onto a coverslip and capping the well.

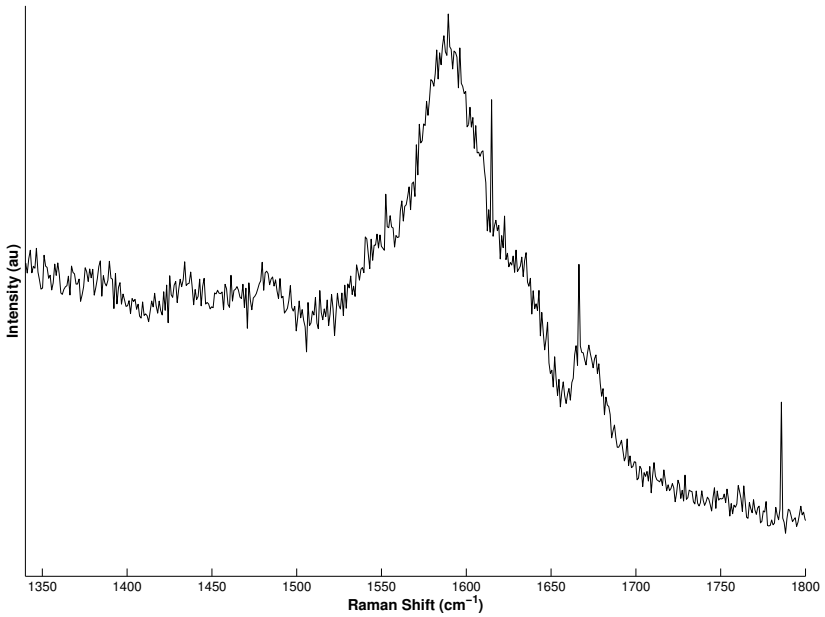

Figure 7.5: Representative SERS spectrum from extracellular NQ-NS after 2 hours equilibration of cells with fresh culture medium. The spikes at ~1615, 1665 and 1790 cm^{-1} are due to hot pixels on the CCD camera.

reduced to be determined from the SERS spectra, i.e. <-400 mV. The redox potential of culture medium only was then measured, (i.e. no cells were plated and the device filled with fresh culture medium) and again the potential was too reducing to be determined from the SERS spectra. As the extracellular redox potential is expected to be more oxidising than the intracellular redox potential, this suggests that a longer equilibration time and/or a smaller volume of culture medium is necessary to prevent dilution of cell secretions.

7.4 Discussion

In this chapter, a device was constructed that allowed the acquisition of SERS spectra from both intracellular and extracellular nanosensors in the same experiment. The spatial separation of the intracellular and extracellular nanosensors makes it clear which ones spectra are acquired from. Using this device, SERS spectra can quickly and easily be obtained from both nanosensor locations by inverting the device to acquire spectra from intracellular nanosensors.

Pilot experiments to measure the extracellular redox potential showed that the potential was too reduced (<-400 mV) to be measured by the NQ-NS nanosensor, as was the potential of blank culture medium. The extracellular redox potential is expected to be more oxidised than the intracellular redox potential, and as the intracellular redox potential is within the range of NQ-NS, it is surprising that extracellular potential measured was more reduced. However, the cell culture medium does contain several redox-active ingredients, such as the amino acids glycine, tyrosine, tryptophan and cystine (not cysteine). Studies have shown that the extracellular redox potential in human plasma is more oxidised than the intracellular redox potential due to the increased abundance of the Cys/CySS redox couple [92]. However, the overall extracellular redox potential of cell culture may not mirror this and hasn't been previously measured to the best of our knowledge. Studies reporting the extracellular redox potential of cell cultures added different ratios of Cys/CySS to the culture medium and monitored the change in the ratios over time [94, 219]. The different initial ratios of Cys/CySS tended towards the same value over time and this

value was reported as the extracellular redox potential. Therefore it may be informative to measure the redox potential of human plasma using our method and compare the results with these other studies.

If the extracellular redox potential of the cell culture medium is not physiologically representative, then it does at least allow investigation of intracellular redox potential changes in response to manipulation of the redox potential of the cell culture medium. Such manipulations include the addition of various ratios of Cys/CySS as in the studies mentioned above, or the addition of drugs that cause oxidative stress (e.g. AAPH - see Chapter 5), or have antioxidant properties (e.g. N-acetyl-cysteine).

To measure how cells condition the redox potential of their microenvironment, a physiological extracellular redox potential could be achieved by reducing the height of the PDMS slab, which varied between 4-6 mm, giving a volume of ~200-300 μl. Reducing the height to 2 mm would give a volume of ~100 μl, a reduction of 50-66%. Additionally, the equilibration time of cells with fresh culture medium after overnight incubation with nanosensors should be extended from 2 hours to allow cell secretions to build up.

Conclusions and future work

Prior work in our research group led to the development of the NQ molecule, and provided basic proof-of-principle for its use in measuring intracellular redox potential. In this thesis, the method has been greatly extended, with improvements in production and toxicity testing of the nanosensors, robustness of SERS data acquisition and analysis, environmental control of measured cells, and application to disease-relevant cell culture models. As a result, we are now able to rapidly and reproducibly determine intracellular redox potential in single cells. In addition, the methods that have been developed have broad applicability to SERS nanosensors for other physiological parameters, and development of these modalities is ongoing by others within our research group.

The initial stages of the project focused on standardising the functionalisation of gold nanoshells with the redox-active NQ probe molecule (Chapter 3). The standardised protocols that were developed gave reproducible results and enabled accurate concentrations of nanosensors to be added to cell cultures. The pathologically relevant A549 human lung cancer cell line was used in this work, as it is a well-characterised model of lung cancer, inflammation and nanoparticle toxicity. NQ-NS nanosensors were shown to be non-toxic in this cell line, using assays of membrane integrity and cell viability, and were taken up freely into the cytoplasm. Previous work using the dichloro-dihydro-fluorescein diacetate (DCFH-DA) assay showed that NQ-NS did not cause oxidative stress in NIH/3T3 murine fibroblast cells, i.e. that the intracellular redox potential was not perturbed beyond the ability of the cell to cope with an increase in ROS. Although this is reassuring, it could also be useful in the future to confirm that NQ-NS do not affect intracellular redox potential in A549 cells by examining transcriptome profiles using qRT-PCR, as this would give a more sensitive measure of oxidative stress. qRT-PCR measures the levels of mRNA transcripts of a particular gene present in a sample, so comparing the levels of mRNA transcripts of various anti-oxidant genes of cells containing NQ-NS with

those of cells containing no nanosensors would indicate whether NQ-NS caused small changes in intracellular redox potential.

Previously, locating NQ-NS within cells was time-intensive and unreliable. A method was therefore developed to rapidly locate intracellular NQ-NS and obtain SERS spectra from them in the form of maps (Chapter 3). 'Pre-scanning' cells with a high laser power and short integration time gave a rough location of any NQ-NS within a cell. Once located, spectra could be acquired with a lower laser power and longer integration time to produce spectra with a high enough SNR from which to determine the redox potential. This method was a success, enabling more rapid acquisition of high quality spectra from cells, improving throughput and laying a necessary foundation for time-sensitive measurements. It has general applicability as it can also be used with any combination of adherent cell type and intracellular nanosensor, and has been used by several group members in different cell lines (such as prostate and breast cancer cell lines) and nanosensors for different redox potential ranges and pH.

Given the large increase in data volume following improvements in data acquisition, an automated approach to spectral analysis was needed to improve the speed and accuracy of the determination of redox potential or pH. In response to this need, a bespoke piece of software was created to determine redox potential and pH from SERS maps, and allowed automated production of a colour-map showing the spatial variation of redox potential or pH with subcellular resolution (Chapter 4). The software performed background subtraction followed by peak fitting to extract information on peak centre, height and area. Calibration curves were constructed from data from each of three nanosensors and two Raman spectrometers, and the resultant redox potential or pH value quoted with a 95% confidence interval. It was found that a greater number of calibration curves for a nanosensor resulted in more accurate determination of pH or redox potential, however more calibration datasets for the NQ-NS and AQ-NS nanosensors would also improve their accuracy. Comparison to the manual method of processing spectra showed that not only was the automated method >50 times faster and also more precise, but bias and variance

were minimised. Flexibility built into the software means that it has already been adapted for both new probe molecules developed by the group and also for a new spectrometer. Furthermore the software could easily be modified for multiplexed spectra containing signals from two or more probe molecules, as long as the individual probe spectra are sufficiently spectrally separated.

Chapter 5 used the methods established in Chapters 3 and 4 to investigate the change in intracellular redox potential in response to metal nanoparticle treatment. This is a highly pathologically relevant treatment to use as a case-study, as engineered metal nanoparticles are known to cause cellular oxidative stress and be damaging to lung tissue. The results showed that our SERS nanosensor method of measuring intracellular redox potential is capable of measuring this pathologically relevant oxidative stress in cultured human lung A549 cells, and these measurements were corroborated by traditional assays of oxidative stress. Intracellular redox potential was shown to be more oxidised after metal nanoparticle treatment, with the effects lasting for at least 4-5 hours after treatment. This successfully confirms previous work performed by others in the nanoparticle toxicity field, and our use of a novel assay strengthens the conclusion that metal nanoparticles indeed trigger oxidative stress. However, a limitation of the SERS measurements was that intracellular redox potential could only be determined in cells that had survived up to the time of measurement, so it is possibile that greater effects on redox potential would have been seen in apoptotic or necrotic cells. To counter this problem, the intracellular redox potential of a single cell would need to be followed chronically. Unfortunately acquiring spectra from cells held in medium exposed to normal air at room-temperature conditions results in cell death after only a few hours. Therefore the ability to acquire spectra under more physiological conditions would avoid experimental artifacts, and also enable intracellular redox potential to be investigated in cell cycle as well as cell death studies.

Chapter 6 addressed this issue of environmental control during spectra acquisition. A portable, airtight chamber was designed, constructed and tested and was shown to be suitable for acquiring SERS spectra from intracellular nanosensors in a defined gas

mix at room temperature in short-term experiments where physiological temperature is not critical. This chamber is now used by a member of the group to provide a 5% CO_2 atmosphere for short-term experiments investigating the pH gradient inside multicellular tumour spheroids. The design of this chamber was then modified to incorporate temperature control and humidification of the chosen gas mix for long-term experiments. However these additions resulted in water condensation on the chamber lid, disrupting visibility and impeding transmission of the laser beam. The design could be modified further to reduce condensation by heating the lid, either separately or by embedding the chamber in a directly controlled thermal block. It will be very useful to perfect the enviromental control aspect of the system, as an ability to both perform measurements chronically and manipulate the gas environment will enable the response to these alterations to be studied. For example, cellular redox responses to hypoxia are currently poorly understood, and investigation of the change in intracellular redox potential over time when subjected to a hypoxic environment would yield much useful information. Most importantly, better environmental control will be critical for further extending the applicability of this measurement method, as biological model systems need to reproduce animal physiology as closely as possible in order to give results that are meaningful in the study of health and disease.

Finally, a device was constructed that allowed the acquisition of SERS spectra from both intracellular and extracellular nanosensors in the same experiment (Chapter 7). This enables experiments where the extracellular redox potential is manipulated and the effects on intracellular redox potential measured. The device was sealed and intracellular nanosensors were spatially separated from extracellular nanosensors, allowing clear discrimination of the SERS spectra obtained simply by changing the orientation of the device. This approach gave successful proof-of-principle data showing that correlated intra/extracellular measurements are possible. However, the data obtained from the extracellular NQ-NS was limited, as redox potential in the culture medium produced measurements that were outwith the sensor range (no such problems occurred in the intracellular measurements). It would be useful in the

future to attempt these measurements again using an alternative probe that covers a more reduced range of redox potentials. Alternatively, the extracellular potential could be manipulated to bring it within the range of the NQ-NS. These possibilities are worth exploring further, as the biological relationship between intracellular and extracellular redox potential is incompletely understood.

Use of this technology in animal models is problematic, primarily due to excessive light scattering, but it is very well suited to making measurments from *in vitro* cell culture model systems. Refinements in the types of cell culture system that is used may be made. For example, induced pluripotent stem cell (iPSC) techniques for making well-defined differentiated cells in culture is rapidly maturing, and would allow experimental questions to be asked in cells that model healthy and diseased human tissues very accurately. It would also be possible to use 3D cell culture techniques to create living models of different tissue types found in the body. This would be useful because redox potential and pH measurements performed throughout a tissue rather than in just a 2D cell culture and would give more physiologically accurate values. The fact that our NQ-NS technology is best suited to *in vitro* systems is also a strength, as it means that it can be applied to cells whose genetic state or environment is altered in ways that would be impossible in living animals. For example, transfection of small interfering RNA (siRNA) libraries for screening the involvement of candidate genes in particular processes, or treatment of cells with drugs that modify cellular signalling pathways that would be lethal if disrupted in a whole organism. This means that it can be used to answer basic biological and pathological questions directly, in a significantly more quantitative way than was possible previously, which in turn will lead to more accurate experimental conclusions. Development of additional probes for other physiological parameters is possible, and extension of the method to measurement of pH has already been achieved by others in our research group. Other parameters that could be monitored using SERS nanosensors could include ATP, oxygen, specific types of ROS/RNS or ions such as Ca^{2+}. The only limitation is finding probe molecules that exhibit specific and reversible reactions in the presence of an analyte. As mentioned

above, if future probes are sufficiently spectrally separated, multiplexed measurements of multiple parameters could be performed. This would allow correlation of these parameters, which again will be useful in developing an understanding of cellular physiology.

In summary, the work in this thesis has successfully extended previous work into a pathologically relevant cell line, and established methods for applying it to meaningful biological questions. I have begun by validating the technique in a well characterised pathological model, and it will be exciting in the future to watch how the technique is deployed to improve our understanding of important diseases whose pathology remains to be understood.

Bibliography

[1] Fisher, A. C. *Electrode Dynamics* (Oxford University Press, 1996).

[2] Schafer, F. & Buettner, G. Redox environment of the cell as viewed through the redox state of the glutathione disulfide/glutathione couple. *Free Radical Biology & Medicine* **30**, 1191–1212 (2001).

[3] Menon, S. G. & Goswami, P. C. A redox cycle within the cell cycle: ring in the old with the new. *Oncogene* **26**, 1101–1109 (2007).

[4] Kemp, M., Go, Y.-M. & Jones, D. P. Nonequilibrium thermodynamics of thiol/disulfide redox systems: a perspective on redox systems biology. *Free Radical Biology & Medicine* **44**, 921–937 (2008).

[5] Berg, J. M., Tymoczko, J. L. & Stryer, L. *Biochemistry* (W.H. Freeman and Company, New York, 2007), 6 edn.

[6] Turrens, J. F., Freeman, B. A., Levitt, J. G. & Crapo, J. D. The effect of hyperoxia on superoxide production by lung submitochondrial particles. *Archives of Biochemistry and Biophysics* **217**, 401–410 (1982).

[7] Seo, B. B., Marella, M., Yagi, T. & Matsuno-Yagi, A. The single subunit NADH dehydrogenase reduces generation of reactive oxygen species from complex I. *FEBS Letters* **580**, 6105–6108 (2006).

[8] Korshunov, S. S., Skulachev, V. P. & Starkov, A. A. High protonic potential actuates a mechanism of production of reactive oxygen species in mitochondria. *FEBS Letters* **416**, 15–18 (1997).

[9] Lambert, A. J. & Brand, M. D. Superoxide production by NADH:ubiquinone oxidoreductase (complex I) depends on the pH gradient across the mitochondrial inner membrane. *The Biochemical Journal* **382**, 511–517 (2004).

[10] Babior, B. M., Kipnes, R. S. & Curnutte, J. T. Biological defense mechanisms. The production by leukocytes of superoxide, a potential bactericidal agent. *The Journal of Clinical Investigation* **52**, 741–744 (1973).

[11] Bedard, K. & Krause, K.-H. The NOX family of ROS-generating NADPH oxidases: physiology and pathophysiology. *Physiological Reviews* **87**, 245–313 (2007).

[12] Brown, D. I. & Griendling, K. K. Nox proteins in signal transduction. *Free Radical Biology & Medicine* **47**, 1239–1253 (2009).

[13] Pollard, M. G., Travers, K. J. & Weissman, J. S. Ero1p: a novel and ubiquitous protein with an essential role in oxidative protein folding in the endoplasmic reticulum. *Molecular Cell* **1**, 171–182 (1998).

[14] Frand, A. R. & Kaiser, C. A. Ero1p oxidizes protein disulfide isomerase in a pathway for disulfide bond formation in the endoplasmic reticulum. *Molecular Cell* **4**, 469–477 (1999).

[15] Tu, B. P. & Weissman, J. S. The FAD-and O 2-dependent reaction cycle of Ero1-mediated oxidative protein folding in the endoplasmic reticulum. *Molecular Cell* **10**, 983–994 (2002).

[16] Gross, E. *et al.* Generating disulfides enzymatically: reaction products and electron acceptors of the endoplasmic reticulum thiol oxidase Ero1p. *Proceedings of the National Academy of Sciences of the United States of America* **103**, 299–304 (2006).

[17] Fridovich, I. Superoxide radical and superoxide dismutases. *Annual Review of Biochemistry* **64**, 97–112 (1995).

[18] Nordberg, J. & Arnér, E. S. Reactive oxygen species, antioxidants, and the mammalian thioredoxin system. *Free Radical Biology & Medicine* **31**, 1287–1312 (2001).

[19] Mates, J. Effects of antioxidant enzymes in the molecular control of reactive oxygen species toxicology. *Toxicology* **153**, 83–104 (2000).

[20] Dröge, W. Free radicals in the physiological control of cell function. *Physiological Reviews* **82**, 47–95 (2002).

[21] MILLS, G. C. Hemoglobin catabolism. I. Glutathione peroxidase, an erythrocyte enzyme which protects hemoglobin from oxidative breakdown. *The Journal of Biological Chemistry* **229**, 189–197 (1957).

[22] Gravina, S. A. & Mieyal, J. J. Thioltransferase is a specific glutathionyl mixed-disulfide oxidoreductase. *Biochemistry* **32**, 3368–3376 (1993).

[23] Toppo, S., Flohé, L., Ursini, F. & Vanin, S. Catalytic mechanisms and specificities of glutathione peroxidases: variations of a basic scheme. *Biochimica et Biophysica Acta* **1790**, 1486–1500 (2009).

[24] Pannala, V. R., Bazil, J. N., Camara, A. K. S. & Dash, R. K. A mechanistic mathematical model for the catalytic action of glutathione peroxidase. *Free Radical Research* **48**, 487–502 (2014).

[25] Berkholz, D. S., Faber, H. R., Savvides, S. N. & Karplus, P. A. Catalytic cycle of human glutathione reductase near 1 A resolution. *Journal of Molecular Biology* **382**, 371–384 (2008).

[26] Hill, B. G. & Bhatnagar, A. Protein S-glutathiolation: redox-sensitive regulation of protein function. *Journal of Molecular and Cellular Cardiology* **52**, 559–567 (2012).

[27] Watson, W. H. *et al.* Redox potential of human thioredoxin 1 and identification of a second dithiol/disulfide motif. *The Journal of Biological Chemistry* **278**, 33408–33415 (2003).

[28] Chae, H. Z., Chung, S. J. & Rhee, S. G. Thioredoxin-dependent peroxide reductase from yeast. *The Journal of Biological Chemistry* **269**, 27670–27678 (1994).

[29] Wood, Z. A., Schröder, E., Robin Harris, J. & Poole, L. B. Structure, mechanism and regulation of peroxiredoxins. *Trends in Biochemical Sciences* **28**, 32–40 (2003).

[30] Rhee, S. G., Chae, H. Z. & Kim, K. Peroxiredoxins: a historical overview and speculative preview of novel mechanisms and emerging concepts in cell signaling. *Free Radical Biology & Medicine* **38**, 1543–1552 (2005).

[31] Arscott, L. D., Gromer, S., Schirmer, R. H., Becker, K. & Williams, C. H. The mechanism of thioredoxin reductase from human placenta is similar to the mechanisms of lipoamide dehydrogenase and glutathione reductase and is distinct from the mechanism of thioredoxin reductase from Escherichia coli. *Proceedings of the National Academy of Sciences of the United States of America* **94**, 3621–3626 (1997).

[32] Zhong, L. & Arnér, E. Structure and mechanism of mammalian thioredoxin reductase: Rhe active site is a redox-active selenolthiol/selenenylsulfide formed from the conserved cysteine-selenocysteine sequence. In *Proceedings of the National Academy of Sciences of the United States of America*, 5854–5859 (2000).

[33] Ying, W. NAD+/NADH and NADP+/NADPH in cellular functions and cell death: regulation and biological consequences. *Antioxidants & Redox Signaling* **10**, 179–206 (2008).

[34] Sies, H., Stahl, W. & Sundquist, A. R. Antioxidant functions of vitamins. *Annals New York Academy of Sciences* **30**, 7–20 (1992).

[35] Winkler, B. S., Orselli, S. M. & Rex, T. S. The redox couple between glutathione and ascorbic acid: a chemical and physiological perspective. *Free Radical Biology & Medicine* **17**, 333–349 (1994).

[36] May, J. M., Cobb, C. E., Mendiratta, S., Hill, K. E. & Burk, R. F. Reduction of the ascorbyl free radical to ascorbate by thioredoxin reductase. *The Journal of Biological Chemistry* **273**, 23039–23045 (1998).

[37] Jones, D. P. *et al.* Cysteine/cystine couple is a newly recognized node in the circuitry for biologic redox signaling and control. *The FASEB Journal* **18**, 1246–1248 (2004).

[38] May, J. M. & Qu, Z.-C. Nitric oxide-induced oxidant stress in endothelial cells: amelioration by ascorbic acid. *Archives of Biochemistry and Biophysics* **429**, 106–113 (2004).

[39] Rao, A. R., Quach, H., Smith, E., Vatassery, G. T. & Rao, R. Changes in ascorbate, glutathione and α-tocopherol concentrations in the brain regions during normal development and moderate hypoglycemia in rats. *Neuroscience letters* **568**, 67–71 (2014).

[40] Arrigo, A. P. Gene expression and the thiol redox state. *Free Radical Biology & Medicine* **27**, 936–944 (1999).

[41] Go, Y.-M. *et al.* Selective protection of nuclear thioredoxin-1 and glutathione redox systems against oxidation during glucose and glutamine deficiency in human colonic epithelial cells. *Free Radical Biology & Medicine* **42**, 363–370 (2007).

[42] Dardalhon, M. *et al.* Redox-sensitive YFP sensors monitor dynamic nuclear and cytosolic glutathione redox changes. *Free Radical Biology & Medicine* **52**, 2254–2265 (2012).

[43] Dimauro, I., Pearson, T., Caporossi, D. & Jackson, M. J. In vitro susceptibility of thioredoxins and glutathione to redox modification and aging-related changes in skeletal muscle. *Free Radical Biology & Medicine* **53**, 2017–2027 (2012).

[44] Go, Y.-M. & Jones, D. P. Redox compartmentalization in eukaryotic cells. *Biochimica et Biophysica Acta* **1780**, 1273–1290 (2008).

[45] Hu, J., Dong, L. & Outten, C. E. The redox environment in the mitochondrial intermembrane space is maintained separately from the cytosol and matrix. *The Journal of Biological Chemistry* **283**, 29126–29134 (2008).

[46] Waypa, G. B. *et al.* Hypoxia triggers subcellular compartmental redox signaling in vascular smooth muscle cells. *Circulation Research* **106**, 526–535 (2010).

[47] Kojer, K. *et al.* Glutathione redox potential in the mitochondrial intermembrane space is linked to the cytosol and impacts the Mia40 redox state. *The EMBO Journal* **31**, 3169–3182 (2012).

[48] HALVEY, P. J. *et al.* Compartmental oxidation of thiol-disulphide redox couples during epidermal growth factor signalling. *The Biochemical Journal* **386**, 215–219 (2005).

[49] Appenzeller-Herzog, C. Glutathione- and non-glutathione-based oxidant control in the endoplasmic reticulum. *Journal of Cell Science* **124**, 847–855 (2011).

[50] Delic, M., Mattanovich, D. & Gasser, B. Monitoring intracellular redox conditions in the endoplasmic reticulum of living yeasts. *FEMS Microbiology Letters* **306**, 61–66 (2010).

[51] van Lith, M., Tiwari, S., Pediani, J., Milligan, G. & Bulleid, N. J. Real-time monitoring of redox changes in the mammalian endoplasmic reticulum. *Journal of Cell Science* **124**, 2349–2356 (2011).

[52] Chiu, J. & Dawes, I. W. Redox control of cell proliferation. *Trends in Cell Biology* **22**, 592–601 (2012).

[53] Janssen-Heininger, Y. M. W. *et al.* Redox-based regulation of signal transduction: principles, pitfalls, and promises. *Free Radical Biology & Medicine* **45**, 1–17 (2008).

[54] Winterbourn, C. C. Reconciling the chemistry and biology of reactive oxygen species. *Nature Chemical Biology* **4**, 278–286 (2008).

[55] Dickinson, B. C. & Chang, C. J. Chemistry and biology of reactive oxygen species in signaling or stress responses. *Nature Chemical Biology* **7**, 504–511 (2011).

[56] Finkel, T. Signal transduction by reactive oxygen species. *The Journal of Cell Biology* **194**, 7–15 (2011).

[57] Wood, Z. A., Poole, L. B. & Karplus, P. A. Peroxiredoxin evolution and the regulation of hydrogen peroxide signaling. *Science* **300**, 650–653 (2003).

[58] Salsbury, F. R., Knutson, S. T., Poole, L. B. & Fetrow, J. S. Functional site profiling and electrostatic analysis of cysteines modifiable to cysteine sulfenic acid. *Protein Science* **17**, 299–312 (2008).

[59] Winterbourn, C. & Metodiewa, D. Reactivity of biologically important thiol compounds with superoxide and hydrogen peroxide. *Free Radical Biology & Medicine* **27**, 322–328 (1999).

[60] Lohse, D. L., Denu, J. M., Santoro, N. & Dixon, J. E. Roles of aspartic acid-181 and serine-222 in intermediate formation and hydrolysis of the mammalian protein-tyrosine-phosphatase PTP1. *Biochemistry* **36**, 4568–4575 (1997).

[61] Denu, J. M., Zhou, G., Guo, Y. & Dixon, J. E. The catalytic role of aspartic acid-92 in the human dual-specific protein-tyrosine-phosphatase vaccinia h1-related. *Biochemistry* **34**, 3396–3403 (1995).

[62] Lee, S. R., Kwon, K. S., Kim, S. R. & Rhee, S. G. Reversible inactivation of protein-tyrosine phosphatase 1B in A431 cells stimulated with epidermal growth factor. *The Journal of Biological Chemistry* **273**, 15366–15372 (1998).

[63] Salmeen, A. *et al.* Redox regulation of protein tyrosine phosphatase 1B involves a sulphenyl-amide intermediate. *Nature* **423**, 769–773 (2003).

[64] Denu, J. M. & Tanner, K. G. Specific and reversible inactivation of protein tyrosine phosphatases by hydrogen peroxide: evidence for a sulfenic acid intermediate and implications for redox regulation. *Biochemistry* **37**, 5633–5642 (1998).

[65] Barrett, W. C. *et al.* Regulation of PTP1B via glutathionylation of the active site cysteine 215. *Biochemistry* **38**, 6699–6705 (1999).

[66] Sullivan, D. M., Wehr, N. B., Fergusson, M. M., Levine, R. L. & Finkel, T. Identification of oxidant-sensitive proteins: TNF-alpha induces protein glutathiolation. *Biochemistry* **39**, 11121–11128 (2000).

[67] Peskin, A. V. *et al.* The high reactivity of peroxiredoxin 2 with H(2)O(2) is not reflected in its reaction with other oxidants and thiol reagents. *The Journal of Biological Chemistry* **282**, 11885–11892 (2007).

[68] Findlay, V. J. *et al.* A novel role for human sulfiredoxin in the reversal of glutathionylation. *Cancer Research* **66**, 6800–6806 (2006).

[69] Peltoniemi, M. J., Karala, A.-R., Jurvansuu, J. K., Kinnula, V. L. & Ruddock, L. W. Insights into deglutathionylation reactions. Different intermediates in the glutaredoxin and protein disulfide isomerase catalyzed reactions are defined by the gamma-linkage present in glutathione. *The Journal of Biological Chemistry* **281**, 33107–33114 (2006).

[70] Schwertassek, U., Haque, A., Krishnan, N. & Greiner, R. Reactivation of oxidized PTP1B and PTEN by thioredoxin 1. *The FEBS Journal* **281**, 3545–3558 (2014).

[71] Peters, G. H., Frimurer, T. M. & Olsen, O. H. Electrostatic evaluation of the signature motif (H/V) CX5R (S/T) in protein-tyrosine phosphatases. *Biochemistry* **37**, 5383–5393 (1998).

[72] Tonks, N. K. Protein tyrosine phosphatases: from genes, to function, to disease. *Nature Reviews Molecular Cell Biology* **7**, 833–846 (2006).

[73] Östman, A., Frijhoff, J., Sandin, Å. & Böhmer, F.-D. Regulation of protein tyrosine phosphatases by reversible oxidation. *Journal of Biochemistry* **150**, 345–356 (2011).

[74] Itoh, K. *et al.* Keap1 represses nuclear activation of antioxidant responsive elements by Nrf2 through binding to the amino-terminal Neh2 domain. *Genes & Development* **13**, 76–86 (1999).

[75] Zhang, D. D. & Hannink, M. Distinct cysteine residues in Keap1 are required for Keap1-dependent ubiquitination of Nrf2 and for stabilization of Nrf2 by chemopreventive agents and oxidative stress. *Molecular and Cellular Biology* **23**, 8137–8151 (2003).

[76] Thimmulappa, R. K. *et al.* Identification of Nrf2-regulated genes induced by the chemopreventive agent sulforaphane by oligonucleotide microarray. *Cancer Research* **62**, 5196–5203 (2002).

[77] Brigelius-Flohe, R. & Flohe, L. Basic principles and emerging concepts in the redox control of transcription factors. *Antioxidants & Redox Signaling* **15**, 2335–2381 (2011).

[78] Toledano, M. B., Ghosh, D., Trinh, F. & Leonard, W. J. N-terminal DNA-binding domains contribute to differential DNA-binding specificities of NF-kappa B p50 and p65. *Molecular and Cellular Biology* **13**, 852–860 (1993).

[79] Pineda-Molina, E. *et al.* Glutathionylation of the p50 subunit of NF-kappaB: a mechanism for redox-induced inhibition of DNA binding. *Biochemistry* **40**, 14134–14142 (2001).

[80] Matthews, J. R., Botting, C. H., Panico, M., Morris, H. R. & Hay, R. T. Inhibition of NF-kappaB DNA binding by nitric oxide. *Nucleic acids research* **24**, 2236–2242 (1996).

[81] Kelleher, Z. T., Matsumoto, A., Stamler, J. S. & Marshall, H. E. NOS2 regulation of NF-kappaB by S-nitrosylation of p65. *The Journal of Biological Chemistry* **282**, 30667–30672 (2007).

[82] Matthews, J. R., Wakasugi, N., Virelizier, J. L., Yodoi, J. & Hay, R. T. Thioredoxin regulates the DNA binding activity of NF-kappa B by reduction of a disulphide bond involving cysteine 62. *Nucleic acids research* **20**, 3821–3830 (1992).

[83] Hayashi, T., Ueno, Y. & Okamoto, T. Oxidoreductive regulation of nuclear factor kappa B. Involvement of a cellular reducing catalyst thioredoxin. *The Journal of Biological Chemistry* **268**, 11380–11388 (1993).

[84] Hirota, K. *et al.* Distinct roles of thioredoxin in the cytoplasm and in the nucleus. A two-step mechanism of redox regulation of transcription factor NF-kappaB. *The Journal of Biological Chemistry* **274**, 27891–27897 (1999).

[85] Guttridge, D. C., Albanese, C., Reuther, J. Y., Pestell, R. G. & Baldwin, A. S. NF-κB Controls Cell Growth and Differentiation through Transcriptional Regulation of Cyclin D1. *Molecular and Cellular Biology* **19**, 5785–5799 (1999).

[86] Menon, S. G. *et al.* Redox regulation of the G1 to S phase transition in the mouse embryo fibroblast cell cycle. *Cancer Research* **63**, 2109–2117 (2003).

[87] Wang, H. P., Schafer, F. & Goswami, P. C. Phospholipid hydroperoxide glutathione peroxidase induces a delay in G1 of the cell cycle. *Free Radical Research* **37**, 621–630 (2003).

[88] Conour, J. E., Graham, W. V. & Gaskins, H. R. A combined in vitro/bioinformatic investigation of redox regulatory mechanisms governing cell cycle progression. *Physiological Genomics* **18**, 196–205 (2004).

[89] Mallikarjun, V., Clarke, D. J. & Campbell, C. J. Cellular redox potential and the biomolecular electrochemical series: a systems hypothesis. *Free Radical Biology & Medicine* **53**, 280–288 (2012).

[90] Banerjee, R. Redox outside the box: linking extracellular redox remodeling with intracellular redox metabolism. *The Journal of Biological Chemistry* **287**, 4397–4402 (2012).

[91] Jones, D. P. *et al.* Redox state of glutathione in human plasma. *Free Radical Biology & Medicine* **28**, 625–635 (2000).

[92] Jones, D. P., Mody, V. C., Carlson, J. L., Lynn, M. J. & Sternberg, P. Redox analysis of human plasma allows separation of pro-oxidant events of aging from decline in antioxidant defenses. *Free Radical Biology & Medicine* **33**, 1290–1300 (2002).

[93] Ramirez, A. *et al.* Extracellular cysteine/cystine redox potential controls lung fibroblast proliferation and matrix expression through upregulation of transforming growth factor-beta. *American Journal of Physiology-Lung Cellular and Molecular Physiology* **293**, L972–81 (2007).

[94] Go, Y.-M. & Jones, D. P. Intracellular proatherogenic events and cell adhesion modulated by extracellular thiol/disulfide redox state. *Circulation* **111**, 2973–2980 (2005).

[95] Choi, Y., Chen, H. V. & Lipton, S. A. Three pairs of cysteine residues mediate both redox and zn2+ modulation of the nmda receptor. *The Journal of Neuroscience* **21**, 392–400 (2001).

[96] Nkabyo, Y. S., Go, Y.-M., Ziegler, T. R. & Jones, D. P. Extracellular cysteine/cystine redox regulates the p44/p42 MAPK pathway by metalloproteinase-dependent epidermal growth factor receptor signaling. *American Journal of Physiology-Gastrointestinal and Liver Physiology* **289**, G70–8 (2005).

[97] Xu, S. Z. *et al.* TRPC channel activation by extracellular thioredoxin. *Nature* **451**, 69–72 (2008).

[98] Zhang, M.-M. *et al.* Probing the Redox States of Sodium Channel Cysteines at the Binding Site of μO§-Conotoxin GVIIJ. *Biochemistry* **54**, 3911–3920 (2015).

[99] Angelini, G. *et al.* Antigen-presenting dendritic cells provide the reducing extracellular microenvironment required for T lymphocyte activation. *Proceedings of the National Academy of Sciences of the United States of America* **99**, 1491–1496 (2002).

[100] Messina, J. P. & Lawrence, D. A. Cell cycle progression of glutathione-depleted human peripheral blood mononuclear cells is inhibited at S phase. *Journal of Immunology* **143**, 1974–1981 (1989).

[101] Suthanthiran, M., Anderson, M. E., Sharma, V. K. & Meister, A. Glutathione regulates activation-dependent DNA synthesis in highly purified normal human T lymphocytes stimulated via the CD2 and CD3 antigens. *Proceedings of the National Academy of Sciences of the United States of America* **87**, 3343–3347 (1990).

[102] Yan, Z., Garg, S. K., Kipnis, J. & Banerjee, R. Extracellular redox modulation by regulatory T cells. *Nature Chemical Biology* **5**, 721–723 (2009).

[103] Sagara, J. I., Miura, K. & Bannai, S. Maintenance of neuronal glutathione by glial cells. *Journal of Neurochemistry* **61**, 1672–1676 (1993).

[104] Dringen, R. & Gutterer, J. M. Glutathione metabolism in brain. *European Journal of Biochemistry* **267**, 4912–4916 (2000).

[105] Berger, U. V. & Hediger, M. A. The vitamin C transporter SVCT2 is expressed by astrocytes in culture but not in situ. *Neuroreport* **11**, 1395–1399 (2000).

[106] Meister, A. Glutathione-ascorbic acid antioxidant system in animals. *Journal of Biological Chemistry* **269**, 9397–9400 (1994).

[107] Andersen, J. K. Oxidative stress in neurodegeneration: cause or consequence? *Nature Reviews Neuroscience* **10 Suppl**, S18–25 (2004).

[108] Valko, M. *et al.* Free radicals and antioxidants in normal physiological functions and human disease. *The International Journal of Biochemistry & Cell Biology* **39**, 44–84 (2007).

[109] Iyer, S. S. *et al.* Cysteine redox potential determines pro-inflammatory IL-1beta levels. *PLoS One* **4**, e5017 (2009).

[110] Ghosh, D. & Brewer, G. J. External cys/cySS redox state modification controls the intracellular redox state and neurodegeneration via Akt in aging and Alzheimer's disease mouse model neurons. *Journal of Alzheimer's Disease* **42**, 313–324 (2014).

[111] Aoyama, K. & Nakaki, T. Impaired glutathione synthesis in neurodegeneration. *International Journal of Molecular Sciences* **14**, 21021–21044 (2013).

[112] Gherghel, D., Mroczkowska, S. & Qin, L. Reduction in Blood Glutathione Levels Occurs Similarly in Patients With Primary-Open Angle or Normal Tension Glaucoma. *Investigative Opthalmology & Visual Science* **54**, 3333–3339 (2013).

[113] Yuki, K., Murat, D., Kimura, I. & Ohtake, Y. Reduced-serum vitamin C and increased uric acid levels in normal-tension glaucoma. *Graefe's Archive for Clinical and Experimental Ophthalmology* **248**, 243–248 (2010).

[114] Lim, J. C. *et al.* Irreversible oxidation of the active-site cysteine of peroxiredoxin to cysteine sulfonic acid for enhanced molecular chaperone activity. *The Journal of Biological Chemistry* **283**, 28873–28880 (2008).

[115] Maity-Kumar, G., Thal, D. R., Baumann, B., Scharffetter-Kochanek, K. & Wirth, T. Neuronal redox imbalance results in altered energy homeostasis and early postnatal lethality. *The FASEB Journal* **29**, 2843–2858 (2015).

[116] Baldus, S. *et al.* Myeloperoxidase enhances nitric oxide catabolism during myocardial ischemia and reperfusion. *Free Radical Biology & Medicine* **37**, 902–911 (2004).

[117] Brennan, M.-L. *et al.* Prognostic value of myeloperoxidase in patients with chest pain. *The New England Journal of Medicine* **349**, 1595–1604 (2003).

[118] Vissers, M. & Thomas, C. Hypochlorous acid disrupts the adhesive properties of subendothelial matrix. *Free Radical Biology & Medicine* **23**, 401–411 (1997).

[119] Rees, M. D. *et al.* Targeted subendothelial matrix oxidation by myeloperoxidase triggers myosin II-dependent de-adhesion and alters signaling in endothelial cells. *Free Radical Biology & Medicine* **53**, 2344–2356 (2012).

[120] Semenza, G. L. Hypoxia-inducible factors in physiology and medicine. *Cell* **148**, 399–408 (2012).

[121] Majmundar, A. J., Wong, W. J. & Simon, M. C. Hypoxia-inducible factors and the response to hypoxic stress. *Molecular Cell* **40**, 294–309 (2010).

[122] Jiang, J., Auchinvole, C., Fisher, K. & Campbell, C. J. Quantitative measurement of redox potential in hypoxic cells using SERS nanosensors. *Nanoscale* **6**, 12104–12110 (2014).

[123] Kuppusamy, P. *et al.* Noninvasive imaging of tumor redox status and its modification by tissue glutathione levels. *Cancer Research* **62**, 307–312 (2002).

[124] Bobko, A. A. *et al.* In vivo monitoring of pH, redox status, and glutathione using L-band EPR for assessment of therapeutic effectiveness in solid tumors. *Magnetic Resonance in Medicine* **67**, 1827–1836 (2012).

[125] Hamanaka, R. B. & Chandel, N. S. Mitochondrial reactive oxygen species regulate hypoxic signaling. *Current Opinion in Cell Biology* **21**, 894–899 (2009).

[126] Lee, S.-R. *et al.* Reversible inactivation of the tumor suppressor PTEN by H2O2. *The Journal of Biological Chemistry* **277**, 20336–20342 (2002).

[127] Lou, Y. W., Chen, Y. Y., Hsu, S. F., Chen, R. K. & Lee, C. L. Redox regulation of the protein tyrosine phosphatase PTP1B in cancer cells. *The FEBS Journal* **275**, 69–88 (2008).

[128] Yuan, T. L. & Cantley, L. C. PI3K pathway alterations in cancer: variations on a theme. *Oncogene* **27**, 5497–5510 (2008).

[129] Waypa, G. B. *et al.* Superoxide generated at mitochondrial complex III triggers acute responses to hypoxia in the pulmonary circulation. *American Journal of Respiratory and Critical Care Medicine* **187**, 424–432 (2013).

[130] Yuan, G. *et al.* Hypoxia-inducible factor 1 mediates increased expression of NADPH oxidase-2 in response to intermittent hypoxia. *Journal of Cellular Physiology* **226**, 2925–2933 (2011).

[131] DeNicola, G. M. *et al.* Oncogene-induced Nrf2 transcription promotes ROS detoxification and tumorigenesis. *Nature* **475**, 106–109 (2011).

[132] Bunt, G. & Wouters, F. S. Visualization of molecular activities inside living cells with fluorescent labels. *International Review of Cytology* **237**, 205–277 (2004).

[133] Ray, A., Koo Lee, Y.-E., Epstein, T., Kim, G. & Kopelman, R. Two-photon nano-PEBBLE sensors: subcellular pH measurements. *The Analyst* **136**, 3616–3622 (2011).

[134] Albertazzi, L. *et al.* Synthesis, cellular delivery and in vivo application of dendrimer-based pH sensors. *Journal of Cisualized Experiments : JoVE* **79**, e50545 (2013).

[135] Wencel, D., Abel, T. & McDonagh, C. Optical Chemical pH Sensors. *Analytical Chemistry* **86**, 15–29 (2014).

[136] Day, R. N. & Davidson, M. W. The fluorescent protein palette: tools for cellular imaging. *Chemical Society Reviews* **38**, 2887–2921 (2009).

[137] Xia, Z. & Rao, J. Biosensing and imaging based on bioluminescence resonance energy transfer. *Current Opinion in Biotechnology* **20**, 37–44 (2009).

[138] Zhang, Y., Xie, Q., Robertson, J. B. & Johnson, C. H. pHlash: a new genetically encoded and ratiometric luminescence sensor of intracellular pH. *PLoS One* **7**, e43072 (2012).

[139] Saito, K. *et al.* Auto-luminescent genetically-encoded ratiometric indicator for real-time Ca2+ imaging at the single cell level. *PLoS One* **5**, e9935 (2010).

[140] De, A., Jasani, A., Arora, R. & Gambhir, S. S. Evolution of BRET Biosensors from Live Cell to Tissue-Scale In vivo Imaging. *Frontiers in Endocrinology* **4**, 131 (2013).

[141] Chen, C. Y. & Chen, C. T. Reaction-Based and Single Fluorescent Emitter Decorated Ratiometric Nanoprobe to Detect Hydrogen Peroxide. *Chemistry (Weinheim an der Bergstrasse, Germany)* **19**, 16050–16057 (2013).

[142] Ko, S.-K., Yang, Y.-K., Tae, J. & Shin, I. In vivo monitoring of mercury ions using a rhodamine-based molecular probe. *Journal of the American Chemical Society* **128**, 14150–14155 (2006).

[143] Nakai, J., Ohkura, M. & Imoto, K. A high signal-to-noise Ca2+ probe composed of a single green fluorescent protein. *Nature Biotechnology* **19**, 137–141 (2001).

[144] Benčina, M. Illumination of the spatial order of intracellular pH by genetically encoded pH-sensitive sensors. *Sensors* **13**, 16736–16758 (2013).

[145] D'Autréaux, B. & Toledano, M. B. ROS as signalling molecules: mechanisms that generate specificity in ROS homeostasis. *Nature Reviews Molecular Cell Biology* **8**, 813–824 (2007).

[146] Bryan, N. S., Bian, K. & Murad, F. Discovery of the nitric oxide signaling pathway and targets for drug development. *Frontiers in Bioscience (Landmark edition)* **14**, 1–18 (2009).

[147] Harrison, J. E. & Schultz, J. Studies on the chlorinating activity of myeloperoxidase. *The Journal of Biological Chemistry* **251**, 1371–1374 (1976).

[148] Klebanoff, S. J. Myeloperoxidase: friend and foe. *Journal of Leukocyte Biology* **77**, 598–625 (2005).

[149] Radi, R. Peroxynitrite, a stealthy biological oxidant. *The Journal of Biological Chemistry* **288**, 26464–26472 (2013).

[150] Tian, J. *et al.* A highly selective, cell-permeable fluorescent nanoprobe for ratiometric detection and imaging of peroxynitrite in living cells. *Chemistry (Weinheim an der Bergstrasse, Germany)* **17**, 6626–6634 (2011).

[151] Hanahan, D. & Weinberg, R. A. Hallmarks of Cancer: The Next Generation. *Cell* **144**, 646–674 (2011).

[152] Zackrisson, S., van de Ven, S. M. W. Y. & Gambhir, S. S. Light in and sound out: emerging translational strategies for photoacoustic imaging. *Cancer Research* **74**, 979–1004 (2014).

[153] Pu, K., Shuhendler, A. J., Jokerst, J. V. & Mei, J. Semiconducting polymer nanoparticles as photoacoustic molecular imaging probes in living mice. *Nature* **9**, 233–239 (2014).

[154] Zhuang, M., Ding, C., Zhu, A. & Tian, Y. Ratiometric fluorescence probe for monitoring hydroxyl radical in live cells based on gold nanoclusters. *Analytical Chemistry* **86**, 1829–1836 (2014).

[155] Dooley, C. T. *et al.* Imaging dynamic redox changes in mammalian cells with green fluorescent protein indicators. *The Journal of Biological Chemistry* **279**, 22284–22293 (2004).

[156] Meyer, A. J. *et al.* Redox-sensitive GFP in Arabidopsis thaliana is a quantitative biosensor for the redox potential of the cellular glutathione redox buffer. *Plant Journal* **52**, 973–986 (2007).

[157] Morgan, B., Sobotta, M. C. & Dick, T. P. Measuring E(GSH) and H2O2 with roGFP2-based redox probes. *Free Radical Biology & Medicine* **51**, 1943–1951 (2011).

[158] Schickinger, S. *et al.* Nanosecond ratio imaging of redox states in tumor cell spheroids using light sheet-based fluorescence microscopy. *Journal of Biomedical Optics* **18**, 126007 (2013).

[159] Roma, L. P. *et al.* Dynamic measurements of mitochondrial hydrogen peroxide concentration and glutathione redox state in rat pancreatic β-cells using ratiometric fluorescent proteins: confounding effects of pH with HyPer but not roGFP1. *The Biochemical Journal* **441**, 971–978 (2012).

[160] Niu, L.-Y. *et al.* BODIPY-based ratiometric fluorescent sensor for highly selective detection of glutathione over cysteine and homocysteine. *Journal of the American Chemical Society* **134**, 18928–18931 (2012).

[161] Zhu, B., Guo, B., Zhao, Y., Zhang, B. & Du, B. A highly sensitive ratiometric fluorescent probe with a large emission shift for imaging endogenous cysteine in living cells. *Biosensors & Bioelectronics* **55**, 72–75 (2014).

[162] Lv, H. *et al.* Native chemical ligation combined with spirocyclization of benzopyrylium dyes for the ratiometric and selective fluorescence detection of cysteine and homocysteine. *Analytical Chemistry* **86**, 1800–1807 (2014).

[163] Auchinvole, C. A. R. *et al.* Monitoring intracellular redox potential changes using SERS nanosensors. *ACS Nano* **6**, 888–896 (2012).

[164] Bantz, K. C. *et al.* Recent progress in SERS biosensing. *Physical Chemistry Chemical Physics* **13**, 11551–11567 (2011).

[165] Smith, E. & Dent, G. *Modern Raman Spectroscopy*. A Practical Approach (John Wiley & Sons, 2013).

[166] McCreery, R. L. *Raman Spectroscopy for Chemical Analysis* (Wiley-Interscience, 2000).

[167] Kneipp, J., Kneipp, H. & Kneipp, K. SERS–a single-molecule and nanoscale tool for bioanalytics. *Chemical Society Reviews* **37**, 1052–1060 (2008).

[168] Fleischmann, M., Hendra, P. J. & McQuillan, A. J. Raman spectra of pyridine adsorbed at a silver electrode. *Chemical Physics Letters* **26**, 163–166 (1974).

[169] Jeanmaire, D. L. & Van Duyne, R. P. Surface Raman spectroelectrochemistry: Part I. Heterocyclic, aromatic, and aliphatic amines adsorbed on the anodized silver electrode. *Journal of Electroanalytical Chemistry* **84**, 1–20 (1977).

[170] Kneipp, J., Kneipp, H., Wittig, B. & Kneipp, K. Novel optical nanosensors for probing and imaging live cells. *Nanomedicine : Nanotechnology, Biology, and Medicine* **6**, 214–226 (2010).

[171] Willets, K. A. Surface-enhanced Raman scattering (SERS) for probing internal cellular structure and dynamics. *Analytical and Bioanalytical Chemistry* **394**, 85–94 (2009).

[172] Lombardi, J. R. & Birke, R. L. A unified view of surface-enhanced Raman scattering. *Accounts of Chemical Research* **42**, 734–742 (2009).

[173] Chourpa, I., Lei, F. H., Dubois, P., Manfait, M. & Sockalingum, G. D. Intracellular applications of analytical SERS spectroscopy and multispectral imaging. *Chemical Society Reviews* **37**, 993–1000 (2008).

[174] Kneipp, K., Kneipp, H., Itzkan, I., Dasari, R. R. & Feld, M. S. Surface-enhanced Raman scattering and biophysics. *Journal of Physics: Condensed Matter* **14**, R597 (2002).

[175] Ochsenkuhn, M. A., Jess, P. R. T., Stoquert, H., Dholakia, K. & Campbell, C. J. Nanoshells for Surface-Enhanced Raman Spectroscopy in Eukaryotic Cells: Cellular Response and Sensor Development. *ACS Nano* **3**, 3613–3621 (2009).

[176] Jeon, S.-M., Chandel, N. S. & Hay, N. AMPK regulates NADPH homeostasis to promote tumour cell survival during energy stress. *Nature* **485**, 661–665 (2012).

[177] Kim, T. R., Cho, E. W., Paik, S. G. & Kim, I. G. Hypoxia-induced SM22 alpha in A549 cells activates the IGF1R/PI3K/Akt pathway, conferring cellular resistance against chemo- and radiation therapy. *FEBS Letters* **586**, 303–309 (2012).

[178] Standiford, T. J. *et al.* Interleukin-8 gene expression by a pulmonary epithelial cell line. A model for cytokine networks in the lung. *The Journal of Clinical Investigation* **86**, 1945–1953 (1990).

[179] Brown, D., Wilson, M., MacNee, W., Stone, V. & Donaldson, K. Size-dependent proinflammatory effects of ultrafine polystyrene particles: A role for surface area and oxidative stress in the enhanced activity of ultrafines. *Toxicology and Applied Pharmacology* **175**, 191–199 (2001).

[180] Simon-Deckers, A. *et al.* In vitro investigation of oxide nanoparticle and carbon nanotube toxicity and intracellular accumulation in A549 human pneumocytes. *Toxicology* **253**, 137–146 (2008).

[181] dos Santos, T., Varela, J., Lynch, I., Salvati, A. & Dawson, K. A. Effects of Transport Inhibitors on the Cellular Uptake of Carboxylated Polystyrene Nanoparticles in Different Cell Lines. *PLoS One* **6**, e24438 (2011).

[182] Chuang, S.-M. *et al.* Extensive evaluations of the cytotoxic effects of gold nanoparticles. *Biochimica et Biophysica Acta* **1830**, 4960–4973 (2013).

[183] Tiseo, M. *et al.* FGFR as potential target in the treatment of squamous non small cell lung cancer. *Cancer Treatment Reviews* **41**, 527–539 (2015).

[184] Pocock, G. & Richards, C. D. *Human Physiology: The Basis of Medicine*. Oxford Core Texts (Oxford University Press, 2006), third edn.

[185] Auchinvole, C. A. R. *SERS nanosensors for intracellular redox potential measurements*. Ph.D. thesis, University of Edinburgh (2012).

[186] Khlebtsov, N. G. Determination of size and concentration of gold nanoparticles from extinction spectra. *Analytical Chemistry* **80**, 6620–6625 (2008).

[187] Edinger, A. L. & Thompson, C. B. Death by design: apoptosis, necrosis and autophagy. *Current Opinion in Cell Biology* **16**, 663–669 (2004).

[188] Denecker, G. *et al.* Death receptor-induced apoptotic and necrotic cell death: differential role of caspases and mitochondria. *Cell Death and Differentiation* **8**, 829–840 (2001).

[189] Al-Nasiry, S., Geusens, N., Hanssens, M., Luyten, C. & Pijnenborg, R. The use of Alamar Blue assay for quantitative analysis of viability, migration and invasion of choriocarcinoma cells. *Human Reproduction* **22**, 1304–1309 (2007).

[190] Lévy, R., Shaheen, U., Cesbron, Y. & Sée, V. Gold nanoparticles delivery in mammalian live cells: a critical review. *Nano reviews* **1**, 4889 (2010).

[191] Khlebtsov, N. & Dykman, L. Biodistribution and toxicity of engineered gold nanoparticles: a review of in vitro and in vivo studies. *Chemical Society Reviews* **40**, 1647–1671 (2011).

[192] He, H., Xie, C. & Ren, J. Nonbleaching fluorescence of gold nanoparticles and its applications in cancer cell imaging. *Analytical Chemistry* **80**, 5951–5957 (2008).

[193] Kong, K. *et al.* Diagnosis of tumors during tissue-conserving surgery with integrated autofluorescence and Raman scattering microscopy. *Proceedings of the National Academy of Sciences of the United States of America* **110**, 15189–15194 (2013).

[194] Kong, K. *et al.* Towards intra-operative diagnosis of tumours during breast conserving surgery by selective-sampling Raman micro-spectroscopy. *Physics in medicine and biology* **59**, 6141–6152 (2014).

[195] Takamori, S. *et al.* Optimization of multimodal spectral imaging for assessment of resection margins during Mohs micrographic surgery for basal cell carcinoma. *Biomedical optics express* **6**, 98–111 (2015).

[196] Maddams, W. F. The scope and limitations of curve fitting. *Applied Spectroscopy* **34**, 245–267 (1980).

[197] Robinson, J. W., EM, S. F. & Frame, G. M., II. *Undergraduate Instrumental Analysis* (Marcel Dekker, 2005), sixth edn.

[198] Zhao, J., Lui, H., McLean, D. I. & Zeng, H. Automated autofluorescence background subtraction algorithm for biomedical Raman spectroscopy. *Applied Spectroscopy* **61**, 1225–1232 (2007).

[199] Beattie, J. R. Optimising reproducibility in low quality signals without smoothing; an alternative paradigm for signal processing. *Journal of Raman Spectroscopy* **42**, 1419–1427 (2011).

[200] Schulze, H. G., Foist, R. B., Okuda, K., Ivanov, A. & Turner, R. F. B. A model-free, fully automated baseline-removal method for Raman spectra. *Applied Spectroscopy* **65**, 75–84 (2011).

[201] Lau, S. K. *et al.* A Bayesian Whittaker-Henderson smoother for general-purpose and sample-based spectral baseline estimation and peak extraction. *Journal of Raman Spectroscopy* **43**, 1299–1305 (2012).

[202] Sharma, B., Frontiera, R. R., Henry, A.-I., Ringe, E. & Van Duyne, R. P. SERS: materials, applications, and the future. *Materials Today* **15**, 16–25 (2012).

[203] Mosier-Boss, P. A. & Lieberman, S. H. Fluorescence rejection in Raman spectroscopy by shifted-spectra, edge detection, and FFT filtering techniques. *Applied Spectroscopy* **49**, 630–638 (1995).

[204] Bishnoi, S. W. *et al.* All-optical nanoscale pH meter. *Nano Letters* **6**, 1687–1692 (2006).

[205] Kneipp, J., Kneipp, H., Wittig, B. & Kneipp, K. One- and two-photon excited optical ph probing for cells using surface-enhanced Raman and hyper-Raman nanosensors. *Nano Letters* **7**, 2819–2823 (2007).

[206] Stone, V., Johnston, H. & Clift, M. Air pollution, ultrafine and nanoparticle toxicology: cellular and molecular interactions. *IEEE Transactions on Nanobioscience* **6**, 331–340 (2007).

[207] Vandebriel, R. J. & De Jong, W. H. A review of mammalian toxicity of ZnO nanoparticles. *Nanotechnology, Science and Applications* **5**, 61–71 (2012).

[208] Lu, S. *et al.* Comparison of cellular toxicity caused by ambient ultrafine particles and engineered metal oxide nanoparticles. *Particle and Fibre Toxicology* **12**, 5 (2015).

[209] Deng, X. *et al.* PM2.5-induced oxidative stress triggers autophagy in human lung epithelial A549 cells. *Toxicology in vitro* **27**, 1762–1770 (2013).

[210] Pisani, C. *et al.* High-throughput, quantitative assessment of the effects of low-dose silica nanoparticles on lung cells: grasping complex toxicity with a great depth of field. *BMC Genomics* **16**, 315 (2015).

[211] Casey, J. R., Grinstein, S. & Orlowski, J. Sensors and regulators of intracellular pH. *Nature Reviews Molecular Cell Biology* **11**, 50–61 (2010).

[212] Osman, J. J., Birch, J. & Varley, J. The response of GS-NS0 myeloma cells to single and multiple pH perturbations. *Biotechnology and Bioengineering* **79**, 398–407 (2002).

[213] Khajah, M. A., Almohri, I., Mathew, P. M. & Luqmani, Y. A. Extracellular alkaline pH leads to increased metastatic potential of estrogen receptor silenced endocrine resistant breast cancer cells. *PLoS One* **8**, e76327 (2013).

[214] Yoon, S. K., Song, J. Y. & Lee, G. M. Effect of low culture temperature on specific productivity, transcription level, and heterogeneity of erythropoietin in Chinese hamster ovary cells. *Biotechnology and Bioengineering* **82**, 289–298 (2003).

[215] Frigault, M. M., Lacoste, J., Swift, J. L. & Brown, C. M. Live-cell microscopy - tips and tools. *Journal of Cell Science* **122**, 753–767 (2009).

[216] DeBerardinis, R. J. Good neighbours in the tumour stroma reduce oxidative stress. *Nature Cell Biology* **14**, 235–236 (2012).

[217] Khramtsov, V. V. & Gillies, R. J. Janus-faced tumor microenvironment and redox. *Antioxidants & Redox Signaling* **21**, 723–729 (2014).

[218] Ren, K., Chen, Y. & Wu, H. New materials for microfluidics in biology. *Current Opinion in Biotechnology* **25**, 78–85 (2014).

[219] Jiang, S. *et al.* Oxidant-induced apoptosis in human retinal pigment epithelial cells: dependence on extracellular redox state. *Investigative Opthalmology & Visual Science* **46**, 1054–1061 (2005).

Appendix

Biochemical Society TRANSACTIONS

Redox Regulation in Health and Disease: a Celebration of 50 Years of the Keilin Memorial Lecture

A Biochemical Society Focused Meeting held at The Royal Society, Edinburgh, U.K., 19–21 March 2014. Organized and Edited by Colin Campbell (University of Edinburgh, U.K.), Ian Megson (University of the Highlands and Islands, U.K.) and Mark Miller (University of Edinburgh, U.K.).

Ratiometric biological nanosensors

Kate M. Fisher* **and Colin J. Campbell*[1]**

*EaStCHEM School of Chemistry, University of Edinburgh, Edinburgh EH9 3JJ, U.K.

Abstract

The measurement of intracellular analytes has been key in understanding cellular processes and function, and the use of biological nanosensors has revealed the spatial and temporal variation in their concentrations. In particular, ratiometric nanosensors allow quantitative measurements of analyte concentrations. The present review focuses on the recent advances in ratiometric intracellular biological nanosensors, with an emphasis on their utility in measuring analytes that are important in cell function.

Introduction

Intracellular biological nanosensors are an important tool in the biochemist's arsenal of techniques for the study of cellular processes. They can provide information about changes in highly regulated properties critical to cell survival, such as pH, redox potential and concentrations of oxygen and Ca^{2+}. For the purposes of the present review, we limit ourselves to sensors whose output is a ratio of two signals and which respond reversibly to changes in the intracellular environment. In our opinion, such sensors are desirable since their output is independent of absolute sensor concentration and they can be used to monitor concentrations in live cells. Furthermore, we limit ourselves to sensors whose utility has been verified in live cells.

The most common intracellular nanosensors are those based on fluorescence. Fluorescence is an established imaging modality that is highly sensitive and can have excellent spatial resolution [1]. Broadly speaking, there are two types of fluorescent sensors: small-molecule dyes and proteins. Dyes can be synthesized using well-established chemical routes and their photophysical characteristics are generally well understood. Fluorescent proteins derived from jellyfish and corals have enabled researchers to develop a range of proteins, which (through genetic engineering) can be adapted to sensing specific analytes and be targeted to specific organelles. Derivatives have been developed that are photostable and have a range of excitation/emission wavelengths that allow spectral multiplexing [2].

The following sections describe selected examples of the latest advances in nanosensors for the monitoring of various components important for cellular function.

pH

pH is a tightly regulated parameter in cells, because protein structure and function can be regulated by pH changes and pH differences drive critically important metabolic processes such as oxidative phosphorylation [3]. pH is known to be modulated during many different cellular processes (cell cycle, apoptosis and signalling) and can be regulated by many different methods, for example the pH-buffering capacity provided by weak acids and bases, and the various exchanger and co-transporter proteins which couple proton or HCO_3^- transport across the plasma membrane with other ions.

Dysregulation of metabolism caused by factors such as hypoxia, or high demand for ATP (in organs such as the brain or heart), can lead to the build-up of acidic products such as lactic acid. This acidification is thought to play a role

Key words: fluorescence, nanosensor, surface-enhanced Raman spectroscopy (SERS), ratiometric nanosensor.

Abbreviations: GECI, genetically encoded Ca^{2+} indicator; HPF, 2-[6-(4′-hydroxy)phenoxy-3*H*-xanthen-3-on-9-yl]benzoic acid; LPS, lipopolysaccharide; RNS, reactive nitrogen species; roGFP, reduction–oxidation-sensitive GFP; ROS, reactive oxygen species; SERS, surface-enhanced Raman spectroscopy.

[1]To whom correspondence should be addressed (email colin.campbell@ed.ac.uk).

in the pathology of cancer [4] and neurodegenerative diseases [5].

The endosome–lysosome pathway is an important cellular mechanism in sorting material and defence from foreign bodies, and the pH change in the pathway is in the order of more than 2 pH units (or a 100-fold change in concentration of H^+) [6]. This is a challenge for single-dye pH sensors as the effective dynamic range of most commercially available dyes is less than 2 pH units [7]. However, two separate groups have developed triple-labelled nanosensors containing one reference dye and two sensor dyes whose multiplexing allows the effective pH range of the sensor to be extended to over 3 pH units and, in both cases, the dyes were incorporated within a cross-linked polymer nanoparticle [7,8]. The nanosensors were taken up into endosomes and transported to lysosomes, and the pH was measured to be approximately pH 4.5 and 5.08 after 24 h respectively. This is an interesting approach to sensor design, since the particle allows several 'modules' to be assembled and protects the dyes from direct interaction with cellular components without stopping the diffusion of protons.

To extend the utility of these nanosensors, they can be targeted to specific organelles by adding specific targeting molecules. One study used a targeting peptide that allowed the nanosensors to escape endosomes, and measured the cytoplasmic pH to be 7.1 [9]. Using two-photon fluorescence improved the signal to noise ratio and reduced cellular autofluorescence compared with one-photon fluorescence.

Since the performance of many nanosensors for other analytes can be affected by pH fluctuations, a useful approach is to use dual probes so that a correction for pH can be made for the analyte under investigation. This requires that the excitation or emission wavelengths of the individual probes do not overlap. For example, a GFP ATP sensor has been partnered with a RFP pH sensor [10]. Not only does this allow ATP measurements to be corrected for pH, but also pH levels themselves can be measured, as pH changes are associated with changes in metabolism. Co-expression of the pH sensor with the ATP sensor in the cytoplasm showed that complete glucose withdrawal decreased cytoplasmic pH and ATP levels, and pH recovery from an acid insult was delayed in glucose-starved cells that were subsequently re-fed glucose.

Ca^{2+} ion concentration

Ca^{2+} is an important ion, used as a second messenger in cell signalling, and has many different signalling functions. The diverse effects are distinguished via differences in location, amplitude, duration and frequency of the Ca^{2+} signal, so measuring Ca^{2+} levels with temporal and spatial resolution is key in the study of cell physiology and signalling [11]. Examples of the diversity of Ca^{2+} function include build-up of Ca^{2+} in mitochondria in the regulation of apoptosis [12], influx of Ca^{2+} into the nerve terminal causing neurotransmitter release into the synaptic cleft [13], and the Ca^{2+} wave that triggers oocyte activation after fertilization [14].

GECIs (genetically encoded Ca^{2+} indicators) are fusions of a Ca^{2+} sensor domain and a combination of two fluorescent proteins, and can be expressed in the cells of interest. They exhibit good brightness and photostability, and they can also be targeted to specific organelles, thus allowing the spatial and temporal resolution required to untangle the mechanisms causing the signalling [11].

In GECIs, the sensor domain consists of a known Ca^{2+}-binding protein, commonly calmodulin, and a linker. Ca^{2+} binding causes a structural shift in the linker, altering the distance between the fluorescent proteins [15]. However, calmodulin is known to have different targets in the cell, which could interfere with cellular processes. New probes based on aequorin [16,17] or troponin [18] do not interfere with endogenous calmodulin, but it is uncertain whether they might bind to other targets and interfere with cellular function in other ways. Both calmodulin and troponin can bind up to four Ca^{2+} ions per molecule [19], so binding is non-linear and buffering of Ca^{2+} could occur [20]. Recent advances have been in the areas of optimizing FRET linkers and varying donor and receptor fluorescent proteins to improve stability and brightness and by engineering a smaller troponin to only bind one or two Ca^{2+} ions [20].

Ding et al. [21] expressed two spectrally distinct Ca^{2+} nanosensors in the cytoplasm and nucleus of HeLa cells, and showed histidine-evoked Ca^{2+} spikes in both compartments. They also expressed both Ca^{2+} and caspase 3 nanosensors in the cytoplasm of HeLa cells and induced apoptosis with staurosporine. The caspase 3 nanosensor was able to detect increased levels of caspase 3, without any change in Ca^{2+} levels detected by the Ca^{2+} nanosensor. This method provides a useful way to monitor the dynamics of signalling and execution during apoptosis.

Some cells have voltage-gated Ca^{2+} channels that open in response to action potentials; these short-lived Ca^{2+} pulses can be used to investigate neural activity in living animals. Expression of a Cameleon GECI in mouse barrel cortex allowed the detection of Ca^{2+} channel activation in freely moving animals in response to movement [22]. Expression of a troponin-based FRET GECI in mouse retinal cone receptors was used to investigate the effects on Ca^{2+} levels of light-stimulation and •NO application [23]. This showed large changes in Ca^{2+} in cone terminals, but not in other areas, indicating tight spatial control of Ca^{2+} dynamics.

Oxygen

Oxygen is needed for cellular respiration, and any deficiency in oxygen causes ischaemia, as seen in conditions such as heart attack and stroke. Many cancer therapies rely on oxygen being present in tumours, as they convert triplet O_2 into the more destructive singlet O_2 [24]. However, as tumours grow, abnormal formation of blood vessels results in regions of tumours that are hypoxic; this may mean that treatments are ineffective and lead to disease relapse [25]. Imaging the distribution of oxygen in tumours is therefore essential to understand tumour growth, heterogeneity and response to therapy. Similarly, imaging the distribution of oxygen in

Figure 1 | Pathways of intracellular ROS/RNS production: breakdown of $O_2^{\bullet -}$ leading to various ROS/RNS

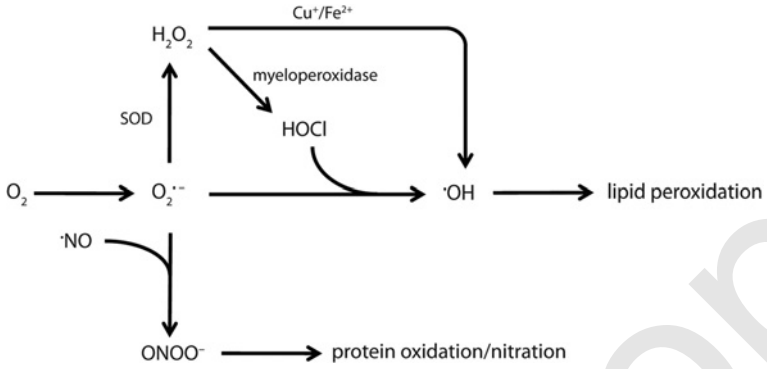

the stem cell niche is important since oxygen tension is thought to be central in controlling pathways responsible for proliferation and differentiation [26,27].

The oxygen levels throughout neurospheres (clusters of neural stem cells) were measured with a polymer nanoparticle encapsulating reference and O_2-sensor dyes [28]. Adding the nanosensor during formation of the neurospheres ensured distribution of the nanosensor throughout the neurospheres. The O_2 concentration was found to be significantly lower in the interior of the neurosphere than at the surface. Inhibiting cellular respiration increased O_2 levels, whereas chemical deoxygenation of the medium showed decreased O_2 levels.

Reactive oxygen and nitrogen species

ROS (reactive oxygen species) and RNS (reactive nitrogen species) are a by-product of cellular respiration (Figure 1) and appear to play an important role in signalling [29,30]. In order to understand the roles of these ROS and RNS better, there is currently a significant effort in developing tools that allow quantification with good spatiotemporal resolution. The following section details some recent studies where nanosensors have been employed to study ROS and RNS in cells.

HOCl (hypochlorous acid) is produced in leucocytes through peroxidation of Cl^- ions, and is involved in pathogen destruction [31]. However, unnecessary production of HOCl can lead to inflammatory problems, as in atherosclerosis, neurodegenerative diseases, rheumatoid arthritis and cancer [32]. Peroxynitrite, $ONOO^-$, is formed from $^{\bullet}NO$ and $O_2^{\bullet -}$, and is highly reactive, oxidizing and nitrating proteins and affecting mitochondrial metabolism, and is also involved in pathogen destruction [33]. Differentiating peroxynitrite from other ROS is difficult since probes must use a selective reaction between peroxynitrite and another molecule that does not occur with other oxidizing molecules. Polymeric micelles have been developed that are optically bright and photostable, and which react selectively for $ONOO^-$ over $^{\bullet}NO$, $O_2^{\bullet -}$, $^{\bullet}OH$ and ClO^- [34]. They have been used to demonstrate that tumour cells generate a higher concentration of $ONOO^-$ compared with normal cells. The generation of such ROS may underpin the genomic instability that is a hallmark of cancer [35].

Photoacoustic imaging detects the ultrasound waves generated from localized heating of tissue resulting from near-IR laser radiation and enables non-invasive imaging of tissues at high spatial resolution [36]. Pu et al. [37] designed fluorescent semiconducting polymer nanoparticles that were photoacoustically active. Coupling these to a ROS-sensitive dye that was selective for $ONOO^-$ and ClO^- allowed the detection of increased concentrations of these species in macrophages stimulated with LPS (lipopolysaccharide) or IFNγ (interferon γ). Furthermore, this nanosensor was able to detect *in situ* generated $ONOO^-$ and ClO^- in living mice injected with zymosan.

BSA-protected gold nanoclusters conjugated with a $^{\bullet}OH$-specific probe HPF {2-[6-(4′-hydroxy)phenoxy-3*H*-xanthen-3-on-9-yl]benzoic acid}, designed so that HPF emission reports on $^{\bullet}OH$ and the emission of the nanoclusters acts as a reference signal, have been used to measure $^{\bullet}OH$ concentrations in HeLa cells [38]. The nanoclusters displayed a basal level of fluorescence in resting cells and were able to detect the production of $^{\bullet}OH$ due to LPS stimulation; however, pre-treatment with DMSO, an $^{\bullet}OH$ scavenger, resulted in no increase in $^{\bullet}OH$ concentration.

Redox potential and antioxidants

Antioxidants are enzymes [e.g. catalase and SOD (superoxide dismutase)] or small molecules (e.g. glutathione, cysteine and thioredoxin) that degrade oxidants such as ROS/RNS (Figure 2). Intracellular redox potential is a balance of ROS and antioxidants and is tightly controlled by the cell; too high a potential leads to oxidative stress which is associated with many diseases, e.g. cancer, inflammation, cardiovascular and neurodegenerative diseases [39–41].

The 'gold standard' for ratiometric redox potential measurements is the use of roGFPs (reduction–oxidation-sensitive GFPs), a GFP modified with redox-active surface cysteine residues. Many roGFPs have now been engineered to cover different potential ranges and, like other GFP sensors,

Figure 2 | Degradation of ROS

(**A**) Degradation of $O_2^{\bullet -}$ and H_2O_2. (**B**) Degradation of H_2O_2 and lipid peroxides (LOOH) via the reversible oxidation of glutathione (GSH) and thioredoxin (Trx) by glutathione peroxidases (GPx) and peroxiredoxins (Prx).

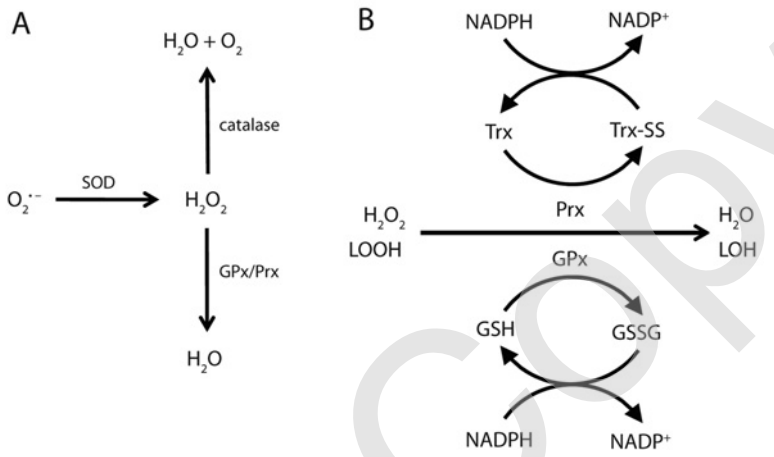

can be expressed in the organelle of choice, including the more oxidizing environment of the endoplasmic reticulum [42].

Recent advances in this field include the use of light sheet-based fluorescent microscopy where the plane is illuminated by two lasers with different emission wavelengths, to detect the oxidized and reduced forms of roGFP. The ratio of the emission intensities at the different excitation wavelengths provides a ratiometric output of glutathione redox potential. This technique was used to measure the effect of staurosporine in glioblastoma spheroids (a 3D tissue model), and showed an increase in oxidation in both the cytoplasm and the mitochondria, with higher levels in the centre of the spheroids compared with the periphery [43]. In another example of organelle-specific targeting, expression of a roGFP in the mitochondria of rat islet β-cells measured an increase in mitochondrial oxidation on addition of exogenous H_2O_2 and on glucose starvation [44].

Cysteine is discriminated from most other amino acids by its strong nucleophilicity, but it is difficult to distinguish between different thiols, e.g. glutathione and cysteine, using dye-based nanosensors [45]. However, progress has been made in this area with the development of fluorescent nanosensors that use the cysteine-mediated cleavage of an acrylic acid moiety [46] or cysteine-mediated spirocyclization [47]. Since the reaction requires the presence of a free amine adjacent to the thiol group, these nanosensors are specific to free cysteine and homocysteine, and are unreactive when cysteine is incorporated in a larger peptide or protein such as glutathione.

Fluorescent nanosensors have been an invaluable tool in the measurement of analytes and in the elucidation of Ca^{2+}-mediated signalling. However, the drawbacks of using fluorescent nanosensors include problems with photostability, photobleaching and cell autofluorescence at visible wavelengths. Furthermore, for investigating parameters

Figure 3 | Redox-active reporter molecules can report on redox potential

Top: structure, electron transfer scheme and standard reduction potential for a reporter molecule; bottom: potential-dependent changes in SER spectra.

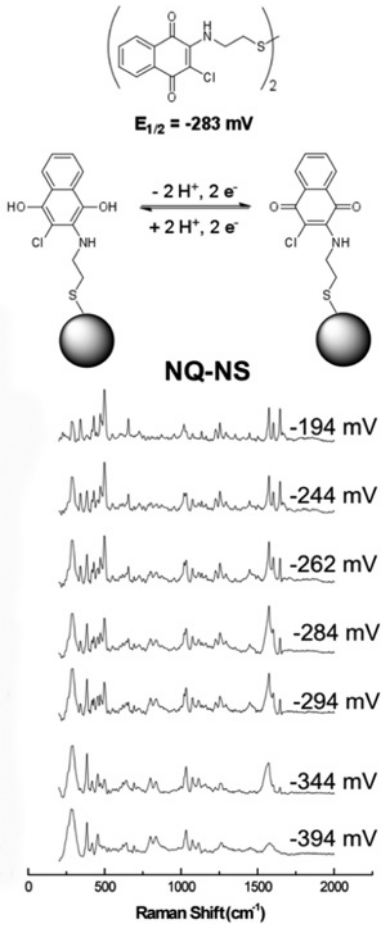

such as redox potential, which is not an analyte, but a consequence of the concentrations of ROS and antioxidants, measuring the contribution of all the individual species is not feasible.

Our laboratory has developed a method of measuring intracellular redox potential independently of individual ROS/antioxidants, using SERS (surface-enhanced Raman spectroscopy). Raman spectroscopy detects inelastic Stokes scattering of photons by molecular bonds, and is used to identify the types of bonds present in molecules. We have designed redox-sensitive reporter molecules, adsorbed on to gold nanoshells [48]; the use of gold nanoshells allows an intensity enhancement of $>10^6$. The reporter molecules change structure depending on their oxidation state, and SERS of the coated nanoshells allows spectral discrimination between the reduced and oxidized forms. By recording spectra at different redox potentials using a potentiostat, a calibration curve can be obtained that shows how the SERS spectrum changes in response to local redox potential changes (Figure 3).

The coated nanoshells are easily taken up into the cytoplasm and cause no toxic effects in the cells that we have used [49]. Our method does not suffer from photostability or photobleaching problems and also does not require the time-consuming expression of fluorescent proteins in cells. Changes in redox potential can be measured with spatial and temporal resolution, and live-cell imaging techniques can be utilized to enable long-term monitoring of redox potential. Furthermore, the use of IR wavelengths minimizes phototoxicity and cellular autofluorescence. We have used our nanosensors to show the correlation between redox potential and caspase activity during apoptosis in mouse fibroblast cells [48]. We believe that the benefits offered through the use of ratiometric nanosensors will lead to their continued and increased use in studies of cell biology.

References

1 Bunt, G. and Wouters, F.S. (2004) Visualization of molecular activities inside living cells with fluorescent labels. Int. Rev. Cytol. **237**, 205–277 CrossRef PubMed

2 Day, R.N. and Davidson, M.W. (2009) The fluorescent protein palette: tools for cellular imaging. Chem. Soc. Rev. **38**, 2887–2921 CrossRef PubMed

3 Casey, J.R., Grinstein, S. and Orlowski, J. (2010) Sensors and regulators of intracellular pH. Nat. Rev. Mol. Cell Biol. **11**, 50–61 CrossRef PubMed

4 Parks, S.K., Chiche, J. and Pouysségur, J. (2011) pH control mechanisms of tumor survival and growth. J. Cell. Physiol. **226**, 299–308 CrossRef PubMed

5 Ruffin, V.A., Salameh, A.I., Boron, W.F. and Parker, M.D. (2014) Intracellular pH regulation by acid–base transporters in mammalian neurons. Front. Physiol. **5**, 43 CrossRef PubMed

6 Paroutis, P., Touret, N. and Grinstein, S. (2004) The pH of the secretory pathway: measurement, determinants, and regulation. Physiology **19**, 207–215 CrossRef PubMed

7 Benjaminsen, R.V., Sun, H., Henriksen, J.R., Christensen, N.M., Almdal, K. and Andresen, T.L. (2011) Evaluating nanoparticle sensor design for intracellular pH measurements. ACS Nano **5**, 5864–5873 CrossRef PubMed

8 Song, X., Li, H., Tong, W. and Gao, C. (2014) Fabrication of triple-labeled polyelectrolyte microcapsules for localized ratiometric pH sensing. J. Colloid Interface Sci. **416**, 252–257 CrossRef PubMed

9 Ray, A., Koo Lee, Y.-E., Epstein, T., Kim, G. and Kopelman, R. (2011) Two-photon nano-PEBBLE sensors: subcellular pH measurements. Analyst **136**, 3616–3622 CrossRef PubMed

10 Tantama, M., Hung, Y.P. and Yellen, G. (2011) Imaging intracellular pH in live cells with a genetically encoded red fluorescent protein sensor. J. Am. Chem. Soc. **133**, 10034–10037 CrossRef PubMed

11 Grienberger, C. and Konnerth, A. (2012) Imaging calcium in neurons. Neuron **73**, 862–885 CrossRef PubMed

12 Duchen, M.R. (1999) Contributions of mitochondria to animal physiology: from homeostatic sensor to calcium signalling and cell death. J. Physiol. **516**, 1–17 CrossRef PubMed

13 Südhof, T.C. (2013) Neurotransmitter release: the last millisecond in the life of a synaptic vesicle. Neuron **80**, 675–690 CrossRef PubMed

14 Machaca, K. (2007) Ca^{2+} signaling differentiation during oocyte maturation. J. Cell. Physiol. **213**, 331–340 CrossRef PubMed

15 Miyawaki, A., Llopis, J., Heim, R., McCaffery, J.M., Adams, J.A., Ikura, M. and Tsien, R.Y. (1997) Fluorescent indicators for Ca^{2+} based on green fluorescent proteins and calmodulin. Nature **388**, 882–887 CrossRef PubMed

16 Brini, M., Marsault, R., Bastianutto, C., Alvarez, J., Pozzan, T. and Rizzuto, R. (1995) Transfected aequorin in the measurement of cytosolic Ca^{2+} concentration ($[Ca^{2+}]_c$): a critical evaluation. J. Biol. Chem. **270**, 9896–9903 CrossRef PubMed

17 Rodriguez-Garcia, A., Rojo-Ruiz, J., Navas-Navarro, P., Aulestia, F.J., Gallego-Sandin, S., Garcia-Sancho, J. and Alonso, M.T. (2014) GAP, an aequorin-based fluorescent indicator for imaging Ca^{2+} in organelles. Proc. Natl. Acad. Sci. U.S.A. **111**, 2584–2589 CrossRef PubMed

18 Garaschuk, O., Griesbeck, O. and Konnerth, A. (2007) Troponin C-based biosensors: a new family of genetically encoded indicators for *in vivo* calcium imaging in the nervous system. Cell Calcium **42**, 351–361 CrossRef PubMed

19 Nelson, M.R. and Chazin, W.J. (1998) An interaction-based analysis of calcium-induced conformational changes in Ca^{2+} sensor proteins. Protein Sci. **7**, 270–282 CrossRef PubMed

20 Thestrup, T., Litzlbauer, J., Bartholomäus, I., Mues, M., Russo, L., Dana, H., Kovalchuk, Y., Liang, Y., Kalamakis, G., Laukat, Y. et al. (2014) Optimized ratiometric calcium sensors for functional *in vivo* imaging of neurons and T lymphocytes. Nat. Methods **11**, 175–182 CrossRef PubMed

21 Ding, Y., Ai, H.-W., Hoi, H. and Campbell, R.E. (2011) Forster resonance energy transfer-based biosensors for multiparameter ratiometric imaging of Ca^{2+} dynamics and caspase-3 activity in single cells. Anal. Chem. **83**, 9687–9693 CrossRef PubMed

22 Lütcke, H., Murayama, M., Hahn, T., Margolis, D.J., Astori, S., Meyer, S., Göbel, W., Yang, Y., Tang, W., Kügler, S. et al. (2010) Optical recording of neuronal activity with a genetically-encoded calcium indicator in anesthetized and freely moving mice. Front. Neural Circuits **4**, 9 PubMed

23 Wei, T., Schubert, T., Paquet-Durand, F., Tanimoto, N., Chang, L., Koeppen, K., Ott, T., Griesbeck, O., Seeliger, M.W., Euler, T. et al. (2012) Light-driven calcium signals in mouse cone photoreceptors. J. Neurosci. **32**, 6981–6994 CrossRef PubMed

24 Oleinick, N.L., Morris, R.L. and Belichenko, I. (2002) The role of apoptosis in response to photodynamic therapy: what, where, why, and how. Photochem. Photobiol. Sci. **1**, 1–21 CrossRef PubMed

25 Moeller, B.J., Richardson, R.A. and Dewhirst, M.W. (2007) Hypoxia and radiotherapy: opportunities for improved outcomes in cancer treatment. Cancer Metastasis Rev. **26**, 241–248 CrossRef PubMed

26 Gassmann, M., Fandrey, J., Bichet, S., Wartenberg, M., Marti, H.H., Bauer, C., Wenger, R.H. and Acker, H. (1996) Oxygen supply and oxygen-dependent gene expression in differentiating embryonic stem cells. Proc. Natl. Acad. Sci. U.S.A. **93**, 2867–2872 CrossRef PubMed

27 Ji, A.-R., Ku, S.-Y., Cho, M.S., Kim, Y.Y., Kim, Y.J., Oh, S.K., Kim, S.H., Moon, S.Y. and Choi, Y.M. (2010) Reactive oxygen species enhance differentiation of human embryonic stem cells into mesendodermal lineage. Exp. Mol. Med. **42**, 175–186 CrossRef PubMed

28 Kondrashina, A.V., Dmitriev, R.I., Borisov, S.M., Klimant, I., O'Brien, I., Nolan, Y.M., Zhdanov, A.V. and Papkovsky, D.B. (2012) A phosphorescent nanoparticle-based probe for sensing and imaging of (intra) cellular oxygen in multiple detection modalities. Adv. Funct. Mater. **22**, 4931–4939 CrossRef

29 D'Autréaux, B. and Toledano, M.B. (2007) ROS as signalling molecules: mechanisms that generate specificity in ROS homeostasis. Nat. Rev. Mol. Cell. Biol. **8**, 813–824 CrossRef PubMed

30 Bryan, N.S., Bian, K. and Murad, F. (2009) Discovery of the nitric oxide signaling pathway and targets for drug development. Front. Biosci. (Landmark Ed.) **14**, 1–18 CrossRef PubMed

31 Harrison, J.E. and Schultz, J. (1976) Studies on the chlorinating activity of myeloperoxidase. J. Biol. Chem. **251**, 1371–1374 PubMed
32 Klebanoff, S.J. (2005) Myeloperoxidase: friend and foe. J. Leukoc. Biol. **77**, 598–625 CrossRef PubMed
33 Radi, R. (2013) Peroxynitrite, a stealthy biological oxidant. J. Biol. Chem. **288**, 26464–26472 CrossRef PubMed
34 Tian, J., Chen, H., Zhuo, L., Xie, Y., Li, N. and Tang, B. (2011) A highly selective, cell-permeable fluorescent nanoprobe for ratiometric detection and imaging of peroxynitrite in living cells. Chemistry **17**, 6626–6634 CrossRef PubMed
35 Hanahan, D. and Weinberg, R.A. (2011) Hallmarks of cancer: the next generation. Cell **144**, 646–674 CrossRef PubMed
36 Zackrisson, S., van de Ven, S.M.W.Y. and Gambhir, S.S. (2014) Light in and sound out: emerging translational strategies for photoacoustic imaging. Cancer Res. **74**, 979–1004 CrossRef PubMed
37 Pu, K., Shuhendler, A.J., Jokerst, J.V., Mei, J., Gambhir, S.S., Bao, Z. and Rao, J. (2014) Semiconducting polymer nanoparticles as photoacoustic molecular imaging probes in living mice. Nat. Nanotechnol. **9**, 233–239 CrossRef PubMed
38 Zhuang, M., Ding, C., Zhu, A. and Tian, Y. (2014) A ratiometric fluorescence probe for monitoring hydroxyl radical in live cells based on gold nanoclusters. Anal. Chem. **86**, 1829–1836 CrossRef PubMed
39 Barnham, K.J., Masters, C.L. and Bush, A.I. (2004) Neurodegenerative diseases and oxidative stress. Nat. Rev. Drug Discov. **3**, 205–214 CrossRef PubMed
40 Benz, C.C. and Yau, C. (2008) Ageing, oxidative stress and cancer: paradigms in parallax. Nat. Rev. Cancer **8**, 875–879 CrossRef PubMed
41 Kim, Y.-W., West, X.Z. and Byzova, T.V. (2013) Inflammation and oxidative stress in angiogenesis and vascular disease. J. Mol. Med. **91**, 323–328 CrossRef PubMed
42 van Lith, M., Tiwari, S., Pediani, J., Milligan, G. and Bulleid, N.J. (2011) Real-time monitoring of redox changes in the mammalian endoplasmic reticulum. J. Cell Sci. **124**, 2349–2356 CrossRef PubMed
43 Schickinger, S., Bruns, T., Wittig, R., Weber, P., Wagner, M. and Schneckenburger, H. (2013) Nanosecond ratio imaging of redox states in tumor cell spheroids using light sheet-based fluorescence microscopy. J. Biomed. Opt. **18**, 126007 CrossRef PubMed
44 Roma, L.P., Duprez, J., Takahashi, H.K., Gilon, P., Wiederkehr, A. and Jonas, J.C. (2012) Dynamic measurements of mitochondrial hydrogen peroxide concentration and glutathione redox state in rat pancreatic β-cells using ratiometric fluorescent proteins: confounding effects of pH with HyPer but not roGFP1. Biochem. J. **441**, 971–978 CrossRef PubMed
45 Niu, L.-Y., Guan, Y.-S., Chen, Y.-Z., Wu, L.-Z., Tung, C.-H. and Yang, Q.-Z. (2012) BODIPY-based ratiometric fluorescent sensor for highly selective detection of glutathione over cysteine and homocysteine. J. Am. Chem. Soc. **134**, 18928–18931 CrossRef PubMed
46 Zhu, B., Guo, B., Zhao, Y., Zhang, B. and Du, B. (2014) A highly sensitive ratiometric fluorescent probe with a large emission shift for imaging endogenous cysteine in living cells. Biosens. Bioelectron. **55**, 72–75 CrossRef PubMed
47 Lv, H., Yang, X.-F., Zhong, Y., Guo, Y., Li, Z. and Li, H. (2014) Native chemical ligation combined with spirocyclization of benzopyrylium dyes for the ratiometric and selective fluorescence detection of cysteine and homocysteine. Anal. Chem. **86**, 1800–1807 CrossRef PubMed
48 Auchinvole, C.A. R., Richardson, P., McGuinnes, C., Mallikarjun, V., Donaldson, K., McNab, H. and Campbell, C.J. (2012) Monitoring intracellular redox potential changes using SERS nanosensors. ACS Nano **6**, 888–896 CrossRef PubMed
49 Ochsenkuhn, M.A., Jess, P.R. T., Stoquert, H., Dholakia, K. and Campbell, C.J. (2009) Nanoshells for surface-enhanced Raman spectroscopy in eukaryotic cells: cellular response and sensor development. ACS Nano **3**, 3613–3621 CrossRef PubMed

Received 30 May 2014
doi:10.1042/BST20140161